Karlsruher Institut für Technologie

Schriftenreihe
Kontinuumsmechanik im Maschinenbau

24

Sebastian Gajek

Deep material networks for efficient scale-bridging in thermomechanical simulations of solids

KIT Scientific Publishing

Sebastian Gajek

Deep material networks for efficient scale-bridging in thermomechanical simulations of solids

Schriftenreihe
Kontinuumsmechanik im Maschinenbau
Band 24

Karlsruher Institut für Technologie (KIT)
Institut für Technische Mechanik
Bereich Kontinuumsmechanik

Hrsg. Prof. Dr.-Ing. habil. Thomas Böhlke

Eine Übersicht aller bisher in dieser Schriftenreihe erschienenen Bände finden Sie am Ende des Buchs.

Deep material networks for efficient scale-bridging in thermomechanical simulations of solids

by
Sebastian Gajek

KIT Scientific Publishing

Karlsruher Institut für Technologie
Institut für Technische Mechanik
Bereich Kontinuumsmechanik

Deep material networks for efficient scale-bridging
in thermomechanical simulations of solids

Zur Erlangung des akademischen Grades eines Doktor-Ingenieurs
von der KIT-Fakultät für Maschinenbau des Karlsruher Instituts für
Technologie (KIT) genehmigte Dissertation

von Sebastian Gajek, M.Sc.

Tag der mündlichen Prüfung: 22. Februar 2023
Hauptreferenten: Prof. Dr.-Ing. Thomas Böhlke
Korreferent: Jun.-Prof. Dr. rer. nat. Matti Schneider
Korreferent: Prof. Dr. Jan Zeman

Impressum

Scientific Publishing

Karlsruher Institut für Technologie (KIT)
KIT Scientific Publishing
Straße am Forum 2
D-76131 Karlsruhe

KIT Scientific Publishing is a registered trademark
of Karlsruhe Institute of Technology.
Reprint using the book cover is not allowed.

www.ksp.kit.edu

Print on Demand 2023 – Gedruckt auf FSC-zertifiziertem Papier

ISSN 2192-693X
ISBN 978-3-7315-1278-3
DOI 10.5445/KSP/1000155688

To my beloved daughters Charlotte and Amilia. From the moment you were born, you have brought so much joy and happiness into my life.

Zusammenfassung

Viele Verbundwerkstoffe weisen ein stark nichtlineares und inelastisches Materialverhalten auf. Hierbei hängt das makroskopische mechanische Verhalten von der geometrischen Komposition der Einzelphasen und deren individuelle Materialverhalten auf der mikroskopischen Skala ab. Multiskalensimulationen sind Werkzeuge, um solche gekoppelten Probleme zu lösen. Konventionelle Ansätze, die beispielsweise die Finite Elemente Methode zur Diskretisierung und dem gekoppelten Lösen des makroskopischen und mikroskopischen Problems verwenden, fehlen jedoch die numerische Effizienz, um auch Probleme industrieller Komplexität auf handelsüblicher Hardware berechnen zu können.

Diese Arbeit untersucht einen datengetriebenen und mikromechanisch inspirierten Homogenisierungsansatz, der als Deep Material Networks (DMN) bezeichnet wird. In Zweiskalensimulationen fungieren DMNs als Ersatzmodelle für das mikroskopische Problem. Hierdurch lässt sich Mikrostrukturinformation in eine makroskopische Simulation integrieren.

Zu Beginn dieser Arbeit werden die mathematischen Grundlagen der DMNs gelegt. Das auf linear elastischen Vorberechnungen beruhende Training und die mit außerordentlicher Genauigkeit mögliche Extrapolation auf nichtlineare und inelastische Problemen wird analysiert. Hierfür werden Techniken aus der Theorie dynamischer Systeme verwendet und gezeigt, dass das effektive inelastische Materialverhalten jeder Mikrostruktur in erster Ordnung in der Dehnrate durch lineare Lokalisierung bestimmt wird.

Im Weiteren wird eine neue DMN-Formulierung vorgestellt, die sich durch eine reduzierte Anzahl von Freiheitsgraden auszeichnet und somit die Robustheit der Parameteridentifikation verbessert. Ein robustes und effizientes Verfahren zum Lösen von nichtlinearen DMNs wird vorgestellt, welches die Simulation von komplexen makroskopischen Strukturen mit geringem Berechnungsaufwand ermöglicht. Weiterhin wird gezeigt, dass DMNs sowohl thermodynamische Konsistenz als auch Monotonie der Einzelphasen erhalten. Beides sind essenzielle Eigenschaften, die von vielen anderen datengetriebenen Homogenisierungsansätzen nicht ohne Weiteres gewährleistet werden können.

Ein neuer Interpolationsansatz wird vorgestellt, der die Berücksichtigung von fluktuierenden Mikrostrukturcharakteristiken in makroskopischen Simulationen ermöglicht. Die Effizienz des Ansatzes wird demonstriert, indem die komplette Prozesskette eines Bauteils aus kurzfaserverstärktem Polyamid simuliert wird. Im Weiteren wir der Ansatz verwendet, um durch den Herstellungsprozess bedingte Unsicherheiten in Bauteilen aus Sheet Molding Compound simulativ zu ermitteln.

DMNs werden erweitert, um mehrskalige, thermomechanisch gekoppelte Problemstellungen zu berechnen. Die thermomechanische Kopplung zeichnet sich durch die Kopplung der makroskopischen absoluten Temperatur auf das mechanische Verhalten der Einzelphasen auf der mikroskopischen Skala aus. Weiterhin sind deformationsinduzierte Änderungen der makroskopischen absoluten Temperatur als Folge von mechanischer Dissipation und Entropieänderungen auf der mikroskopischen Skala zu beobachten. Es wird gezeigt, dass der gewählte Ansatz Selbsterwärmungseffekte in kurzfaserverstärkten Polymeren mit hoher Genauigkeit vorhersagt und demonstriert, dass die Berücksichtigung solcher Effekte unerlässlich für Multiskalensimulationen von polymerbasierten Verbundwerkstoffen ist.

Summary

Many composite materials exhibit a highly nonlinear and inelastic material behavior. In this context, the macroscopic mechanical behavior depends on the geometric composition of the phases and their individual material behavior on the microscopic scale. Concurrent multiscale simulation approaches are powerful tools to solve such coupled problems. However, conventional approaches, such as using the finite element method to discretize and solve the macroscopic and microscopic problem in a coupled fashion, lack the numerical efficiency to solve problems of industrial complexity on commodity hardware.

In this thesis, we investigate the data-driven and micromechanics-inspired homogenization approach called deep material networks (DMN). In two-scale simulations, DMNs act as surrogate models for the microscopic problem. This allows for microstructure information to be integrated into a macroscopic simulation.

At the beginning of this thesis, we lay the mathematical foundation of DMNs. We analyze the training based on linear elastic precomputations and the extrapolation to nonlinear and inelastic problems with extraordinary accuracy. For this purpose, techniques from dynamical systems theory are used, and it is shown that the effective inelastic material behavior of any microstructure is determined by linear elastic localization to first order in the strain rate.

Furthermore, we present a new DMN formulation which is characterized by a reduced number of degrees of freedom, thus improving the robustness of the parameter identification process. We present a robust and efficient solution technique for nonlinear DMNs allowing

for the simulation of complex macroscopic structures with minimal computational effort. In addition, it is shown that DMNs preserve both thermodynamic consistency and monotonicity of the phases. Both are essential properties that typically cannot be guaranteed by many other data-driven homogenization approaches.

A new interpolation technique is presented that enables the consideration of fluctuating microstructure characteristics in macroscopic simulations. We demonstrate the efficiency of the approach by considering a complete process chain of a component made of a short fiber reinforced polyamide. Furthermore, the approach is used to determine process-induced uncertainties in sheet molding compound components.

We extend the DMN framework to treat thermomechanically coupled multiscale problems. The thermomechanical coupling is characterized by the coupling of the macroscopic absolute temperature to the mechanical behavior of the constituents on the microscopic scale. Furthermore, deformation-induced changes of the macroscopic absolute temperature as a consequence of mechanical dissipation and entropy changes on the microscopic scale can be observed. We show that our approach predicts self-heating effects in short fiber reinforced polymers with high accuracy and demonstrate that considering such effects is essential for the multiscale analysis of polymer-based composite materials.

Acknowledgments

First and foremost, I would like to express my deepest gratitude to both of my supervisors, Prof. Thomas Böhlke and Jun.-Prof. Matti Schneider. Without their guidance and constant constructive feedback, this endeavor would not have been possible. In particular, navigating through the intricate fields of continuum mechanics and mathematics has been challenging and stimulating. It has decisively shaped my scientific work. I would also like to thank Prof. Dr. Jan Zeman for kindly reviewing this dissertation, for his interest in my work and for his many helpful comments and remarks. I very much appreciate that you took the long journey from Prague to Karlsruhe to attend the examination in person.

I am very grateful to the whole staff at the Institute of Engineering Mechanics, Chair for Continuum Mechanics, for the many pleasant hours spent together in the coffee kitchen (in the winter) or on the fire escape (in the summer), at conferences or during private activities. I would especially like to thank my colleagues for always making coffee when I needed it the most, for always having someone around to help me return my apocalyptic amount of returnable bottles, and for many more fond memories of barbecues, hot dog parties, beer breaks, coffee breaks, mate breaks, Spezi breaks, cake breaks and so forth. In particular, I would like to give credit where credit is due to Ute, Ariane, Tom and Helga for their invaluable administrative support and their willingness to deal with all teaching, non-teaching, research and non-research related problems that came up and which they so meticulously dealt with. How many hours of work you have saved me and the rest of the institute I would rather not quantify.

Many thanks also go to my mother and my in-laws for many years of support and for putting up with my grumpy monosyllabic answers to any work-related question. I am most grateful to my wife Nigora for having my back during this whole time. Throughout the years, you have been my constant source of inspiration and motivation, pushing me to pursue my dreams and reach for the stars.

Elsevier, Springer and Wiley are gratefully acknowledged for providing the opportunity to incorporate my corresponding publications into this thesis.

The research documented in this doctoral thesis has been partially funded by the German Research Foundation (DFG), both within the funded project "Kontinuumsmechanische Modellierung des prozessabhängigen kalorischen und thermomechanischen Verhaltens teilkristalliner Polymere" (BO 1466/11-1) and within the International Research Training Group "Integrated engineering of continuous-discontinuous long fiber reinforced polymer structures" (IRTG 2078). The support by the DFG is gratefully acknowledged.

Karlsruhe, May 2023 Sebastian Gajek

Contents

Chapter 1

Introduction[1]

1.1 Motivation

1.1.1 On the need for multiscale simulation approaches

Driven by the need for short development cycles, industrial product development is relying more and more on numerical methods. Computer-aided engineering (CAE) (Rix et al., 1995) bundles a set of powerful tools for simulation and optimization of virtual products with the main goal of reducing the need for physical prototyping and testing to lower costs as well as resource expenditure. Restricting to solid mechanics, the finite element method (FEM) (Fish and Belytschko, 2008) is arguably one of the most commonly used tools for simulating the deformation of solid structures and therefore indispensable for the weight-optimized virtual design of products. Owing its popularity to its versatility, the FEM allows for treating complex geometries as well as enables multiphysics simulations, e.g., considering the coupling of thermal and mechanical problems.

[1] This chapter, and in particular Section 1.2, is based in parts on the introductions of the publications "On the micromechanics of deep material networks" (Gajek et al., 2020), "An FE-DMN method for the multiscale analysis of short fiber reinforced plastic components" (Gajek et al., 2021a), "Efficient two-scale simulations of microstructured materials using deep material networks" (Gajek et al., 2021b) and "An FE-DMN method for the multiscale analysis of thermomechanical composites" (Gajek et al., 2022).

In addition to kinematic relations, universal balance equations and problem-dependent boundary conditions, the FEM requires constitutive laws which capture the material behavior with sufficient accuracy. For material modeling, opposing objectives need to be considered. For instance, a material law should be sufficiently accurate, even for complex multiaxial loading, it should be robust but also quick to evaluate.

A widely used modeling approach, still enjoying great popularity in industry, are phenomenological material models, see, e.g., v. Mises (1913), Hill (1948), Gurson (1977), de Souza Neto et al. (2008) or Dyck and Böhlke (2020) for modeling isotropic and anisotropic plasticity or Bere et al. (2012), Camanho et al. (2013) and Guo and Wu (1999) for phenomenological models of fracture. A phenomenological material model itself is postulated and does not necessarily emerge from physical considerations. The unknown parameters of the model are determined based on real or virtual experiments by minimizing an error function. Indeed, these approaches are typically fast and robust if properly designed. However, they are highly problem-dependent, often need to be identified in a time-consuming and cost-intensive way, and require knowledge and experience to model nonlinear effects, especially if the underlying physical mechanisms are not yet fully understood.

To complicate matters, many structural materials are, in fact, strongly inhomogeneous. Typically, these inhomogeneities manifest at length scales much smaller than the macroscopic component level. The inhomogeneities on the microscopic scale are a product of the internal composition of the material from multiple phases, hence the name composite materials. In addition, many common engineering materials are characterized by a two-way thermomechanical coupling. More precisely, variations in the macroscopic temperature may affect the mechanical performance of the phases on the lower scale, e.g., by thermal softening commonly observed in polymers. Microscopic deformations may lead to changes in the macroscopic temperature as well, for instance,

via changes in entropy or energy dissipation. Consequently, considering the geometry of the microstructure and also taking into account thermo-mechanically coupled phases for predicting the mechanical response of composite materials is a daunting task.

To give an example with a complexity routinely encountered in industrial applications, Figure 1.1a shows a connecting rod made of a metal matrix composite, i.e., an aluminum matrix reinforced by $30\,\mathrm{vol}\%$ ceramic particles. The ceramic particles have a diameter in the micrometer range and thus are much smaller than the component itself. The material properties of aluminum may be considered constant for non-isothermal processes, at least as long as the temperature remains well below the melting point. Yet, aluminum tends to self-heat as a result of plastic deformation, which in turn might lead to thermally induced eigenstrains both on the microscopic and macroscopic scale.

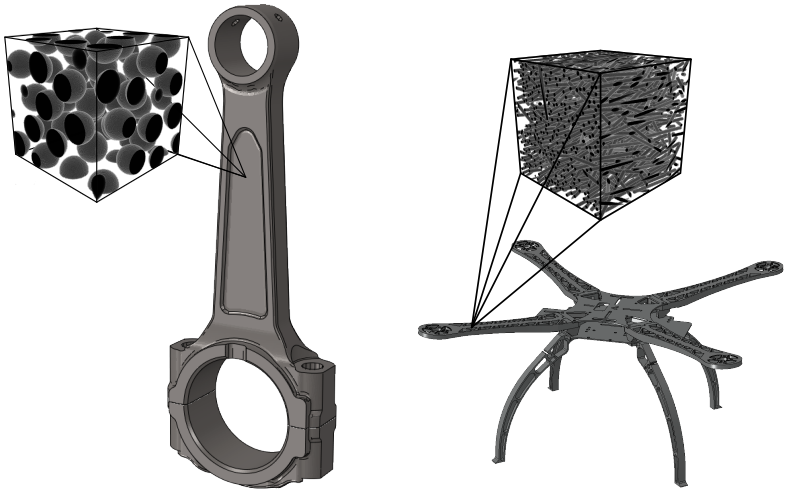

(a) Connecting rod made of a metal matrix composite (Gajek et al., 2021b)

(b) Drone frame made of a short fiber reinforced polyamide (Gajek et al., 2021a)

Figure 1.1: Two examples of macroscopic components with a complex microstructure

As a second example, we consider a short fiber reinforced plastic (SFRP) component. Owing to their formability, short cycle times and low manufacturing costs, SFRP components are commonly used for semi-structural applications. Typically, they comprise fibers with a diameter in the micrometer range which are embedded into a polymer matrix. Usually fillers are added and pores may also be observed. Figure 1.1b depicts an injection molded quadcopter frame made of a short glass fiber reinforced polyamide containing $16\,\mathrm{vol}\%$ fibers with an aspect ratio[2] of 20. The microstructure characteristics, in this example the fiber orientation and the fiber volume fraction, strongly depend on the manufacturing process and fluctuate throughout the component. Both microstructure characteristics have a significant influence on the material behavior, e.g., an anisotropic fiber orientation is expected to lead to an anisotropic material behavior of the composite. In addition, dissipation-induced self-heating is commonly observed for thermoplastic polymers subjected to cyclic loading. As such polymers are particularly sensitive to temperature fluctuations, especially in the vicinity of their glass transition temperature, deformation-induced self-heating effects may significantly influence the mechanical properties of the composite and even lead to premature failure (Katunin, 2019).

A monolithic finite element model of a structural component, also resolving the microstructure heterogeneities, is typically not feasible with today's computational power. As a remedy, many composite materials, including the examples from above, are idealized as homogeneous on the macroscopic scale. Of interest is the effective material behavior, which is obtained by homogenization and which accounts for the geometric composition of the microstructure and the thermomechanically coupled material behavior of the constituents on the lower scale.

[2] The aspect ratio measures the length to diameter ratio.

1.1.2 Key questions of the present work

In this thesis, we restrict to first-order asymptotic homogenization, see also Bensoussan et al. (1978), Sanchez-Palencia (1980) or Bakhvalov and Panasenko (1989) for an overview. Considering thermomechanically coupled constituents, Chatzigeorgiou et al. (2016) applied first-order asymptotic homogenization to composites of small-strain non-isothermal generalized standard materials (Halphen and Nguyen, 1975) and deduced the governing equation on the microscopic scale, the *thermomechanical cell problem*. By solving the thermomechanical cell problem on a suitable microstructure model, the effective, non-isothermal model of the composite emerges naturally.

Using homogenization to obtain an effective material model has the distinct advantage that effects arising from the microstructure are implicitly accounted for. Furthermore, the thermomechanical coupling of the phases may be considered in a natural way.

However, using homogenization introduces additional difficulties, which might be condensed into the following four questions:

1. How can the cell problem be solved efficiently and robustly, or at least the effective material response be approximated with sufficient accuracy, both for arbitrarily nonlinear and inelastic isothermal and non-isothermal phases and complex microstructure morphologies?
2. How can such a method be incorporated into a state-of-the-art FE solver, preferably only relying on the provided interfaces?
3. How can spatially varying microstructure characteristics be accounted for?
4. How can the two-way thermomechanical coupling between the microscopic and macroscopic scale be included into a concurrent two-scale simulation?

To address Question 1, different techniques have been developed for solving the cell problem, ranging from simple analytical approximations

to complicated numerical methods. For instance, analytical homogenization techniques rely on closed-form solutions of the cell problem which may be evaluated cheaply and thus be included in a component scale simulation. Typically, this comes at the cost of using simplifying micromechanical assumptions, e.g., Eshelby's (1957; 1959) solution is only applicable to an isotropic elastic matrix and assumes an infinite domain. Other commonly used analytical homogenization techniques, suitable for elastic as well as inelastic materials, are, e.g., the Mori-Tanaka method (Mori and Tanaka, 1973; Stránský et al., 2011; Kehrer et al., 2020), the self-consistent method (Hill, 1965; Hutchinson, 1976; Nebozhyn et al., 2001), the differential scheme (Norris, 1985) or the Hashin-Shtrikman lower and upper bounds (Hashin and Shtrikman, 1961; 1962; Hashin, 1970; Neumann and Böhlke, 2016; Kehrer et al., 2020). Since analytical homogenization techniques typically depend on simplifying assumptions regarding the statistical properties of the microstructure, they are not suitable for problems with complex microstructure morphologies, complex interactions between the material constituents or a highly nonlinear material behavior of the phases. Also, for heterogeneous materials with a morphology that strongly differs from matrix-inclusion microstructures, analytical methods may yield poor results, see, e.g., Schneider et al. (2018) and Ettemeyer et al. (2020) for examples of such structures.

To consider composites with a complex microstructure and highly nonlinear and inelastic constituents, alternative strategies need to be sought. Here, the major challenge lies with considering internal variables, which encode the deformation history of inelastic materials. As internal variables live naturally on the microscopic scale, they cannot be, in general, "homogenized" to the macroscopic scale. As a remedy, multiscale computational homogenization offers a set of powerful tools for bridging both scales.

1.1.3 Concluding remarks

Before recapitulating the state of the art in multiscale computational homogenization, we finish with some concluding remarks. Using computational homogenization techniques requires an accurate description of the microstructure. In principle, microstructure data may be obtained directly from micro computed tomography (μCT) scans, see, e.g., de Paiva et al. (1996), Shen et al. (2004a) or Schöttl et al. (2020). Typically, operating directly on μCT data is a challenging task for numerous reasons, i.e., high costs for data acquisition, necessary data cleansing, influence of randomness and lack of periodicity. As a remedy, artificial microstructures may be used, which serve as substitutes for real microstructures, and for which essential microstructure characteristics can be controlled, e.g., the fiber volume fraction and fiber orientation in the case of SFRP.

In this thesis, different microstructure generation algorithms are used to obtain realistic microstructure models for different classes of composite materials. For instance, the sequential addition and migration method of Schneider (2017); Mehta and Schneider (2022) for generating short fiber reinforced plastic microstructures, see Figure 1.1b, the RSA-type algorithm of Görthofer et al. (2020) for generating sheet molding compound composite microstructures, and the mechanical contraction method of Williams and Philipse (2003) for generating particle reinforced microstructures, see Figure 1.1a, proved to be powerful tools. Note that microstructure generation is not the focus of this work, we refer the reader to Bargmann et al. (2018) for more information. Furthermore, for efficient stochastic microstructure generation and challenges arising from dealing with randomness, we refer to Novák et al. (2012; 2013) and Doškář et al. (2014; 2020) for microstructure generation and compression based on Wang tiles.

1.2 State of the art

1.2.1 Concurrent two-scale simulations

FE^2 methods, introduced by Renard and Marmonier (1987) and subsequently refined by Smit et al. (1998), Feyel (1999; 2003) and Feyel and Chaboche (2000), furnish each Gauss point of the macroscopic finite element model with a finite element model of the microstructure for which the (thermomechanical) cell problem is solved. Thus, the evolution of the internal variables is accounted for. The FE^2 method for thermomechanical composites was investigated, for instance, in the context of thermo-elastoplasticity (Özdemir et al., 2008b;a), phase transforming polycrystals under dynamic loading (Sengupta et al., 2012) or single-crystal thermo-elastoviscoplasticity (Li et al., 2019). Recently, Tikarrouchine et al. (2019) investigated a short fiber reinforced composite in a concurrent two-scale setting accounting for heat conduction and convection but temperature-independent material properties.

To improve time to solution for solving the (discretized) cell problem, fast Fourier transform (FFT) based micromechanics as envisioned by Moulinec and Suquet (1994; 1998) may be used. For instance, Wicht et al. (2020b) proposed an efficient, fully implicit FFT-based solution scheme for thermomechanically coupled problems. See also the recent review of Schneider (2021) for a comprehensive overview of discretizations and solver technologies used in FFT-based computational homogenization. In the concurrent multiscale setting, FFT-based micromechanics gives rise to the FE-FFT method (Spahn et al., 2014; Kochmann et al., 2016; 2018).

The FE^2 and the FE-FFT represent powerful and robust frameworks for solving the cell problem in a thermomechanically coupled two-scale setting, effectively addressing Questions 1, 2 and 4. However, considering Question 3 might prove challenging, especially from a point

of view of memory consumption. Furthermore, despite recent progress in computational efficiency and parallel computing strategies, see Geers et al. (2010) and Matouš et al. (2017) for overviews, concurrent multiscale methods with full-field models on the microscopic scale are typically too computationally demanding for treating two-scale problems of industrial complexity as presented in Figure 1.1a and Figure 1.1b.

1.2.2 Model order reduction techniques

Based on the insight that for such multiscale techniques the cell problem has to be solved repeatedly, several techniques have been developed to accelerate its solution. In this context, the cell problem is considered as a parametric partial differential equation (PDE), i.e., a PDE which is solved repeatedly for slightly different input parameters. As such methods aim at providing local solution fields, they are of localization type and make use of model order reduction techniques.

As a prototype for methods of localization type and motivated by classical mean-field methods, the transformation field analysis (TFA) was proposed by Dvorak and Benveniste (1992); Dvorak et al. (1994a;b). The TFA applies to small strain (visco-)plastic material models and assumes the inelastic strains to be piece-wise uniform on specific subdomains, and accounts for the resulting elastic deformations via strain localization tensors. In this way, effective models with a finite number of internal variables arise, see also Chaboche et al. (2005). Applications include damage in composites (Chaboche et al., 2001), SiC/Ti composites (Carrere et al., 2004) and shape-memory alloys (Marfia, 2005; Marfia and Sacco, 2005; 2007).

Originally restricted to materials based on Hooke's law with eigenstrain, Liu et al. (2016; 2018a;b); Yu et al. (2018) introduced the self-consistent clustering analysis (SCA), an extension of the TFA, applicable to any kind of material law. The SCA is inspired by the variational principle of

Hashin and Shtrikman (1961; 1962) as pointed out by Wulfinghoff et al. (2018).

Albeit applicable to general material laws, both TFA and SCA exhibit a very slow convergence rate in terms of the number of clusters (Chaboche et al., 2005). This phenomenon is intrinsically rooted in the weak approximation capabilities of piecewise constant functions (Schneider, 2019b). To overcome this limitation, the non-uniform transformation field analysis (NTFA) was introduced by Michel and Suquet (2003), relying upon problem-dependent inelastic basis functions and inspired by modern, nonlinear variational estimates (Ponte Castañeda and Suquet, 1997). For the NTFA, the approximation errors of the fields can be made as small as desired. However, the difficulty is shifted to efficiently evaluating the material law (Fritzen and Leuschner, 2013), i.e., the free energy and the force potential. As a remedy, series expansions of the force potential (Michel and Suquet, 2016a;b; 2017), a GPU implementation (Fritzen et al., 2014) or using dedicated "reducible" models (Köbler et al., 2021; Magino et al., 2022a;b) were proposed. Another difficulty is the selection strategy for the basis functions (Fritzen and Böhlke, 2013; Largenton et al., 2014), as they have to be chosen in advance.

The TFA, SCA or NTFA can be incorporated into a concurrent two-scale framework giving rise to the FE^{2R} (R for reduced) method (Fritzen and Hodapp, 2016; Fritzen and Böhlke, 2011). To avoid identifying and storing a reduced order model (ROM) for each Gaussian point, Köbler et al. (2018) proposed the fiber orientation interpolation for the analysis of SFRP, which, by interpolating the effective stresses of different ROMs, allows to take into account the spatially varying fiber orientation on the macroscopic scale. However, following this approach comes at the cost of three stress evaluations for each Gaussian point and time step. Furthermore, the TFA, SCA and NTFA allow for incorporating thermomechanical loading, thermal eigenstrains and temperature-dependent material parameters, see, e.g., Mojumder et al. (2021). However, they typ-

ically do not consider the back-coupling of the mechanical deformation onto the temperature evolution in the composite.

1.2.3 Machine learning approaches

In recent years, phenomenological modeling approaches gained new momentum, benefiting from advancements in machine learning techniques. Such methods dispense with local solution fields, but approximate the effective mechanical properties directly. Motivated by the high regularity of the effective stress, a machine learning model, preferably an artificial neural network[3] (ANN), is identified based on some labeled training data, e.g., sampled effective stress-strain paths. Such approaches come with the distinct advantage that a specific form of the model, except for choosing suitable hyperparameters, does not need to be supplied a priori. Typically, the functions to be approximated are defined on a high-dimensional domain of interest, constituting the primary difficulty to be overcome for these methods.

For directly approximating effective quantities, a number of works address training artificial neural networks to approximate the effective elastic energy of a medium and using automatic differentiation for obtaining the effective stress, see Yvonnet et al. (2009; 2013), Le et al. (2015), Nguyen-Thanh et al. (2019) and Shen et al. (2004b). In addition, the regularity of the effective stress facilitates the direct approximation of the stress-strain relationship of inelastic problems, see the works of Jadid (1997), Penumadu and Zhao (1999) or Srinivasu et al. (2012) for different approaches. By considering the temperature as an additional degree of freedom of the feature space, ANNs can be extended to

[3] Alternative approaches, for instance, support vector machine regression (Zhao et al., 2014; Zhou and Shen, 2015) was successfully applied to approximate the effective stress-strain relationship of microstructures. However, due to their greater flexibility, we restrict to artificial neural networks and related approaches in this section.

thermomechanical problems, see for example the works of Ji et al. (2011) or Li et al. (2012).

However, using vanilla ANNs for predicting the effective properties comes with two significant drawbacks. For a start, the capabilities to extrapolate beyond the training domain is limited, in general. Secondly, the underlying physical principles, e.g., thermodynamic consistency or preservation of stress-strain monotonicity, may be violated unless specifically accounted for.

As a remedy, physics-informed neural networks (PINN) (Raissi et al., 2019) were proposed. For PINNs, the solution field of a PDE is approximated by an artificial neural network. The PDE-error, evaluated at certain collocation points, is added to the loss to account for the inherent physics of the problem. For a non-exhaustive overview, we refer to Zhu et al. (2021) for applications in additive manufacturing simulations, to Wessels et al. (2020) for treating free surface flows and to Henkes et al. (2022) for investigating applications in solid mechanics. Still, some challenges have to be resolved. For instance, as the inherent physics of a problem is only accounted for in a soft way, it might not always be fulfilled. Furthermore, choosing suitable collocation points might be challenging and, as a product of globally approximating the solution of a PDE, PINNs may have difficulties in displaying localized effects or capturing strong nonlinear effects. As a remedy, adaptive training strategies and domain decompositions were studied, see Henkes et al. (2022).

To account for physical principles in a hard way, e.g., material objectivity or ellipticity, Fernández et al. (2021) proposed physics-augmented neural networks. They showed that accounting for the physics of a problem implicitly greatly improves the results. Physics-augmented neural networks have been applied to cubic beam lattice unit cells (Fernández et al., 2021; 2022; Klein et al., 2022) and were also investigated in a two-scale setting by Gärtner et al. (2021).

The previously mentioned approaches do not offer a natural way to consider history dependence as the problem of accounting for internal variables appears to be unresolved. Motivated by natural language processing, recurrent neural networks (RNN) may provide a framework for incorporating such history dependence into the approximation of the stress-strain relationship, see Mozaffar et al. (2019) and Koeppe et al. (2019). Gorji et al. (2020) demonstrated that RNNs are able to capture effects such as the Bauschinger effect, permanent softening or latent hardening in the context of elastoplasticity.

As an alternative approach for treating inelastic behavior, Masi et al. (2021b;a) introduced thermodynamics-based artificial neural networks (TANN). In their approach, they rely on approximating the free energy by means of an artificial neural network. In addition, they use a second neural network to account for the evolution of internal variables. Their findings indicate that the predictive capabilities of TANNs outperform those of standard ANNs.

ANNs may be used in a concurrent two-scale setting both for isothermal and non-isothermal problems, see, e.g., Acuna et al. (2020) or Fritzen et al. (2019). Also, RNNs may be employed in a multiscale setting, see Ghavamian and Simone (2019), Xu et al. (2021) and Wu et al. (2020). PINNs may also be used to accelerate a two-scale concurrent simulation giving rise to the FE-ANN method as proposed by Kalina et al. (2022). Although only studied on rather simple geometries, TANNs were also investigated in a two-scale setting by Masi and Stefanou (2022).

Note that using, for instance, an ANN as an effective material model in a two-scale simulation may introduce severe numerical robustness issues. More precisely, local stress peaks, typically occurring in the vicinity of notches, may cause the surrogate model to be evaluated outside of its training domain, which in turn may lead to thermodynamical inconsistent effective properties and thus divergence of the macroscopic simulation, see Fritzen et al. (2019) for a discussion. Increasing the mesh

density may even increase this effect. Also, the approaches mentioned above only consider a one-way thermomechanical coupling, i.e., from the temperature onto the effective properties, and not vice versa.

1.2.4 Deep material networks

Applying the concepts of deep learning in a more micromechanics-aware context, Liu et al. (2019a) and Liu and Wu (2019) introduced a data driven modeling approach based on an explicit microstructure model consisting of hierarchical laminates. In analogy to deep artificial neural networks, they called such a model a deep material network (DMN). To be more precise, they consider an N-phase DMN to be an N-ary tree of N-phase laminates as nodes with intermittent rotations associated to the edges of the tree.

Instead of approximating the effective energy or the effective stress-strain relationship, DMNs seek an approximation of the underlying microstructure by means of hierarchical laminates. In this sense, DMNs may be regarded as statistically similar representative volume elements (Balzani et al., 2014; Scheunemann et al., 2015), i.e., they may reflect, at least on an abstract level, the topology of the microstructure which they serve as a surrogate for (Dey et al., 2022b). As a byproduct of seeking to approximate the underlying microstructure independently of the phases, DMNs offer a natural way to account for internal variables and thus allow for considering inelastic problems with ease.

DMNs are trained on linear elastic data, where the effective stiffness of a fixed microstructure is considered as a function of the input stiffness tensors of the constituents. For the identification of the unknown parameters, i.e., the volume fractions of all laminates and the intermittent rotations, automatic differentiation (Paszke et al., 2017; Rall, 1981), back propagation (Rumelhart et al., 1986b;a) and stochastic gradient descent (Ruder, 2016) are used. After training, volume fractions and rotations are fixed and the hierarchical laminate can be applied to

inelastic problems, even at finite strains, and the resulting effective stress-strain curves match closely with direct numerical simulations. DMNs were augmented by cohesive zone models to account for interface damage (Liu, 2020) or multiscale strain localization modeling (Liu, 2021). Most importantly, the model identification on linear elastic data is independent from the online evaluation of the surrogate model. More precisely, an identified DMN may be applied to any nonlinear material behavior of the constituents after training. This property contrasts with other machine learning approaches, where the model identification is typically problem-dependent and thus linked to the material behavior of the constituents.

Discarding intermittent rotations and using laminates with a variable direction of lamination, Gajek et al. (2020) introduced direct DMNs which are particularly suitable for problems with isotropic phases. Later, Meyer et al. (2023) introduced micro-oriented direct DMNs to treat problems with a distinct micro-orientation, i.e., polycrystals or fiber reinforced composites with anisotropic fibers. Direct DMNs enable a faster and more robust identification process compared to the original formulation of Liu et al. (2019a) and Liu and Wu (2019), and also compare favorably for inelastic constituents. Furthermore, Gajek et al. (2020) motivated the effect of training on linear elastic data and generalizing to the nonlinear regime by showing that, to first order in the strain rate, the effective inelastic behavior of composite materials is determined by linear elastic localization. As a byproduct, Gajek et al. (2020) showed that deep material networks inherit thermodynamic consistency and stress-strain monotonicity from their phases. These properties are of utmost importance for accelerating two-scale simulations, as they ensure that the effective model inherits stabilizing numerical properties, like strong convexity, from the phases. Thus, the aforementioned robustness issues, typical for many other data-driven approaches, are not observed for DMNs.

The extension of the DMN framework to accelerate two-scale concurrent simulations of short fiber reinforced composites was proposed by Liu et al. (2020) and Gajek et al. (2021a;b), giving rise to the FE-DMN method. More precisely, Liu et al. (2019b; 2020) proposed a transfer learning approach, see also Huang et al. (2022). In contrast, Gajek et al. (2021a) went beyond this a posteriori approach and identified a single DMN, covering the entire spectrum of fiber orientations, by interpolating the fitting parameters during training. Gajek et al. (2021a) showed the efficiency of their approach by performing a large-scale concurrent two-scale simulation of an injection molded quadcopter frame comprising about two million elements as a benchmark. Additionally, Meyer et al. (2023) introduced micro-oriented direct DMNs and proposed to use a volume fraction interpolation in conjunction with a fiber orientation interpolation to accelerate two-scale simulations of sheet molding compound composite components. Gajek et al. (2022) recently extended the DMN framework to account for the two-way thermomechanical coupling in a large-scale concurrent simulation.

To improve upon the linear training, Nguyen and Noels (2022) proposed to train the DMN on nonlinear data. A large number of inelastic load paths must be sampled, so that the computational effort may become prohibitive, depending on the complexity of the underlying microstructure. Furthermore, the implementation of the model identification routine must be adapted each time different material models for the phases are considered. As a remedy, Dey et al. (2022b) proposed a novel early-stopping technique to retain the favorable properties of the linear training but still include nonlinear data intro the training. They showed that direct DMNs can efficiently represent highly nonlinear creep in short fiber reinforced plastic components. Dey et al. (2022a) suggested to use direct DMNs as a surrogate for inversely identifying material parameters of a constitutive inelastic model for short fiber reinforced thermoplastics.

1.3 Outline and originality of this thesis

In this thesis, we contribute to the framework of deep material networks by addressing Questions 1 to 4 for which we restrict to the setting of small strains and materials without pores and defects. DMNs serve as surrogate models for full-field simulations on the microscopic scale, offering speed-ups of several orders of magnitudes. In this way, DMNs might be regarded as the missing key to finally realize the promise of concurrent two-scale simulations of large-scale industrial problems.

The remainder of this thesis is organized as follows:

- In **Chapter 2**, small-strain continuum thermomechanics and its fundamental building blocks, i.e., kinematic relations, universal balance laws and constitutive relations, are briefly recapitulated.
- In **Chapter 3**, we investigate the framework of deep material networks from the viewpoint of classical small-strain micromechanics. We aim to establish the basic micromechanical principles of DMNs and shed light on the characteristics of the building blocks.

  In their original formulation, DMNs are solely trained by linear elastic data, but applied to nonlinear and inelastic problems with astonishing accuracy. We clarify this phenomenon theoretically by showing that, to first order in the strain rate, the effective inelastic behavior of composite materials is determined by linear elastic localization. Our argumentation applies to arbitrary microstructures comprising nonlinear small-strain generalized standard materials. The main technical tool is a Volterra series approximation of the stress of a generalized standard material, which we adapt from nonlinear dynamical systems theory.
- In **Chapter 4**, we show that DMNs inherit thermodynamic consistency and stress-strain monotonicity from their phases. We introduce direct DMNs which feature a reduced number of degrees of freedom compared to the original formulation of Liu et al. (2019a) and

Liu and Wu (2019) by omitting intermittent rotations and utilizing laminate building blocks with arbitrary direction of lamination. We present how such building blocks may be efficiently evaluated for the affine-linear elastic case. In addition, we present a novel solution technique for nonlinear DMNs with arbitrary tree topologies and multi-phase laminates, addressing Question 1. We apply our insights to microstructures of industrial complexity.

- In **Chapter 5**, we address Questions 2 and 3 by proposing a fully coupled two-scale strategy for components made of short fiber reinforced composites. In such a two-scale simulation, we assume a constant fiber volume fraction and equip each Gauss point of the macroscopic finite element model with a direct DMN which covers different fiber orientation states. Furthermore, we propose a simplified sampling strategy of the training data which significantly speeds up the training process. To enable concurrent multiscale simulations, evaluating the DMNs efficiently is crucial. We discuss dedicated techniques for exploiting sparsity and high-performance linear algebra modules, and demonstrate the power of the proposed approach on an injection molded quadcopter frame as a benchmark component.
- **Chapter 6** is concerned with the development of a virtual process chain to quantify process-induced uncertainties in sheet molding compound (SMC) composites. Here, we build upon the results of Chapter 5, introduce micro-oriented direct DMNs and augment the framework by a fiber orientation and fiber volume fraction interpolation schemes. This approach allows for fully resolving the spatially varying fiber volume fraction as well as the spatially varying fiber orientation in a component scale simulation. By comparing with experimental results, we demonstrate that process-induced uncertainties, prevalent in SMC components, can be captured with good accuracy by our approach.

- For addressing Question 4, we extend the FE-DMN method to fully coupled thermomechanical two-scale simulations of composite materials in **Chapter 7**. We provide details on the efficient implementation of the approach as a user-material subroutine and validate our approach on the microscopic scale. We show that the identified direct DMN predicts the effective stress, the effective dissipation and the change of the macroscopic absolute temperature with high accuracy. After validation, we demonstrate the capabilities of our approach on a concurrent two-scale thermomechanical simulation on the macroscopic component scale.
- We briefly summarize this thesis in **Chapter 8** and close with concluding remarks.

1.4 Notation and frequently used symbols

We follow a direct tensor notation, and we denote scalar quantities either by non-bold letters $\{a, b, \dots, A, B, \dots\}$ or by non-bold Greek symbols $\{\varepsilon, \sigma, \dots\}$. Vectors are notated by lower case bold letters $\{\boldsymbol{a}, \boldsymbol{b}, \dots\}$. Second-order tensors are either denoted by upper case bold letters $\{\boldsymbol{A}, \boldsymbol{B}, \dots\}$ or by bold Greek symbols $\{\boldsymbol{\varepsilon}, \boldsymbol{\sigma}, \dots\}$. Fourth-order tensors are noted by upper case blackboard bold letters $\{\mathbb{A}, \mathbb{B}, \dots\}$. We notate n-tuples of scalars, second-order, fourth-order tensors or other n-tuples by $\vec{\square}$, i.e., $\vec{\boldsymbol{p}} = [\boldsymbol{a}, \boldsymbol{b}, \boldsymbol{c}]$ or $\vec{\boldsymbol{q}} = [\boldsymbol{d}, \boldsymbol{e}, \boldsymbol{f}]$, for which we define element-wise addition $\vec{\boldsymbol{p}} + \vec{\boldsymbol{q}} = [\boldsymbol{a}+\boldsymbol{d}, \boldsymbol{b}+\boldsymbol{e}, \boldsymbol{c}+\boldsymbol{f}]$ and element-wise scalar multiplication $\lambda\vec{\boldsymbol{p}} = [\lambda\boldsymbol{a}, \lambda\boldsymbol{b}, \lambda\boldsymbol{c}]$.

Although the type of an element is implied by its notation, all newly-introduced quantities of any kind are defined upon their first appearance in each section such as tensor order, domain of definition or function space.

We denote the Euclidean vector space in $d = 2, 3$ spatial dimensions by V^d. Its orthonormal base vectors are noted as $\{\boldsymbol{e}_i\}_{i=1}^d$. The following spaces are repeatedly used:

- We denote the special orthogonal group acting on V^d by $\mathrm{SO}(d)$.
- We name S^{d-1} the $(d-1)$-dimensional unit sphere associated to V^d.
- The space of symmetric second-order tensors is denotes by $\mathrm{Sym}_2(d)$.
- The space of fourth-order tensors, endowed with minor and major symmetries, is denoted by $\mathrm{Sym}_4(d)$.
- The spaces of positive definite second and fourth-order tensors are noted as $\mathrm{Sym}_2^+(d)$ and $\mathrm{Sym}_4^+(d)$, respectively.

The components of a tensor are indexed by Latin indices $\{i, j, k, l, \ldots\}$. The Einstein's summation convention applies, i.e., we sum over identical indices from 1 to d, and the following tensor operations are used:

- The inner product between vectors and the Frobenius inner product between second-order tensors is denoted by $\boldsymbol{a} \cdot \boldsymbol{b} = a_i b_i$ and $\boldsymbol{A} : \boldsymbol{B} = A_{ij} B_{ij}$, respectively.
- The linear mapping between a second-order tensor and a vector is noted as $\boldsymbol{A}\boldsymbol{b} = A_{ij} b_j \, \boldsymbol{e}_i$.
- Likewise, the linear mapping between two second-order or two fourth-order tensors is denoted by $\boldsymbol{A}\boldsymbol{B} = A_{ij} B_{jk} \, \boldsymbol{e}_i \otimes \boldsymbol{e}_k$ and $\mathbb{A}\mathbb{B} = A_{ijkl} B_{klmn} \, \boldsymbol{e}_i \otimes \boldsymbol{e}_j \otimes \boldsymbol{e}_m \otimes \boldsymbol{e}_n$.
- For the linear mapping of a fourth-order and a second-order tensor, we write $\mathbb{A} : \boldsymbol{B} = A_{ijkl} B_{kl} \, \boldsymbol{e}_i \otimes \boldsymbol{e}_j$. Alternatively, for notating the stress evaluation, we use the equivalent form $\mathbb{C}[\boldsymbol{\varepsilon}] = C_{ijkl} \varepsilon_{kl} \, \boldsymbol{e}_i \otimes \boldsymbol{e}_j$ for reasons of exposition.

We denote the direct product $\times$, the tensor product $\otimes$ and the direct sum $\oplus$ and use the following shorthand notations $\boldsymbol{A}^{\otimes^N} = \boldsymbol{A} \otimes \ldots \otimes \boldsymbol{A}$ and $\boldsymbol{A}^{\oplus^N} = \boldsymbol{A} \oplus \ldots \oplus \boldsymbol{A}$ (N repetitions).

The material time derivative is denoted by $\dot{\square}$. Effective quantities are referred to by $\bar{\square}$.

Acronyms

μCT	Micro computed tomography
ANN	Artificial neural network
DMN	Deep material network
FE	Finite elements
FEM	Finite element method
FFT	Fast Fourier transform
FOD	Fiber orientation distribution
FRP	Fiber reinforced polyamide
MIMO	Multiple-input-multiple-output
MMC	Metal matrix composite
NTFA	Non-uniform transformation field analysis
PDE	Partial differential equation
PINN	Physics-informed neural network
ROM	Reduced order model
RVE	Representative volume element
SCA	Self-consistent clustering analysis
SFRP	Short fiber reinforced plastic
SISO	Single-input-single-output
SMC	Sheet molding compound
TANN	Thermodynamics-based artificial neural network
TFA	Transformation field analysis

Sets

$\mathcal{AL}$	Affine-linear GSMs
$\mathcal{C\Lambda}$	Admissible fiber volume fractions and orientations
$\mathfrak{D}_4, \mathfrak{D}_{10}, \mathfrak{D}_{31}$	Orientation triangle discretizations
$\mathrm{Dev}_2(d)$	Deviatoric second-order tensors
$\mathcal{GSM}$	GSMs
$\mathcal{I}$	Loading directions
$\mathcal{L}$	Linear GSMs
Λ	Admissible fiber orientations
$\mathcal{LV}$	Linear viscoelastic GSMs
$\mathbb{N}$	Natural numbers
Ω	Macroscopic body
$\mathbb{R}$	Real numbers
S^{d-1}	Unit sphere associated to V^d
$\mathcal{S}$	Material singular surface
$\mathrm{Skw}_2(d)$	Skew-symmetric second-order tensors
$\mathrm{SO}(d)$	Special orthogonal group acting on V^d
$\mathrm{Sph}_2(d)$	Spherical second-order tensors
$\mathrm{Sym}_2(d)$	Symmetric second-order tensors
$\mathrm{Sym}_2^+(d)$	Symmetric positive definite second-order tensors
$\mathrm{Sym}_4(d)$	Fourth-order tensors, endowed with minor and major symmetries
$\mathrm{Sym}_4^+(d)$	Positive definite fourth-order tensors, endowed with minor and major symmetries
$\mathcal{T}$	Simulation time interval
$\mathcal{V}$	Material volume
V^d	d-dimensional Euclidean vector space
Y	Periodic rectangular unit cell
$\mathcal{Z}$	Vector space of internal variables

Latin letters

$\mathcal{A}$	Phase-wise average strain localization function
$\boldsymbol{A}_2$	Second-order fiber orientation tensor
$\boldsymbol{a}$	Acceleration vector
a	Temperature-dependent shift factor
$\boldsymbol{B}$	Averaging operator
$\mathcal{B}$	Homogenization function of a rank-one laminate
$\mathbb{B}$	Damage stress extraction tensor
$\boldsymbol{b}$	Body force density
$\mathbb{C}$	Stiffness tensor
c_ε	Heat capacity at constant strain
c	Volume fraction
$\boldsymbol{D}$	Symmetrized gradient operator
$\mathcal{D}$	Dissipation
$\mathcal{DMN}$	Homogenization function of a DMN
D_f	Fiber diameter
d	Dimension
$\boldsymbol{d}$	Direction vector
E	Young's modulus
$\{\boldsymbol{e}_i\}_{i=1}^d$	Euclidian base vectors
e	Internal energy density
$\boldsymbol{F}$	Deformation gradient
$\mathcal{G}$	Generalized standard material
G	Shear modulus
$\mathbb{G}$	Relaxation function
$\boldsymbol{H}$	Displacement gradient
h	Heat source density
h_t	Heat transfer coefficient
$\boldsymbol{I}$	Identity on V^d
$\mathbb{I}_\mathrm{s}$	Identity on $\mathrm{Sym}_2(d)$

K	Number of consecutive laminations
L_f	Fiber length
L	Microstructure edge length
$\mathcal{M}$	Homogenization function
$\boldsymbol{N}$	Symmetrized rank-one gradient
N	Number of phases
$\boldsymbol{n}$	Normal vector
P	Thermomechanical coupling term
$\vec{\boldsymbol{p}}$	Parameter vector
p_Θ	Generic production density of Θ
$\boldsymbol{Q}$	Rotation matrix
$\boldsymbol{q}_\Theta$	Generic flux density of Θ
$\boldsymbol{R}$	Rotation operator
ρ	Fiber orientation distribution function
$\mathbb{S}$	Compliance tensor
s_Θ	Generic supply density of Θ
s	Entropy
T	Simulation time
T_c	Period of sinusoidal loading
$\boldsymbol{U}, \boldsymbol{V}$	Stretch tensors
$\boldsymbol{u}$	Displacement vector
v	Unconstrained weight
$\boldsymbol{v}$	Velocity vector
$\boldsymbol{W}$	Weight operator
w	Constrained weight
$\boldsymbol{x}, \boldsymbol{X}$	Material points
Z	Number of internal variables
$\boldsymbol{z}$	Vector of internal variables

Greek letters

α	Thermal expansion (scalar valued)
$\boldsymbol{\alpha}$	Thermal expansion tensor
β	Step size
χ	Characteristic function
$\boldsymbol{\chi}$	Kinematic function
δ	Linear error
ε	Infinitisimal strain (scalar valued)
$\boldsymbol{\varepsilon}$	Infinitisimal strain tensor
η	Nonlinear error
γ	Backtracking factor and learning rate decay factor
κ	Thermal conductivity (scalar valued)
$\boldsymbol{\kappa}$	Thermal conductivity tensor
λ_0	Reference stiffness
λ_p	Penalty parameter
μ	Shear viscosity
ν	Poisson's ratio
$\boldsymbol{\omega}$	Infinitisimal rotation tensor
ϕ	Dissipation potential
ϕ^*	Force potential
$\{\varphi_i\}_{i=1}^d$	Barycentric coordinates
Ψ	Condensed Helmholtz free energy potential
ψ	Helmholtz free energy density
ϱ	Mass density
σ	Cauchy stress (scalar valued)
$\boldsymbol{\sigma}$	Cauchy stress tensor
θ	Absolute temperature
Θ	Generic m-th order tensorial field
ζ	Material contrast

Operators

$\dot{\square}$	Material time derivative
$\bar{\square}$	Effective quantity
$\square^{-1}$	Inverse
$\square^{-\mathsf{T}}$	Transposed inverse
$\square^{\mathsf{T}}$	Transpose
$\mathrm{block\text{-}diag}\,(\square)$	Block-diagonal matrix
$\partial\square$	Subdifferential
$\det(\square)$	Determinant
$\mathrm{diag}\,(\square)$	Diagonal matrix
$\mathrm{div}(\square)$	Spatial divergence
$\langle\square\rangle_+$	Macaulay bracket
$\langle\square\rangle_Y$	Volumetric mean
$\nabla\square$	Spatial gradient
$\nabla^{\mathrm{s}}\square$	Symmetrized spatial gradient
$\mathrm{tr}\,(\square)$	Trace

Chapter 2

Fundamentals of small-strain continuum thermomechanics

2.1 Introduction

This chapter is dedicated to giving a short summary of small-strain continuum thermomechanics and its elementary building blocks, i.e., kinematic relations, balance equations and constitutive relations. In rational thermodynamics, the last two points may not be considered separately as thermodynamically consistent constitutive relations depend implicitly on the balance of entropy and need to fulfill the second law of thermodynamics.

2.2 Kinematics

In $d \in \{2, 3\}$ spatial dimensions, we consider a body of material points in an arbitrarily chosen reference configuration $\Omega_0 \subseteq \mathrm{V}^d$ (Šilhavý, 1997). The position of each material point in reference configuration is measured by $\boldsymbol{X} \in \Omega_0$. For every point in time $t \in [0, T]$, with end time $T \in (0, \infty]$, we describe the current position of each material point by the continuously differentiable and invertible function

$$\boldsymbol{\chi} : \Omega_0 \times [0, T] \to \mathrm{V}^d, \quad \boldsymbol{x} = \boldsymbol{\chi}(\boldsymbol{X}, t) \quad \text{with} \quad \boldsymbol{X} = \boldsymbol{\chi}(\boldsymbol{X}, 0), \tag{2.1}$$

which lets us define the current placement of the body (Šilhavý, 1997)

$$\Omega_t = \{\boldsymbol{x} = \boldsymbol{\chi}(\boldsymbol{X}, t) \in \mathrm{V}^d \mid \boldsymbol{X} \in \Omega_0\}. \tag{2.2}$$

With these definitions at hand, we might parameterize any tensorial field $\Theta_{\mathrm{L}} : \Omega_0 \times [0, T] \to (\mathrm{V}^d)^{\otimes^m}$ of order m w.r.t. the reference configuration, which we call *Lagrangian* description. Similarly, the description of the tensorial field $\Theta_{\mathrm{E}} : \Omega_t \times [0, T] \to (\mathrm{V}^d)^{\otimes^m}$ as a function of the current position is commonly referred to as the *Eulerian* description. Both descriptions are related by (Haupt, 2002)

$$\Theta_{\mathrm{L}}(\boldsymbol{X}, t) = \Theta_{\mathrm{E}}(\boldsymbol{\chi}(\boldsymbol{X}, t), t) \quad \text{and} \quad \Theta_{\mathrm{E}}(\boldsymbol{x}, t) = \Theta_{\mathrm{L}}(\boldsymbol{\chi}^{-1}(\boldsymbol{x}, t), t). \tag{2.3}$$

The material time derivative of a tensorial field $\Theta_{\mathrm{L}}(\boldsymbol{X}, t)$ in Lagrangian description is defined (Haupt, 2002; Truesdell and Toupin, 1960) via

$$\dot{\Theta}_{\mathrm{L}}(\boldsymbol{X}, t) = \frac{\partial \Theta_{\mathrm{L}}}{\partial t}(\boldsymbol{X}, t), \tag{2.4}$$

which let us defined the velocity $\boldsymbol{v}_{\mathrm{L}}$ and acceleration $\boldsymbol{a}_{\mathrm{L}}$ of the body as

$$\boldsymbol{v}_{\mathrm{L}}(\boldsymbol{X}, t) = \frac{\partial \boldsymbol{\chi}}{\partial t}(\boldsymbol{X}, t) \quad \text{and} \quad \boldsymbol{a}_{\mathrm{L}}(\boldsymbol{X}, t) = \frac{\partial^2 \boldsymbol{\chi}}{\partial t^2}(\boldsymbol{X}, t). \tag{2.5}$$

Similarly, by applying the chain rule, the material time derivative of a tensorial field $\Theta_{\mathrm{E}}(\boldsymbol{x}, t)$ in Eulerian description computes to

$$\dot{\Theta}_{\mathrm{E}}(\boldsymbol{x}, t) = \frac{\partial \Theta_{\mathrm{E}}}{\partial \boldsymbol{x}}(\boldsymbol{x}, t) \cdot \boldsymbol{v}_{\mathrm{E}}(\boldsymbol{x}, t) + \frac{\partial \Theta_{\mathrm{E}}}{\partial t}(\boldsymbol{x}, t). \tag{2.6}$$

Indeed, any tensorial field can be uniquely attributed to one of the two descriptions via the type of its arguments. Thus, we may refrain from explicitly distinguishing between both descriptions via subscripts. In the following, the Lagrangian description is mainly used.

For measuring the deformation of the body, we introduce the deformation gradient

$$\boldsymbol{F} : \Omega_0 \times [0,T] \to \mathrm{V}^d \otimes \mathrm{V}^d, \quad (\boldsymbol{X}, t) \mapsto \boldsymbol{F} = \frac{\partial \boldsymbol{\chi}}{\partial \boldsymbol{X}}(\boldsymbol{X}, t), \tag{2.7}$$

which describes how infinitesimal line $\mathrm{d}\boldsymbol{X}$, area $\mathrm{d}\boldsymbol{A}$ and volume $\mathrm{d}V$ elements are transformed from the reference Ω_0 to the current Ω_t configuration by the following relations (Haupt, 2002)

$$\mathrm{d}\boldsymbol{x} = \boldsymbol{F}\,\mathrm{d}\boldsymbol{X}, \quad \mathrm{d}\boldsymbol{a} = \det(\boldsymbol{F})\,\boldsymbol{F}^{-\mathsf{T}}\,\mathrm{d}\boldsymbol{A} \quad \text{and} \quad \mathrm{d}v = \det(\boldsymbol{F})\,\mathrm{d}V. \tag{2.8}$$

However, the deformation gradient may not be a suitable measure for measuring the deformation of a body. For instance, $\boldsymbol{F}$ does not necessarily vanish for a vanishing deformation, i.e., evaluating $\boldsymbol{F}$ in the (undeformed) reference configuration, we obtain

$$\boldsymbol{F}(\boldsymbol{X}, 0) = \boldsymbol{I}, \tag{2.9}$$

where $\boldsymbol{I} \in \mathrm{Sym}_2(d)$ denotes the identity on V^d. Furthermore, the deformation gradient $\boldsymbol{F}$ may include rigid body rotations. As a remedy, we may use a polar decomposition to represent the deformation gradient as the product of a special orthogonal part $\boldsymbol{R} \in \mathrm{SO}(d)$, accounting for the rotation, and symmetric positive definite parts $\boldsymbol{U}$, $\boldsymbol{V} \in \mathrm{Sym}_2^+(d)$, representing the stretch, for which the relation

$$\boldsymbol{F} = \boldsymbol{R}\boldsymbol{U} = \boldsymbol{V}\boldsymbol{R} \tag{2.10}$$

holds (Haupt, 2002). More precisely, the local deformation consists of a rotation $\boldsymbol{R}$ followed by a subsequent stretch $\boldsymbol{V}$ or a stretch $\boldsymbol{U}$ followed by a rotation $\boldsymbol{R}$. Note that the two stretches $\boldsymbol{U}$, $\boldsymbol{V}$ do not vanish for an undeformed body as we also observed for the deformation gradient itself.

In this work, we restrict to small strains. For this, further simplifying assumptions can be made. First, we introduce the displacement field $\boldsymbol{u} : \Omega_0 \times [0,T] \to \mathrm{V}^d$ as the difference between current and reference position of each material point via

$$\boldsymbol{u}(\boldsymbol{X},t) = \boldsymbol{\chi}(\boldsymbol{X},t) - \boldsymbol{X}. \tag{2.11}$$

With the displacement $\boldsymbol{u}$ at hand, we define the displacement gradient

$$\boldsymbol{H} : \Omega_0 \times [0,T] \to \mathrm{V}^d \otimes \mathrm{V}^d, \quad (\boldsymbol{X},t) \mapsto \boldsymbol{H} = \frac{\partial \boldsymbol{u}}{\partial \boldsymbol{X}}(\boldsymbol{X},t) \tag{2.12}$$

which relates to the deformation gradient by the relation

$$\boldsymbol{H} = \boldsymbol{F} - \boldsymbol{I}. \tag{2.13}$$

Then, we may speak of small strains if the Frobenius norm of the displacement gradient

$$\|\boldsymbol{H}\|_{\mathrm{F}} = \sqrt{\boldsymbol{H}\boldsymbol{H}^{\mathsf{T}}} \ll 1 \tag{2.14}$$

is small (Bertram, 2005). If Relation (2.14) holds, we may linearize the deformation gradient at $\boldsymbol{F} = \boldsymbol{I}$, giving rise to the two stretches and the rotation

$$\boldsymbol{U} \approx \boldsymbol{I} + \boldsymbol{\varepsilon}, \quad \boldsymbol{V} \approx \boldsymbol{I} + \boldsymbol{\varepsilon} \quad \text{and} \quad \boldsymbol{R} \approx \boldsymbol{I} + \boldsymbol{\omega}. \tag{2.15}$$

Here, $\boldsymbol{\varepsilon} \in \mathrm{Sym}_2(d)$ is called the *infinitisimal strain tensor* and $\boldsymbol{\omega} \in \mathrm{Skw}_2(d)$ is denoted the *infinitisimal rotation tensor* (Haupt, 2002). Both are given as the symmetric and skew symmetric parts of the displacement gradient

$$\boldsymbol{\varepsilon} = \frac{1}{2}(\boldsymbol{H} + \boldsymbol{H}^{\mathsf{T}}) \quad \text{and} \quad \boldsymbol{\omega} = \frac{1}{2}(\boldsymbol{H} - \boldsymbol{H}^{\mathsf{T}}). \tag{2.16}$$

Indeed, the infinitisimal strain tensor vanishes for a vanishing deformation and excludes infinitisimal rotations.

By assuming small displacements (in conjunction with small strains), the difference between reference and current configuration is negligible such that a distinction between Lagrangian and Eulerian description is no longer necessary and the approximation

$$\Theta(\boldsymbol{X}, t) \approx \Theta(\boldsymbol{x}, t) \tag{2.17}$$

holds (Haupt, 2002).

2.3 Balance laws

Besides kinematic relations and the formulation of constitutive laws, the thermomechanical behavior of a body is determined by physical principles, which are typically stated in the form of so-called balance laws. For the case of continuum thermomechanics, the balance of mass, linear and angular momentum, inner energy and entropy form a complete[1] system of governing partial (integro-)differential equations.

Indeed, these equations share a common form such that we may express them by a general balance equation. To fix ideas, we consider an arbitrary material volume $\mathcal{V}_t \subseteq \Omega_t$, which is divided by a material singular surface $\mathcal{S}_t$ into the two sub-volumes $\mathcal{V}_t^+$ and $\mathcal{V}_t^-$ with $\mathcal{V}_t = \mathcal{V}_t^+ \cup \mathcal{V}_t^-$. The boundary of $\mathcal{V}_t$ is denotes by $\partial\mathcal{V}_t$ also consisting of the two parts $\partial\mathcal{V}_t^+$ and $\partial\mathcal{V}_t^-$ with $\partial\mathcal{V}_t = \partial\mathcal{V}_t^+ \cup \partial\mathcal{V}_t^-$ and with the outer normal vector denoted by $\boldsymbol{n}_{\mathcal{V}} \in \mathrm{S}^{d-1}$. The normal vector of the material singular surface $\mathcal{S}_t$, which is directed from $\partial\mathcal{V}_t^-$ to $\partial\mathcal{V}_t^+$, is denotes by $\boldsymbol{n}_{\mathcal{S}} \in \mathrm{S}^{d-1}$. Following Liu (2002), we express the general balance of the tensorial

[1] Typically, the balance of entropy is not solved explicitly but used to derive restrictions on the constitutive relations as we will see in Section 2.4.

field $\Theta : \Omega_t \times [0,T] \to (\mathrm{V}^d)^{\otimes^m}$ of order m in integral form by

$$\frac{\mathrm{d}}{\mathrm{d}t}\int_{\mathcal{V}_t} \Theta \; \mathrm{d}v = \int_{\mathcal{V}_t} p_\Theta + s_\Theta \; \mathrm{d}v + \int_{\partial\mathcal{V}_t} \boldsymbol{q}_\Theta \cdot \boldsymbol{n}_\mathcal{V} \; \mathrm{d}a, \tag{2.18}$$

where $p_\Theta : \Omega_t \times [0,T] \to (\mathrm{V}^d)^{\otimes^m}$ and $s_\Theta : \Omega_t \times [0,T] \to (\mathrm{V}^d)^{\otimes^m}$ name the internal production and the external supply of quantity Θ in each regular point $\boldsymbol{x} \in \mathcal{V}_t \setminus \mathcal{S}_t$. In addition, $\boldsymbol{q}_\Theta : \Omega_t \times [0,T] \to (\mathrm{V}^d)^{\otimes^{m+1}}$ denotes the non-convective flux over $\partial\mathcal{V}_t$. Please note that we assume a vanishing flux on $\partial\mathcal{S}_t$, the intersection of $\mathcal{S}_t$ and $\partial\mathcal{V}_t$, and no production and supply of Θ on $\mathcal{S}_t$. For the general balance equation including these terms, we refer to Müller (1985).

Using Reynolds transport theorem (Liu, 2002) and the divergence theorem (Haupt, 2002), the general balance equation in integral form (2.18) translates to its local form in regular points $\boldsymbol{x} \in \mathcal{V}_t \setminus \mathcal{S}_t$,

$$\frac{\partial\Theta}{\partial t} + \mathrm{div}(\Theta \otimes \boldsymbol{v}) = p_\Theta + s_\Theta + \mathrm{div}(\boldsymbol{q}_\Theta), \tag{2.19}$$

where $\boldsymbol{v} : \Omega_t \times [0,T] \to \mathrm{V}^d$ denotes the tensorial velocity field. For each point on the material singular surface $\boldsymbol{x} \in \mathcal{S}_t$, we obtain the jump condition

$$[\![\boldsymbol{q}_\Theta]\!] \cdot \boldsymbol{n}_{\mathcal{S}_t} = 0 \quad \text{with} \quad [\![\boldsymbol{q}_\Theta]\!] = \overset{+}{\boldsymbol{q}}_\Theta - \overline{\boldsymbol{q}}_\Theta, \tag{2.20}$$

with the right- and left-hand limits $\overset{+}{\boldsymbol{q}}_\Theta$ and $\overline{\boldsymbol{q}}_\Theta$ of $\boldsymbol{q}_\Theta$, respectively.

Balance of mass

For deriving the balance of mass, we identify the quantity to be balanced Θ with the mass density $\varrho : \Omega_t \times [0,T] \to \mathbb{R}$. Furthermore, the production p_Θ, supply s_Θ and flux $\boldsymbol{q}_\Theta$ vanish identically (Liu, 2002). Then, the local form of the balance of mass in regular points reads

$$\dot{\varrho} + \varrho \; \mathrm{div}(\boldsymbol{v}) = 0. \tag{2.21}$$

As we consider a material singular surface with a vanishing flux $\boldsymbol{q}_\Theta$, the balance of mass on $\mathcal{S}_t$ is identically fulfilled.

Note that for continuum solid mechanics, the balance of mass (2.21) is usually not solved explicitly. Indeed, for any given deformation gradient $\boldsymbol{F}$, the density ϱ at a material point may be expressed by the density ϱ_0, associated to the reference configuration, via $\varrho = \det(\boldsymbol{F})^{-1}\varrho_0$, see Liu (2002). For the special case of small strains, see Section 2.2, the former equation reformulates to $\varrho = (1 - \operatorname{tr}(\boldsymbol{\varepsilon}))\varrho_0$. We see that as long as we consider small strains, we may approximate the density as constant, i.e., $\varrho \approx \varrho_0$ holds.

Balances of linear and angular momentum

With the mass density ϱ and the velocity $\boldsymbol{v}$ at hand, we consider the linear momentum density $\varrho\boldsymbol{v}$ as the quantity to be balanced. In addition, we associate the external supply term s_Θ with the volume force density $\boldsymbol{b} : \Omega_t \times [0,T] \to \mathrm{V}^d$ and the flux $\boldsymbol{q}_\Theta$ with the Cauchy stress $\boldsymbol{\sigma} : \Omega_t \times [0,T] \to \mathrm{V}^d \otimes \mathrm{V}^d$. As we consider the conservation of linear momentum, the production term p_Θ vanishes identically. Then, assuming the balance of mass holds, the local balance of linear momentum in regular points reads

$$\varrho\dot{\boldsymbol{v}} = \boldsymbol{b} + \operatorname{div}(\boldsymbol{\sigma}). \tag{2.22}$$

For points on the material singular surface, the jump condition (2.20) reformulates to

$$[\![\boldsymbol{\sigma}]\!]\boldsymbol{n}_\mathcal{V} = \boldsymbol{0} \quad \Longleftrightarrow \quad \boldsymbol{\sigma}^+\boldsymbol{n}_\mathcal{V} = \boldsymbol{\sigma}^-\boldsymbol{n}_\mathcal{V}, \tag{2.23}$$

i.e., the stress vector $\boldsymbol{t} = \boldsymbol{\sigma}\boldsymbol{n}_\mathcal{V}$ is continuous on the material singular surface. For the special case of quasi-static processes, the acceleration term vanishes and we obtain the quasi-static balance of linear momentum in regular points

$$\boldsymbol{0} = \boldsymbol{b} + \operatorname{div}(\boldsymbol{\sigma}). \tag{2.24}$$

Following a similar argument, we derive the balance of angular momentum Liu (2002) which reads in local form

$$\boldsymbol{\sigma} = \boldsymbol{\sigma}^{\mathsf{T}}. \tag{2.25}$$

In other words, for non-polar materials (no moment densities acting on the material volume $\mathcal{V}_t$), the symmetry of the Cauchy stress tensor ensures the conservation of angular momentum.

Balance of energy

First, we consider the volume-specific internal energy density $e : \Omega_t \times [0, T] \to \mathbb{R}$, which measures the stored energy of a thermodynamical system excluding kinetic or potential energy contributions. Typically, the mass-specific internal energy $\hat{e} = e/\varrho$ is the quantity of interest in classical thermodynamics. However, as we derived earlier, the mass density ϱ might be approximated by a constant factor in the small-strain setting such that volume-specific and mass-specific energy formulations might be used for formulating balance equations. Indeed, considering volume-specific energetic quantities such as the internal energy, the free Helmholtz energy or the entropy is more convenient for the considerations in Section 2.4, such that we follow this approach subsequently.

We consider the sum of the internal energy density e and the kinetic energy density $\frac{1}{2}\,\varrho(\boldsymbol{v} \cdot \boldsymbol{v})$ as quantities to be balanced. With the sum of the internal heat source density $h : \Omega_t \times [0, T] \to \mathbb{R}$ and the power of volume forces $\boldsymbol{b} \cdot \boldsymbol{v}$ as supply term s_Θ, the sum of the negative heat flux $-\boldsymbol{q}$ and the power of external forces $\boldsymbol{\sigma}^{\mathsf{T}}\boldsymbol{v}$ as flux term $\boldsymbol{q}_\Theta$ and a vanishing production term p_Θ, we arrive at the local balance of total energy in regular points

$$\dot{e} + \frac{1}{2}\varrho(\boldsymbol{v} \cdot \boldsymbol{v})^{\cdot} = -\operatorname{div}(\boldsymbol{q}) + \operatorname{div}(\boldsymbol{\sigma}^{\mathsf{T}}\boldsymbol{v}) + \boldsymbol{b} \cdot \boldsymbol{v} + h. \tag{2.26}$$

The former equation is commonly referred to as the first law of thermodynamics. For points on the material singular surface, we obtain the jump condition

$$[\![\boldsymbol{\sigma}^{\mathsf{T}}\boldsymbol{v}]\!] \cdot \boldsymbol{n}_{\mathcal{S}} = [\![\boldsymbol{q}]\!] \cdot \boldsymbol{n}_{\mathcal{S}}. \tag{2.27}$$

By assuming that the balance of linear momentum (2.22) holds, we may multiply Equation (2.22) by the velocity field $\boldsymbol{v}$ and subtract it from the balance of total energy (2.26) to obtain the balance of internal energy in local form

$$\dot{e} = h - \operatorname{div}(\boldsymbol{q}) + \boldsymbol{\sigma} : \dot{\boldsymbol{\varepsilon}}. \tag{2.28}$$

Note that the internal energy is not conserved. Thus, we refrain from evaluating the jump condition (2.20) on the material singular surface.

Balance of entropy

While the equations stated above are universal in nature, a universal balance of entropy may not be found without making additional constitutive assumptions on the flux and the supply of entropy, see for instance Cimmelli et al. (2014) for a summary of different approaches. To arrive at the balance of entropy in its most universal form, we consider the volume-specific[2] entropy density $s : \Omega_t \times [0,T] \to \mathbb{R}$ as the quantity to be balanced and introduce the general entropy flux $\boldsymbol{q}_s : \Omega_t \times [0,T] \to \mathrm{V}^d$, the general entropy production density $p_s : \Omega_t \times [0,T] \to \mathbb{R}$ and the general supply density of entropy $s_s : \Omega_t \times [0,T] \to \mathbb{R}$, giving rise to the local balance of entropy in regular points

$$\dot{s} = \operatorname{div}(\boldsymbol{q}_s) + p_s + s_s. \tag{2.29}$$

[2] As for the internal energy e, we work with volume-specific quantities. The mass-specific entropy $\hat{s} = s/\varrho$ may be computed using the mass density ϱ.

For points on the material singular surface, we obtain

$$[\![\boldsymbol{q}_s]\!] \cdot \boldsymbol{n}_{\mathcal{S}} = 0. \tag{2.30}$$

The second law of thermodynamics states that the production density of entropy may never be negative (Coleman and Noll, 1963)

$$p_s \geq 0. \tag{2.31}$$

As abstract as this statement may be, it has far-reaching implications for the direction of thermomechanical processes, as we will see in the next section.

2.4 The Clausius-Duhem inequality

For any thermomechanical process, the balance of mass, linear and angular momentum as well as the first and second law of thermodynamics need to be universally fulfilled. In continuum solid mechanics, the entropy balance is typically not solved explicitly. Rather, the second law of thermodynamics, i.e., a non-negative entropy production, is embedded implicitly in the constitutive relations so that Relation (2.31) holds universally. This approach is commonly referred to as *rational thermodynamics* (Truesdell, 1984).

We combine the balance of internal energy (2.28), the balance of entropy (2.29) and the second law of thermodynamics (2.31). For this, constitutive assumptions on the entropy flux $\boldsymbol{q}_s$ and the entropy supply density s_s need to be made first. We follow the work of Coleman and Noll (1963) and assume for the flux and supply density of entropy the constitutive relations

$$\boldsymbol{q}_s \equiv \frac{\boldsymbol{q}}{\theta} \quad \text{and} \quad s_s \equiv \frac{h}{\theta} \tag{2.32}$$

to hold, where $\theta : \Omega_t \times [0,T] \to \mathbb{R}_{>0}$ denotes the absolute temperature. With the volume-specific[3] Helmholtz free energy density $\psi = e - s\theta$, we obtain the so-called Clausius-Duhem inequality

$$\boldsymbol{\sigma} : \dot{\boldsymbol{\varepsilon}} - \dot{\psi} - s\dot{\theta} - \frac{\boldsymbol{q} \cdot \nabla\theta}{\theta} \geq 0. \tag{2.33}$$

For deriving meaningful restrictions imposed by the seconds law of thermodynamics, we assume[4] the Helmholtz free energy density

$$\psi : \mathrm{Sym}_2(d) \times \mathbb{R}_{>0} \times \mathcal{Z}, \quad (\boldsymbol{\varepsilon}, \theta, \boldsymbol{z}) \mapsto \psi(\boldsymbol{\varepsilon}, \theta, \boldsymbol{z}) \tag{2.34}$$

to be a function of the strain $\boldsymbol{\varepsilon} : \Omega_t \times [0,T] \to \mathrm{Sym}_2(d)$, the absolute temperature $\theta : \Omega_t \times [0,T] \to \mathbb{R}_{>0}$, and an n-tuple of internal variables $\boldsymbol{z} : \Omega_t \times [0,T] \to \mathcal{Z}$, living in a sufficiently large Banach vector space $\mathcal{Z}$. By assuming that the Helmholtz free energy density ψ is sufficiently smooth in all its arguments, we obtain the following form of the Clausius-Duhem inequality

$$\left[\boldsymbol{\sigma} - \frac{\partial\psi}{\partial\boldsymbol{\varepsilon}}(\boldsymbol{\varepsilon}, \theta, \boldsymbol{z})\right] : \dot{\boldsymbol{\varepsilon}} + \left[-s - \frac{\partial\psi}{\partial\theta}(\boldsymbol{\varepsilon}, \theta, \boldsymbol{z})\right] \dot{\theta} - \frac{\boldsymbol{q} \cdot \nabla\theta}{\theta} - \frac{\partial\psi}{\partial\boldsymbol{z}}(\boldsymbol{\varepsilon}, \theta, \boldsymbol{z}) \cdot \dot{\boldsymbol{z}} \geq 0. \tag{2.35}$$

The former equation has to hold for any feasible thermomechanical process. Consequently, restrictions on the Helmholtz free energy might be derived.

For instance, as $\dot{\boldsymbol{\varepsilon}}$ and $\dot{\theta}$ might be chosen arbitrarily (assuming suitably boundary conditions have been chosen), the first two terms in

[3] See Footnote 2.

[4] Here, assuming a variety of functional arguments of ψ is possible. However, this is not always reasonable, as a variety of other physical principles have to be fulfilled as well, for instance the principle of material objectivity or determinism. We refer the interested reader to Liu (2002) for a summary.

the Clausius-Duhem (2.35) inequality must vanish identically. This is ensured by choosing the following potential relations for the stress and the entropy density

$$\boldsymbol{\sigma} = \frac{\partial \psi}{\partial \boldsymbol{\varepsilon}}(\boldsymbol{\varepsilon}, \theta, \boldsymbol{z}) \quad \text{and} \quad s = -\frac{\partial \psi}{\partial \theta}(\boldsymbol{\varepsilon}, \theta, \boldsymbol{z}). \tag{2.36}$$

By this choice, the Clausius-Duhem inequality is certainly fulfilled if the thermal $\mathcal{D}_{\text{heat}}$ and mechanical $\mathcal{D}_{\text{mech}}$ dissipation

$$\mathcal{D}_{\text{heat}} = -\frac{\boldsymbol{q} \cdot \nabla \theta}{\theta} \quad \text{and} \quad \mathcal{D}_{\text{mech}} = -\frac{\partial \psi}{\partial \boldsymbol{z}}(\boldsymbol{\varepsilon}, \theta, \boldsymbol{z}) \cdot \dot{\boldsymbol{z}} \tag{2.37}$$

are non-negative. Typically, both terms are treated separately for reasons of simplicity, giving rise to two remaining residual inequalities

$$\mathcal{D}_{\text{heat}} \geq 0 \tag{2.38}$$

and

$$\mathcal{D}_{\text{mech}} \geq 0. \tag{2.39}$$

The objective of material modeling is to propose constitutive relations that satisfy the above-mentioned potential relations and adhere to these two residual inequalities. Such a material model is then called *thermomechanically consistent*.

For instance, restricting to linear heat conduction, we might ensure the non-negativity of the thermal dissipation $\mathcal{D}_{\text{heat}}$ by modeling the heat flux $\boldsymbol{q}$ in terms of Fourier's law

$$\boldsymbol{q} = -\boldsymbol{\kappa} \nabla \theta, \tag{2.40}$$

where $\boldsymbol{\kappa} \in \mathrm{Sym}_2^+(d)$ denotes the positive definite second-order thermal conductivity tensor and $\nabla \theta$ denotes the spatial gradient of the absolute temperature.

In the following sections, we consider the two-potential framework of generalized standard materials, a powerful tool for material modeling, which ensures thermodynamic consistency and encompasses many commonly used material models such as (visco-)elasticity, (visco-)plasticity or non-softening damage (Görthofer et al., 2022b).

2.5 Generalized standard materials

We consider a small-strain, quasi-static, non-isothermal generalized standard material (GSM) (Biot, 1954; Halphen and Nguyen, 1975; Germain et al., 1983) to be a quadruple $\mathcal{G} = (\mathcal{Z}, \psi, \phi, \boldsymbol{z}_0)$ consisting of

- a (sufficiently large) Banach vector space $\mathcal{Z}$ of internal variables,
- a Helmholtz free energy density $\psi : \mathrm{Sym}_2(d) \times \mathbb{R}_{>0} \times \mathcal{Z} \to \mathbb{R}$,

$$(\boldsymbol{\varepsilon}, \theta, \boldsymbol{z}) \mapsto \psi(\boldsymbol{\varepsilon}, \theta, \boldsymbol{z}), \tag{2.41}$$

  which we assume to be differentiable w.r.t. all its arguments,
- an extended-real-valued dissipation potential $\phi : \mathbb{R}_{>0} \times \mathcal{Z} \to \mathbb{R} \cup \{+\infty\}$,

$$(\theta, \dot{\boldsymbol{z}}) \mapsto \phi(\theta, \dot{\boldsymbol{z}}), \tag{2.42}$$

  which we assume to be proper, convex, lower semicontinuous in its second argument, and to satisfy $\phi(\cdot, \mathbf{0}) = 0$ as well as $\mathbf{0} \in \partial_{\dot{\boldsymbol{z}}} \phi(\cdot, \mathbf{0})$, where $\partial_{\dot{\boldsymbol{z}}} \phi$ denotes the subdifferential of the convex function ϕ w.r.t. its second argument,
- and a field $\boldsymbol{z}_0 : \Omega_t \to \mathcal{Z}$ serving as initial condition for the dynamics.

For every strain $\boldsymbol{\varepsilon} : \Omega_t \times [0, T] \to \mathrm{Sym}_2(d)$, temperature $\theta : \Omega_t \times [0, T] \to \mathbb{R}_{>0}$ and internal variables $\boldsymbol{z} : \Omega_t \times [0, T] \to \mathcal{Z}$ with final time $T \in (0, \infty]$, the Cauchy stress $\boldsymbol{\sigma} : \Omega_t \times [0, T] \to \mathrm{Sym}_2(d)$ is expressed in terms of the potential relation

$$\boldsymbol{\sigma} = \frac{\partial \psi}{\partial \boldsymbol{\varepsilon}}(\boldsymbol{\varepsilon}, \theta, \boldsymbol{z}). \tag{2.43}$$

Furthermore, the evolution of the internal variables $\boldsymbol{z}$ is governed by the initial value problem described by Biot's (generalized) equation

$$-\frac{\partial \psi}{\partial \boldsymbol{z}}(\boldsymbol{\varepsilon}, \theta, \boldsymbol{z}) \in \partial_{\dot{\boldsymbol{z}}}\, \phi(\theta, \dot{\boldsymbol{z}}) \tag{2.44}$$

with the initial condition $\boldsymbol{z}(\cdot, 0) = \boldsymbol{z}_0$. Here, the dot $\dot{\square}$ denotes the material time derivative, which in the context of small strains is equal to the local time derivative. For GSMs, the internal variables may be considered, in general, as unobservable. Nevertheless, there might be cases where observable state variables are chosen as internal variables.

Any GSM, which fulfills the assumptions stated above, is thermodynamically consistent, i.e., conforms to the Clausius-Duhem inequality (2.35). Clearly, by definition, the stress and entropy follows the potential relations (2.36). Furthermore, we will show that the residual inequality (2.39) is fulfilled as well. For this, we use the definition of the subdifferential (Rockafellar, 1970, Theorem 25.1) of $\phi(\theta, \dot{\boldsymbol{z}})$ and rewrite Equation (2.44) as

$$\phi(\theta, \dot{\boldsymbol{y}}) \geq \phi(\theta, \dot{\boldsymbol{z}}) - \frac{\partial \psi}{\partial \boldsymbol{z}}(\boldsymbol{\varepsilon}, \theta, \boldsymbol{z}) \cdot (\dot{\boldsymbol{y}} - \dot{\boldsymbol{z}}) \quad \forall \dot{\boldsymbol{y}} \in \mathcal{Z}. \tag{2.45}$$

As Equation (2.45) holds for any $\dot{\boldsymbol{y}} \in \mathcal{Z}$, we choose $\dot{\boldsymbol{y}} \equiv \boldsymbol{0}$ and, using the assumptions for the dissipation potential $\phi(\theta, \dot{\boldsymbol{z}})$ from above, we obtain

$$\mathcal{D}_{\text{mech}} = -\frac{\partial \psi}{\partial \boldsymbol{z}}(\boldsymbol{\varepsilon}, \theta, \boldsymbol{z}) \cdot \dot{\boldsymbol{z}} \geq \phi(\theta, \boldsymbol{z}) \geq 0. \tag{2.46}$$

In other words, as long as the dissipation is non-negative, we obtain a thermodynamically consistent material model regardless of the exact form of both potentials.

The previous considerations focused on the continuous-time setting. To use a GSM in a discrete-time context, for instance, as a constitutive law in a finite element simulation, a time discretization needs to be supplied first. Owing to its absolute stability and ease of implementation, the implicit Euler method is the tool of choice. Thus, discretizing Biot's

equation (2.44) in time with the implicit Euler method gives rise to the condensed free energy potential $\Psi : \mathrm{Sym}_2(d) \times \mathbb{R}_{>0} \times \mathcal{Z} \to \mathbb{R}$,

$$\Psi(\boldsymbol{\varepsilon}^{n+1}, \theta^{n+1}, \boldsymbol{z}^n) = \inf_{\boldsymbol{z}^{n+1} \in \mathcal{Z}} \left(\psi\left(\boldsymbol{\varepsilon}^{n+1}, \theta^{n+1}, \boldsymbol{z}^{n+1}\right) + \triangle t \, \phi\left(\theta^{n+1}, \frac{\boldsymbol{z}^{n+1} - \boldsymbol{z}^n}{\triangle t}\right)\right), \quad (2.47)$$

where $\triangle t = t^{n+1} - t^n$ denotes the current time increment and the superscript n refers to the n-th time step at time t^n. This process is commonly referred to as the condensation of the internal variables, hence the name "condensed potential", see also Lahellec and Suquet (2007a;b). Indeed, the condensed free energy potential (2.47) solely depends on the strain $\boldsymbol{\varepsilon}^{n+1} \in \mathrm{Sym}_2(d)$ and temperature $\theta^{n+1} \in \mathbb{R}_{>0}$ of the current time step $n+1$ and the internal variables $\boldsymbol{z}^n \in \mathcal{Z}$ of the last converged time step n.

For a fixed temperature θ^{n+1}, the stress

$$\boldsymbol{\sigma}^{n+1} = \frac{\partial \Psi}{\partial \boldsymbol{\varepsilon}}\left(\boldsymbol{\varepsilon}^{n+1}, \theta^{n+1}, \boldsymbol{z}^n\right) \quad (2.48)$$

is given by a nonlinear elastic law as it only depends on the strain increment $\boldsymbol{\varepsilon}^{n+1}$. The internal variables $\boldsymbol{z}^n$ of the last converged time step are considered fixed. Indeed, the internal variables of the current time step $\boldsymbol{z}^{n+1}$ are determined in a post-processing step.

Chapter 3

On the micromechanics of deep material networks[1]

3.1 Introduction

In this chapter, we investigate deep material networks from the viewpoint of classical small-strain micromechanics, where we restrict to materials without pores or defects. In the original formulation presented by Liu et al. (2019a) and Liu and Wu (2019), one- and two-phase deep material networks are trained on linear elastic data and afterwards applied to nonlinear and inelastic problems with astonishing accuracy. We investigate this phenomenon from a theoretical viewpoint. More precisely, we wish to understand in which sense linear elastic homogenization determines the homogenization of inelastic problems on the same microstructure.

It is well-known from elementary mathematics that a continuously differentiable function f on Euclidean space is well-approximated at a point x_0 by its linear approximation $f(x_0) + f'(x_0)(x - x_0)$. Thus, we may similarly hope that the homogenization of linear problems approximates the nonlinear homogenization as well, at least in a local

[1] This chapter is based on Section 2 and 5 of the publication "On the micromechanics of deep material networks" (Gajek et al., 2020). The introduction has been shortened to avoid redundancy with Chapter 1. The notation has been harmonized.

sense. However, turning the latter idea into mathematical statements is not so straightforward, for a variety of reasons:

1. What is actually the function to approximate? One problem is that inelastic problems may feature internal variables, which are not accounted for in the linear homogenization.
2. What is the analogue of the Taylor approximation in our context?
3. When linearizing, the Taylor argument above suggests looking at the homogenization of linear elasticity with eigenstrains, but Liu et al. (2019a) and Liu and Wu (2019) only consider linear elastic homogenization. Is there a difference?

This chapter approaches these questions as follows. As our basic objects, we consider what we call microstructure functions. These take as input a number of generalized standard materials, see Section 2.5, one for each phase, and return as output another GSM. We show that periodic homogenization naturally gives rise to a homogenization function, answering Question 1, see Section 3.2. Motivated by the homogenization of linear viscoelasticity, which we recall in Appendix A.1, Section 3.3 is devoted to showing that the affine-linear homogenization function determines the inelastic homogenization function to first order in the strain rate. The key technical idea is to regard the generalized standard material as a dynamical system which may be approximated by a Volterra series. The latter procedure eliminates the internal variables from the picture. The terms of degree 0 and 1 in the strain rate entering the Volterra series precisely correspond to linear viscoelastic material behavior. In this sense, a linear viscoelastic material may approximate a general standard material in the same way a general nonlinear function is approximated by its linear approximation, addressing Question 2.

Then, we shall turn our attention to Question 3. We show that, for a general N-phase microstructure, the affine-linear homogenization function is determined by linear elastic homogenization, as long as the phase-wise averaged localization tensors are tracked, see Section 3.4.

Here, micromechanics comes into play in the form of the celebrated Mandel-Levin formula. Last but not least, in Section 3.5, we answer Question 3 by showing that for two-phase materials it suffices to track the effective stiffness only, i.e., it is not necessary to account for the individual strain localization functions. This is interesting, as Liu et al. (2019a) and Liu and Wu (2019) restrict to two-phase materials only. For more than two phases, it appears imperative to track the average stresses per phase, and not only the effective stress.

3.2 Homogenization functions for periodic homogenization

We consider small-strain generalized standard materials as our basic material model to which we apply homogenization. In contrast to Section 2.5, we restrict to the isothermal setting for now and denote with $\mathcal{GSM}$ the set of all generalized standard materials.

To summarize ideas, we consider a small-strain isothermal GSM in $d \in \{2, 3\}$ spatial dimensions to be the quadruple $\mathcal{G} = (\mathcal{Z}, \psi, \phi, \boldsymbol{z}_0) \in \mathcal{GSM}$ consisting of

1. a (Banach) vector space $\mathcal{Z}$ of internal variables,
2. a free energy density $\psi : \mathrm{Sym}_2(d) \times \mathcal{Z} \to \mathbb{R}$, which we assume to be continuously differentiable w.r.t. all its arguments,
3. an extended-real-valued dissipation potential $\phi : \mathcal{Z} \to \mathbb{R} \cup \{+\infty\}$, which we assume to be proper, convex, lower semicontinuous and to satisfy $\phi(\mathbf{0}) = 0$ as well as $\mathbf{0} \in \partial\phi(\mathbf{0})$, where $\partial\phi$ denotes the subdifferential of ϕ,
4. an element $\boldsymbol{z}_0 \in \mathcal{Z}$ serving as initial condition for the dynamics.

For a prescribed strain path $\boldsymbol{\varepsilon} : [0, T] \to \mathrm{Sym}_2(d)$ with $\boldsymbol{\varepsilon}(0) = \mathbf{0}$ and $T \in (0, \infty]$, the Cauchy stress $\boldsymbol{\sigma} : [0, T] \to \mathrm{Sym}_2(d)$ associated to the

GSM $(\mathcal{Z}, \psi, \phi, \boldsymbol{z}_0)$ is given by the potential relation

$$\boldsymbol{\sigma} = \frac{\partial \psi}{\partial \boldsymbol{\varepsilon}}(\boldsymbol{\varepsilon}, \boldsymbol{z}), \tag{3.1}$$

where the internal variables $\boldsymbol{z} : [0, T] \to \mathcal{Z}$ solve the initial value problem described by Biot's (generalized) equation

$$-\frac{\partial \psi}{\partial \boldsymbol{z}}(\boldsymbol{\varepsilon}, \boldsymbol{z}) \in \partial \phi(\dot{\boldsymbol{z}}) \tag{3.2}$$

with initial condition $\boldsymbol{z}(0) = \boldsymbol{z}_0$.

It might be possible to choose two different GSMs which are indistinguishable from a mechanical point of view. More precisely, we consider two GSMs $\mathcal{G}_1 \in \mathcal{GSM}$ and $\mathcal{G}_2 \in \mathcal{GSM}$ equivalent if, for any strain path, the resulting stress paths $\boldsymbol{\sigma}_1$ and $\boldsymbol{\sigma}_2$ are identical.

Suppose an N-phase periodic microstructure is given, i.e., a rectangular unit cell $Y \subseteq \mathrm{V}^d$ and N (measurable) characteristic functions $\{\chi_i\}_{i=1}^N$ whose associated sets are mutually disjoint and cover all of Y, i.e.,

$$\chi_i \chi_j = 0 \quad (i \neq j) \quad \text{and} \quad \sum_{i=1}^{N} \chi_i = 1 \tag{3.3}$$

hold almost everywhere. It is well-known that GSMs are closed under homogenization. More precicely, if all N phases of a microstructure are generalized standard materials, then the effective material law is a GSM as well, see for instance Michel and Suquet (2003). Thus, periodic homogenization gives rise to the nonlinear homogenization function

$$\begin{gathered} \mathcal{M}_Y : \mathcal{GSM}^N \to \mathcal{GSM}, \\ ((\mathcal{Z}_1, \psi_1, \phi_1, \boldsymbol{z}_{0,1}), \ldots, (\mathcal{Z}_N, \psi_N, \phi_N, \boldsymbol{z}_{0,N})) \mapsto (\bar{\mathcal{Z}}, \bar{\psi}, \bar{\phi}, (\boldsymbol{0}, \bar{\boldsymbol{z}}_0)), \end{gathered} \tag{3.4}$$

where

1. $\bar{\mathcal{Z}}$ is the set of tuples $(\boldsymbol{u}, \boldsymbol{z})$ for the periodic displacement fluctuation $\boldsymbol{u} : Y \to \mathrm{V}^d$ with anti-periodic normal derivative and mapping $\boldsymbol{z} : Y \to \mathcal{Z}_1 \oplus \mathcal{Z}_2 \oplus \ldots \oplus \mathcal{Z}_N$, which inherits the vector space structure from the codomain,
2. $\bar{\psi}(\bar{\boldsymbol{\varepsilon}}, \boldsymbol{u}, \boldsymbol{z}) = \left\langle \sum_{i=1}^{N} \chi_i \psi_i(\bar{\boldsymbol{\varepsilon}} + \nabla^{\mathrm{s}} \boldsymbol{u}, \boldsymbol{z}_i) \right\rangle_Y$, where $\bar{\boldsymbol{\varepsilon}}$ denotes the macro strain, ∇^{s} denotes the symmetrized spatial gradient and $\boldsymbol{z}_i : Y \to \mathcal{Z}_i$ is the i-th part of $\boldsymbol{z} : Y \to \mathcal{Z}_1 \oplus \mathcal{Z}_2 \oplus \ldots \oplus \mathcal{Z}_N$,
3. $\bar{\phi}(\dot{\boldsymbol{u}}, \dot{\boldsymbol{z}}) = \left\langle \sum_{i=1}^{N} \chi_i \phi_i(\dot{\boldsymbol{z}}_i) \right\rangle_Y$, where $\dot{\boldsymbol{z}}_i : Y \to \mathcal{Z}_i$ is the i-th part of $\dot{\boldsymbol{z}} : Y \to \mathcal{Z}_1 \oplus \mathcal{Z}_2 \oplus \ldots \oplus \mathcal{Z}_N$ and
4. $\bar{\boldsymbol{z}}_0 = \sum_{i=1}^{N} \chi_i \boldsymbol{z}_{0,i}$.

Here, $\langle \square \rangle_Y = \frac{1}{|Y|} \int_Y \square \, \mathrm{d}\boldsymbol{x}$ denotes taking the mean value of the quantity in brackets. The effective stress $\bar{\boldsymbol{\sigma}}$, is defined via

$$\bar{\boldsymbol{\sigma}}(\bar{\boldsymbol{\varepsilon}}, \boldsymbol{u}, \boldsymbol{z}) = \left\langle \sum_{i=1}^{N} \chi_i \frac{\partial \psi_i}{\partial \boldsymbol{\varepsilon}}(\bar{\boldsymbol{\varepsilon}} + \nabla^{\mathrm{s}} \boldsymbol{u}, \boldsymbol{z}_i) \right\rangle_Y . \tag{3.5}$$

The displacement fluctuation $\boldsymbol{u}$ satisfies the static balance of linear momentum on the microscopic scale

$$\operatorname{div} \left[\sum_{i=1}^{N} \chi_i \frac{\partial \psi_i}{\partial \boldsymbol{\varepsilon}}(\bar{\boldsymbol{\varepsilon}} + \nabla^{\mathrm{s}} \boldsymbol{u}, \boldsymbol{z}_i) \right] = \boldsymbol{0}, \tag{3.6}$$

which is, as $\partial \bar{\phi} / \partial \dot{\boldsymbol{u}}$ vanishes, equivalent to Biot's equation for the displacement fluctuation $\boldsymbol{u}$.

Several comments are in order:

1. The definition associates a homogenization function $\mathcal{M}_Y$ to every periodic microstructure Y. Although we cannot compare two periodic microstructures Y_1 and Y_2 directly, for instance because of mismatching size, it is possible to compare their associated homogenization functions $\mathcal{M}_{Y_1}$ and $\mathcal{M}_{Y_2}$. We say that Y_1 and Y_2 are equivalent if, for any N-tuple of GSMs $(\mathcal{G}_1, \mathcal{G}_2, \dots, \mathcal{G}_N)$ the homogenized GSMs $\mathcal{M}_{Y_1}(\mathcal{G}_1, \mathcal{G}_2, \dots, \mathcal{G}_N)$ and $\mathcal{M}_{Y_2}(\mathcal{G}_1, \mathcal{G}_2, \dots, \mathcal{G}_N)$ are equivalent. We call such an equivalence class $\mathcal{Y}$ a microstructure class, and each representative $Y \in \mathcal{Y}$ is called a representative volume element.
2. The definition of homogenization functions extend to stochastic homogenization in a straightforward way. Thus, we may treat stochastic microstructures and periodic unit cells in the same framework. However, for the sake of exposition, we restrict to the periodic setting.
3. Suppose a periodic microstructure Y is given. The purpose of homogenization theory is to find $\mathcal{M}_Y$. For practical reasons, only an approximation of $\mathcal{M}_Y$ can be provided. To each of these approximations, an error is associated, which has to be balanced with the effort of obtaining the approximation. For instance, analytical approximations are typically cheap to evaluate, but are limited in terms of accuracy. On the other hand, full-field approaches can be very accurate, but may require considerable computational effort, in particular in a concurrent multiscale framework. For deep material networks, $\mathcal{M}_Y$ is approximated by $\mathcal{M}_{Y'}$ by choosing Y' as a hierarchical laminate, see Chapter 4.
4. In engineering practice, microstructures with micro-oriented phases are also of interest, i.e., in addition to the cell Y and the characteristic functions $\{\chi_i\}_{i=1}^N$, a rotation field $\boldsymbol{R} : Y \to \mathrm{SO}(d)$ is given, where $\mathrm{SO}(d)$ denotes the special orthogonal group acting on V^d. Furthermore, to each GSM $(\mathcal{Z}, \psi, \phi, \boldsymbol{z}_0) \in \mathcal{GSM}$, an action by rotation on the internal variables $\rho : \mathrm{SO}(d) \to \mathrm{Aut}(\mathcal{Z})$ should be provided, where

$\mathrm{Aut}(\mathcal{Z})$ denotes the set of linear automorphisms of $\mathcal{Z}$. In this context, a homogenization function can be associated to $(Y, \{\chi_i\}_{i=1}^N, \boldsymbol{R})$, acting on all GSMs with an $\mathrm{SO}(d)$-representation in a straightforward way. We shall not focus on this case, but highlight two possible applications: crystallographic texture in polycrystals (Kuhn et al., 2020; 2022) and composites with anisotropic fibers, e.g., carbon fibers, both of which are considered by Liu and Wu (2019).

5. Although every periodic N-phase microstructure gives rise to a homogenization function, not every function $\mathcal{M}_Y : \mathcal{GSM}^N \to \mathcal{GSM}$ is induced by an N-phase microstructure. For instance, Voigt averaging gives rise to a homogenization function, but cannot – except for degenerated cases – be represented by a specific microstructure in finite dimensions. Still, it might be worth mentioning that the framework of homogenization functions permits treating both micromechanical bounding techniques and mathematical homogenization methods within the same theory.

   It is an interesting problem to determine which homogenization functions are induced by a microstructure. There are some obvious constraints, for instance

   $$\mathcal{M}_Y(\mathcal{G}, \ldots, \mathcal{G}) = \mathcal{G} \tag{3.7}$$

   should hold for any fixed $\mathcal{G} \in \mathcal{GSM}$. Also, a number of inequality constraints should hold, for instance those induced by Voigt averaging, or on the subset of monotonic GSMs. Notice, however, that all these (equality and inequality) constraints are preserved by convex combinations - and it might be hard to combine two unit cells! For the problem at hand, we shall not be concerned with the question of realizability, but focus on a constructive approach for realizing homogenization functions.
6. Hierarchical homogenization gives rise to a product structure on homogenization functions. More precisely, suppose an N-phase

microstructure Y is given, together with N microstructures Y_i, each with M_i phases. Then, if the i-th phase of Y is a material homogenized from Y_i, the resulting $(M_1 + M_2 + \ldots + M_N)$-phase microstructure has the homogenization function

$$(\mathcal{G}_1, \ldots, \mathcal{G}_{\sum M_i}) \mapsto \mathcal{M}_Y(\mathcal{M}_{Y_1}(\mathcal{H}_1), \mathcal{M}_{Y_2}(\mathcal{H}_2), \ldots, \mathcal{M}_{Y_N}(\mathcal{H}_N)) \quad (3.8)$$

with

$$\mathcal{H}_1 = (\mathcal{G}_1, \ldots, \mathcal{G}_{M_1}), \quad \mathcal{H}_2 = (\mathcal{G}_{M_1+1}, \ldots, \mathcal{G}_{M_1+M_2}), \quad \ldots. \quad (3.9)$$

Furthermore, any embedding $\iota : \mathcal{GSM}^M \to \mathcal{GSM}^N$ converts an N-phase homogenization function $\mathcal{M}$ to an M-phase homogenization function via

$$\mathcal{M} \circ \iota : \mathcal{GSM}^M \to \mathcal{GSM}, \quad (\mathcal{G}_1, \ldots, \mathcal{G}_M) \mapsto \mathcal{M}\left(\iota(\mathcal{G}_1, \ldots, \mathcal{G}_M)\right). \quad (3.10)$$

These two ideas can be combined. Suppose, for instance, that three two-phase microstructure functions $\mathcal{M}_Y$, $\mathcal{M}_{Y_1}$ and $\mathcal{M}_{Y_2}$ are given. These can be combined to a new two-phase microstructure function via

$$(\mathcal{G}_1, \mathcal{G}_2) \mapsto \mathcal{M}_Y\left(\mathcal{M}_{Y_1}(\mathcal{G}_1, \mathcal{G}_2), \mathcal{M}_{Y_2}(\mathcal{G}_1, \mathcal{G}_2)\right). \quad (3.11)$$

A hierarchical version of this construction is fundamental for constructing deep material networks, see Chapter 4.

Although the equivalence of two homogenization functions $\mathcal{M}_{Y_1}$ and $\mathcal{M}_{Y_2}$ for two microstructures Y_1 and Y_2 is easy to write down, checking the validity of the statement is not so straightforward. Indeed, it needs to be checked for any N-tuple of GSMs, any strain path $\boldsymbol{\varepsilon} : [0,T] \to \mathrm{Sym}_2(d)$, and on any time interval $[0,T]$. Thus, we consider the restriction of homogenization functions to affine-linear elastic materials, which we consider as linear elastic materials with residual strains. More precisely, we say a GSM $(\mathcal{Z}, \psi, \phi, \boldsymbol{z}_0) \in \mathcal{GSM}$ is affine-linear elastic if $\mathcal{Z} = \{0\}$ ("the" trivial vector space), $\phi \equiv 0$, $\boldsymbol{z}_0 = 0$ and

$$\psi(\boldsymbol{\varepsilon}) = \frac{1}{2}(\boldsymbol{\varepsilon} - \boldsymbol{\varepsilon}_{\mathrm{in}}) : \mathbb{C}\,[\boldsymbol{\varepsilon} - \boldsymbol{\varepsilon}_{\mathrm{in}}] \tag{3.12}$$

in terms of a positive definite stiffness tensor $\mathbb{C} \in \mathrm{Sym}_4^+(d)$ and a residual strain $\boldsymbol{\varepsilon}_{\mathrm{in}} \in \mathrm{Sym}_2(d)$. We denote the set of all affine-linear elastic GSMs by $\mathcal{AL} \subset \mathcal{GSM}$. By linearity, for any periodic microstructure Y, the homogenization function $\mathcal{M}_Y$ restricts to a mapping $\mathcal{M}_Y^{\mathcal{AL}} : \mathcal{AL}^N \to \mathcal{AL}$. Checking $\mathcal{M}_{Y_1}^{\mathcal{AL}} = \mathcal{M}_{Y_2}^{\mathcal{AL}}$ for two microstructures Y_1 and Y_2 is much simpler, because $\mathcal{AL}^N$ is a cone in finite dimensions and no internal variables need to be taken care of. Furthermore, no time-dependent strain paths need to be considered.

Clearly, $\mathcal{M}_{Y_1} = \mathcal{M}_{Y_2}$ implies $\mathcal{M}_{Y_1}^{\mathcal{AL}} = \mathcal{M}_{Y_2}^{\mathcal{AL}}$. The converse may not hold, in general. However, we shall show that $\mathcal{M}_{Y_1}^{\mathcal{AL}} = \mathcal{M}_{Y_2}^{\mathcal{AL}}$ implies that $\mathcal{M}_{Y_1} \approx \mathcal{M}_{Y_2}$ in a suitable sense if the arc length of the strain path is not too large, i.e.,

$$\int_0^T \|\dot{\boldsymbol{\varepsilon}}(t)\| \,\mathrm{d}t \ll 1 \tag{3.13}$$

holds. This is precisely the type of local approximation result replacing the Taylor approximation which we discussed in the beginning of this chapter.

3.3 Homogenization of generalized standard materials in terms of Volterra series

This section is devoted to showing that the affine-linear elastic homogenization function $\mathcal{M}_Y^{\mathcal{AL}}$ determines the nonlinear homogenization function $\mathcal{M}_Y$ to first order in the strain rate. Our treatment is motivated by the special case of linear viscoelasticity, which is completely determined by $\mathcal{M}_Y^{\mathcal{AL}}$. Homogenizing linear viscoelasticity is a classic in the literature, and typically based on Laplace transform techniques, see, e.g., Hashin (1970). For the sake of completeness, a streamlined presentation is included in Appendix A.1.

There are a couple of things to be learned from Appendix A.1:

1. No intrinsic meaning is associated to internal variables, manifesting in the equivalence relation inherent to generalized standard materials. The first step in understanding viscoelasticity consists of eliminating the internal variables from the representation, see Relation (A.6). The latter is realized by regarding linear viscoelasticity as a (linear and time-invariant) dynamical system. Here, the strain rate $\dot{\boldsymbol{\varepsilon}}$ serves as the system's input, and the current stress $\boldsymbol{\sigma}$ is regarded as the output of the dynamical system.
2. Our approach differs from the standard literature by avoiding Laplace and Fourier transform techniques. Fourier transforms only work for strain inputs defined on the entire time line, but require finite energy, i.e.,
$$\int_{-\infty}^{\infty} \|\dot{\boldsymbol{\varepsilon}}(t)\|^2 \, \mathrm{d}t < \infty \tag{3.14}$$
needs to hold. However, this rules out simple inputs of interest, for instance periodic loadings. In contrast, the Laplace transform can treat such signals. However, the Laplace transform does not – in contrast to the Fourier transform – give rise to an isomorphism of reasonable Banach spaces, rendering all arguments on the homogenization more

or less formal. Our presentation, however, can be made fully rigorous and extends to some nonlinear problems as well.

3. Interestingly, the intraphase heterogeneity for a general linear viscoelastic material subjected to arbitrary loadings appears to play no role. However, this is only partly true. Due to the linearity, the strain fields on the microstructure are realized as superpositions of strain fields resulting from linear elastic homogenization, but with general elastic material laws per phase. Put differently, the intraphase heterogeneity generated by arbitrary elastic behavior of the phases is "rich" enough to cover the intraphase heterogeneity of a phase-wise linear viscoelastic medium.

To generalize the approach beyond linear viscoelasticity, we shall seek a class of dynamical system representations of material laws similar to Relation (A.6)

$$\boldsymbol{\sigma}(t) = \boldsymbol{\sigma}_0(t) + \int_0^t \mathbb{G}(t-\tau)[\dot{\boldsymbol{\varepsilon}}(\tau)]\ \mathrm{d}\tau \tag{3.15}$$

of linear viscoelasticity in hereditary integral form. Motivated by results from dynamical systems theory, see Rugh (1981), we shall consider materials whose response to a strain-rate loading $\dot{\boldsymbol{\varepsilon}}$ is governed by a Volterra (1887) series

$$\begin{aligned}\boldsymbol{\sigma}(t) = \boldsymbol{\sigma}_0(t) + \sum_{k=1}^{\infty} \int_0^t \int_0^{\tau_1} \cdots \int_0^{\tau_{k-1}} \mathbb{G}_k(t-\tau_1, \tau_1-\tau_2, \ldots, \tau_{k-1}-\tau_k) \\ [\dot{\boldsymbol{\varepsilon}}(\tau_k), \dot{\boldsymbol{\varepsilon}}(\tau_{k-1}), \ldots, \dot{\boldsymbol{\varepsilon}}(\tau_1)] \\ \mathrm{d}\tau_k\ \mathrm{d}\tau_{k-1} \cdots \mathrm{d}\tau_1\end{aligned} \tag{3.16}$$

with kernel functions $\mathbb{G}_k$, or can, at least, be approximated with sufficient accuracy by such a series.

Before discussing which materials may be well-approximated by series of the form (3.16), we shall first discuss its *use* in the current context.

Assume, for the moment, that we have identified a class of materials which may be well-approximated by Volterra series, and which is closed under homogenization. Then, for a fixed N-phase microstructure, we may approximate the material model of each phase by a corresponding Volterra series. Also, we approximate the effective behavior of the microstructure by a Volterra series. Retaining only the term with $k = 1$ of the Volterra series expansion, we precisely obtain linear viscoelastic materials (3.15). Clearly, if the arc length

$$\int_0^T \|\dot{\boldsymbol{\varepsilon}}(t)\| \, \mathrm{d}t \ll 1 \tag{3.17}$$

of the considered time interval is small, the Volterra series response is dominated by the first-order term, i.e., the viscoelastic behavior. However, upon homogenization, the first-order approximations of the materials of each phase determines the first-order approximation of the effective material law. In this sense, the linear viscoelastic homogenization function *approximates* a general homogenization function $\mathcal{M}_Y$. As, in turn, the affine-linear elastic homogenization $\mathcal{M}_Y^{\mathcal{AL}}$ function determines the linear viscoelastic homogenization function, it *approximates* the general homogenization function $\mathcal{M}_Y$, as well.

Thus, it remains to discuss the circumstances when a material model may be approximated by a Volterra series of the form (3.16). There are rather general results on approximating the input/output operator of continuous dynamical systems by a series of Volterra type. However, these results are based on indirect functional-analytic arguments, which is why we delay discussing them until the end of this section. To provide some insight, we shall discuss a case where the generalized standard material is represented by a Volterra series (3.16) *exactly*, at least for short time, and the procedure for obtaining the representation is constructive. Essentially, both the free energy and the dissipation potential have to be analytic functions of their arguments, i.e., admit

a multi-dimensional power-series expansion, see Assumptions 1 to 3 below. These assumptions are, of course, very restrictive, and do not cover many practical cases of interest.

We first represent generalized standard materials as strain-rate controlled dynamical systems. Let $(\mathcal{Z}, \psi, \phi, \boldsymbol{z}_0) \in \mathcal{GSM}$ be a GSM with a continuously differentiable dissipation potential ϕ. For prescribed strain $\boldsymbol{\varepsilon} : [0,T] \to \mathrm{Sym}_2(d)$, we seek internal variables $\boldsymbol{z} : [0,T] \to \mathcal{Z}$ and the stress $\boldsymbol{\sigma} : [0,T] \to \mathrm{Sym}_2(d)$, s.t. Biot's equation (3.2)

$$\frac{\partial \psi}{\partial \boldsymbol{z}}(\boldsymbol{\varepsilon}, \boldsymbol{z}) + \frac{\partial \phi}{\partial \dot{\boldsymbol{z}}}(\dot{\boldsymbol{z}}) = \boldsymbol{0} \tag{3.18}$$

for which the initial condition $\boldsymbol{z}(0) = \boldsymbol{z}_0$ is satisfied and

$$\boldsymbol{\sigma} = \frac{\partial \psi}{\partial \boldsymbol{\varepsilon}}(\boldsymbol{\varepsilon}, \boldsymbol{z}) \tag{3.19}$$

holds. Equivalently, Biot's equation can be rewritten in terms of the force potential (Halphen and Nguyen, 1975)

$$\phi^* : \mathcal{Z}^* \to \mathbb{R}, \quad \boldsymbol{\beta} \mapsto \phi^*(\boldsymbol{\beta}) = \sup_{\dot{\boldsymbol{z}} \in \mathcal{Z}} \dot{\boldsymbol{z}} \cdot \boldsymbol{\beta} - \phi(\dot{\boldsymbol{z}}) \tag{3.20}$$

in the form

$$\dot{\boldsymbol{z}} = \left. \frac{\partial \phi^*}{\partial \boldsymbol{\beta}} \right|_{\boldsymbol{\beta} = -\frac{\partial \psi}{\partial \boldsymbol{z}}(\boldsymbol{\varepsilon}, \boldsymbol{z})}. \tag{3.21}$$

Under appropriate hypotheses, the latter system can be equivalently rewritten as a nonlinear dynamical system (Isidori, 1995)

$$\begin{aligned} \dot{\boldsymbol{\xi}} &= \boldsymbol{f}(\boldsymbol{\xi}) + \boldsymbol{g}(\boldsymbol{\xi}) : \dot{\varepsilon}, \\ \boldsymbol{\sigma} &= \boldsymbol{P}\boldsymbol{\xi}, \end{aligned} \tag{3.22}$$

for the initial condition $\boldsymbol{\xi}(0) = \boldsymbol{\xi}_0$, where $\boldsymbol{\xi} : [0,T] \to \mathcal{X}$ takes values in some vector space $\mathcal{X}$. The important observations for the dynamical system formulation (3.22) in its form are:

1. The stress $\boldsymbol{\sigma}$ serves as a (vectorial) output variable,
2. the strain rate $\dot{\boldsymbol{\varepsilon}}$ may be interpreted as the control variable,
3. $\boldsymbol{\xi}$ encodes the black-box dynamics and may be regarded as the state,
4. $\boldsymbol{P} : \mathcal{X} \to \mathrm{Sym}_2(d)$ is linear,
5. the control variable $\dot{\boldsymbol{\varepsilon}}$ enters linearly into Equation (3.22).

To prove Representation (3.22), we assume:

1. The free energy is twice continuously differentiable and the force potential is (once) continuously differentiable.
2. For fixed internal variable $\boldsymbol{z}$, the stress-strain relationship $\boldsymbol{\varepsilon} \mapsto \frac{\partial \psi}{\partial \boldsymbol{\varepsilon}}(\boldsymbol{\varepsilon}, \boldsymbol{z})$ is invertible, i.e.,

$$\boldsymbol{\varepsilon} = \left[\frac{\partial \psi}{\partial \boldsymbol{\varepsilon}}(\cdot, \boldsymbol{z})\right]^{-1}(\boldsymbol{\sigma}) = \mathcal{E}(\boldsymbol{\sigma}, \boldsymbol{z}) \tag{3.23}$$

   holds.
3. $\boldsymbol{\varepsilon}(t) = \mathbf{0}$ for $t \leq 0$.

For Assumption 2, it is sufficient that the stress-strain relationship $\boldsymbol{\varepsilon} \mapsto \frac{\partial \psi}{\partial \boldsymbol{\varepsilon}}(\boldsymbol{\varepsilon}, \boldsymbol{z})$ is, for any fixed $\boldsymbol{z} \in \mathcal{Z}$, strictly monotone, i.e., for fixed $\boldsymbol{z}$,

$$\left[\frac{\partial \psi}{\partial \boldsymbol{\varepsilon}}(\boldsymbol{\varepsilon}_1, \boldsymbol{z}) - \frac{\partial \psi}{\partial \boldsymbol{\varepsilon}}(\boldsymbol{\varepsilon}_2, \boldsymbol{z})\right] : (\boldsymbol{\varepsilon}_1 - \boldsymbol{\varepsilon}_2) > 0 \tag{3.24}$$

holds for all $\boldsymbol{\varepsilon}_1, \boldsymbol{\varepsilon}_2 \in \mathrm{Sym}_2(d)$ with $\boldsymbol{\varepsilon}_1 \neq \boldsymbol{\varepsilon}_2$. Indeed, by the Browder-Minty theorem, see Theorem 10.49 in Renardy and Rogers (2004), strictly monotone operators (under appropriate continuity hypotheses) are invertible. The latter condition encompasses all GSM where the internal variables are split into an inelastic strain $\boldsymbol{\varepsilon}_{\mathrm{in}}$ and a hardening-related variable $\varepsilon_{\mathrm{in}}$, s.t. the free energy that takes the form

$$\psi(\boldsymbol{\varepsilon}, \boldsymbol{\varepsilon}_{\mathrm{in}}, \varepsilon_{\mathrm{in}}) = \frac{1}{2}(\boldsymbol{\varepsilon} - \boldsymbol{\varepsilon}_{\mathrm{in}}) : \mathbb{C}\left[\boldsymbol{\varepsilon} - \boldsymbol{\varepsilon}_{\mathrm{in}}\right] + \frac{1}{2}\boldsymbol{\varepsilon}_{\mathrm{in}} : \mathbb{K}\left[\boldsymbol{\varepsilon}_{\mathrm{in}}\right] + H(\varepsilon_{\mathrm{in}}) \tag{3.25}$$

in terms of a non-degenerated stiffness tensor $\mathbb{C}$, a kinematic hardening tensor $\mathbb{K}$ and an isotropic hardening potential H. In the following, only Assumption 2 is needed.

So, let us write down the dynamical system (3.22) explicitly. Differentiating the stress-strain relationship

$$\boldsymbol{\sigma} = \frac{\partial \psi}{\partial \boldsymbol{\varepsilon}}(\boldsymbol{\varepsilon}, \boldsymbol{z}) \tag{3.26}$$

yields

$$\dot{\boldsymbol{\sigma}} = \frac{\partial^2 \psi}{\partial \boldsymbol{\varepsilon} \partial \boldsymbol{z}}(\boldsymbol{\varepsilon}, \boldsymbol{z}) \cdot \dot{\boldsymbol{z}} + \frac{\partial^2 \psi}{\partial \boldsymbol{\varepsilon}^2}(\boldsymbol{\varepsilon}, \boldsymbol{z}) : \dot{\boldsymbol{\varepsilon}}. \tag{3.27}$$

Accounting for Biot's equation (3.21) leads to the coupled system

$$\begin{aligned} \dot{\boldsymbol{\sigma}} &= \frac{\partial^2 \psi}{\partial \boldsymbol{\varepsilon} \partial \boldsymbol{z}}(\boldsymbol{\varepsilon}, \boldsymbol{z}) \cdot \left. \frac{\partial \phi^*}{\partial \boldsymbol{\beta}} \right|_{\boldsymbol{\beta} = -\frac{\partial \psi}{\partial \boldsymbol{z}}(\boldsymbol{\varepsilon}, \boldsymbol{z})} + \frac{\partial^2 \psi}{\partial \boldsymbol{\varepsilon}^2}(\boldsymbol{\varepsilon}, \boldsymbol{z}) : \dot{\boldsymbol{\varepsilon}}, \\ \dot{\boldsymbol{z}} &= \left. \frac{\partial \phi^*}{\partial \boldsymbol{\beta}} \right|_{\boldsymbol{\beta} = -\frac{\partial \psi}{\partial \boldsymbol{z}}(\boldsymbol{\varepsilon}, \boldsymbol{z})}. \end{aligned} \tag{3.28}$$

Inserting the inverted stress-strain relationship (3.23) yields, in appropriate vector notation,

$$\begin{aligned} \begin{bmatrix} \dot{\boldsymbol{\sigma}} \\ \dot{\boldsymbol{z}} \end{bmatrix} = &\begin{bmatrix} \dfrac{\partial^2 \psi}{\partial \boldsymbol{\varepsilon} \partial \boldsymbol{z}}(\mathcal{E}(\boldsymbol{\sigma}, \boldsymbol{z}), \boldsymbol{z}) \cdot \left. \dfrac{\partial \phi^*}{\partial \boldsymbol{\beta}} \right|_{\boldsymbol{\beta} = -\frac{\partial \psi}{\partial \boldsymbol{z}}(\mathcal{E}(\boldsymbol{\sigma}, \boldsymbol{z}), \boldsymbol{z})} \\ \left. \dfrac{\partial \phi^*}{\partial \boldsymbol{\beta}} \right|_{\boldsymbol{\beta} = -\frac{\partial \psi}{\partial \boldsymbol{z}}(\mathcal{E}(\boldsymbol{\sigma}, \boldsymbol{z}), \boldsymbol{z})} \end{bmatrix} \\ &+ \begin{bmatrix} \dfrac{\partial^2 \psi}{\partial \boldsymbol{\varepsilon}^2}(\mathcal{E}(\boldsymbol{\sigma}, \boldsymbol{z}), \boldsymbol{z}) \\ \mathbf{0} \end{bmatrix} : \dot{\boldsymbol{\varepsilon}}. \end{aligned} \tag{3.29}$$

Thus, we have shown the claim by defining $\boldsymbol{\xi} = [\boldsymbol{\sigma}, \boldsymbol{z}] \in \mathcal{X} = \mathrm{Sym}_2(d) \oplus \mathcal{Z}$ and

$$\begin{aligned}
\boldsymbol{f}(\boldsymbol{\xi}) &= \begin{bmatrix} \dfrac{\partial^2 \psi}{\partial \boldsymbol{\varepsilon} \partial \boldsymbol{z}}(\mathcal{E}(\boldsymbol{\sigma}, \boldsymbol{z}), \boldsymbol{z}) \cdot \left.\dfrac{\partial \phi^*}{\partial \boldsymbol{\beta}}\right|_{\boldsymbol{\beta} = -\frac{\partial \psi}{\partial \boldsymbol{z}}(\mathcal{E}(\boldsymbol{\sigma}, \boldsymbol{z}), \boldsymbol{z})} \\ \left.\dfrac{\partial \phi^*}{\partial \boldsymbol{\beta}}\right|_{\boldsymbol{\beta} = -\frac{\partial \psi}{\partial \boldsymbol{z}}(\mathcal{E}(\boldsymbol{\sigma}, \boldsymbol{z}), \boldsymbol{z})} \end{bmatrix}, \\
\boldsymbol{g}(\boldsymbol{\xi}) &= \begin{bmatrix} \dfrac{\partial^2 \psi}{\partial \boldsymbol{\varepsilon}^2}(\mathcal{E}(\boldsymbol{\sigma}, \boldsymbol{z}), \boldsymbol{z}) \\ \mathbf{0} \end{bmatrix}, \\
\boldsymbol{\sigma} &= \boldsymbol{P}\boldsymbol{\xi} \quad (\boldsymbol{P} \text{ is the projector onto the first element}),
\end{aligned} \tag{3.30}$$

obtaining the desired form (3.22) with initial condition

$$\boldsymbol{\xi}(0) = \left[\frac{\partial \psi}{\partial \boldsymbol{\varepsilon}}(\mathbf{0}, \boldsymbol{z}_0), \boldsymbol{z}_0 \right]. \tag{3.31}$$

Last but not least, let us remark that if ψ and ϕ^* are analytic, so are the functions $\boldsymbol{f}$ and $\boldsymbol{g}$.

Thus, under Observations 1 to 5, the generalized standard material $(\mathcal{Z}, \psi, \phi, \boldsymbol{z}_0)$ can be equivalently rewritten as the (abstract) dynamical system (3.22)

$$\begin{aligned}
\dot{\boldsymbol{\xi}} &= \boldsymbol{f}(\boldsymbol{\xi}) + \boldsymbol{g}(\boldsymbol{\xi}) : \dot{\boldsymbol{\varepsilon}}, \\
\boldsymbol{\sigma} &= \boldsymbol{P}\boldsymbol{\xi},
\end{aligned} \tag{3.32}$$

with the initial condition $\boldsymbol{\xi}(0) = \boldsymbol{\xi}_0$. In fact, any dynamical system of the form (3.32) with analytic coefficients admits a representation by a Volterra series (3.16), at least for short time. The derivation is standard in control-theory literature, see Rugh (1981), and is based on Carleman bilinearization (1932). Indeed, Carleman observed that, for analytic coefficents $\boldsymbol{f}$ and $\boldsymbol{g}$, the dynamical system (3.32) may be equivalently rewritten as a bilinear dynamical system, i.e., a system linear in the state and the input $\dot{\boldsymbol{\varepsilon}}$, if a new state variable is defined,

encompassing all possible monomials, i.e., homogenenous polynomials, in the components of $\boldsymbol{\xi}$. For such a bilinear dynamical system, the Volterra series approximation is obtained by the method of successive integration, see Rugh (1981). For the convenience of the reader, and as Rugh restricts to systems with single input and single output, the procedure is outlined in Appendix A.2.

As already stated, the assumptions on the analyticity of the free energy and the dissipation potential exclude a variety of material models of interest. For instance in the context of quasi-static (associated) elastoplasticity, the force potential is extended-valued, and attains the values 0 and $+\infty$, exclusively. Nevertheless, Sandberg (1982a;b; 1983) established that a wide range of causal time-invariant nonlinear dynamical systems, satisfying more general conditions, can be expressed in terms of a Volterra series expansion with $\dot{\boldsymbol{\sigma}}_0 \equiv \mathbf{0}$. Still, we presume that dynamical systems associated to such GSMs cannot, in general, be represented by a Volterra series (3.16) exactly. However, one might seek an approximation by a Volterra series. There are quite general results on approximating time-invariant input/output operators of dynamical systems in terms of a Volterra series. For instance, Boyd and Chua (1985) showed that any causal, time-invariant nonlinear operator $\mathcal{N}$ on $C(\mathbb{R})$, the Banach space of continuous functions on the real line, with *fading memory*, may be approximated, in the weak operator topology and on equi-bounded sets, by a Volterra series $\widetilde{\mathcal{N}}$ with $\dot{\boldsymbol{\sigma}}_0 \equiv \mathbf{0}$, see Theorem 1 in Boyd and Chua (1985). Here, the fading-memory concept deserves some attention. Informally speaking, it asserts that, "if two input signals which are close in the recent past, but not necessarily close in the remote past, yield present outputs which are close", see p. 1152 in Boyd and Chua (1985). Mathematically speaking, fading memory is a continuity assumption of the nonlinear operator in question w.r.t. a weighted maximum norm, see Boyd and Chua (1985) for details. Also, causal time-invariant nonlinear operators which are merely continuous on $C(\mathbb{R})$ may be approximated

by a Volterra series on compact subsets and for short time, see Rugh (1981).

General standard materials give rise to causal nonlinear operators on $C(\mathbb{R}; \mathrm{Sym}_2(d))$, mapping a history of strain rates to a history of stresses, under technical conditions, see, for instance, Mielke (2006). Whether they are fading-memory or are merely continuous has to be decided on a case-to-case basis. Still, the concepts appear general enough to encompass GSM of interest. Indeed, the assumption that small changes in the strain-rate history lead to small changes in the resulting stress seems physically plausible, at least if fracture models are excluded. Also, the fading-memory concept is related to purely viscous material models.

Of course, the Volterra series expansion results are stated for single-input-single-output systems. However, the approximation arguments stated above carry over to multiple-input-multiple-output systems, at least if the number of inputs and outputs is finite. To conclude this part, let us remark that the practical usefulness of the Volterra series form (3.16) of material models appears limited. The latter has mainly been introduced for theoretical reasons.

3.4 Linear elastic localization determines affine-linear elastic homogenization

Recall the affine-linear elastic homogenization function

$$\mathcal{M}_Y^{\mathcal{AL}} : \mathcal{AL}^N \to \mathcal{AL} \tag{3.33}$$

of an N-phase microstructure Y with phases $\{\chi_i\}_{i=1}^N$. By definition, any affine-linear elastic GSM $(\mathcal{Z}, \psi, \phi, \boldsymbol{z}_0) \in \mathcal{AL}$ is determined by the phase-wise constant stiffness tensor $\mathbb{C}$ and the phase-wise constant inelastic strain $\boldsymbol{\varepsilon}_{\mathrm{in}}$. Thus, by abusing notation, we may also regard $\mathcal{M}_Y^{\mathcal{AL}}$ as a

function

$$\mathcal{M}_Y^{\mathcal{AL}} : ((\mathbb{C}_1, \boldsymbol{\varepsilon}_{\text{in},1}), (\mathbb{C}_2, \boldsymbol{\varepsilon}_{\text{in},2}), \dots, (\mathbb{C}_N, \boldsymbol{\varepsilon}_{\text{in},N})) \mapsto (\bar{\mathbb{C}}, \bar{\boldsymbol{\varepsilon}}_{\text{in}}). \tag{3.34}$$

Thus, in three spatial dimensions, $d = 3$, the input is $(21 + 6)N$-dimensional. However, we shall show that it is in fact sufficient to consider homogenization of linear elasticity, as long as the strain concentration tensors per phase are recorded. More precisely, we denote by

$$\mathcal{A}_Y : \mathrm{Sym}_4^+(d)^N \to L(\mathrm{Sym}_2(d))^N \tag{3.35}$$

the phase-wise average strain localization function associated to an N-phase microstructure Y, where $\mathrm{Sym}_4^+(d)$ denotes the convex cone of stiffness tensors and $L(\mathrm{Sym}_2(d))$ denotes the set of linear operators on $\mathrm{Sym}_2(d)$, defined via

$$\mathcal{A}_Y(\mathbb{C}_1, \mathbb{C}_2, \dots, \mathbb{C}_N) = (\langle \chi_1 \mathbb{A} \rangle_Y , \langle \chi_2 \mathbb{A} \rangle_Y , \dots, \langle \chi_N \mathbb{A} \rangle_Y) , \tag{3.36}$$

where $\mathbb{A} : Y \to \mathrm{Sym}_2(d) \otimes \mathrm{Sym}_2(d)$ is the linear elastic strain localization tensor associated to the stiffness tensor $\mathbb{C} : Y \to \mathrm{Sym}_4^+(d)$ with $\mathbb{C} = \sum_{i=1}^N \chi_i \mathbb{C}_i$. In contrast to the affine-linear elastic homogenization function (3.34), only $21N$ scalar input arguments are required for evaluating the linear elastic localization function (3.36) in three spatial dimensions.

The key observation for this section is that the data encoded in the affine-linear elastic homogenization function (3.34) and the linear elastic localization function (3.36) is identical, which is evident from the Mandel-Levin formula (Mandel, 1965; Levin, 1967). More precisely, let $(\mathbb{C}_1, \mathbb{C}_2, \dots, \mathbb{C}_N) \in \mathrm{Sym}_4^+(d)^N$ be given, together with N residual strains $(\boldsymbol{\varepsilon}_{\text{in},1}, \dots, \boldsymbol{\varepsilon}_{\text{in},N}) \in \mathrm{Sym}_2(d)$. Then, denoting by $\bar{\mathbb{C}}$ the effective stiffness, $\bar{\boldsymbol{\varepsilon}}_{\text{in}}$ the effective residual strain and by $\mathbb{A}$ the linear elastic strain localization tensor associated to $\mathbb{C} = \sum_{i=1}^N \chi_i \mathbb{C}_i$, we get

$$\bar{\mathbb{C}} = \langle \mathbb{C} : \mathbb{A} \rangle_Y \quad \text{and} \quad \bar{\boldsymbol{\varepsilon}}_{\text{in}} = \bar{\mathbb{C}}^{-1} : \langle \boldsymbol{\varepsilon}_{\text{in}} : \mathbb{C} : \mathbb{A} \rangle_Y \tag{3.37}$$

for $\boldsymbol{\varepsilon}_{\text{in}} = \sum_{i=1}^{N} \chi_i \boldsymbol{\varepsilon}_{\text{in},i}$. Since $\mathbb{C}$ and $\boldsymbol{\varepsilon}_{\text{in}}$ are phase-wise constant, we can also write the former as

$$\bar{\mathbb{C}} = \sum_{i=1}^{N} \mathbb{C}_i : \langle \chi_i \mathbb{A} \rangle_Y \quad \text{and} \quad \bar{\boldsymbol{\varepsilon}}_{\text{in}} = \bar{\mathbb{C}}^{-1} : \sum_{i=1}^{N} \boldsymbol{\varepsilon}_{\text{in},i} : \mathbb{C}_i : \langle \chi_i \mathbb{A} \rangle_Y \,. \tag{3.38}$$

The latter equations directly establishes the equivalence of $\mathcal{M}_Y^{\mathcal{AC}}$ and $\mathcal{A}_Y$.

3.5 Linear elastic homogenization determines elastic localization for two-phase materials

In the previous Section 3.4, we have seen that the affine-linear elastic homogenization function $\mathcal{M}_Y^{\mathcal{AC}}$ is determined by the linear elastic localization function $\mathcal{A}_Y$. The purpose of this section is to show that in the special case of two-phase materials, the affine-linear elastic homogenization function $\mathcal{M}_Y^{\mathcal{AC}}$ is determined by the elastic homogenization function $\mathcal{M}_Y^{\mathcal{C}}$. Thus, it is not necessary to track the phase-wise averaged stresses, but only the stresses averaged over the entire microstructure.

The statement is proved by observing that for almost all stiffness tensors, the phase-wise averaged stresses can be computed from the effective stiffness, provided the volume fractions are known. The statement is extended to all possible stiffness tensors by a continuity argument. To proceed, consider the strain localization function (3.36)

$$\mathcal{A}_Y(\mathbb{C}_1, \mathbb{C}_2) = (\langle \chi_1 \mathbb{A} \rangle_Y \,, \langle \chi_2 \mathbb{A} \rangle_Y) \tag{3.39}$$

of a two-phase medium. Denote by

$$\mathcal{M}_Y^{\mathcal{C}} : \mathrm{Sym}_4^+(d) \times \mathrm{Sym}_4^+(d) \to \mathrm{Sym}_4^+(d), \quad (\mathbb{C}_1, \mathbb{C}_2) \mapsto \bar{\mathbb{C}}, \tag{3.40}$$

the corresponding linear elastic homogenization function. The claim is equivalent to showing that, for two-phase materials with phase-wise constant properties, this linear elastic homogenization function determines the strain localization function.

Let two stiffness tensors $\mathbb{C}_1$ and $\mathbb{C}_2$ be given. Then, by the definition of the effective stiffness tensor, we obtain

$$\bar{\mathbb{C}} = \mathbb{C}_1 : \langle \chi_1 \mathbb{A} \rangle_Y + \mathbb{C}_2 : \langle \chi_2 \mathbb{A} \rangle_Y \,. \tag{3.41}$$

Thus, localization determines homogenization, so that the converse statement shall be our concern. So, suppose the difference of the stiffness tensors $(\mathbb{C}_1 - \mathbb{C}_2)$ is non-singular. Then, the linear system

$$\begin{aligned} \bar{\mathbb{C}} &= \mathbb{C}_1 : \langle \chi_1 \mathbb{A} \rangle_Y + \mathbb{C}_2 : \langle \chi_2 \mathbb{A} \rangle_Y \,, \\ \mathbb{I}_{\mathrm{s}} &= \langle \chi_1 \mathbb{A} \rangle_Y + \langle \chi_2 \mathbb{A} \rangle_Y \,, \end{aligned} \tag{3.42}$$

can be solved explicitly, see Hill (1963),

$$\langle \chi_1 \mathbb{A} \rangle_Y = (\mathbb{C}_1 - \mathbb{C}_2)^{-1} (\bar{\mathbb{C}} - \mathbb{C}_2) \quad \text{and} \quad \langle \chi_2 \mathbb{A} \rangle_Y = (\mathbb{C}_2 - \mathbb{C}_1)^{-1} (\bar{\mathbb{C}} - \mathbb{C}_1). \tag{3.43}$$

If $(\mathbb{C}_1 - \mathbb{C}_2)$ is singular, we conclude by continuity of $\mathcal{A}_Y$. More precisely, $\mathcal{A}_Y$ is an analytic function on $\mathrm{Sym}_4^+(d)^2$. In particular, it is continuous and finite-valued. The condition that $(\mathbb{C}_1 - \mathbb{C}_2)$ is singular determines an at most d-dimensional subset of $\mathrm{Sym}_4^+(d)^2$. However, $\mathrm{Sym}_4^+(d)^2$ is $d(d+1)$-dimensional. Thus, $\mathcal{A}_Y$ is determined on an d-codimensional set in $d(d+1)$-dimensional space. We conclude by continuity of $\mathcal{A}_Y$. Put differently, the Formula (3.43) has a removable singularity – if $(\mathbb{C}_1 - \mathbb{C}_2)$ is singular, so is $(\bar{\mathbb{C}} - \mathbb{C}_2)$.

3.6 Conclusion

For two-phase microstructures and isotropic conducting phases with thermal conductivities κ_1 and κ_2, series expansions of the effective thermal conductivity like

$$\bar{\boldsymbol{\kappa}}(\kappa_1, \kappa_2) = \frac{\kappa_1 + \kappa_2}{2} \sum_{k=0}^{\infty} \boldsymbol{A}_k x^k \quad \text{with} \quad x = \frac{\kappa_1 - \kappa_2}{\kappa_1 + \kappa_2} \tag{3.44}$$

in terms of a sequence $\{\boldsymbol{A}_k\}_{k=0}^{\infty}$ of symmetric second-order tensor are well-known, see Milton (2002) or Torquato (2005). The advantage of series expansions like (3.44) is their ability to separate the influence of the physical parameters (via x) and the influence of the geometrical arrangement of the phases (via $\boldsymbol{A}_k$) on the effective property in question. In particular, $\{\boldsymbol{A}_k\}_{k=0}^{\infty}$ characterizes the underlying microstructure from the viewpoint of (isotropic) heat conduction completely. Extended to elasticity, expansions of the type (3.44) become less useful, because the power series becomes multi-dimensional, and the number of scalar expansion coefficients becomes prohibitive quickly. In this chapter, we have provided a framework for extending Equation (3.44) to generalized standard material inputs by introducing homogenization functions, which generalize the sequences $\{\boldsymbol{A}_k\}_{k=0}^{\infty}$.

To understand to which degree linear (in)elastic homogenization determines the general homogenization function, we have advocated a reinterpretation of generalized standard materials as dynamical systems, utilizing the rich theory of dynamical systems (Rugh, 1981) to show that the affine-linear elastic homogenization function determines the nonlinear homogenization function to first order in the strain rate. It is of great interest to characterize explicitly which generalized standard material may be approximated by Volterra series (and in which sense, i.e., in which norm and on which time-scale), providing impetus for future work.

Combining the individual statements of this entire chapter, we have provided the mathematical underpinnings of the approach of Liu et al. (2019a) and Liu and Wu (2019): For two-phase materials, linear elastic homogenization determines nonlinear homogenization to first order in the strain rate. In particular, approximating the linear elastic homogenization function is sufficient to characterize the nonlinear behavior to first order, as well. In addition to understanding the previous approach more thoroughly, we have learned that for materials with more than two constituents, linear elastic localization needs to be learned instead of linear elastic homogenization.

Chapter 4

The framework of direct deep material networks[1]

4.1 Introduction

The goal of micromechanical theories may be stated as follows. Suppose a microstructure Y is given. For a given class of constitutive laws, we wish to identify an approximation to the nonlinear homogenization function $\mathcal{M}_Y$, s.t.

1. the approximation is close to the original function and
2. the approximation is reasonably fast to evaluate.

Clearly, these two objectives are opposing each other. Liu et al. (2019a) and Liu and Wu (2019) introduced deep material networks as a hierarchy of nested laminates to approximate the nonlinear homogenization function $\mathcal{M}_Y$. They main idea behind DMNs can be summarized as follows: The DMN is trained to approximate the affine-linear elastic homogenization function $\mathcal{M}_Y^{\mathcal{AL}}$ using machine learning techniques. Subsequently, the identified model is applied to nonlinear and inelastic problems with good accuracy. In addition, the DMN's nonlinear homogenization function is reasonably fast to evaluate.

[1] This chapter is based on Section 3, 4 and 5 of the publication "On the micromechanics of deep material networks" (Gajek et al., 2020). The introduction has been shortened to avoid redundancy with Chapter 1. The notation has been harmonized.

In Section 4.2, we introduce *direct DMNs*[2], which feature a reduced number of degrees of freedom compared to the original formulation of Liu et al. (2019a) and Liu and Wu (2019) by omitting rotations and utilizing laminate building blocks with arbitrary direction of lamination. In Section 4.2.2, we present how such building blocks may be efficiently evaluated for the N-phase homogenization of linear elasticity with eigenstrains. Furthermore, we introduce a novel solution technique for nonlinear DMNs with arbitrary tree topologies and multi-phase laminates in Section 4.2.3.

We establish that (direct) DMNs inherit thermodynamic consistency and stress-strain monotonicity from their phases by interpreting them as hierarchical microstructures. The former properties contrast with less sophisticated applications of neural networks to approximate the stress-strain response of a microstructure, where thermodynamic consistency and preservation of monotonicity is not guaranteed, in general.

In Section 4.3, we elaborate essential implementation details followed by Section 4.4, where we apply direct DMNs to microstructures of industrial complexity: A short glass fiber reinforced polyamide (FRP) and a metal matrix composite (MMC). We evaluate offline training and online evaluation separately and show that direct DMNs are capable of predicting the stress-strain response of the FRP and MMC to engineering accuracy, respectively.

[2] Originally, Gajek et al. (2020) introduced their formulation as "rotation-free" DMNs. However, to keep the nomenclature consistent with later publications (Gajek et al., 2021a;b; 2022; Meyer et al., 2023), the term "rotation-free" was changed to "direct" throughout this chapter.

4.2 Considering deep material networks with a variable direction of lamination

4.2.1 Direct DMNs with N phases

Suppose we wish to approximate the homogenization function

$$\mathcal{M}_Y : \mathcal{GSM}^N \to \mathcal{GSM} \tag{4.1}$$

of an N-phase microstructure. Deep material networks take as starting point the homogenization function

$$\mathcal{B} : \mathcal{GSM}^N \to \mathcal{GSM} \tag{4.2}$$

associated to an N-phase laminate microstructure, see Figure 4.1. The latter homogenization function will not serve as an accurate approximation of the former homogenization function unless the original microstructure is a laminate.

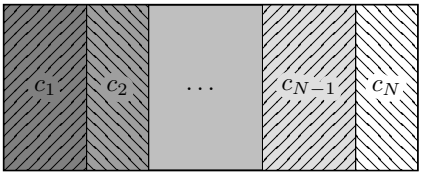

Figure 4.1: N-phase laminate microstructure with volume fractions $c_1,\ c_2, \ldots, c_N$.

We noticed in Section 3.2 that it is possible to concatenate homogenization functions. Motivated by the deep learning paradigm (Aizenberg et al., 2013), this observation led Liu et al. (2019a) to introduce deep material networks. They defined deep material networks as a hierarchy of nested laminates where both the input and output of each laminate

are furnished by rotation matrices. For the chapter at hand, we follow an alternative path replacing the rotation steps by laminates with a variable direction of lamination.

We define a direct deep material network

$$\mathcal{DMN}_Y : \mathcal{GSM}^N \to \mathcal{GSM} \tag{4.3}$$

as a perfect, ordered[3] N-ary tree of depth K, where an N-phase laminate (4.2) is assigned to each node of the tree, see Figure 4.2 for an illustration. We may refer to the DMN as "direct", because we, in contrast to Liu et al. (2019a) and Liu and Wu (2019), do not furnish the phases of the laminates with rotation matrices, see Comment 6. For the sake of exposition, we will use the terms "direct DMN" and "DMN" as synonyms and refer explicitly to the formulation of Liu et al. (2019a) and Liu and Wu (2019) if necessary. Recall that a full N-ary tree is a tree where each node, except for the leaves, has precisely N child nodes. A perfect tree is a full tree in which all leaf nodes are at the same level. Thus, such a tree of depth K involves

$$1 + N + N^2 + \ldots + N^{K-1} = \frac{N^K - 1}{N - 1} \tag{4.4}$$

nodes, each of which we assign to an N-phase laminate. We denote the laminate or building block of the i-th node on the k-th level of the tree by $\mathcal{B}_k^i$.

An N-phase direct DMN of depth K has N^K inputs. We assign the leaves of the bottom level the inputs

$$(\mathcal{G}_{K+1}^1, \mathcal{G}_{K+1}^2, \ldots, \mathcal{G}_{K+1}^{N^K-1}, \mathcal{G}_{K+1}^{N^K}) = (\mathcal{G}_1, \ldots, \mathcal{G}_N, \ldots, \mathcal{G}_1, \ldots, \mathcal{G}_N), \tag{4.5}$$

i.e., the N given materials $(\mathcal{G}_1, \ldots, \mathcal{G}_N) \in \mathcal{GSM}^N$ are repeated N^{K-1} times in a cyclic fashion. For prescribed inputs $(\mathcal{G}_{K+1}^1, \ldots, \mathcal{G}_{K+1}^{N^K})$, the

[3] By ordered we mean that the children of each node are ordered.

direct DMN is evaluated to $\mathcal{G}_1^1$, where we recursively define

$$\mathcal{G}_k^i = \mathcal{B}_k^i(\mathcal{G}_{k+1}^{N(i-1)+1}, \mathcal{G}_{k+1}^{N(i-1)+2}, \ldots, \mathcal{G}_{k+1}^{Ni}) \tag{4.6}$$

with $k = 1, \ldots, K$ and $i = 1, \ldots, N^{k-1}$. The process of recursively evaluating $\mathcal{B}_k^i$ by traversing the tree from the K-th to the first level is illustrated in Figure 4.2. The effective material behavior of the DMN is then given by $\bar{\mathcal{G}} = \mathcal{G}_1^1$.

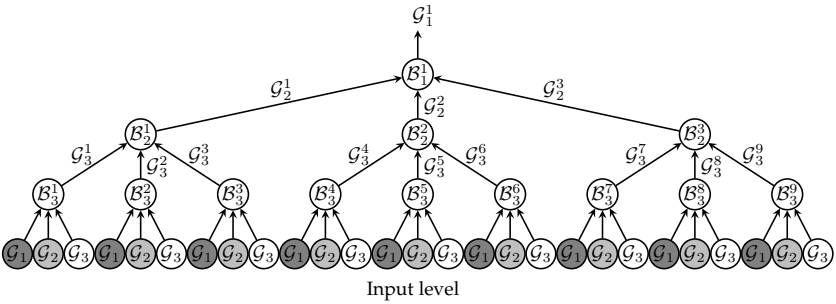

Figure 4.2: A three-phase DMN described by a ternary tree of depth three (the input level is not counted)

Several comments are in order:

1. Geometrically, a DMN of depth K and N phases consists of a hierarchical laminate with K scales $L_1 \gg L_2 \gg \ldots \gg L_K$. Each scale corresponds to a level of the tree.
2. Any DMN preserves thermodynamic consistency of the material models for trivial reasons. For our material models at hand, the thermodynamic consistency of the generalized standard materials is encoded by the convexity of the potentials involved. It is well-known, see for instance Suquet (1985), that periodic homogenization preserves thermodynamic consistency of GSMs. As the building blocks of the DMN are laminates, which are, in particular, microstructures,

each block preserves thermodynamic consistency. As a result, the entire DMN also preserves thermodynamic consistency of the input material models.

3. DMNs preserve monotonicity of material models, strengthening the purely qualitative previous remark. More precisely, suppose that, after a time discretization, the eigenvalues of the material tangents of all materials are contained in the interval $[C_-, C_+]$ for $C_- \geq 0$. Then, the eigenvalues of the material tangent of the effective material produced by the DMN are also contained in this interval. The latter statement is true for periodic homogenization of any real microstructure. As laminates are microstructures, the statement continues to hold for DMNs as well. For the convenience of the reader, we included the definition of monotonicity and a stream-lined derivation of the former result in Appendix B.

   It is well known that every microstructure inherently meets the Voigt/Reuss upper and lower bounds on the effective stiffness and the Taylor/Sachs upper and lower bounds on the effective potential, e.g., see Section 5.1 in Suquet (1997) for a derivation. This statement continues to hold for DMNs, as can be directly seen by applying Suquet's arguments in a hierarchical fashion.

4. In principle, any other N-phase microstructure may be used as the building block of a corresponding deep material network. Then, preservation of thermodynamic consistency and bounds on the material tangent would be preserved as well. However, two difficulties may arise. On the one hand, fast evaluation of the homogenization function is mandatory. On the other hand, the structure needs to be sufficiently anisotropic to be of use. To elaborate, suppose the building block would have isotropic geometric statistics. Then, if the input materials were isotropic, also the effective material would be isotropic. If the microstructure to be approximated features anisotropic geometric characteristics, an isotropic building block will fail to produce a

useful approximation. However, morphological anisotropy is only a sufficient condition for approximability. Understanding the approximation capabilities of DMNs with laminate building blocks is beyond the scope of this chapter.

5. Each building block $\mathcal{B}_k^i$ of the DMN is an N-phase laminate microstructure. Each such laminate is characterized by the direction of lamination $\boldsymbol{n}_k^i \in \mathrm{S}^{d-1}$, the unit sphere in d dimensions, and N non-negative volume fractions $c_{k,1}^i, \dots, c_{k,N}^i$ which sum to unity, i.e.,

$$\sum_{n=1}^{N} c_{k,n}^i = 1. \tag{4.7}$$

6. Liu et al. (2019a) and Liu and Wu (2019) use micro-oriented N-phase laminates, i.e., a fixed direction of lamination with rotated inputs and output, as their building blocks. However, in this chapter, we focus on undirected materials such that our choice is sufficient. For an extension of the direct DMN framework to treat micro-oriented materials, see Chapter 6.

Concerning the degrees of freedom, notice that a direct DMN of N phases and depth K may be parameterized by one lamination direction $\boldsymbol{n}_k^i \in \mathrm{S}^{d-1}$ and volume fractions $c_{k,1}^i, \dots, c_{k,N}^i$ for every laminate. In total, a three-dimensional ($d = 3$) DMN of depth K involving N phases is characterized by $\frac{N^K-1}{N-1}(N+1)$ degrees of freedom , i.e., $\frac{N^K-1}{N-1}$ lamination directions and $N^K - 1$ volume fractions (if also considering Relation (4.7)).

Instead of prescribing independent volume fractions to every laminate, Liu et al. (2019a) and Liu and Wu (2019) proposed to assign a weight w_{K+1}^i to every input, N^K inputs in total, of the DMN. The weights on level k are computed as the sum of weights of the respective laminates

when traversing the tree from the leaves to the root, i.e.,

$$w_k^i = \sum_{j=1}^{N} w_{k+1}^{N(i-1)+j} = w_{k+1}^{N(i-1)+1} + w_{k+1}^{N(i-1)+2} + \ldots + w_{k+1}^{Ni} \qquad (4.8)$$

holds. This weight propagation process is illustrated in Figure 4.3. Thus, the prescribed N^K input weights uniquely determine the weights on all levels of the deep material network. In particular, the weights w_{K+1}^i, $i = 1, \ldots, N^K$, are non-negative and sum to unity. Geometrically, they weight the influence of the i-th input material on the effective response of the DMN.

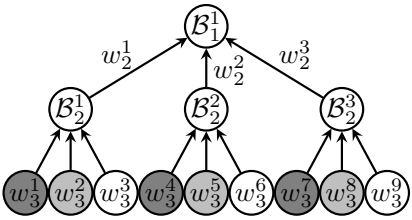

Figure 4.3: Weight propagation in a three-phase DMN of depth two

Notice the distinction between weights and volume fractions. The volume fractions of each laminate are computed from the propagated weights by normalization, i.e., the volume fractions $c_{k,1}^i, \ldots, c_{k,N}^i$ of the $\mathcal{B}_k^i$ laminate are computed as

$$c_{k,1}^i = \frac{w_{k+1}^{N(i-1)+1}}{\sum_{j=1}^{N} w_{k+1}^{N(i-1)+j}}, \quad \ldots \quad c_{k,N}^i = \frac{w_{k+1}^{Ni}}{\sum_{j=1}^{N} w_{k+1}^{N(i-1)+j}}. \qquad (4.9)$$

Working with weights instead of volume fractions preserves the number of degrees of freedom of $\frac{N^K-1}{N-1}(N+1)$, i.e., $\frac{N^K-1}{N-1}$ unit normals and $N^K - 1$ independent weights, for a three-dimensional DMN.

4.2.2 Fast evaluation of the affine-linear homogenization function

N-phase deep material networks are defined as trees of N-phase laminates, see Section 4.2. Thus, to evaluate the affine-linear elastic homogenization function of the DMN

$$\mathcal{DMN}_Y^{\mathcal{AL}} : ((\mathbb{C}_1, \boldsymbol{\varepsilon}_{\text{in},1}), (\mathbb{C}_2, \boldsymbol{\varepsilon}_{\text{in},2}), \dots, (\mathbb{C}_N, \boldsymbol{\varepsilon}_{\text{in},N})) \mapsto (\bar{\mathbb{C}}, \bar{\boldsymbol{\varepsilon}}_{\text{in}}) \tag{4.10}$$

it is necessary to repeatedly evaluate the affine-linear elastic homogenization function of a single laminate

$$\mathcal{B}^{\mathcal{AL}} : ((\mathbb{C}_1, \boldsymbol{\varepsilon}_{\text{in},1}), (\mathbb{C}_2, \boldsymbol{\varepsilon}_{\text{in},2}), \dots, (\mathbb{C}_N, \boldsymbol{\varepsilon}_{\text{in},N})) \mapsto (\bar{\mathbb{C}}, \bar{\boldsymbol{\varepsilon}}_{\text{in}}). \tag{4.11}$$

Traversing the tree from the leaves to the root by recursively evaluating $\mathcal{B}^{\mathcal{AL}}$, see Figure 4.2, yields the effective stiffness $\bar{\mathbb{C}}$ and residual strain $\bar{\boldsymbol{\varepsilon}}_{\text{in}}$. To arrive at a formula to efficiently evaluate $\mathcal{B}^{\mathcal{AL}}$, we use that any affine-linear elastic material can be represented in terms of a stiffness tensor $\mathbb{C}$ and a residual strain $\boldsymbol{\varepsilon}_{\text{in}}$ in the affine form

$$\begin{bmatrix} \boldsymbol{\sigma} \\ 1 \end{bmatrix} = \begin{bmatrix} \mathbb{C} & -\mathbb{C} : \boldsymbol{\varepsilon}_{\text{in}} \\ 0 & 1 \end{bmatrix} \begin{bmatrix} \boldsymbol{\varepsilon} \\ 1 \end{bmatrix}. \tag{4.12}$$

Choosing this particular form permits computing the effective stiffness $\bar{\mathbb{C}}$ and the residual strain $\bar{\boldsymbol{\varepsilon}}_{\text{in}}$ simultaneously, as explained in the following. Suppose a laminate with lamination direction $\boldsymbol{n} \in \mathrm{S}^{d-1}$ is given. Following Section 9.5 in Milton (2002), the effective affine-linear elastic material

behavior is given by the implicit formula

$$\left(\mathbb{\Gamma}+\lambda_0\begin{bmatrix}\bar{\mathbb{C}}-\lambda_0\mathbb{I}_{\mathrm{s}} & -\bar{\mathbb{C}}:\bar{\boldsymbol{\varepsilon}}_{\mathrm{in}}\\ 0 & 1-\lambda_0\end{bmatrix}^{-1}\right)^{-1}= \left\langle\left(\mathbb{\Gamma}+\lambda_0\begin{bmatrix}\mathbb{C}-\lambda_0\mathbb{I}_{\mathrm{s}} & -\mathbb{C}:\boldsymbol{\varepsilon}_{\mathrm{in}}\\ 0 & 1-\lambda_0\end{bmatrix}^{-1}\right)^{-1}\right\rangle, \quad (4.13)$$

where $\mathbb{I}_{\mathrm{s}}:\mathrm{Sym}_2(d)\to\mathrm{Sym}_2(d)$ denotes the identity on $\mathrm{Sym}_2(d)$ and $\mathbb{\Gamma}$ refers to the projection operator acting on $(\boldsymbol{\varepsilon},\omega)\in\mathrm{Sym}_2(d)\oplus\mathbb{R}$ via the formula

$$\mathbb{\Gamma}(\boldsymbol{\varepsilon},\omega)=[(\boldsymbol{\varepsilon}\boldsymbol{n})\otimes\boldsymbol{n}+\boldsymbol{n}\otimes(\boldsymbol{\varepsilon}\boldsymbol{n})-(\boldsymbol{n}\cdot\boldsymbol{\varepsilon}\boldsymbol{n})\,\boldsymbol{n}\otimes\boldsymbol{n},\omega]. \quad (4.14)$$

By abusing notation, the latter may be written as a matrix in the form of

$$\mathbb{\Gamma}=\begin{bmatrix}\mathbb{\Gamma}_{\boldsymbol{n}} & 0\\ 0 & 1\end{bmatrix} \quad (4.15)$$

where $\mathbb{\Gamma}_{\boldsymbol{n}}$ is the Mandel representation of the fourth-order tensor in Cartesian coordinates

$$(\mathbb{\Gamma}_{\boldsymbol{n}})_{ijlm}=\frac{1}{2}(n_i\delta_{jl}n_m+n_j\delta_{il}n_m+n_i\delta_{jm}n_l+n_j\delta_{im}n_l)-n_in_jn_ln_m \quad (4.16)$$

and δ denotes the Kronecker symbol. By $\langle\,\square\,\rangle$, we denote averaging on the N-phase laminate, and λ_0 is a parameter with the dimension of a Young's modulus which needs to be chosen sufficiently large for all the inversions involved in Formula (4.13) to make sense. It can be shown that it suffices for λ_0 to exceed the largest eigenvalue of all stiffness matrices involved, in Mandel's notation. This statement follows from the purely elastic case, see Kabel et al. (2015), as the augmented stiffness matrix in Formula (4.12), regarded as a 2×2 matrix with blocks of

different sizes, is upper triangular. An upper bound on the eigenvalues, in turn, can be easily obtained by evaluating the Frobenius norm of the input stiffness tensors, also in Mandel's notation.

Formula (4.13) has several advantages:

1. It treats normals of arbitrary direction,
2. any number of phases is supported,
3. the Formula (4.13) is already in matrix form, supporting a simple implementation which also supports automatic differentation, see Section 4.3.2, and
4. the linear elastic case is covered, by setting $\boldsymbol{\varepsilon}_{\text{in}} = \mathbf{0}$.

4.2.3 Flexible evaluation of the nonlinear homogenization function

In the previous section, we have seen how to efficiently evaluate the (affine-)linear homogenization function of a direct DMN by exploiting, on the one hand, explicit formulae for the effective affine-linear elastic response of an N-phase laminate and, on the other hand, the hierarchical nature of the deep material network. Notice that the approach we followed for the linear case can also be carried out for the nonlinear case: Provided a time discretization and a strain increment were supplied, we could compute the effective stress of an N-phase laminate, and "propagate" this effective stress to the next higher level. Unfortunately, due to the iterative nature of the solution process involved, for each level a tolerance needs to be supplied which determines how accurate the residual equations are solved. Unless this tolerance depends on the level, the algorithms will not converge, in general. Unfortunately,

we noticed that for a certain depth of the deep material network, the solution process becomes unstable[4].

Thus, it appears imperative to consider the problem of computing the effective stress of a DMN as a single, global problem. Liu et al. (2019a) noticed that such an approach may be carried out by exploiting the specific form of the deep material network. As the DMN is given by an ordered tree of (nonlinear) laminates, the algorithmic tangent of the full DMN can be computed by linearly homogenizing the algorithmic tangents of the individual laminates using linear elastic homogenization, see (4.13), in a hierarchical way.

We tested the approach of Liu et al. (2019a) and Liu and Wu (2019), and it worked well. However, we strived for higher flexibility of the implementation. To be more precise, the hierarchical evaluation of the algorithmic tangent via evaluating the affine-linear homogenization funcion (4.13) is quite natural for "modern" codes supporting the recursive evaluation inherent to deep learning. However, most finite element codes for solid mechanics supporting user-provided material subroutines grant their users only a restricted flexibility concerning the implementation.

From hierarchical laminates to a flattened representation

With these considerations in mind, we came up with an alternative way of solving the global nonlinear DMN system associated to given nonlinear material laws. More precisely, we separate the material nonlinearity and the topography (topology, normals and volume fractions) of the DMN into separate matrices to be elaborated subsequently. This is accomplished by showing that the "deep" material network may be flattened to a "shallow" network, which has a form very similar to a conventional laminate with a lot of phases.

[4] More precisely, we decreased the tolerance by an order of magnitude for each level, and for more than 7 levels, we encountered problems.

To keep notation as simple as possible, we discuss a two-phase DMN, i.e.,

$$\mathcal{DMN}_Y : \mathcal{GSM} \times \mathcal{GSM} \to \mathcal{GSM}. \tag{4.17}$$

The nonlinear material behavior of the two phases, $i = 1, 2$, is given by two isothermal GSMs $(\mathcal{Z}_1, \psi_1, \phi_1, \boldsymbol{z}_{0,1}) \in \mathcal{GSM}$ and $(\mathcal{Z}_2, \psi_2, \phi_2, \boldsymbol{z}_{0,2}) \in \mathcal{GSM}$, including the free-energy densities $\psi_i : \mathrm{Sym}_2(d) \times \mathcal{Z}_i \to \mathbb{R}$, the dissipation potentials $\phi_i : \mathcal{Z}_i \to \mathbb{R} \cup \{+\infty\}$ and the initial conditions $\boldsymbol{z}_{0,i} \in \mathcal{Z}_i$. Due to time discretization and freezing of the internal variables, each GSM reduces to a nonlinear elastic material

$$\boldsymbol{\sigma}_i = \frac{\partial \Psi_i}{\partial \boldsymbol{\varepsilon}} \left(\boldsymbol{\varepsilon}_i, \boldsymbol{z}_i^n \right), \tag{4.18}$$

which is given in terms of the condensed free energy potential $\Psi_i : \mathrm{Sym}_2(d) \times \mathcal{Z} \to \mathbb{R}$ and only depends on the strain $\boldsymbol{\varepsilon}_i$ and the internal variables $\boldsymbol{z}_i^n$ of the last (converged) time step, see Section 2.5 for more information.

We start by examining a two-phase DMN of depth one, i.e., a simple two-phase rank-one laminate, with volume fractions $c_{1,1}^1, c_{1,2}^1 \in \mathbb{R}_{\geq 0}$ and lamination direction $\boldsymbol{n}_1^1 \in \mathrm{S}^{d-1}$, see Figure 4.4a. Let $\boldsymbol{\varepsilon}_1 \in \mathrm{Sym}_2(d)$ and $\boldsymbol{\varepsilon}_2 \in \mathrm{Sym}_2(d)$ denote the phase-wise constant strains of the rank-one laminate. Then, the kinematic compatibility condition (Glüge and Kalisch, 2014)

$$[\![\boldsymbol{\varepsilon}]\!] = \boldsymbol{\varepsilon}_2 - \boldsymbol{\varepsilon}_1 = \boldsymbol{N}_1^1 \boldsymbol{u}_1^1 \tag{4.19}$$

is expressed in terms of the symmetrization operator

$$\boldsymbol{N}_k^i : \mathrm{V}^d \to \mathrm{Sym}_2(d), \quad \boldsymbol{N}_k^i \boldsymbol{u} = \frac{1}{2} \left(\boldsymbol{u} \otimes \boldsymbol{n}_k^i + \boldsymbol{n}_k^i \otimes \boldsymbol{u} \right) \tag{4.20}$$

and the (unknown) displacement jump vector $\boldsymbol{u}_1^1 \in \mathrm{V}^d$. Thus, for a prescribed effective strain increment $\bar{\boldsymbol{\varepsilon}} \in \mathrm{Sym}_2(d)$ and using Relation (4.19),

we obtain for the phase strains the following relations

$$\boldsymbol{\varepsilon}_1 = \bar{\boldsymbol{\varepsilon}} + c^1_{1,2}\boldsymbol{N}^1_1\boldsymbol{u}^1_1 \quad \text{and} \quad \boldsymbol{\varepsilon}_2 = \bar{\boldsymbol{\varepsilon}} - c^1_{1,1}\boldsymbol{N}^1_1\boldsymbol{u}^1_1. \tag{4.21}$$

The problem to be solved may be written as

$$\bar{\Psi} = c^1_{1,1}\Psi_1(\bar{\boldsymbol{\varepsilon}} + c^1_{1,2}\boldsymbol{N}^1_1\boldsymbol{u}^1_1, \boldsymbol{z}^n_1) + c^1_{1,2}\Psi_2(\bar{\boldsymbol{\varepsilon}} - c^1_{1,1}\boldsymbol{N}^1_1\boldsymbol{u}^1_1, \boldsymbol{z}^n_2) \longrightarrow \min_{\boldsymbol{u}^1_1}, \tag{4.22}$$

which states that the effective incremental potential $\bar{\Psi}$ is to be minimized w.r.t. the phase-wise affine strain fields, see Kabel et al. (2017). Critical points of the optimization problem (4.22) are given by solving the linear system

$$\left(\boldsymbol{N}^1_1\right)^{\mathsf{T}} \frac{\partial \Psi_1}{\partial \boldsymbol{\varepsilon}}(\bar{\boldsymbol{\varepsilon}} + c^1_{1,2}\boldsymbol{N}^1_1\boldsymbol{u}^1_1, \boldsymbol{z}^n_1) = \left(\boldsymbol{N}^1_1\right)^{\mathsf{T}} \frac{\partial \Psi_2}{\partial \boldsymbol{\varepsilon}}(\bar{\boldsymbol{\varepsilon}} - c^1_{1,1}\boldsymbol{N}^1_1\boldsymbol{u}^1_1, \boldsymbol{z}^n_2) \tag{4.23}$$

for the unknown displacement jump vector $\boldsymbol{u}^1_1$. Indeed, the former equation represents the balance of linear momentum (2.23) of the rank-two laminate, i.e., the stress vector is continuous on the (singular) surface separating both phases of the laminate, see also Section 2.3 for more information.

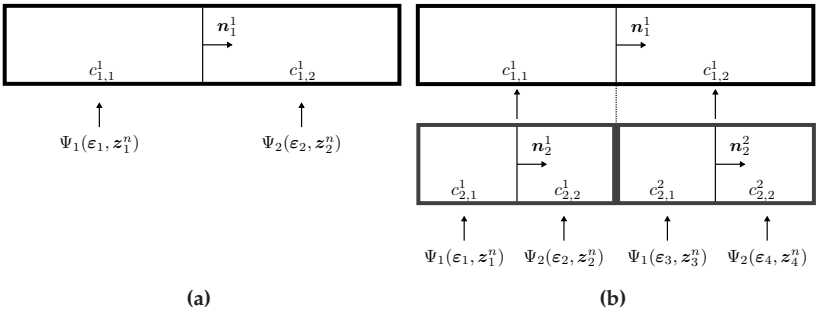

Figure 4.4: Schematic illustration of a two-phase direct DMN of depth one (a) and depth two (b)

After this preliminary step, suppose a DMN of depth two is given. We assign to both laminates on level 2 the condensed free energies Ψ_1 and Ψ_2 in alternating order, see Figure 4.4b, i.e., we consider the problem

$$c^1_{1,1}\Psi^1_2(\bar{\boldsymbol{\varepsilon}} + c^1_{1,2}\boldsymbol{N}^1_1\boldsymbol{u}^1_1, \boldsymbol{z}^n_1, \boldsymbol{z}^n_2) + c^1_{1,2}\Psi^2_2(\bar{\boldsymbol{\varepsilon}} - c^1_{1,1}\boldsymbol{N}^1_1\boldsymbol{u}^1_1, \boldsymbol{z}^n_3, \boldsymbol{z}^n_4) \longrightarrow \min_{\boldsymbol{u}^1_1}, \tag{4.24}$$

where

$$\Psi^1_2(\tilde{\boldsymbol{\varepsilon}}, \boldsymbol{z}^n_1, \boldsymbol{z}^n_2) = \min_{\boldsymbol{u}^1_2} c^1_{2,1}\Psi_1(\tilde{\boldsymbol{\varepsilon}} + c^1_{2,2}\boldsymbol{N}^1_2\boldsymbol{u}^1_2, \boldsymbol{z}^n_1) + c^1_{2,2}\Psi_2(\tilde{\boldsymbol{\varepsilon}} - c^1_{2,1}\boldsymbol{N}^1_2\boldsymbol{u}^1_2, \boldsymbol{z}^n_2) \tag{4.25}$$

and

$$\Psi^2_2(\tilde{\boldsymbol{\varepsilon}}, \boldsymbol{z}^n_3, \boldsymbol{z}^n_4) = \min_{\boldsymbol{u}^2_2} c^2_{2,1}\Psi_1(\tilde{\boldsymbol{\varepsilon}} + c^2_{2,2}\boldsymbol{N}^2_2\boldsymbol{u}^2_2, \boldsymbol{z}^n_3) + c^2_{2,2}\Psi_2(\tilde{\boldsymbol{\varepsilon}} - c^2_{2,1}\boldsymbol{N}^2_2\boldsymbol{u}^2_2, \boldsymbol{z}^n_4). \tag{4.26}$$

These three minimization problems may be combined into the single problem

$$\begin{aligned}\bar{\Psi} = {} & c^1_{1,1}c^1_{2,1}\Psi_1(\bar{\boldsymbol{\varepsilon}} + c^1_{1,2}\boldsymbol{N}^1_1\boldsymbol{u}^1_1 + c^1_{2,2}\boldsymbol{N}^1_2\boldsymbol{u}^1_2, \boldsymbol{z}^n_1) \\ & + c^1_{1,1}c^1_{2,2}\Psi_2(\bar{\boldsymbol{\varepsilon}} + c^1_{1,2}\boldsymbol{N}^1_1\boldsymbol{u}^1_1 - c^1_{2,1}\boldsymbol{N}^1_2\boldsymbol{u}^1_2, \boldsymbol{z}^n_2) \\ & + c^1_{1,2}c^2_{2,1}\Psi_1(\bar{\boldsymbol{\varepsilon}} - c^1_{1,1}\boldsymbol{N}^1_1\boldsymbol{u}^1_1 + c^2_{2,2}\boldsymbol{N}^2_2\boldsymbol{u}^2_2, \boldsymbol{z}^n_3) \\ & + c^1_{1,2}c^2_{2,2}\Psi_2(\bar{\boldsymbol{\varepsilon}} - c^1_{1,1}\boldsymbol{N}^1_1\boldsymbol{u}^1_1 - c^2_{2,1}\boldsymbol{N}^2_2\boldsymbol{u}^2_2, \boldsymbol{z}^n_4) \longrightarrow \min_{\boldsymbol{u}^1_1, \boldsymbol{u}^1_2, \boldsymbol{u}^2_2}\end{aligned} \tag{4.27}$$

where $\boldsymbol{z}^n_1, \boldsymbol{z}^n_3 \in \mathcal{Z}_1$ and $\boldsymbol{z}^n_2, \boldsymbol{z}^n_4 \in \mathcal{Z}_2$ denote the vectors of internal variables. Note that every node at the input level of the DMN has its own vector of internal variables. For Representation (4.27), the similarity to a four-phase laminate becomes apparent. The respective volume fractions enter the effective energy $\bar{\Psi}$, and the strain for each phase may

be computed from the prescribed average strain $\bar{\boldsymbol{\varepsilon}}$ and a fluctuation term, which depends linearly on the displacement jumps $\boldsymbol{u}_k^i$.

In analogy to Formula (4.27), we may write down a flattened representation for a two-phase DMN of depth K. To this end, we virtually plug in the K-th level into the $(K-1)$-th level, which is in return inserted into the $(K-2)$-th level and so on. A schematic of this process is shown in Figure 4.5a for a DMN of depth three. Furthermore, in Figure 4.5b, the resulting one-dimensional representation of the DMN is shown, involving the lamination directions $\boldsymbol{n}_k^i$, and the displacement jump vectors $\boldsymbol{u}_k^i$. In terms of data handling, for a 2^K-phase laminate, we insert all normals into a "long" vector $\vec{\boldsymbol{n}} \in (\mathrm{S}^{d-1})^{2^K-1}$ with the ordering

$$\vec{\boldsymbol{n}} = [\boldsymbol{n}_K^1, \boldsymbol{n}_K^2, \dots \boldsymbol{n}_K^{2^{K-1}}, \boldsymbol{n}_{K-1}^1, \boldsymbol{n}_{K-1}^2, \dots, \boldsymbol{n}_{K-1}^{2^{K-2}}, \dots, \boldsymbol{n}_2^1, \boldsymbol{n}_2^2, \boldsymbol{n}_1^1], \tag{4.28}$$

i.e., we insert the normals of the K-th level in their corresponding order, and add the normals for decreasing level index. Furthermore, we introduce the displacement jump vector $\vec{\boldsymbol{u}} \in (\mathrm{V}^d)^{2^K-1}$, which inherits its ordering from $\vec{\boldsymbol{n}}$, the vector of strains $\vec{\boldsymbol{\varepsilon}} = [\boldsymbol{\varepsilon}_1, \boldsymbol{\varepsilon}_2, \dots, \boldsymbol{\varepsilon}_{2^K}] \in \mathrm{Sym}_2(d)^{2^K}$ and the vector of internal variables of the last converged time step

$$\vec{\boldsymbol{z}}^{\,n} = [\boldsymbol{z}_1^n, \boldsymbol{z}_2^n, \boldsymbol{z}_3^n, \dots, \boldsymbol{z}_{2^K}^n] \in \bar{\mathcal{Z}} = (\mathcal{Z}_1 \oplus \mathcal{Z}_2)^{\oplus^{2^{K-1}}}. \tag{4.29}$$

For the averaged condensed free energies of the flattened laminate

$$\bar{\Psi} : \mathrm{Sym}_2(d)^{2^K} \times \bar{\mathcal{Z}} \to \mathbb{R}, \quad \bar{\Psi}(\vec{\boldsymbol{\varepsilon}}, \vec{\boldsymbol{z}}^{\,n}) = \sum_{i=1}^{2^K} w_{K+1}^i \Psi_i(\boldsymbol{\varepsilon}_i, \boldsymbol{z}_i^n) \tag{4.30}$$

we seek a displacement jump vector $\vec{\boldsymbol{u}}$, s.t.

$$\bar{\Psi}(\vec{\boldsymbol{\varepsilon}} + \boldsymbol{D}\vec{\boldsymbol{u}}, \vec{\boldsymbol{z}}^{\,n}) \to \min_{\vec{\boldsymbol{u}}} \tag{4.31}$$

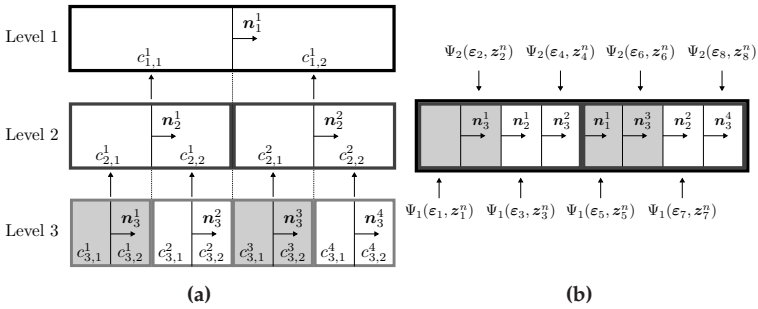

Figure 4.5: Schematic illustration of the transition from a two-phase direct DMN of depth three (a) to a degenerated eight-phase laminate (b)

where the shorthand notation

$$\vec{\bar{\boldsymbol{\varepsilon}}} = \underbrace{[\bar{\boldsymbol{\varepsilon}}, \bar{\boldsymbol{\varepsilon}}, \dots, \bar{\boldsymbol{\varepsilon}}]}_{2^K \text{ times}} \in \mathrm{Sym}_2(d)^{2^K} \tag{4.32}$$

is used, and $\boldsymbol{D} : (\mathrm{V}^d)^{2^K-1} \to \mathrm{Sym}_2(d)^{2^K}$ denotes the linear operator expressing the strain fluctuation in terms of the displacement jumps. Here, for a positive integer i, the notation

$$\Psi_i = \begin{cases} \Psi_1 & i \text{ odd}, \\ \Psi_2 & i \text{ even}, \end{cases} \tag{4.33}$$

encodes that Ψ_i alternates between the two given condensed free energies Ψ_1 and Ψ_2. The Euler-Lagrange equation of Problem (4.31) reads

$$\frac{\partial \bar{\Psi}}{\partial \vec{\boldsymbol{u}}}(\vec{\bar{\boldsymbol{\varepsilon}}} + \boldsymbol{D}\vec{\boldsymbol{u}}, \vec{\boldsymbol{z}}^{\,n}) = \boldsymbol{0} \quad \text{with} \quad \frac{\partial \bar{\Psi}}{\partial \vec{\boldsymbol{u}}}(\vec{\bar{\boldsymbol{\varepsilon}}} + \boldsymbol{D}\vec{\boldsymbol{u}}, \vec{\boldsymbol{z}}^{\,n}) = \boldsymbol{D}^{\mathsf{T}} \frac{\partial \bar{\Psi}}{\partial \vec{\boldsymbol{\varepsilon}}}(\vec{\bar{\boldsymbol{\varepsilon}}} + \boldsymbol{D}\vec{\boldsymbol{u}}, \vec{\boldsymbol{z}}^{\,n}). \tag{4.34}$$

By introducing the vector of phase stresses

$$\vec{\boldsymbol{\sigma}} = [\boldsymbol{\sigma}_1, \dots, \boldsymbol{\sigma}_{2^K}] \in \mathrm{Sym}_2(d)^{2^K} \quad \text{with} \quad \boldsymbol{\sigma}_i = \frac{\partial \Psi_i}{\partial \boldsymbol{\varepsilon}}(\boldsymbol{\varepsilon}_i, \boldsymbol{z}_i^n) \tag{4.35}$$

and defining the weight operator $\boldsymbol{W} : \mathrm{Sym}_2(d)^{2^K} \to \mathrm{Sym}_2(d)^{2^K}$,

$$\boldsymbol{W}(\vec{\boldsymbol{\sigma}}) = [w^1_{K+1}\boldsymbol{\sigma}_1, w^2_{K+1}\boldsymbol{\sigma}_2, \dots, w^{2^K}_{K+1}\boldsymbol{\sigma}_{2^K}], \tag{4.36}$$

which associates the weights $\vec{w}$ to the corresponding stresses $\vec{\boldsymbol{\sigma}}$, the Euler-Lagrange equation (4.34) may be reformulated as

$$\boldsymbol{D}^{\mathsf{T}}\boldsymbol{W}\vec{\boldsymbol{\sigma}}(\vec{\bar{\boldsymbol{\varepsilon}}} + \boldsymbol{D}\vec{\boldsymbol{u}}, \vec{\boldsymbol{z}}^{\,n}) = \boldsymbol{0}, \tag{4.37}$$

which more clearly expresses its form as a balance of linear momentum on the flattened laminate, see also Section 2.3. The gradient operator $\boldsymbol{D}$ may be thought of as an operator of symmetrized-gradient type, and $\boldsymbol{D}^{\mathsf{T}}\boldsymbol{W}$ encodes the corresponding (negative) divergence operator. Indeed, DMNs might be interpreted as an abstract finite element discretization of an N-phase microstructure (Dey et al., 2022b). For instance, compare Equation (4.37) to the discretized balance of linear momentum in Zeman et al. (2017) or Ladecký et al. (2022).

The effective stress of the DMN is computed by averaging, i.e.,

$$\bar{\boldsymbol{\sigma}} = \sum_{i=1}^{2^K} w^i_{K+1}\boldsymbol{\sigma}_i(\boldsymbol{\varepsilon}_i, \boldsymbol{z}^n_i). \tag{4.38}$$

The particular form of the "gradient" operator $\boldsymbol{D}$ is better explained in terms of an example. For the two-phase DMN of depth three shown in Figure 4.5b, it takes the form

$$\boldsymbol{D} = \begin{bmatrix}
-c^1_{3,2}\boldsymbol{N}^1_3 & \boldsymbol{0} & \boldsymbol{0} & \boldsymbol{0} & -c^1_{2,2}\boldsymbol{N}^1_2 & \boldsymbol{0} & -c^1_{1,2}\boldsymbol{N}^1_1 \\
c^1_{3,1}\boldsymbol{N}^1_3 & \boldsymbol{0} & \boldsymbol{0} & \boldsymbol{0} & -c^1_{2,2}\boldsymbol{N}^1_2 & \boldsymbol{0} & -c^1_{1,2}\boldsymbol{N}^1_1 \\
\boldsymbol{0} & -c^2_{3,2}\boldsymbol{N}^2_3 & \boldsymbol{0} & \boldsymbol{0} & c^1_{2,1}\boldsymbol{N}^1_2 & \boldsymbol{0} & -c^1_{1,2}\boldsymbol{N}^1_1 \\
\boldsymbol{0} & c^2_{3,1}\boldsymbol{N}^2_3 & \boldsymbol{0} & \boldsymbol{0} & c^1_{2,1}\boldsymbol{N}^1_2 & \boldsymbol{0} & -c^1_{1,2}\boldsymbol{N}^1_1 \\
\boldsymbol{0} & \boldsymbol{0} & -c^3_{3,2}\boldsymbol{N}^3_3 & \boldsymbol{0} & \boldsymbol{0} & -c^2_{2,2}\boldsymbol{N}^2_2 & c^1_{1,1}\boldsymbol{N}^1_1 \\
\boldsymbol{0} & \boldsymbol{0} & c^3_{3,1}\boldsymbol{N}^3_3 & \boldsymbol{0} & \boldsymbol{0} & -c^2_{2,2}\boldsymbol{N}^2_2 & c^1_{1,1}\boldsymbol{N}^1_1 \\
\boldsymbol{0} & \boldsymbol{0} & \boldsymbol{0} & -c^4_{3,2}\boldsymbol{N}^4_3 & \boldsymbol{0} & c^2_{2,1}\boldsymbol{N}^2_2 & c^1_{1,1}\boldsymbol{N}^1_1 \\
\boldsymbol{0} & \boldsymbol{0} & \boldsymbol{0} & c^4_{3,1}\boldsymbol{N}^4_3 & \boldsymbol{0} & c^2_{2,1}\boldsymbol{N}^2_2 & c^1_{1,1}\boldsymbol{N}^1_1
\end{bmatrix}. \tag{4.39}$$

Solving the balance of linear momentum using Newton's method

For a fixed macro-strain increment $\bar{\varepsilon}$ and internal variables $\vec{\boldsymbol{z}}^{\,n}$, we wish to solve the balance of linear momentum (4.37) for the unknown displacement jumps $\vec{\boldsymbol{u}}$. To find a solution of

$$\boldsymbol{F}(\vec{\boldsymbol{u}}) = \boldsymbol{0} \quad \text{with} \quad \boldsymbol{F}(\vec{\boldsymbol{u}}) = \boldsymbol{D}^{\mathsf{T}}\boldsymbol{W}\vec{\boldsymbol{\sigma}}(\vec{\bar{\varepsilon}} + \boldsymbol{D}\vec{\boldsymbol{u}}, \vec{\boldsymbol{z}}^{\,n}), \tag{4.40}$$

a first-order Taylor approximation

$$\begin{aligned}\boldsymbol{F}(\vec{\boldsymbol{u}} + \triangle\vec{\boldsymbol{u}}) &\approx \boldsymbol{F}(\vec{\boldsymbol{u}}) + \left[\frac{\partial \boldsymbol{F}}{\partial \vec{\boldsymbol{u}}}(\vec{\bar{\varepsilon}} + \boldsymbol{D}\vec{\boldsymbol{u}}, \vec{\boldsymbol{z}}^{\,n})\right] \triangle\vec{\boldsymbol{u}} \\ &= \boldsymbol{D}^{\mathsf{T}}\boldsymbol{W}\vec{\boldsymbol{\sigma}}(\vec{\bar{\varepsilon}} + \boldsymbol{D}\vec{\boldsymbol{u}}, \vec{\boldsymbol{z}}^{\,n}) + \left[\boldsymbol{D}^{\mathsf{T}}\boldsymbol{W}\frac{\partial \vec{\boldsymbol{\sigma}}}{\partial \vec{\bar{\varepsilon}}}(\vec{\bar{\varepsilon}} + \boldsymbol{D}\vec{\boldsymbol{u}}, \vec{\boldsymbol{z}}^{\,n})\boldsymbol{D}\right] \triangle\vec{\boldsymbol{u}}\end{aligned} \tag{4.41}$$

leads to Newton's method. For an initial guess $\vec{\boldsymbol{u}}_0 \in (\mathrm{V}^d)^{N-1}$, the displacement jump vector $\vec{\boldsymbol{u}}$ is iteratively updated $\vec{\boldsymbol{u}}_{j+1} = \vec{\boldsymbol{u}}_j + \beta_j \triangle\vec{\boldsymbol{u}}_j$, where the increment $\triangle\vec{\boldsymbol{u}}_j \in \left(\mathrm{V}^d\right)^{2^K-1}$ solves the linear system

$$\left[\boldsymbol{D}^{\mathsf{T}}\boldsymbol{W}\frac{\partial \vec{\boldsymbol{\sigma}}}{\partial \vec{\bar{\varepsilon}}}(\vec{\bar{\varepsilon}} + \boldsymbol{D}\vec{\boldsymbol{u}}_j, \vec{\boldsymbol{z}}^{\,n})\boldsymbol{D}\right] \triangle\vec{\boldsymbol{u}}_j = -\boldsymbol{D}^{\mathsf{T}}\boldsymbol{W}\vec{\boldsymbol{\sigma}}(\vec{\bar{\varepsilon}} + \boldsymbol{D}\vec{\boldsymbol{u}}_j, \vec{\boldsymbol{z}}^{\,n}), \tag{4.42}$$

and $\beta_j \in (0, 1]$ stands for the step size. The derivative $\partial\vec{\boldsymbol{\sigma}}/\partial\vec{\bar{\varepsilon}}$ comprises the algorithmic tangents of the DMN's input materials and might be represented as a 6×6-block diagonal matrix, i.e.,

$$\frac{\partial \vec{\boldsymbol{\sigma}}}{\partial \vec{\bar{\varepsilon}}}(\vec{\bar{\varepsilon}}, \vec{\boldsymbol{z}}^{\,n}) = \text{block-diag}\left(\frac{\partial^2 \Psi_1}{\partial \boldsymbol{\varepsilon}\partial \boldsymbol{\varepsilon}}(\boldsymbol{\varepsilon}_1, \boldsymbol{z}_1^n), \ldots, \frac{\partial^2 \Psi_{2^K}}{\partial \boldsymbol{\varepsilon}\partial \boldsymbol{\varepsilon}}(\boldsymbol{\varepsilon}_{2^K}, \boldsymbol{z}_{2^K}^n)\right). \tag{4.43}$$

In particular, $\boldsymbol{W}$ and $\partial\vec{\boldsymbol{\sigma}}/\partial\vec{\bar{\varepsilon}}$ commute.

Using the square root of the weight operator $\boldsymbol{W}$, which might be represented as a diagonal matrix, we may rewrite the $\vec{\boldsymbol{u}}$-tangent on the left

hand side of Equation (4.42) in the form

$$\boldsymbol{D}^{\mathsf{T}}\boldsymbol{W}\frac{\partial\vec{\boldsymbol{\sigma}}}{\partial\vec{\boldsymbol{\varepsilon}}}(\vec{\boldsymbol{\varepsilon}}+\boldsymbol{D}\vec{\boldsymbol{u}}_j,\vec{\boldsymbol{z}}^{\,n})\boldsymbol{D}=\boldsymbol{D}^{\mathsf{T}}\boldsymbol{W}^{\frac{1}{2}}\frac{\partial\vec{\boldsymbol{\sigma}}}{\partial\vec{\boldsymbol{\varepsilon}}}(\vec{\boldsymbol{\varepsilon}}+\boldsymbol{D}\vec{\boldsymbol{u}}_j,\vec{\boldsymbol{z}}^{\,n})\boldsymbol{W}^{\frac{1}{2}}\boldsymbol{D} \quad (4.44)$$

to emphasize that this operator inherits the symmetry and definiteness properties of the material tangents

$$\frac{\partial^2\Psi_1}{\partial\boldsymbol{\varepsilon}\partial\boldsymbol{\varepsilon}}(\boldsymbol{\varepsilon}_1,\boldsymbol{z}_1^n),\dots,\frac{\partial^2\Psi_{2^K}}{\partial\boldsymbol{\varepsilon}\partial\boldsymbol{\varepsilon}}(\boldsymbol{\varepsilon}_{2^K},\boldsymbol{z}_{2^K}^n). \quad (4.45)$$

Of interest here is the form of the $\vec{\boldsymbol{u}}$-tangent: It arises as the product of matrices which depend solely on the DMN (i.e., on the normals and the volume fractions comprised in $\boldsymbol{D}$ and $\boldsymbol{W}$) and of the materials' algorithmic tangents $\partial\vec{\boldsymbol{\sigma}}/\partial\vec{\boldsymbol{\varepsilon}}$. In particular, when implementing the nonlinear DMN, the matrices $\boldsymbol{D}$ and $\boldsymbol{D}^{\mathsf{T}}\boldsymbol{W}$ can be precomputed once and for all, and modularity w.r.t. the material behavior is ensured. It is advisable to exploit the aforementioned sparsity pattern of $\boldsymbol{W}$ and $\partial\vec{\boldsymbol{\sigma}}/\partial\vec{\boldsymbol{\varepsilon}}$ to efficiently compute the $\vec{\boldsymbol{u}}$-tangent, see Section 5.3 and 7.3.3.

Several synoptic remarks are in order:

1. For the sake of exposition, we have restricted to two-phase DMNs. Extending our approach to more than two phases is straightforward (but not in terms of notation).
2. The primary variables that are solved for are the displacement jumps gathered in $\vec{\boldsymbol{u}}$. Since an N-phase DMN of depth K comprises $\frac{N^K-1}{N-1}$ laminates, $d\frac{N^K-1}{N-1}$ displacement jump components are updated in every Newton step. Upon convergence, the internal variables are updated and the effective stress is computed.
3. Choosing the last converged displacement jumps, which are carried over from the last converged time step, as an initial guess for $\vec{\boldsymbol{u}}_0 \in (\mathrm{V}^d)^{\frac{N^K-1}{N-1}}$ improves time to solution of Newton's method at the expense of an increased memory consumption.

4. An N-phase DMN of depth K possesses N^{K-1} laminates at the bottom level. We are able to associate each one of these nodes N stress inputs – one for every input material. Assuming $Z_1, \dots, Z_N$ denote the number of internal variables of the phases 1 to N, we conclude that a N-phase DMN of depth K possesses

$$\sum_{i=1}^{N} Z_i N^{K-1} \tag{4.46}$$

internal variables that are updated upon convergence of Newton's method. In addition, $3\frac{N^K-1}{N-1}$ displacement jump components have to be stored as well for a three dimensional DMN.

4.3 Implementation

4.3.1 Material sampling

For simplicity of exposition, we restrict to two-phase materials for the implementation and the subsequent numerical investigations. In particular, it suffices to investigate the linear elastic homogenization function as explained in Section 3.5.

We follow Liu and Wu (2019) and sample orthotropic stiffness matrices whose axes of orthotropy are normal to the faces of the rectangular microstructure instead of stiffness tensors of general anisotropy. This reduces the dimensions of the problem in 3D from 21 to 9. Recall that any orthotropic stiffness tensor $\mathbb{C}$, i.e., orthotropic w.r.t. the Cartesian coordinate axes $\boldsymbol{e}_1$, $\boldsymbol{e}_2$ and $\boldsymbol{e}_3$, may be written in Mandel's notation in

the form

$$\mathbb{C} \mathrel{\widehat{=}} \begin{bmatrix} \boldsymbol{Q}\boldsymbol{E}\boldsymbol{Q}^{\mathsf{T}} & \mathbf{0} & \mathbf{0} & \mathbf{0} \\ \mathbf{0} & 2G_{23} & 0 & 0 \\ \mathbf{0} & 0 & 2G_{13} & 0 \\ \mathbf{0} & 0 & 0 & 2G_{12} \end{bmatrix}, \tag{4.47}$$

where $G_{ij} \in \mathbb{R}_{>0}$ are positive, $\boldsymbol{E} = \operatorname{diag}(E_1, E_2, E_3) \in \mathbb{R}^{3\times3}_{>0}$ is positive definite, and $\boldsymbol{Q} \in \mathrm{SO}(3)$ is a special orthogonal matrix, i.e., satisfies $\boldsymbol{Q}^{\mathsf{T}}\boldsymbol{Q} = \boldsymbol{I}$ and $\det(\boldsymbol{Q}) = +1$. Notice that $\{E_i\}_{i=1}^3$ entering Relation (4.47) only correspond to the axial Young's moduli of $\mathbb{C}$ if $\boldsymbol{Q} \equiv \boldsymbol{I}$. Using Representation (4.47), the set of orthotropic stiffness tensors may be parameterized via

$$(E_1, E_2, E_3, G_{23}, G_{13}, G_{12}, \boldsymbol{Q}) \in \mathbb{R}^6_{>0} \times \mathrm{SO}(3), \tag{4.48}$$

where the first 6 moduli have the dimension of a Young's modulus, and $\boldsymbol{Q}$ has dimension 1. As the latter set is unbounded, we restrict to the subset of elements $(E_1, E_2, E_3, G_{23}, G_{13}, G_{12}, \boldsymbol{Q})$ with

$$\begin{gathered} E_i = 10^{e_i}\mathrm{GPa}, \quad G_{ij} = \gamma_{ij}\sqrt{E_iE_j}, \\ \boldsymbol{Q} : \mathrm{V}^3 \to \mathrm{V}^3,\ \boldsymbol{x} \mapsto \cos(\theta)\boldsymbol{x} + \sin(\theta)\boldsymbol{v} \times \boldsymbol{x} + (1-\cos(\theta))(\boldsymbol{v}\cdot\boldsymbol{x})\boldsymbol{v} \\ \text{and} \quad \boldsymbol{v} \mathrel{\widehat{=}} [\sin(\psi)\cos(\varphi), \sin(\psi)\sin(\varphi), \cos(\psi)], \end{gathered} \tag{4.49}$$

where $e_i \in [-2, 2]$, $\gamma_{ij} \in \left[\frac{1}{4}, \frac{1}{2}\right]$, $\theta - \sin(\theta) \in [0, \pi]$, $\cos(\psi) \in [-1, 1]$ and $\varphi \in [0, 2\pi]$, see Miles (1965).

To study the linear elastic homogenization function of two-phase materials, we need to select two input stiffness tensors $\mathbb{C}_1$ and $\mathbb{C}_2$, which we choose as orthotropic in the mentioned form (4.47) and the parameters are chosen as above, except that we force $e_3^1 = -e_2^1 - e_1^1$, i.e., we force the product $\sqrt[3]{E_1^1E_2^1E_3^1}$ to equal 1 GPa to remove redundancy due to rescaling $(\mathbb{C}_1, \mathbb{C}_2) \mapsto (\lambda\mathbb{C}_1, \lambda\mathbb{C}_2)$ for $\lambda > 0$. Thus, the 17 degrees of

freedom are

$$(e_1^1, e_2^1, e_1^2, e_2^2, e_3^2, \gamma_{23}^1, \gamma_{13}^1, \gamma_{12}^1, \gamma_{23}^2, \gamma_{13}^2, \gamma_{12}^2, \psi^1, \varphi^1, \theta^1, \psi^2, \varphi^2, \theta^2) \quad (4.50)$$

with the domains specified above.

We generate a number N_s of input stiffness tensor pairs $\{(\mathbb{C}_1^s, \mathbb{C}_2^s)\}_{s=1}^{N_\mathrm{s}}$. To sample the input space evenly, we rely upon Latin hypercube sampling (McKay et al., 1979). More precisely, the parameters (4.50) are determined by Latin hypercube sampling, and the stiffness tensors (4.47) are constructed by evaluating Relations (4.49). The corresponding effective stiffness tensors $\left\{\bar{\mathbb{C}}^s\right\}_{s=1}^{N_\mathrm{s}}$ are computed by direct numerical simulation (DNS) of the effective elastic behavior of the unit cell in question with the help of FFT-based micromechanics (Moulinec and Suquet, 1994; 1998), using the FFTW library Frigo and Johnson (2005), the conjugate gradient solver (Zeman et al., 2010; Brisard and Dormieux, 2010) and the staggered grid discretization (Schneider et al., 2016). The triples $\left\{(\bar{\mathbb{C}}^s, \mathbb{C}_1^s, \mathbb{C}_2^s)\right\}_{s=1}^{N_\mathrm{s}}$ serve as training data henceforth.

4.3.2 Offline training[5]

A two-phase direct DMN of depth K is parameterized by $2^K - 1$ lamination directions and 2^K weights, which we collect in the vectors $\vec{\boldsymbol{n}} \in (\mathrm{S}^{d-1})^{2^K-1}$ and $\vec{w} \in \mathbb{R}_{\geq 0}^{2^K}$ with

$$\vec{\boldsymbol{n}} = [\boldsymbol{n}_K^1, \boldsymbol{n}_K^2, \ldots \boldsymbol{n}_K^{2^{K-1}}, \boldsymbol{n}_{K-1}^1, \boldsymbol{n}_{K-1}^2, \ldots, \boldsymbol{n}_{K-1}^{2^{K-2}}, \ldots, \boldsymbol{n}_2^1, \boldsymbol{n}_2^2, \boldsymbol{n}_1^1] \quad (4.51)$$

and

$$\vec{w} = [w_1, \ldots, w_{2^K}]\,. \quad (4.52)$$

[5] This section is based on Gajek et al. (2020, Section 4.4), Gajek et al. (2021a, Section 3.1) and Gajek et al. (2022, Section 3.2) and summarizes the essential details concerning the offline training of direct deep material networks.

In the offline training, we seek to identify these free parameters based on the sampled linear elastic training data $\left\{(\bar{\mathbb{C}}^s, \mathbb{C}_1^s, \mathbb{C}_2^s)\right\}_{s=1}^{N_s}$. We formulated the offline training as the constrained regression problem

$$J(\vec{\boldsymbol{n}}, \vec{w}) \rightarrow \min_{\vec{\boldsymbol{n}}, \vec{w}} \quad \text{s.t.} \quad w_{K+1}^i \geq 0 \quad \text{and} \quad \sum_{i=1}^{2^K} w_{K+1}^i = 1. \tag{4.53}$$

We measure the goodness of fit with the cost function

$$J(\vec{\boldsymbol{n}}, \vec{w}) = \frac{1}{N_s} \sqrt[q]{\sum_{i=1}^{N_s} \left(\frac{||\bar{\mathbb{C}}^s - \mathcal{DMN}_Y^{\mathcal{L}}(\mathbb{C}_1^s, \mathbb{C}_2^s, \vec{\boldsymbol{n}}, \vec{w})||_p}{||\bar{\mathbb{C}}^s||_p} \right)^q}, \tag{4.54}$$

where $p, q \geq 1$, $\mathcal{DMN}_Y^{\mathcal{L}}$ denotes the linear elastic homogenization function of the direct DMN, and the Frobenius-p-norm on stiffness tensors is defined via the ℓ^p-norm of the components in Mandel's notation. As we are considering two-phase DMNs, by Section 3.5, we only fit the linear elastic homogenization function $\mathcal{DMN}_Y^{\mathcal{L}}$ of the DMN. The exponent p weights the deviation of effective and predicted stiffness on the relative error, whereas the parameter q weights the relative error with respect to the loss function J. Liu and Wu (2019) used $p = 2$ and $q = 1$, but we allow for greater flexibility.

For implementation, we follow Liu and Wu (2019) and encode the mixing constraint on the weights

$$\sum_{i=1}^{2^K} w_{K+1}^i = 1 \tag{4.55}$$

by adding the quadratic penalty term

$$\lambda_p \left(\sum_{i=1}^{2^K} w_{K+1}^i - 1 \right)^2 \tag{4.56}$$

to the objective J (4.54), where $\lambda_\mathrm{p} \gg 1$ denotes the penalty parameter. To ensure that the non-negativity constraint on the weights

$$w_{K+1}^i \geq 0 \tag{4.57}$$

holds, we express the vector of constrained weights $\vec{w}$ in terms of the vector of unconstrained weights $\vec{v} = [v_1, \ldots, v_{2^K}] \in \mathbb{R}^{2^K}$ by projecting each element of $\vec{v}$ onto the positive real number line, i.e., $\vec{w} = \langle \vec{v} \rangle_+$ with

$$\langle \square \rangle_+ : \mathbb{R}^{2^K} \to \mathbb{R}_{\geq 0}^{2^K}, \quad \vec{v} \mapsto [\max(0, v_1), \ldots, \max(0, v_{2^K})] \tag{4.58}$$

holds. Thus, by abusing notation, we write for the cost function

$$J(\vec{\boldsymbol{n}}, \vec{w}) = \frac{1}{N_\mathrm{s}} \sqrt[q]{\sum_{i=1}^{N_\mathrm{s}} \left(\frac{\| \mathcal{DMN}_Y^{\mathcal{L}}(\mathbb{C}_1^s, \mathbb{C}_2^s, \vec{\boldsymbol{n}}, \vec{w}) - \bar{\mathbb{C}}^s \|_p}{\| \bar{\mathbb{C}}^s \|_p} \right)^q} + \lambda_\mathrm{p} \left(\sum_{i=1}^{2^K} w_{K+1}^i - 1 \right)^2 \tag{4.59}$$

and obtain the unconstrained regression problem

$$J(\vec{\boldsymbol{n}}, \langle \vec{v} \rangle_+) \longrightarrow \min_{\vec{\boldsymbol{n}}, \vec{v}}, \tag{4.60}$$

which we implement in PyTorch (Paszke et al., 2017) to exploit the framework's automatic differentiation capabilities. The deep material network is trained by means of minimizing the cost function (4.59) with respect to the unknown fitting parameters collected in $\vec{\boldsymbol{n}}$ and $\vec{v}$. The initial weights $\vec{v}_0$ are sampled from a uniform distribution, on $[0, 1]$, and subsequently rescaled to sum to unity. The initial orientations $\vec{\boldsymbol{n}}_0$ of the laminates are sampled uniformly on the unit sphere in analogy to Section 4.3.1.

The training of DMNs follows the general fashion of training deep neural networks. First, for every sample s, the pair of input stiffnesses $(\mathbb{C}_1^s, \mathbb{C}_2^s)$ are assigned to the 2^{K-1} laminates of the K-th layer. The stiffnesses are homogenized in a pairwise fashion by evaluating Equation (4.13) 2^{K-1} times which then serves as the input for the next layer, recursively, until the root of the binary tree is reached, yielding the DMN's predicted stiffness $\bar{\mathbb{C}}_s^{\mathrm{DMN}} = \mathcal{DMN}_Y^{\mathcal{L}}(\mathbb{C}_1^s, \mathbb{C}_2^s, \vec{\boldsymbol{n}}, \langle\vec{v}\rangle_+)$, see Section 4.2. Repeating this procedure for every sample, we evaluate the loss function J, determine the gradients $\partial J/\partial\vec{\boldsymbol{n}}$ and $\partial J/\partial\vec{v}$ by means of automatic differentiation and, subsequently, update the fitting parameters[6]

$$\vec{\boldsymbol{n}}_{j+1} = \vec{\boldsymbol{n}}_j - \beta_{\vec{\boldsymbol{n}}}\frac{\partial J}{\partial\vec{\boldsymbol{n}}}\left(\vec{\boldsymbol{n}}_j, \langle\vec{v}_j\rangle_+\right), \quad \vec{v}_{j+1} = \vec{v}_j - \beta_{\vec{v}}\frac{\partial J}{\partial\vec{v}}\left(\vec{\boldsymbol{n}}_j, \langle\vec{v}_j\rangle_+\right) \tag{4.61}$$

and

$$\vec{w}_{j+1} = \langle\vec{v}_{j+1}\rangle_+, \tag{4.62}$$

where $\beta_{\vec{\boldsymbol{n}}}, \beta_{\vec{v}} \in \mathbb{R}_{\geq 0}$ denote the learning rates. This cycle is repeated for a predefined number of epochs. Upon convergence, the unknown fitting parameters of the DMN, i.e., $\vec{\boldsymbol{n}}$ and $\vec{w}$, are given.

4.3.3 Online evaluation

We implement the Newton's method described in Section 4.2.3 as a user-specified subroutine in our FFT solver which is evaluated on a single voxel microstructure. The algorithm, which computes the effective stress $\bar{\boldsymbol{\sigma}}^{n+1}$ for a given time step $n+1$ and macro strain increment $\bar{\boldsymbol{\varepsilon}}^{n+1}$, is summarized in Algorithm 1.

[6] For implementation, it is more practical to parameterize the directions of lamination via spherical coordinates and to update the angles in each gradient step. This ensures that the directions of lamination have unit norm. However, to keep the notation clear, we represent the update of the lamination directions as shown.

It turned out that very small, almost vanishing weights, which may occur during training, lead to the linear system (4.42), Algorithm 1 line 19, being ill-posed. To mitigate the problem, we regularize the linear system by inserting 1 on the diagonal of the $\vec{\boldsymbol{u}}$-tangent at places associated to vanishing weights and inserting zero at the respective places on the right hand side. We select a direct solver for solving the linear system (4.42). To ensure that the Newton's method is globally convergent, we employ backtracking with the backtracking factor $\gamma \in (0, 1]$ to enforce a decreasing residual. Also, we choose the (converged) displacement jump vector $\vec{\boldsymbol{u}}^{\,n}$ of the last time step as an initial guess for $\vec{\boldsymbol{u}}^{\,n+1}$ to improve convergence.

Note, that we employ BFGS-CG (Wicht et al., 2020c) for the FFT solver and, therefore, do not need to compute the algorithmic tangent. Computation of the algorithmic tangent of the DMN is, however, straightforward and can be derived from Equation (4.34) easily, see Section 5.3.2 and Section 7.3.3 for more information.

Algorithm 1 Pseudo-code for the online phase
Fixed parameters: tol, maxit, maxbacktrack, γ
Input: $\bar{\boldsymbol{\varepsilon}}^{n+1}$, $\vec{\boldsymbol{z}}^{\,n}$, $\vec{\boldsymbol{u}}^{\,n}$
Output: $\bar{\boldsymbol{\sigma}}^{n+1}$, $\vec{\boldsymbol{z}}^{\,n+1}$, $\vec{\boldsymbol{u}}^{\,n+1}$

$\vec{\boldsymbol{u}}^{\,n+1} \leftarrow \vec{\boldsymbol{u}}^{\,n}$ ▷ Assigning old displacement jumps with $\vec{\boldsymbol{u}}^{\,0} \leftarrow \mathbf{0}$.
res $\leftarrow 10^{15}$, $\beta \leftarrow 1.0$
for $i \leftarrow 0$ **to** maxit $- 1$ **do**
    $\text{res}_{\text{old}} \leftarrow$ res
    for $j \leftarrow 0$ **to** maxbacktrack $- 1$ **do**
        $\vec{\boldsymbol{\varepsilon}}^{\,n+1} \leftarrow \bar{\vec{\boldsymbol{\varepsilon}}}^{\,n+1} + \boldsymbol{D}\vec{\boldsymbol{u}}^{\,n+1}$
        Evaluate material laws $\vec{\boldsymbol{\sigma}}(\vec{\boldsymbol{\varepsilon}}^{\,n+1}, \vec{\boldsymbol{z}}^{\,n})$ ▷ $\vec{\boldsymbol{z}}^{\,n}$ is *not* updated
        $\text{res} \leftarrow \dfrac{||\boldsymbol{D}^{\mathsf{T}}\boldsymbol{W}\vec{\boldsymbol{\sigma}}(\vec{\boldsymbol{\varepsilon}}^{\,n+1}, \vec{\boldsymbol{z}}^{\,n})||}{2^K - 1}$
        if res $<$ res_{old} **then** ▷ Evaluates to true for $i = 0$
            break
        end if
        $\beta_{\text{old}} \leftarrow \beta$
        $\beta \leftarrow \gamma\beta$
        $\vec{\boldsymbol{u}}^{\,n+1} \leftarrow \vec{\boldsymbol{u}}^{\,n+1} + (\beta - \beta_{\text{old}})\triangle\vec{\boldsymbol{u}}^{\,n+1}$
    end for
    if res $<$ tol **then**
        break
    end if
    Solve $\left[\boldsymbol{D}^{\mathsf{T}}\boldsymbol{W}\dfrac{\partial\vec{\boldsymbol{\sigma}}}{\partial\vec{\boldsymbol{\varepsilon}}}(\vec{\boldsymbol{\varepsilon}}^{\,n+1}, \vec{\boldsymbol{z}}^{\,n})\boldsymbol{D}\right] \triangle\vec{\boldsymbol{u}}^{\,n+1} = -\boldsymbol{D}^{\mathsf{T}}\boldsymbol{W}\vec{\boldsymbol{\sigma}}(\vec{\boldsymbol{\varepsilon}}^{\,n+1}, \vec{\boldsymbol{z}}^{\,n})$
    $\vec{\boldsymbol{u}}^{\,n+1} \leftarrow \vec{\boldsymbol{u}}^{\,n+1} + \triangle\vec{\boldsymbol{u}}^{\,n+1}$
end for
Compute effective stress $\bar{\boldsymbol{\sigma}}^{n+1} \leftarrow \sum_{i=1}^{2^K} w_{K+1}^{i}\boldsymbol{\sigma}_i(\boldsymbol{\varepsilon}_i^{n+1}, \boldsymbol{z}_i^n)$
Call $\vec{\boldsymbol{\sigma}}(\boldsymbol{\varepsilon}^{\,n+1}, \boldsymbol{z}^n)$ and update $\vec{\boldsymbol{z}}^{\,n}$ to $\vec{\boldsymbol{z}}^{\,n+1}$

4.4 Numerical results

4.4.1 Materials and microstructures

We consider a polyamide microstructure reinforced by $c_\mathrm{f} = 25.09\,\mathrm{vol}\%$ short cylindrical fibers with a length of $L_\mathrm{f} = 200\,\mu\mathrm{m}$ and a diameter of $D_\mathrm{f} = 10\,\mu\mathrm{m}$, dispersed in a cubic volume element with an edge length of $L = 256\,\mu\mathrm{m}$. The fiber orientation is described by a transversely isotropic second-order fiber orientation tensor

$$\boldsymbol{A}_2 = \begin{bmatrix} 0.8 & 0 & 0 \\ 0 & 0.1 & 0 \\ 0 & 0 & 0.1 \end{bmatrix} \boldsymbol{e}_i \otimes \boldsymbol{e}_j, \tag{4.63}$$

i.e., about $80\,\%$ of the fibers point in $\boldsymbol{e}_1$-direction. The periodic microstructure was generated by the sequential addition and migration algorithm (Schneider, 2017) with a minimum distance of $2\,\mu\mathrm{m}$ between the fibers. The resulting microstructure is shown in Figure 4.6a, containing 268 individual fibers. For the material sampling phase using linear elastic materials, a discretization of the microstructure by 128^3 voxels is chosen. For the online evaluation stage involving inelasticity, a discretization by 256^3 voxels is used. For the online evaluation, the glass fibers are modeled as linear elastic, whereas the polyamide matrix is governed by J_2-elasto-plasticity, see Chapter 3 in Simo and Hughes (1998), with exponential-linear hardening

$$\sigma_\mathrm{Y} = \sigma_0 + k_\infty \varepsilon_\mathrm{p} + (\sigma_\infty - \sigma_0)\left(1 - \exp\left(-\frac{k_0 - k_\infty}{\sigma_\infty - \sigma_0}\,\varepsilon_\mathrm{p}\right)\right). \tag{4.64}$$

The material parameters used for the inelastic simulations are summarized in Table 4.1, see Doghri et al. (2011).

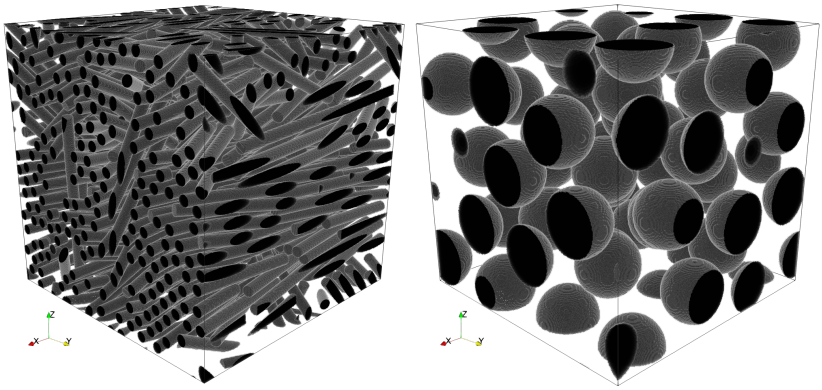

(a) Short glass fiber reinforced polyamide **(b)** Metal matrix composite

Figure 4.6: Investigated microstructure realizations

Matrix	$E = 2.1\,\mathrm{GPa}$	$\nu = 0.3$
	$\sigma_0 = 29.0\,\mathrm{MPa}$	$\sigma_\infty = 61.7\,\mathrm{MPa}$
	$k_0 = 10.6\,\mathrm{GPa}$	$k_\infty = 139.0\,\mathrm{MPa}$
Fibers	$E = 72\,\mathrm{GPa}$	$\nu = 0.22$

Table 4.1: Material parameters for the short glass fiber reinforced polyamide (Doghri et al., 2011)

As our second example, a metal matrix composite (MMC), i.e., an aluminum alloy reinforced by $c_\mathrm{p} = 30\,\mathrm{vol}\%$ ceramic particles, is investigated. The microstructure featuring 50 identically shaped spherical inclusions was generated by the mechanical contraction method of Williams and Philipse (2003), see Figure 4.6b. The cubic unit cell has an edge length of $210\,\mu\mathrm{m}$, and is discretized by 128^3 voxels for the material sampling, and by 256^3 voxels for the online evaluation. The material parameters used for the inelastic computations are taken from Segurado et al. (2002),

see also Michel and Suquet (2003; 2004). The ceramic particles are assumed to be linear elastic, whereas the aluminum matrix is modeled by J_2-elasto-plasticity, see Chapter 3 in Simo and Hughes (1998), with power law hardening

$$\sigma_{\mathrm{Y}} = \sigma_0 + k\,\varepsilon_{\mathrm{p}}^{m}. \tag{4.65}$$

The material parameters used are summarized in Table 4.2.

Matrix	$E = 75.0\,\mathrm{GPa}$	$\nu = 0.3$
	$\sigma_{\mathrm{Y}} = 75.0\,\mathrm{MPa}$	$k = 416.0\,\mathrm{MPa}$
	$m = 0.3895$	
Inclusions	$E = 400.0\,\mathrm{GPa}$	$\nu = 0.2$

Table 4.2: Material parameters for the metal matrix composite (Segurado et al., 2002)

4.4.2 A short glass fiber reinforced polyamide

Offline training

We sample $N_{\mathrm{s}} = 800$ pairs of stiffness tensors $\{(\mathbb{C}_1^s, \mathbb{C}_2^s)\}_{s=1}^{N_{\mathrm{s}}}$ as described in Section 4.3.1, with material contrasts ranging up to $10\,000$ for the fiber reinforced polymer. Liu and Wu (2019) reported that deep material networks are robust with respect to overfitting. To investigate overfitting for direct DMNs, we split the pre-computed data into a training and a validation set comprising 700 and 100 samples, respectively. For network training, we rely upon the AMSGrad method of Reddi et al. (2018), together with a learning rate modulation with warm restarts, as suggested by Loshchilov and Hutter (2017),

$$\beta : \mathbb{N} \to \mathbb{R}_{\geq 0}, \quad m \mapsto \beta_{\mathrm{min}} + \frac{1}{2}\left(\beta_{\mathrm{max}} - \beta_{\mathrm{min}}\right)\left(1 + \cos\left(\pi \frac{m}{M}\right)\right), \tag{4.66}$$

applied to both learning rates $\beta_{\vec{n}}$ and $\beta_{\vec{v}}$, where m designates the epoch. The maximum and minimum learning rates were set to $\beta_{\text{min}} = 0$ and $\beta_{\text{max}} = 10^{-4}$, respectively, and $M = 4\,000$ was selected. The penalty parameter entering the objective function (4.54) was set to $\lambda_{\text{p}} = 10^3$, and the exponents were chosen as $p = 1$ and $q = 10$. Thus, roughly speaking, we enforce the maximum of the component-wise mean error to be minimal.

First, we investigate the influence of different depths on the approximation quality of the DMN for the offline training. To quantify the accuracy of trained DMNs, we define, for a sample s, the error

$$\delta_s = \frac{\|\mathcal{DMN}_Y^{\mathcal{L}}(\mathbb{C}_1^s, \mathbb{C}_2^s, \vec{\boldsymbol{n}}, \vec{w}) - \bar{\mathbb{C}}^s\|_1}{\|\bar{\mathbb{C}}^s\|_1}. \tag{4.67}$$

With $\|\cdot\|_1$ we designate the Frobenius-1-norm defined via the ℓ^1-norm of the stiffness components in Mandel's notation. Additionally, we define over all samples the maximum and mean error indicators via

$$\delta_{\text{max}} = \max_s(\delta_s) \quad \text{and} \quad \delta_{\text{mean}} = \frac{1}{N_{\text{s}}} \sum_{s=1}^{N_{\text{s}}} \delta_s. \tag{4.68}$$

We trained deep material networks with depths $K = 4, 5, 6, 7, 8$ for $36\,000$ epochs. To investigate the reproducibility of the results, we investigated two distinct DMNs with depth 8, which we denote by 8_1 and 8_2. Loss J and mean training error δ_{mean} vs. epoch are shown in Figure 4.7a and Figure 4.7b. For the sake of exposition, only DMNs with an even depth are depicted. For the first $1\,000$ epochs, the loss decreases rapidly and monotonically. For higher epoch count, the learning rate modulation causes a non-monotonic convergence behavior, which eventually leads to a decreased total loss. We see that the loss after training improves for an increasing depth. Furthermore, for the two considered networks with $K = 8$, the converged loss values are

comparable. The observations made for the loss translate almost directly to the mean training and validation errors, see Figure 4.7b. Furthermore, we observe that mean training and validation errors decrease equally during training, indicating that no pronounced overfitting occurs.

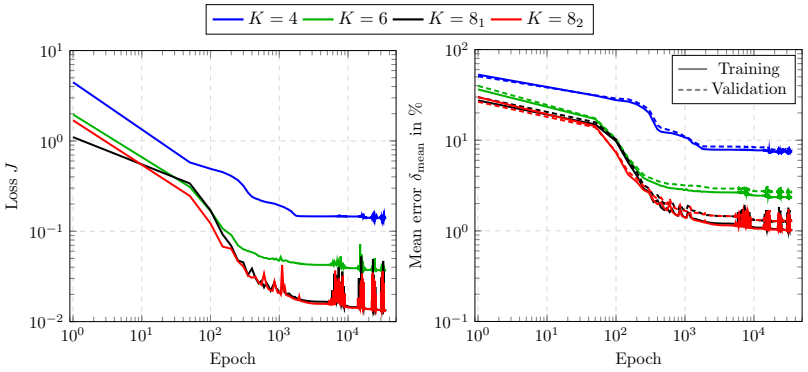

(a) Loss vs. training epoch

(b) Mean error vs. training epoch

Figure 4.7: Loss and mean training and validation errors during training for the short glass fiber reinforced polyamide

The values of the loss and the mean as well as the maximum errors for the training and validation sets are listed in Table 4.3. In addition, the predicted volume fraction of the fibers

$$c_{\mathrm{f}} = \sum_{i=1}^{2^{K-1}} w_{K+1}^{2i-1}, \tag{4.69}$$

computed by summing over all odd weights were included. Both the loss and the mean and maximum training and validation errors decrease for increasing depth. Still, the maximum validation error consistently exceeds the maximum training error, although both are, in general, very close. For quantification, we take a look at the distribution of errors δ_s

on the training and validation set, respectively, for the $K = 8_1$ network, see Figure 4.8. The maximum error on the validation set is significantly larger, and dominated by a single sample. Neglecting the outliers, we see that the the distributions of errors in the training and validation sets are comparable.

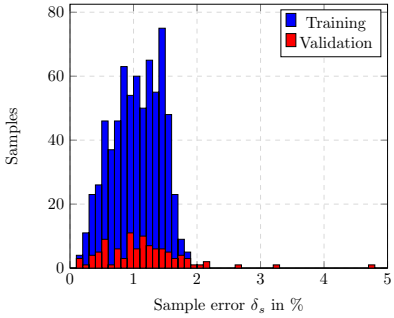

Figure 4.8: Error distribution for $K = 8_1$ after 36 000 epochs

A DMN of depth 4 leads to mean training and validation errors of $8.04\,\%$ and $8.67\,\%$, respectively, which we consider unsuitable for correctly reproducing the effective response of the microstructure. Considering the networks $K = 8_1$ and $K = 8_2$, the mean errors significantly reduce to $1.02\,\%$ and $1.01\,\%$ for the training set and to $1.26\,\%$ and $1.29\,\%$ for the validation set. A distinct reduction of the maximum errors can also be observed, see Table 4.3.

The predicted volume fractions are very close to the volume fraction of the microstructure. Note that the relative error of the volume fractions does not decrease monotonically with increasing depth since the DMN with depth 5 has a relative error of $1.39\,\%$. Nevertheless, for the networks with more than depth 6, the error does not exceed $0.32\,\%$. This is expected as the effective stiffness is dominated by the volume fraction to first order, see for instance Section 20.2.2 in Torquato (2005).

	J	$\delta^{\text{train}}_{\text{mean}}$	$\delta^{\text{train}}_{\text{max}}$	$\delta^{\text{valid}}_{\text{mean}}$	$\delta^{\text{valid}}_{\text{max}}$	c_{f}
$K = 4$	$1.39 \cdot 10^{-1}$	$8.04\,\%$	$20.39\,\%$	$8.67\,\%$	$38.83\,\%$	$0.2499\ (-0.40\,\%)$
$K = 5$	$6.15 \cdot 10^{-2}$	$3.66\,\%$	$9.09\,\%$	$3.91\,\%$	$15.50\,\%$	$0.2544\ (+1.39\,\%)$
$K = 6$	$3.70 \cdot 10^{-2}$	$2.34\,\%$	$5.16\,\%$	$2.68\,\%$	$9.19\,\%$	$0.2501\ (-0.32\,\%)$
$K = 7$	$2.13 \cdot 10^{-2}$	$1.49\,\%$	$2.90\,\%$	$1.60\,\%$	$5.19\,\%$	$0.2505\ (-0.16\,\%)$
$K = 8_1$	$1.34 \cdot 10^{-2}$	$1.02\,\%$	$1.87\,\%$	$1.26\,\%$	$4.76\,\%$	$0.2506\ (-0.12\,\%)$
$K = 8_2$	$1.32 \cdot 10^{-2}$	$1.01\,\%$	$1.80\,\%$	$1.29\,\%$	$5.07\,\%$	$0.2508\ (-0.04\,\%)$

Table 4.3: Training results for the short glass fiber reinforced polyamide

Online evaluation – uniaxial loadings

With these trained networks at hand, we turn our attention to the online prediction using the J_2-elasto-plastic matrix material model as described in Section 4.4.1. The composite is subjected to uniaxial strain loadings

$$\begin{aligned} \bar{\boldsymbol{\varepsilon}} &= \frac{\bar{\varepsilon}}{2} \left(\boldsymbol{e}_i \otimes \boldsymbol{e}_j + \boldsymbol{e}_j \otimes \boldsymbol{e}_i \right), \\ (i,j) \in \mathcal{I} &= \{(1,1),(2,2),(3,3),(2,3),(1,3),(1,2)\}. \end{aligned} \tag{4.70}$$

We use an FFT-based computational micromechanics (Moulinec and Suquet, 1994; 1998) code, written in Python with Cython (Behnel et al., 2011) extensions. For computing the full-field solutions, we use the Eyre-Milton (1999) scheme. The DMN is evaluated on a single voxel microstructure with the help of the BFGS-CG (Wicht et al., 2020c) solver to avoid computing the algorithmic tangents. We examining all three normal and shear strain components separately. In the respective strain direction, a complete hysteresis is simulated with a strain amplitude of $\bar{\varepsilon} = 2.5\,\%$ in 80 equidistant load steps.

First, we investigate the influence of different depths on the approximation quality of the DMN for the online evaluation. In Figure 4.9, the stress-time curves for all six load cases are shown. The full-field solutions serve as the reference. For simplicity of exposition, only the

DMNs of even depth are depicted. Recall that $K = 8_1$ and $K = 8_2$ denote the results of the two distinctly trained 8-level DMNs.

To get a more accurate quantitative comparison of the results, Figure 4.9 also includes the relative errors in the stress components

$$\eta_{ij}(t) = \frac{\left|\bar{\sigma}_{ij}^{\mathrm{DMN}}(t) - \bar{\sigma}_{ij}^{\mathrm{FFT}}(t)\right|}{\max\limits_{\tau \in \mathcal{T}} \left|\bar{\sigma}_{ij}^{\mathrm{FFT}}(\tau)\right|} \tag{4.71}$$

with respect to the maximum absolute effective stress, reached during the entire simulation time-windows $\mathcal{T} = [0\,\mathrm{s}, 4\,\mathrm{s}]$, of the full-field solution. Furthermore, for all six loadcases, we collected the maximum relative errors

$$\eta_{ij}^{\max} = \max_{t \in \mathcal{T}}(\eta_{ij}(t)), \tag{4.72}$$

evaluated for all time steps, in Table 4.4.

Comparing full-field solutions to the DMN predictions, we see even the DMN with depth 4 predicts the material behavior qualitatively. At depth 8, the curves are difficult to distinguish. The maximum relative error decreases with increasing depth with the exception of the DMNs with depth six and seven. For instance, the DMN with $K = 4$ exhibits a maximum approximation error of $12.61\,\%$ whereas the DMN predictions for $K = 8_1$ and $K = 8_2$ deviate from the full-field solution by $6.38\,\%$ and $5.27\,\%$, respectively. Notice that the maximum errors for both 8-level networks are dominated by uniaxial extension in the $\boldsymbol{e}_1$-direction. This may be a result of the morphological anisotropy of the FRP combined with strong plastification in the matrix. Notice that the maximum errors differ for both 8-level networks. For $\eta_{12}^{\max}$, both maximum errors differ by a factor of more than two. In the offline training phase, both networks with depth $K = 8$ showed comparable results. However, larger deviations manifest in the online phase, suggesting possible improvements in the offline training phase. Note that the maximum deviations occur for different stress components, shown in Table 4.4 with

gray-colored cells. Also, the error for a fixed load case is not monotonic in the depth. For instance, the $\eta_{11}^{\max}$-error for $K = 7$ is greater than for $K = 6$, $K = 8_1$ or $K = 8_2$.

max rel. error	$K = 4$	$K = 5$	$K = 6$	$K = 7$	$K = 8_1$	$K = 8_2$
$\eta_{11}^{\max}$	10.05 %	8.54 %	3.51 %	7.82 %	6.38 %	5.27 %
$\eta_{22}^{\max}$	3.73 %	4.78 %	3.82 %	2.69 %	2.33 %	1.66 %
$\eta_{33}^{\max}$	4.89 %	6.14 %	1.47 %	2.57 %	2.27 %	1.42 %
$\eta_{23}^{\max}$	12.61 %	7.11 %	3.38 %	4.77 %	2.42 %	2.96 %
$\eta_{13}^{\max}$	10.57 %	4.37 %	3.15 %	6.13 %	2.55 %	2.25 %
$\eta_{12}^{\max}$	12.45 %	6.87 %	6.21 %	3.04 %	1.87 %	4.16 %
$\max_{(i,j)\in\mathcal{I}}(\eta_{ij}^{\max})$	12.61 %	8.54 %	6.21 %	7.82 %	6.38 %	5.27 %

Table 4.4: Relative errors for the short glass fiber reinforced polyamide and uniaxial loadings

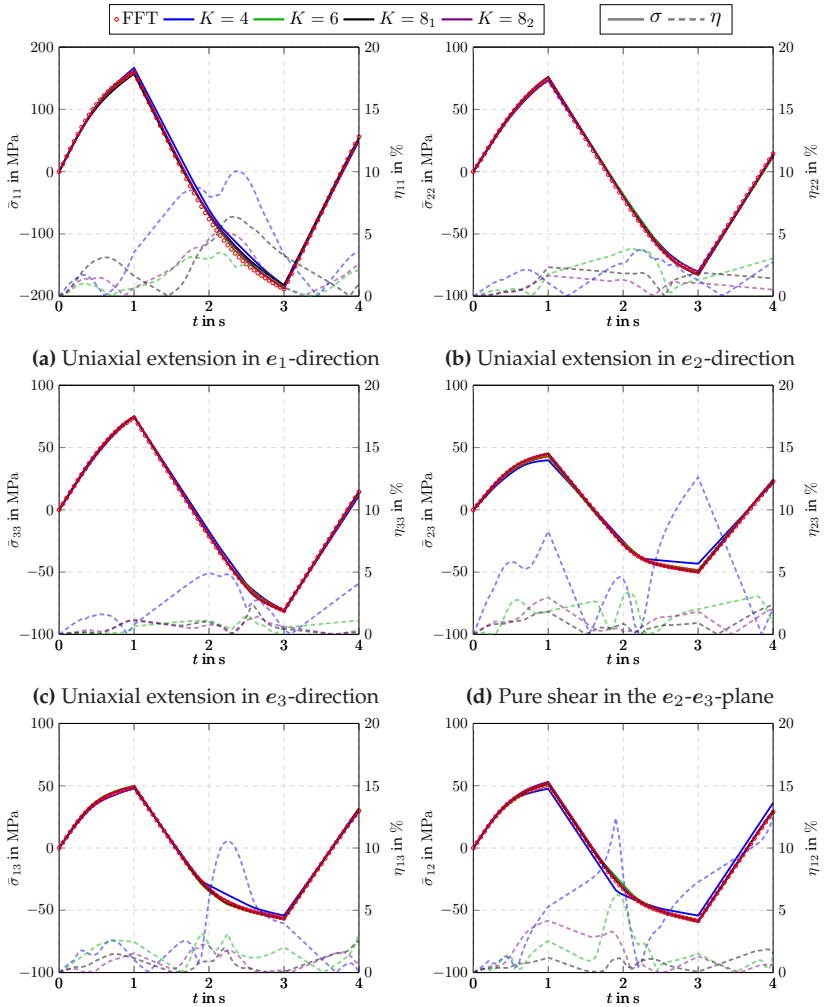

(a) Uniaxial extension in e_1-direction

(b) Uniaxial extension in e_2-direction

(c) Uniaxial extension in e_3-direction

(d) Pure shear in the e_2-e_3-plane

(e) Pure shear in the e_1-e_3-plane

(f) Pure shear in the e_1-e_2-plane

Figure 4.9: Stress vs. time curves for the short glass fiber reinforced polyamide and uniaxial loadings

Online evaluation – biaxial loadings

The previously investigated load cases cover non-monotonic, radial loadings. We furthermore investigate the DMN's response to a biaxial loading. The composite is subjected to a biaxial strain loading

$$\bar{\boldsymbol{\varepsilon}} = \bar{\varepsilon}_1 \, \boldsymbol{e}_1 \otimes \boldsymbol{e}_1 + \bar{\varepsilon}_2 \, \boldsymbol{e}_2 \otimes \boldsymbol{e}_2 \tag{4.73}$$

with principal loading directions aligned to the $\boldsymbol{e}_1$- and $\boldsymbol{e}_2$-axes. We investigate two scenarios with different loading sequences, see Table 4.5. In analogy to the previous section, the simulations are carried out with strain amplitudes of $1.77\,\%$ in the respective load direction and discretized by 80 equidistant load steps.

		$t = 1\,\mathrm{s}$	$t = 2\,\mathrm{s}$	$t = 3\,\mathrm{s}$	$t = 4\,\mathrm{s}$
Loading sequence 1	$\bar{\varepsilon}_1$	$1.77\,\%$	$1.77\,\%$	$1.77\,\%$	$0\,\%$
	$\bar{\varepsilon}_2$	$0\,\%$	$1.77\,\%$	$0\,\%$	$0\,\%$
Loading sequence 2	$\bar{\varepsilon}_1$	$0\,\%$	$1.77\,\%$	$0\,\%$	$0\,\%$
	$\bar{\varepsilon}_2$	$1.77\,\%$	$1.77\,\%$	$1.77\,\%$	$0\,\%$

Table 4.5: Investigated biaxial loading sequences

In Figure 4.10a and 4.10b, the stress-times curve for loading sequence 1 and 2 are shown. The $\bar{\sigma}_{11}$ and $\bar{\sigma}_{22}$ components of the effective stress response is shown, accompanied by the corresponding relative errors η_{11} and η_{22}. As before, the full-field solution serves as the reference.

Examining Figure 4.10a and 4.10b, we observe a pronounced anisotropy of the material's yield behavior. Furthermore, the findings for the uniaxial loadings concerning the error carry over to the case under consideration. The DMN of depth four only qualitatively predicts the material behavior, whereas, for $K = 8_1$ and $K = 8_2$, full-field solution

and DMN predictions are almost indistinguishable. As before, the relative errors are of the same order of magnitude and generally fall with increasing depth. Furthermore, the differences between $K = 8_1$ and $K = 8_2$ should be pointed out. Examining Figure 4.10a and 4.10b shows that the relative errors for $K = 8_1$ generally exceed those for $K = 8_2$. Nevertheless, for $K = 8$, the relative errors are consistently below $5\,\%$ for both loading sequences and stress components.

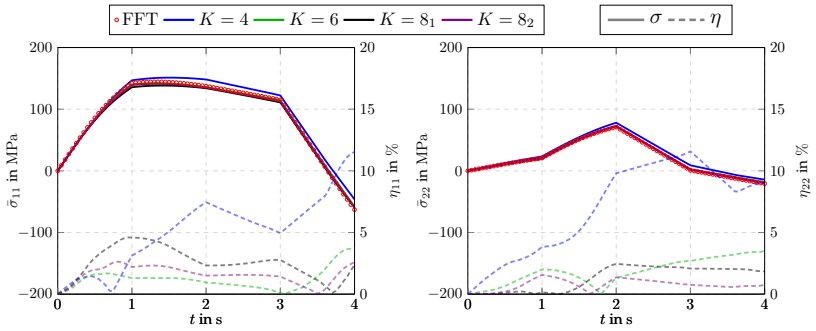

(a) Loading sequence 1

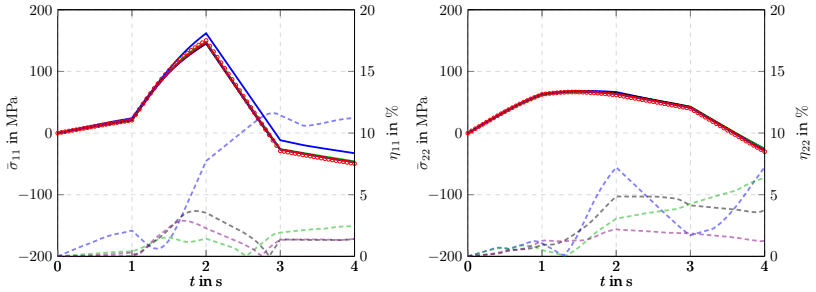

(b) Loading sequence 2

Figure 4.10: Stress vs. time curves for the short glass fiber reinforced polyamide and biaxial loadings

Online evaluation – comparison of higher statistical moments

We have seen that the DMN is able to predict the effective stress response of the composite subjected to uniaxial and biaxial loadings reasonably well. In the following, we investigate the DMN's ability to predict higher statistical moments, i.e., we investigate the DMN's ability to predict the phase-wise average stresses and their standard deviations. As load case, we chose a uniaxial extensions in e_1-direction, i.e., the principal fiber direction.

Computing the phase average and standard deviation of the full-field results is standard. For the DMNs, we compute the phase average of the matrix stress $\boldsymbol{\sigma}_\mathrm{m}$ by summing over all even, weighted stresses and, analogously, we compute the phase average of the stress in the fibers $\boldsymbol{\sigma}_\mathrm{f}$ by summing over all odd, weighted stresses, i.e.,

$$\boldsymbol{\sigma}_\mathrm{m} = \sum_{i=1}^{2^{K-1}} \frac{w_{K+1}^{2i}}{c_\mathrm{m}} \boldsymbol{\sigma}_{2i} \quad \text{and} \quad \boldsymbol{\sigma}_\mathrm{f} = \sum_{i=1}^{2^{K-1}} \frac{w_{K+1}^{2i-1}}{c_\mathrm{f}} \boldsymbol{\sigma}_{2i-1} \tag{4.74}$$

with the volume fractions

$$c_\mathrm{m} = \sum_{i=1}^{2^{K-1}} w_{K+1}^{2i} \quad \text{and} \quad c_\mathrm{f} = \sum_{i=1}^{2^{K-1}} w_{K+1}^{2i-1}. \tag{4.75}$$

Analogously, the standard deviations are computed as

$$\mathrm{Std}(\boldsymbol{\sigma}_\mathrm{m}) = \sqrt{\sum_{i=1}^{2^{K-1}} \frac{w_{K+1}^{2i}}{c_\mathrm{m}} \left(\boldsymbol{\sigma}_{2i} - \boldsymbol{\sigma}_\mathrm{m}\right)^2} \tag{4.76}$$

and

$$\mathrm{Std}(\boldsymbol{\sigma}_\mathrm{f}) = \sqrt{\sum_{i=1}^{2^{K-1}} \frac{w_{K+1}^{2i-1}}{c_\mathrm{f}} \left(\boldsymbol{\sigma}_{2i-1} - \boldsymbol{\sigma}_\mathrm{f}\right)^2}. \tag{4.77}$$

Figure 4.11 comprises the 11-component of the phase-wise average stress in the matrix and fibers and the phase-wise standard deviations.

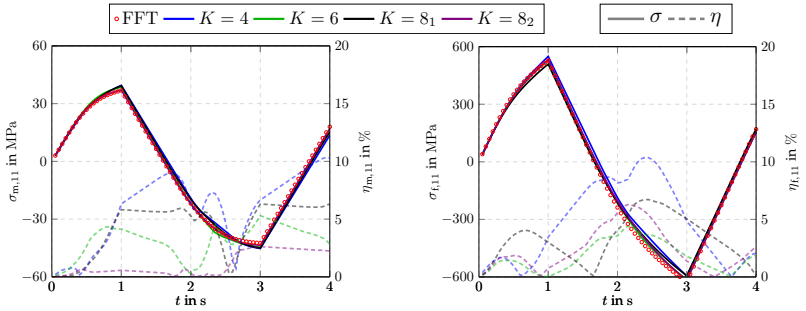

(a) Phase-wise average of the axial stress in the matrix (left) and in the fibers (right)

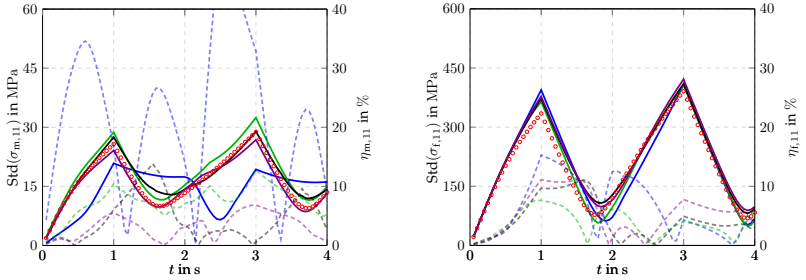

(b) Phase-wise standard deviation of the axial stress in the matrix (left) and the fibers (right)

Figure 4.11: Phase-wise average (a) and standard deviation (b) of the axial stress in the matrix and fibers

Figure 4.11a shows clearly that the fibers carry the majority of the load. Indeed, the average values of the axial stress in the fibers $\sigma_{\mathrm{f},11}$ exceed those of the matrix $\sigma_{\mathrm{m},11}$ by more than one order of magnitude. Comparing DMN and FFT, we see that the DMN is able to predict the phase-wise average stresses reasonably well. The occuring relative errors are on the same order of magnitude as in Figure 4.9a. Turning our attention to the standard deviation of the stresses, we observe

more pronounced differences between DMN predictions and the full-field simulation. Even though the agreement between DMN and FFT improves for increasing depth, there are still clear deviations observable for $K = 8_1$ and $K = 8_2$. The arising relative errors are more than twice as large compared to the phase-average of the stresses. Although the relative errors are quite large, similarities can be observed in the qualitative trends of DMN predictions and full-field solution regarding the standard deviation.

4.4.3 A metal matrix composite

Offline training

Also for the metal matrix composite, $N_\mathrm{s} = 800$ pairs of stiffness tensors $\{(\mathbb{C}_1^s, \mathbb{C}_2^s)\}_{s=1}^{N_\mathrm{s}}$ were sampled as described in Section 4.3.1 and the corresponding effective stiffnesses $\left\{\bar{\mathbb{C}}^s\right\}_{s=1}^{N_\mathrm{s}}$ were computed. As per Section 4.4.2, the pre-computed data is split into a training and a validation set comprising 700 and 100 samples, respectively.

Turning our attention to the offline training, the history of the loss and the mean training and validation errors are shown in Figure 4.12, whereas the values of the loss as well as the mean and maximum errors for the training and validation set at the end of the training are listed in Table 4.6.

The trends that could be observed for the previous example in Section 4.4.2 are also apparent for the case at hand. The converged loss, the mean and the maximum errors decrease monotonically with an increasing depth. The relative errors of the predicted volume fractions are below $1\,\%$ for $K > 4$.

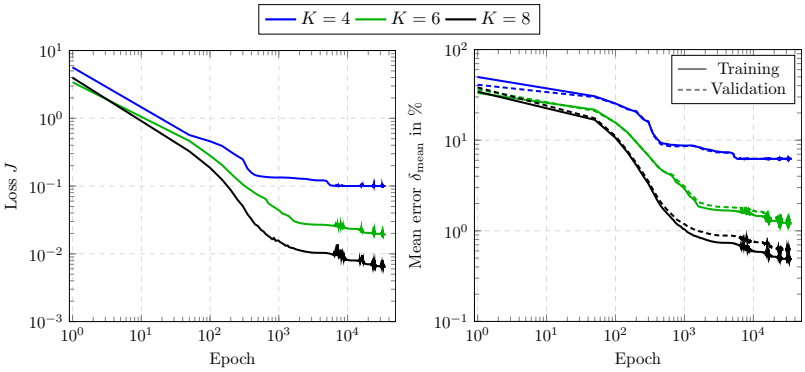

(a) Loss vs. training epoch

(b) Mean error vs. training epoch

Figure 4.12: Loss and mean training and validation errors during training for the metal matrix composite

	J	$\delta^{\text{train}}_{\text{mean}}$	$\delta^{\text{train}}_{\text{max}}$	$\delta^{\text{valid}}_{\text{mean}}$	$\delta^{\text{valid}}_{\text{max}}$	c_{p}
$K = 4$	$1.00 \cdot 10^{-1}$	6.22 %	15.27 %	6.24 %	21.85 %	0.2885 (−3.83 %)
$K = 5$	$4.25 \cdot 10^{-2}$	2.37 %	6.41 %	2.54 %	7.26 %	0.2978 (−0.73 %)
$K = 6$	$1.92 \cdot 10^{-2}$	1.21 %	2.73 %	1.30 %	4.96 %	0.2992 (−0.27 %)
$K = 7$	$1.10 \cdot 10^{-2}$	0.75 %	1.45 %	0.78 %	3.26 %	0.2996 (−0.13 %)
$K = 8$	$6.48 \cdot 10^{-3}$	0.47 %	0.86 %	0.55 %	1.65 %	0.2999 (−0.03 %)

Table 4.6: Training results for the metal matrix composite

Figure 4.13 shows the distribution of the errors on the training and validation set. Also for the MMC, the maximum error of the validation set is dominated by a single sample, even though the mean errors are close, and the error distributions for both sets are comparable, if neglecting the outliers. The distributions of the approximation error is similar to the FRP case. In line with mathematical intuition, this error

distribution is mainly determined by the loss function and the sampling of the training data , and not by the microstructure under consideration.

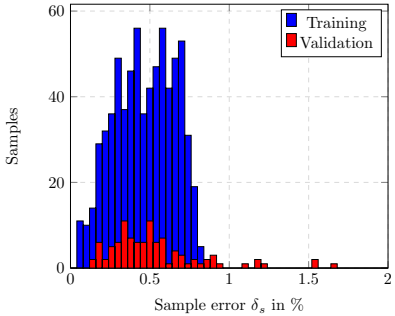

Figure 4.13: Error distribution for $K = 8$ after 36 000 epochs

Online evaluation – uniaxial loadings

The metal matrix composite is subjected to uniaxial strain loadings (4.70) for all three normal and shear strain components separately. In the respective strain direction, a complete hysteresis is simulated with an amplitude of $\bar{\varepsilon} = 1.0\,\%$ strain, distributed over 80 equidistant load steps. In Figure 4.14, the effective stress vs. time curves for full-field simulations are compared to the DMN predictions for even depths. For all six load cases, strong differences are visible for $K = 4$. Only for higher K, a qualitative agreement between full-field solution and DMN prediction may be observed. Still, for $K \geq 6$, only inspecting the stress vs. time curves, the DMN predictions agree reasonably well with the full-field simulations. This difference in required depth might be caused by the power-law plastification employed for the MMC elasto-plastic model, which in turn induces significant local plastification in the metal matrix.

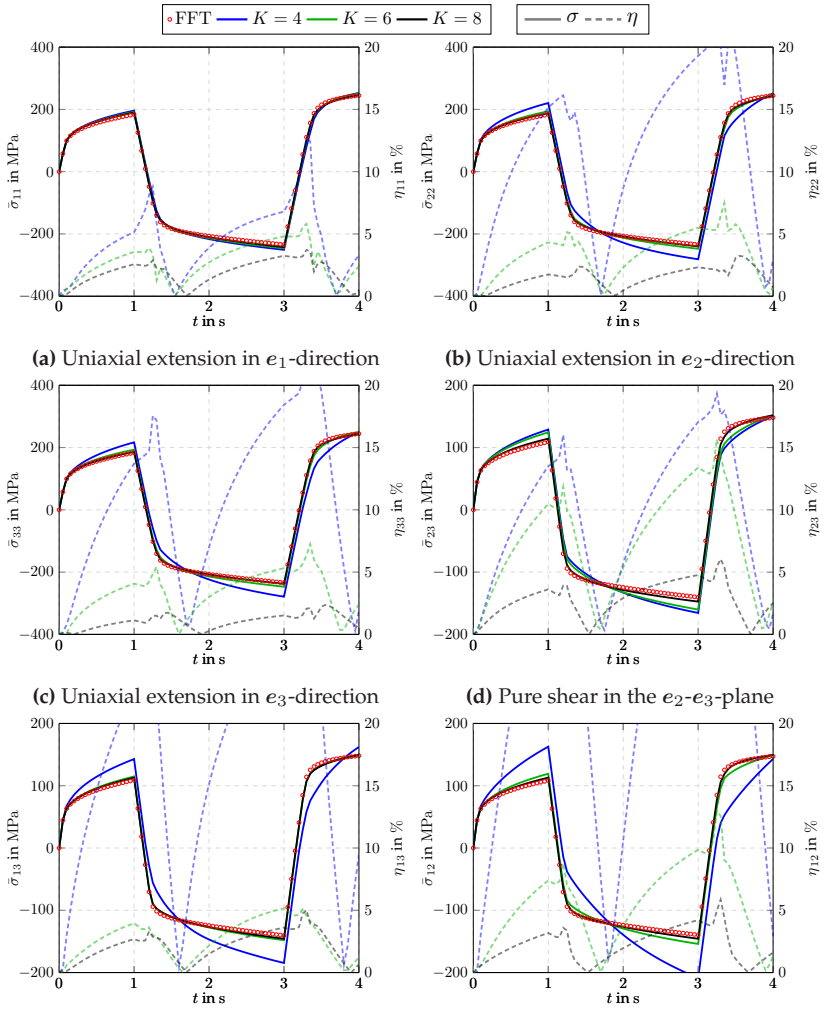

(a) Uniaxial extension in e_1-direction

(b) Uniaxial extension in e_2-direction

(c) Uniaxial extension in e_3-direction

(d) Pure shear in the e_2-e_3-plane

(e) Pure shear in the e_1-e_3-plane

(f) Pure shear in the e_1-e_2-plane

Figure 4.14: Stress vs. time curves for the metal matrix composite and uniaxial loadings

To quantify our observations, we inspect Table 4.7, where the maximum relative errors of the individual stress components are listed. The maximum error decreases for increasing depth. However, the overall error is much larger than for the FRP example. This is surprising, as one might expect the more complex morphological anisotropy of the fiber reinforced composite to manifest. Quite the opposite appears to hold: The degree of nonlinearity and strength of localization appears to be the dominating factor for good approximation quality. For $\eta_{22}^{\max}$, $\eta_{33}^{\max}$ and $\eta_{12}^{\max}$, the relative errors of the individual stress error components decrease monotonically with increasing depth. However, for $\eta_{11}^{\max}$, $\eta_{23}^{\max}$ and $\eta_{13}^{\max}$ this is not the case as it was observed for the FRP.

max rel. error	$K = 4$	$K = 5$	$K = 6$	$K = 7$	$K = 8$
$\eta_{11}^{\max}$	$12.64\,\%$	$13.84\,\%$	$5.82\,\%$	$2.58\,\%$	$3.72\,\%$
$\eta_{22}^{\max}$	$20.72\,\%$	$14.62\,\%$	$7.49\,\%$	$5.94\,\%$	$3.24\,\%$
$\eta_{33}^{\max}$	$25.19\,\%$	$14.99\,\%$	$7.25\,\%$	$5.76\,\%$	$2.36\,\%$
$\eta_{23}^{\max}$	$19.34\,\%$	$15.64\,\%$	$15.67\,\%$	$5.75\,\%$	$6.04\,\%$
$\eta_{13}^{\max}$	$37.89\,\%$	$24.62\,\%$	$5.16\,\%$	$9.31\,\%$	$5.02\,\%$
$\eta_{12}^{\max}$	$50.39\,\%$	$18.87\,\%$	$12.97\,\%$	$6.36\,\%$	$5.85\,\%$
$\max_{(i,j)\in\mathcal{I}}(\eta_{ij}^{\max})$	$50.39\,\%$	$24.62\,\%$	$15.67\,\%$	$9.31\,\%$	$6.04\,\%$

Table 4.7: Relative errors for the metal matrix composite and uniaxial loadings

Online evaluation – biaxial loadings

Next, we investigate the DMN's response to a biaxial strain loading (4.73). We investigate two loading scenarios in analogy to the FRP, see Table 4.5. The simulations are carried out with strain amplitudes of $0.71\,\%$ in the respective loading directions and divided into 80 equidistant load steps.

Figure 4.15a and 4.15b show σ_{11}, σ_{22}, η_{11} and η_{22} for loading sequence 1 and 2, respectively. As before, the full-field solution serves as the

reference for the DMNs. Comparing the stress components of the full-field computations in Figure 4.15a and 4.15b reveals an almost isotropic stress response of the composite. For both loading sequences, strong deviations are visible for $K = 4$. Notice that the DMN with depth $K = 4$ predicts an anisotropic material behaviour, see $\bar{\sigma}_{11}$ and $\bar{\sigma}_{22}$ in Figure 4.15a and 4.15b. Only for $K \geq 6$, a sufficient agreement between full-field solution and DMN prediction emerges. For $K = 8$, the relative error is well below $5\,\%$ for both loading sequences and stress components.

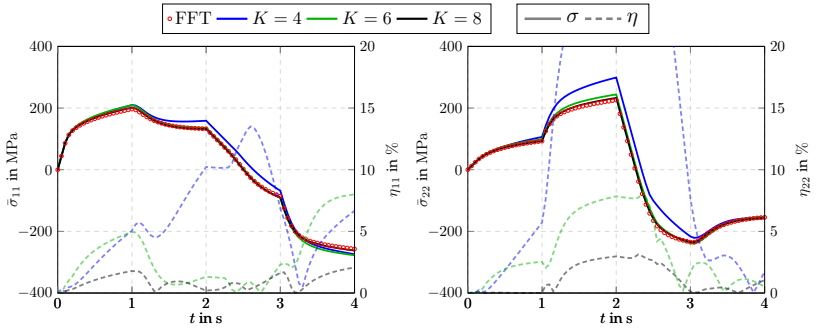

(a) Loading sequence 1

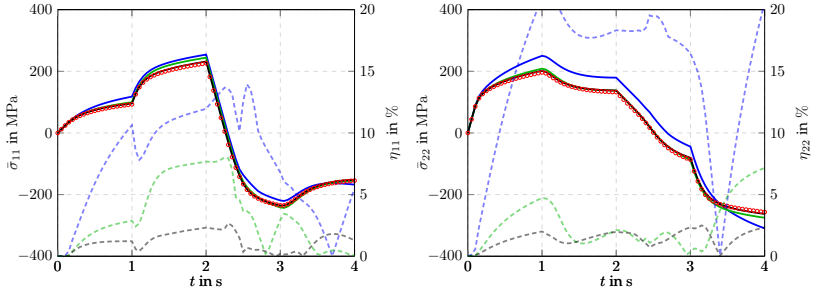

(b) Loading sequence 2

Figure 4.15: Stress vs. time curves for the metal matrix composite and biaxial loadings

4.5 Conclusion

In this chapter, we introduced direct deep material networks which, in contrast to the original formulation of Liu et al. (2019a) and Liu and Wu (2019), omit intermittent rotations and utilize the flexibility of laminate building blocks with arbitrary direction of lamination to reduce the number of fitting parameters of the approach. In Section 4.2.2, we specified helpful formulae, in particular in view of their usefulness in codes supporting automatic differentiation, for the implementation of $\mathcal{DMN}_Y^{\mathcal{AL}}$ for the case of N phases. Furthermore, in Section 4.2.3, we specified a versatile evaluation of the nonlinear homogenization function $\mathcal{DMN}_Y$ of deep material networks greatly simplifying the implementation. For this, we introduced a "flattening" of the DMN tree to arrive at a formulation general enough to encompass arbitrary trees of laminates.

Turning our attention to the building blocks of the (direct) DMNs, we established, in conjunction with Chapter 3, that any microstructure inherits thermodynamic consistency and stress-strain monotonicity from its phases. It is remarkable that the former statements are not restricted to laminates, the building blocks of DMNs, but continue to hold for any microstructure. On the other hand, apparently not every microstructure is suitable as a building block for DMNs. Suppose, for instance, a microstructure with an isotropic effective material behavior for isotropic input materials is given. In particular, with such a microstructure as building block, anisotropic effective material laws cannot be approximated. Thus, the inherent anisotropy of laminates is a key feature for their use as a building block for DMNs.

As a next step, we will investigate numerical strategies to enable mechanical simulations on a component scale with varying microstructure characteristics in Chapter 5 and Chapter 6. Furthermore, we will extend

the range of applicability by considering thermomechanical coupling in a two-scale component simulation in Chapter 7.

Chapter 5

The FE-DMN method for the analysis of short fiber reinforced plastic components[1]

5.1 Introduction

Injection molded short fiber reinforced components are frequently used for industrial applications as they combine favorable mechanical properties, free formability and short cycle times. As a result of the injection molding process, the fiber orientation, and to some degree the fiber volume fraction, may vary continuously within the component. Characterizing all possible orientation states for such materials is an arduous and expensive task, both experimentally and by simulative means.

To illustrate the complexity to be handled routinely, Figure 5.1a shows a quadcopter frame arm made of short fiber reinforced polyamide with a local fiber orientation determined by an injection molding simulation. The color scale encodes the local fiber orientation tensor: Magenta corresponds to a unidirectional, cyan to an isotropic and yellow to a planar isotropic fiber orientation state. We observe that, for the majority

[1] This chapter is based on the publication "An FE-DMN method for the multiscale analysis of short fiber reinforced plastic components" (Gajek et al., 2021a). The introduction has been shortened to avoid redundancy with Chapter 1. The notation has been harmonized.

of the quadcopter arm, the fibers are almost aligned. Moreover, we encounter isotropic and planar isotropic fiber orientations in areas where weld lines have formed. As weld lines correspond to weak spots in the structure, it is critical to account for such regions accurately in mechanical simulations.

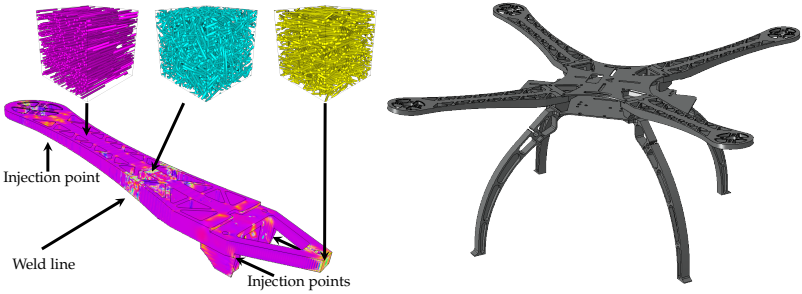

(a) Injection molded quadcopter arm **(b)** Quadcopter frame (GrabCAD, 2022)

Figure 5.1: Injection molded quadcopter arm (a) with local fiber orientation: Magenta, cyan and yellow correspond to unidirectional, isotropic and planar isotropic fiber orientation states. Quadcopter frame used as benchmark geometry (b) for the component scale simulation.

In this chapter, we investigate a multiscale methodology for direct DMNs, which covers all possible variations of the second-order fiber orientation tensors and permits concurrent multiscale simulations with DMNs at the Gauss point level. Similar to the FE^2, FE-FFT and the FE^{2R} methods, we call the ensuing method the FE-DMN method.

As point of departure, we consider direct DMNs as introduced in Chapter 4 and restrict to microstructures without micro-orientations, i.e., microstructures comprising isotropic phases. To account for a spatially varying fiber orientation, see Section 5.2, we augment direct DMNs by the fiber orientation interpolation concept introduced by Köbler et al. (2018). To this end, we assume that the local fiber volume fractions of the individual laminates in the hierarchy are independent of the local

fiber orientation. Therefore, it suffices to fix the fiber volume fractions and to interpolate the lamination directions only. In contrast to Liu et al. (2020), we do not consider a *transfer learning* strategy, i.e., to interpolate already identified models, but propose an a priori interpolation strategy. More precisely, we investigate direct DMNs which explicitly depend on the fiber orientation, and identify the optimal model parameters *jointly*.

For this purpose, we utilize high-fidelity microstructures of fiber reinforced composites (Schneider, 2017), which permit us to routinely cover the possible fiber orientations at industrial filler fraction and fiber aspect ratio. For the sake of simplicity, we assume that both fiber volume fraction and fiber length are fixed for all generated microstructures. We sample the linear elastic training data from up to 31 microstructure realizations. We also improve upon the sampling strategy of Liu et al. (2019a) and Liu and Wu (2019) for the constituents' stiffness tensors used in the offline training. We show by example that it is sufficient to cover those stiffnesses which arise as possible material tangents on the microscopic scale.

For component scale simulations of industrial problems, it is necessary to optimize the user-defined material models based upon the identified DMNs, see Section 5.3. We take special care to ensure that the interpolated DMN generalizes accurately to the inelastic regime. To this end, 78 additional microstructure realizations are generated, exclusively for the inelastic validations. We compute the stress response of each of the 109 generated microstructure representations by an FFT-based computational homogenization (Moulinec and Suquet, 1994; 1998) code and compare the former to the predicted stress response of the interpolated direct DMN. The validation results show that with a maximum error of $5.5\,\%$, the DMN is capable of predicting the effective stress of all investigated 109 discrete fiber orientation states sufficiently. We refer to Section 5.4 for details.

To show that our approach is applicable to state of the art engineering computations, we consider the entire process chain of a quadcopter frame, see Figure 5.1b and Section 5.5. We conduct an injection molding simulation where we assume the fiber volume fraction to be homogeneous throughout the part, map the spatially varying fiber orientations upon a finite element mesh and conduct a two-scale simulation using the identified DMN surrogate model. We implement the DMN as an implicit user-material (UMAT) subroutine in ABAQUS only relying upon the provided software interfaces. In contrast, Liu et al. (2020) employed DMNs in an explicit finite element analysis. The quadcopter consists of four arms made of injection molded short fiber reinforced polyamide, two base plates which are made of aluminum and four legs which are made of pure polyamide. The simulation model of the quadcopter consist of more than two million elements resulting in almost ten million degrees of freedom. In more than 1.9 million elements, a deep material network is integrated implicitly at every Gauss point, accounting for the local microstructure information in the simulation.

Last but not least, we discuss the computational costs accompanied by our approach in Section 5.6, and demonstrate that the educated guess of the potential computational power of DMNs made in the conclusion of Liu et al. (2020) was too pessimistic.

5.2 Two-phase direct DMNs for a variable fiber orientation

5.2.1 Two-phase direct DMNs

We seek to extend direct DMNs to short fiber reinforced composite microstructures parameterized by the second-order fiber orientation tensor. For this, we briefly recall the basic idea of direct DMNs. We

restrict to the special case of two phases and focus only on details relevant for this chapter and refer to Chapter 4 for more information.

Any two-phase periodic microstructure $Y \subseteq \mathrm{V}^d$ in d spatial dimensions gives rise to the (nonlinear) homogenization function

$$\mathcal{M}_Y : \mathcal{GSM} \times \mathcal{GSM} \to \mathcal{GSM}, \quad (\mathcal{G}_1, \mathcal{G}_2) \mapsto \bar{\mathcal{G}}, \tag{5.1}$$

which maps two input GSMs to the effective GSM that emerges by solving the cell problem of first order homogenization, see Chapter 3 for more details. In general, evaluating homogenization functions requires significant computational resources. Only for special microstructures, the evaluation can be performed with minimal effort. An example for such a microstructure is given by a two-phase laminate, uniquely characterized by a direction of lamination $\boldsymbol{n} \in \mathrm{S}^{d-1}$ and the volume fractions $c_1 \in \mathbb{R}_{\geq 0}$ and $c_2 \in \mathbb{R}_{\geq 0}$ of the two phases for which $c_1 + c_2 = 1$ holds.

A two-phase direct DMN is defined as a hierarchy of such two-phase laminates, see Figure 5.2. By combining laminates in a hierarchical manner, the resulting homogenization function

$$\mathcal{DMN}_Y : \mathcal{GSM} \times \mathcal{GSM} \to \mathcal{GSM} \tag{5.2}$$

may be rather complex and, by a judicious choice of the involved laminates, may be used as an approximation of the homogenization function (5.1) corresponding to the original microstructure Y, which is significantly less demanding to evaluate.

On a more formal level, a direct DMN is a perfect, ordered, rooted binary tree of depth K, where a two-phase laminate $\mathcal{B}_k^i$ is assigned to each node of the tree. We reserve the letter k for labeling the depth of a node, whereas the horizontal index is consistently indexed by the letter i. Our layer count only comprises the laminate layers, and the input is counted separately. Thus, the direct DMN comprises $2^K - 1$ laminate nodes. Each

node features a direction of lamination $\boldsymbol{n}_k^i$ and the two volume fractions $c_{k,1}^i$ and $c_{k,2}^i$. For a two-phase DMN of depth K, the homogenization function $\mathcal{DMN}_Y$

$$\bar{\mathcal{G}} = \mathcal{DMN}_Y(\mathcal{G}_1, \mathcal{G}_2) \tag{5.3}$$

is defined recursively by traversing the binary tree from the leaves, at level K, to the root

$$\bar{\mathcal{G}} = \mathcal{G}_1^1 \quad \text{with} \quad \mathcal{G}_k^i = \mathcal{B}_k^i(\mathcal{G}_{k+1}^{2i-1}, \mathcal{G}_{k+1}^{2i}), \quad k = 1, \dots, K,\ i = 1, \dots, 2^{k-1}. \tag{5.4}$$

Input materials are assigned in an alternating fashion, i.e.,

$$\mathcal{G}_{K+1}^i = \begin{cases} \mathcal{G}_1, & i \text{ odd}, \\ \mathcal{G}_2, & i \text{ even}, \end{cases} \tag{5.5}$$

holds. We refer to Figure 5.2 for a schematic.

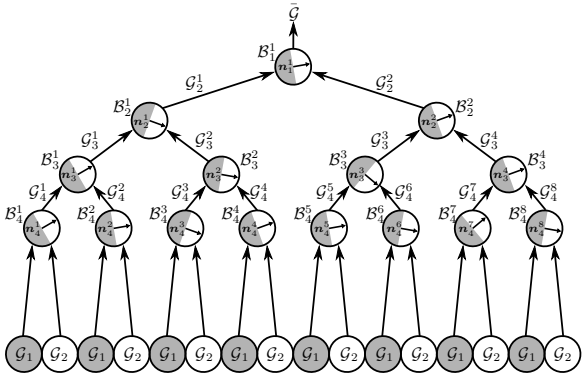

Figure 5.2: Schematic illustration of a two-phase direct DMN of depth four (the input level is not counted)

The laminates' volume fractions are parameterized by assigning pairs of weights w_{K+1}^{2i-1} and w_{K+1}^{2i} to each laminate $\mathcal{B}_K^i$ on the K-th level, see

Section 4.2 for an explanation. These weights should be non-negative and sum to unity. Then, by traversing the binary tree from the leaves to the root, the weights on the k-th level are computed by the sum of weights of the respective laminates on the previous level, i.e.,

$$w_k^i = w_{k+1}^{2i-1} + w_{k+1}^{2i} \tag{5.6}$$

holds. The volume fractions $c_{k,1}^i$ and $c_{k,2}^i$ of each laminate block $\mathcal{B}_k^i$ are then computed by normalization

$$c_{k,1}^i = \frac{w_{k+1}^{2i-1}}{w_{k+1}^{2i-1} + w_{k+1}^{2i}} \quad \text{and} \quad c_{k,2}^i = 1 - c_{k,1}^i. \tag{5.7}$$

For fixed tree topology, a direct DMN is uniquely determined by the directions of lamination, which we collect in the form of a large vector

$$\vec{\boldsymbol{n}} = [\boldsymbol{n}_K^1, \dots, \boldsymbol{n}_K^{2^{K-1}}, \boldsymbol{n}_{K-1}^1, \dots, \boldsymbol{n}_{K-1}^{2^{K-2}}, \dots, \boldsymbol{n}_1^1] \in \left(\mathrm{S}^d\right)^{2^K-1}, \tag{5.8}$$

and the weights of the input layer

$$\vec{w} = [w_{K+1}^1, \dots, w_{K+1}^{2^K}] \in \mathbb{R}_{\geq 0}^{2^K}. \tag{5.9}$$

The free parameters $\vec{\boldsymbol{n}}$ and $\vec{w}$ are identified based on linear elastic precomputations during the offline training. Once the free parameters are identified, the DMN may be applied to nonlinear and inelastic materials during the online evaluation.

5.2.2 Fiber orientation triangle

Suppose a fiber orientation state is given in terms of a fiber orientation distribution (FOD) function $\rho : \mathrm{S}^2 \to \mathbb{R}_{\geq 0}$, which specifies the probability to find fibers in direction $\boldsymbol{d} \in \mathrm{S}^2$. Advani and Tucker (1987) introduced

the volume-weighted second-order fiber orientation tensor

$$\boldsymbol{A}_2 = \int_{\mathrm{S}^2} \rho(\boldsymbol{d})\, \boldsymbol{d} \otimes \boldsymbol{d}\, \mathrm{d}A(\boldsymbol{d}) \tag{5.10}$$

as a compact measure for the current fiber orientation state. Despite its limited information content, its compact form makes it the typical quantity of interest for commercial injection molding simulations (Kennedy, 2013). Higher-order moments of the FOD are then estimated by closure approximations, see Montgomery-Smith et al. (2011).

The tensor $\boldsymbol{A}_2$ is symmetric and positive definite with unit trace. Consequently, only five independent parameters are involved. In terms of an eigenvalue decomposition

$$\boldsymbol{A}_2 \mathrel{\hat{=}} \boldsymbol{Q} \begin{bmatrix} \lambda_1 & 0 & 0 \\ 0 & \lambda_2 & 0 \\ 0 & 0 & \lambda_3 \end{bmatrix} \boldsymbol{Q}^{\mathsf{T}}, \tag{5.11}$$

where the matrix $\boldsymbol{Q} \in \mathrm{SO}(3)$ is orthogonal and the eigenvalues $\lambda_1 \geq \lambda_2 \geq \lambda_3$ are sorted in a descending order, the fiber orientation tensor $\boldsymbol{A}_2$ may be parameterized by the tuple $(\lambda_1, \lambda_2) \in \Lambda$ with

$$\Lambda = \left\{ (\lambda_1, \lambda_2) \in \mathbb{R}^2 \,\middle|\, \frac{1}{3} \leq \lambda_1 \leq 1,\ \frac{1-\lambda_1}{2} \leq \lambda_2 \leq \min\left(\lambda_1, 1-\lambda_1\right) \right\}. \tag{5.12}$$

Thus, up to an orthogonal transformation, every tensor $\boldsymbol{A}_2$ corresponds to a point (λ_1, λ_2) in the triangle Λ, see Figure 5.3. In this chapter, we follow Köbler et al. (2018) and use the CMY coloring scheme for encoding different fiber orientations as shown in Figure 5.3.

The manufacturing process induces local variations of the fiber orientation of short fiber reinforced plastic components. Thus, for component-scale simulations, these variations need to be accounted for by the material models. If the fiber orientation state is described in terms of the

second-order fiber orientation tensor $\boldsymbol{A}_2$, a family of effective material models, one for each such tensor $\boldsymbol{A}_2$, needs to be supplemented.

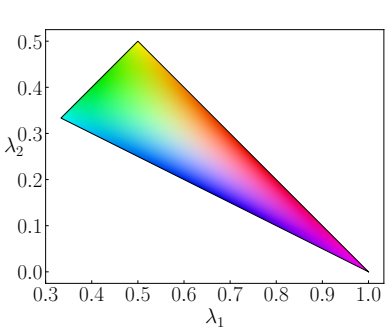

(a) Fiber orientation reference triangle

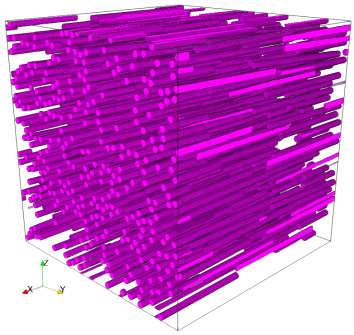

(b) $\lambda_1 = 1.0$, $\lambda_2 = 0.0$

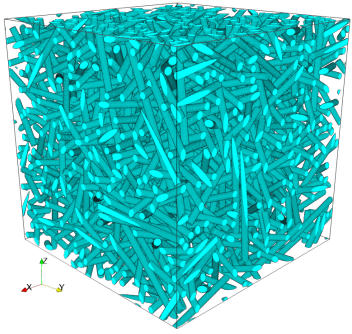

(c) $\lambda_1 = 0.\overline{33}$, $\lambda_2 = 0.\overline{33}$

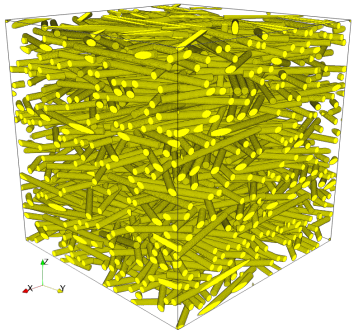

(d) $\lambda_1 = 0.495$, $\lambda_2 = 0.495$

Figure 5.3: Fiber orientation reference triangle (a) illustrating the admissible range of the two largest eigenvalues of the second order fiber orientation tensor $\boldsymbol{A}_2$. The three extreme cases, i.e., (b) unidirectional, (c) isotropic and (d) planar isotropic fiber orientation are shown.

By general covariance considerations, two fiber orientation states which differ only by an orthogonal transformation should give rise to effective material responses which differ only by this orthogonal transformation. Consequently, if the considered fiber orientation states are parameterized

by the second-order fiber orientation tensor, the essentially different fiber orientation states will be parameterized by the points inside the fiber orientation triangle (5.12).

Thus, the material models to be identified are parameterized by a two-dimensional continuum. Furthermore, a certain continuity of the effective response of the material model, considered as a function of the fiber orientation tensor, is expected. Indeed, changing the fiber orientation only slightly is expected to change the effective mechanical response only slightly as well, at least for non-critical loading. Unfortunately, the typical multiscale approach based on representative volume elements is unable to leverage this continuity. Although the effective material response depends continuously on the fiber orientation tensor, the representative volume element does not. Indeed, due to the stochastic nature of such fiber-filled volume elements, infinitely many *different* representative volume elements may be used to give rise to the same effective response.

In particular, this reasoning has the following implication. Suppose that we furnish each point $(\lambda_1, \lambda_2) \in \Lambda$ in the fiber orientation triangle (5.12) with a corresponding representative volume element $Y_{\lambda_1\lambda_2}$. Even if all these elements have the same size, the function $(\lambda_1, \lambda_2) \mapsto Y_{\lambda_1\lambda_2}$ will not be continuous in any useful way.

As an alternative, Köbler et al. (2018) proposed a fiber orientation interpolation procedure on the level of effective stresses. This idea avoids the difficulty of interpolating internal variables which live in different locations for different microstructures. However, this approach comes at a price: The number of stress evaluations is tripled by this approach. Indeed, for any fiber orientation state, the stress response associated to the three corners of the interpolating triangle needs to be evaluated.

5.2.3 Fiber orientation interpolation

Due to their specific structure, direct DMNs may overcome the difficulties mentioned at the end of the previous section. Indeed, for fixed tree topology, the internal variables of the individual phases live on identical locations, also for different DMNs. In any case, the internal variables are tied to the materials on the lowest level of the tree, see Figure 5.2. Of course, if DMNs are identified *independently* for each point in the fiber orientation triangle (5.12), the parameters of the DMN need not depend continuously on the fiber orientation tensor $\boldsymbol{A}_2$. Still, it appears reasonable to identify the DMN's parameters *jointly* over all fiber orientations in the fiber orientation triangle.

More precisely, we consider DMNs which are parameterized by points (λ_1, λ_2) inside the fiber orientation triangle Λ. As observed by Liu et al. (2019a), Liu and Wu (2019) and Gajek et al. (2020), the DMN's weights $\vec{w}$ after training are directly linked to the constituent volume fractions of the underlying microstructure. The former does not come as a surprise, since the effective elastic behavior is determined by the volume fraction to first order, see Chapter 14 in Milton (1986) or Section 20.2.2 in Torquato (2005), and the DMN is fitted on linear elastic data alone. Since, for generating the training data, we assume a constant volume fraction, independent of the fiber orientation, we seek weights $\vec{w}$ which are *independent* of the fiber orientation.

In order to interpolate the lamination directions $\vec{\boldsymbol{n}}$ on the fiber orientation triangle in $d = 3$ spatial dimensions, we parameterize each normal $\boldsymbol{n}_k^i$ by spherical coordinates

$$\boldsymbol{n}_k^i = \begin{bmatrix} \sin\left(\alpha_k^i\right) \cos\left(\beta_k^i\right) \\ \sin\left(\alpha_k^i\right) \sin\left(\beta_k^i\right) \\ \cos\left(\alpha_k^i\right) \end{bmatrix} \boldsymbol{e}_i \tag{5.13}$$

with angles $\alpha_k^i \in [0, \pi]$ and $\beta_k^i \in [0, 2\pi]$. Then, we interpolate the angles α_k^i and β_k^i on the fiber orientation triangle (5.12) by a global (finite element) shape function. Please note the difference to Köbler et al. (2018), who rely upon linear interpolation on a subtriangulation of the fiber orientation triangle.

Particularly compact expressions for the shape functions are obtained by transforming the point $(\lambda_1, \lambda_2) \in \Lambda$ to barycentric coordinates $(\varphi_1, \varphi_2, \varphi_3) \in \mathbb{R}^3$ via $g : \Lambda \to \mathbb{R}^3$, $(\lambda_1, \lambda_2) \mapsto (\varphi_1, \varphi_2, \varphi_3)$ by solving the linear system (Vince, 2017)

$$\begin{bmatrix} 1 & 1/3 & 1/2 \\ 0 & 1/3 & 1/2 \\ 1 & 1 & 1 \end{bmatrix} \begin{bmatrix} \varphi_1 \\ \varphi_2 \\ \varphi_3 \end{bmatrix} = \begin{bmatrix} \lambda_1 \\ \lambda_2 \\ 1 \end{bmatrix}. \tag{5.14}$$

We collect the parameters of the polynomial shape functions, which are parameterized via φ_1, φ_2 and φ_3, in the vector

$$\vec{\phi}(\varphi_1, \varphi_2, \varphi_3) = [\phi_1(\varphi_1, \varphi_2, \varphi_3), \ldots, \phi_M(\varphi_1, \varphi_2, \varphi_3)], \tag{5.15}$$

where M denotes the number of shape functions. Then, the interpolated angles may be expressed as

$$\alpha_k^i(\lambda_1, \lambda_2) = \vec{p}_k^{\,i\,\mathsf{T}} \vec{\phi}(g(\lambda_1, \lambda_2)) \quad \text{and} \quad \beta_k^i(\lambda_1, \lambda_2) = \vec{q}_k^{\,i\,\mathsf{T}} \vec{\phi}(g(\lambda_1, \lambda_2)) \tag{5.16}$$

in terms of the parameter vectors $\vec{p} = [p_1, \ldots, p_M] \in \mathbb{R}^M$ and $\vec{q} = [q_1, \ldots, q_M] \in \mathbb{R}^M$. We investigate linear, trilinear and quadratic shape functions, see Table 5.1.

To sum up, extending DMNs to account for a varying fiber orientation increases the number of unknown parameters. Instead of identifying, per laminate, the angles α_k^i and β_k^i, the parameter vectors $\vec{p}_k^{\,i}$ and $\vec{q}_k^{\,i}$ are sought, in addition to the unknown weights $\vec{w}$.

Linear	$M = 3$	$\phi_1 = \varphi_1$	$\phi_2 = \varphi_2$	$\phi_3 = \varphi_3$
Trilinear	$M = 4$	$\phi_1 = \varphi_1 - 9\varphi_1\varphi_2\varphi_3$ $\phi_4 = 27\varphi_1\varphi_2\varphi_3$	$\phi_2 = \varphi_2 - 9\varphi_1\varphi_2\varphi_3$	$\phi_3 = \varphi_3 - 9\varphi_1\varphi_2\varphi_3$
Quadratic	$M = 6$	$\phi_1 = \varphi_1\,(2\varphi_1 - 1)$ $\phi_4 = 4\varphi_1\varphi_2$	$\phi_2 = \varphi_2\,(2\varphi_2 - 1)$ $\phi_5 = 4\varphi_1\varphi_3$	$\phi_3 = \varphi_3\,(2\varphi_3 - 1)$ $\phi_6 = 4\varphi_2\varphi_3$

Table 5.1: Shape functions used for the orientation interpolation

5.3 Implementation

5.3.1 Offline training

We sample N_s quadruples of input stiffnesses and fiber orientations $(\mathbb{C}_1^s, \mathbb{C}_2^s, \lambda_1^s, \lambda_2^s)$, where s denotes the sample index, generate the respective microstructures and compute the effective stiffnesses $\bar{\mathbb{C}}^s$. We denote the generated training data by a sequence of quintuples $\left\{\left(\bar{\mathbb{C}}^s, \mathbb{C}_1^s, \mathbb{C}_2^s, \lambda_1^s, \lambda_2^s\right)\right\}_{s=1}^{N_\mathrm{s}}$. The actual sampling process will be discussed in Section 5.4.4. For the moment, we assume the training data to be given and fixed.

In the offline training, we seek to identify the free parameters of the DMN based on the sampled training data, namely the weights $\vec{w}$ and the vectors $\{\vec{p}_k^{\,i}\}$ and $\{\vec{q}_k^{\,i}\}$ used for interpolating the angles (5.16), which we collect in the vectors $\vec{p} \in \left(\mathbb{R}^M\right)^{2^K-1}$,

$$\vec{p} = \left[\vec{p}_K^{\,1}, \vec{p}_K^{\,2}, \ldots \vec{p}_K^{\,2^{K-1}}, \vec{p}_{K-1}^{\,1}, \vec{p}_{K-1}^{\,2}, \ldots, \vec{p}_{K-1}^{\,2^{K-2}}, \ldots, \vec{p}_2^{\,1}, \vec{p}_2^{\,2}, \vec{p}_1^{\,1}\right] \quad (5.17)$$

and $\vec{q} \in \left(\mathbb{R}^M\right)^{2^K-1}$,

$$\vec{q} = \left[\vec{q}_K^{\,1}, \vec{q}_K^{\,2}, \ldots \vec{q}_K^{\,2^{K-1}}, \vec{q}_{K-1}^{\,1}, \vec{q}_{K-1}^{\,2}, \ldots, \vec{q}_{K-1}^{\,2^{K-2}}, \ldots, \vec{q}_2^{\,1}, \vec{q}_2^{\,2}, \vec{q}_1^{\,1}\right]. \quad (5.18)$$

More precisely, we choose a reversed breadth-first ordering for $\vec{p}$ and $\vec{q}$, i.e., we insert the parameters of laminates on level K first and add the

parameters of laminates for decreasing level index in their corresponding order.

For a start, we represent the DMN's linear elastic homogenization function in the form

$$\bar{\mathbb{C}} = \mathcal{DMN}_{\Lambda}^{\mathcal{L}} \left(\mathbb{C}_1, \mathbb{C}_2, \lambda_1, \lambda_2, \vec{p}, \vec{q}, \vec{w} \right), \tag{5.19}$$

which maps the input stiffnesses $\mathbb{C}_1$ and $\mathbb{C}_2$, the fiber orientation parameters λ_1 and λ_2 and the unknown fitting parameters $\vec{p}$, $\vec{q}$ and $\vec{w}$ to the DMN's effective stiffness. Then, the offline training is given by solving the unconstrained optimization problem

$$J \left(\vec{p}, \vec{q}, \langle \vec{v} \rangle_+ \right) \longrightarrow \min_{\vec{p}, \vec{q}, \vec{v}} \tag{5.20}$$

involving the objective function

$$J \left(\vec{p}, \vec{q}, \vec{w} \right) = \frac{1}{N_{\mathrm{s}}} \sqrt[q]{\sum_{s=1}^{N_{\mathrm{s}}} \left(\frac{\left\| \mathcal{DMN}_{\Lambda}^{\mathcal{L}} \left(\mathbb{C}_1^s, \mathbb{C}_2^s, \lambda_1^s, \lambda_2^s, \vec{p}, \vec{q}, \vec{w} \right) - \bar{\mathbb{C}}^s \right\|_p}{\left\| \bar{\mathbb{C}}^s \right\|_p} \right)^q} + \lambda_{\mathrm{p}} \left(\sum_{i=1}^{2^K} w_{K+1}^i - 1 \right)^2 . \tag{5.21}$$

The quadratic penalty term encodes the mixing constraint on the weights. Furthermore, the non-negativity constraint on the weights $w_{K+1}^i \geq 0$ is enforced by expressing the vector of weights $\vec{w} = \langle \vec{v} \rangle_+$ in terms of the vector of unconstrained weights $\vec{v} \in \mathbb{R}^{2^K}$, where $\langle \square \rangle_+ : \mathbb{R}^{2^K} \to \mathbb{R}^{2^K}_{\geq 0}$ defines the Macaulay bracket, i.e., the ReLu activation functions applied to the components of $\vec{v}$, see also Section 4.3.2 for more information.

In Chapter 4, we have learned that the specific binary tree structure of the DMN can be exploited to evaluate $\mathcal{DMN}_{\Lambda}^{\mathcal{L}}$ efficiently. Indeed, computing the effective stiffness of a two-phase DMN reduces to recursively computing a sequence of effective stiffnesses of two-phase laminates,

see Figure 5.4 for a schematic. As per Section 4.2.2, the linear elastic homogenization function of a single laminate

$$\mathbb{C}_k^i = \mathcal{B}_k^i(\mathbb{C}_{k+1}^{2i-1}, \mathbb{C}_{k+1}^{2i}) \tag{5.22}$$

may be determined by solving the implicit equation

$$\begin{aligned}\left(\mathbb{\Gamma}_{\boldsymbol{n}_k^i} + \lambda_0 \left[\mathbb{C}_k^i - \lambda_0 \mathbb{I}_\mathrm{s}\right]^{-1}\right)^{-1} = c_{k,1}^i \left(\mathbb{\Gamma}_{\boldsymbol{n}_k^i} + \lambda_0 \left[\mathbb{C}_{k+1}^{2i-1} - \lambda_0 \mathbb{I}_\mathrm{s}\right]^{-1}\right)^{-1} \\ + c_{k,2}^i \left(\mathbb{\Gamma}_{\boldsymbol{n}_k^i} + \lambda_0 \left[\mathbb{C}_{k+1}^{2i} - \lambda_0 \mathbb{I}_\mathrm{s}\right]^{-1}\right)^{-1}\end{aligned} \tag{5.23}$$

for the effective stiffness $\mathbb{C}_k^i$.

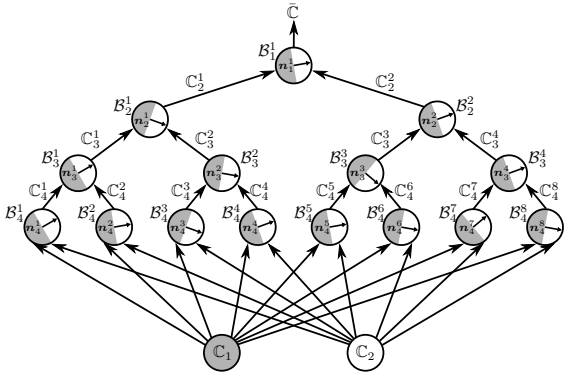

Figure 5.4: Schematic illustration of the stiffness propagation in a two-phase direct DMN of depth four

The offline training is implemented in PyTorch (Paszke et al., 2017), see Gajek et al. (2020) or Section 4.3.2, making use of the framework's automatic differentiation capabilities to solve the regression problem (5.20) by means of accelerated stochastic gradient descent methods using mini batches of predefined size. An epoch j consists of evaluating

(5.19) for all samples of the respective mini batch, evaluating the loss function (5.21), computing the gradients $\partial J/\partial \vec{p}$, $\partial J/\partial \vec{q}$ and $\partial J/\partial \vec{v}$ by means of automatic differentiation and updating the fitting parameters

$$\vec{p}_{j+1} = \vec{p}_j - \beta_{\vec{p}} \frac{\partial J}{\partial \vec{p}} \left(\vec{p}_j, \vec{q}_j, \langle \vec{v}_j \rangle_+\right), \quad \vec{q}_{j+1} = \vec{q}_j - \beta_{\vec{q}} \frac{\partial J}{\partial \vec{q}} \left(\vec{p}_j, \vec{q}_j, \langle \vec{v}_j \rangle_+\right),$$
$$\vec{v}_{j+1} = \vec{v}_j - \beta_{\vec{v}} \frac{\partial J}{\partial \vec{v}} \left(\vec{p}_j, \vec{q}_j, \langle \vec{v}_j \rangle_+\right) \quad \text{and} \quad \vec{w}_{j+1} = \langle \vec{v}_{j+1} \rangle_+. \tag{5.24}$$

Typically, during the offline training, a portion of weights w^i_{K+1} becomes equal to zero and remains zero due to the vanishing gradient. Liu and Wu (2019) removed such sub-trees from the binary tree by deleting nodes and merging the respective subtrees. In this chapter, we compress the binary tree in order to speed-up the training, and eventually, the online evaluation. Figure 5.5 shows a schematic of how to remove laminates from the binary tree. The former illustrates a weighted tree with edge weights corresponding to the propagated weights w^i_k. Remember that the volume fractions of the individual laminates are computed from these weights by normalization.

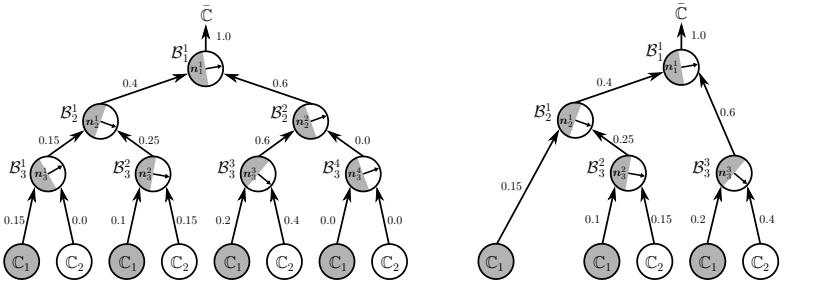

(a) Perfect binary tree **(b)** Binary tree with removed laminates

Figure 5.5: Binary tree compression to speed up offline training and online evaluation. Laminates corresponding to zero weights are removed from the binary tree.

During training, superfluous laminates are removed from the binary tree to minimize the number of computed laminate homogenization steps (5.22). The former happens dynamically during every forward pass. For the example in Figure 5.5, only four out of seven laminate homogenization functions are computed in a forward pass, resulting in a speed-up of about $43\,\%$ compared to a perfect binary tree.

5.3.2 Online evaluation

We seek to employ DMNs to speed up a two-scale simulation, i.e., for every Newton iteration and at every Gauss point of a finite element model, a direct DMN needs to be integrated implicitly. At the same time, we want to account for arbitrary eigenvalues λ_1 and λ_2 of the fiber orientation tensor at every Gauss point of the macroscopic simulation.

We restrict to the two-potential framework of small-strain isothermal GSMs as summarized in Section 3.2. More precisely, we consider the quadruple $(\mathcal{Z}, \psi, \phi, \boldsymbol{z}_0) \in \mathcal{GSM}$ comprising a (Banach) vector space $\mathcal{Z}$ of internal variables, a free energy density $\psi : \mathrm{Sym}_2(d) \times \mathcal{Z} \to \mathbb{R}$, a dissipation potential $\phi : \mathcal{Z} \to \mathbb{R} \cup \{+\infty\}$ and an initial condition $\boldsymbol{z}_0 \in \mathcal{Z}$. Suppose that the two isothermal GSMs $\mathcal{G}_1 = (\mathcal{Z}_1, \psi_1, \phi_1, \boldsymbol{z}_{0,1})$ and $\mathcal{G}_2 = (\mathcal{Z}_2, \psi_2, \phi_2, \boldsymbol{z}_{0,2})$ are given. A time discretization of both phases $i \in \{1, 2\}$ by the implicit Euler method gives rise to the condensed free energy potential $\Psi_i : \mathrm{Sym}_2(d) \times \mathcal{Z}_i \to \mathbb{R}$, see Section 2.5 for more information and a detailed derivation. With the condensed free energy potential Ψ_i at hand, the Cauchy stress is given by the potential relation

$$\boldsymbol{\sigma}_i = \frac{\partial \Psi_i}{\partial \boldsymbol{\varepsilon}} \left(\boldsymbol{\varepsilon}_i, \boldsymbol{z}_i^n \right). \tag{5.25}$$

which only depends on the input strain $\boldsymbol{\varepsilon}_i$ and the internal variables $\boldsymbol{z}_i^n$ of the last (converged) time step.

We consider the displacement jump vector $\vec{\boldsymbol{u}} \in (\mathrm{V}^d)^{2^K - 1}$, which features the same ordering that we used for the vectors $\vec{p}$ and $\vec{q}$, and the vector

of phase strains $\vec{\boldsymbol{\varepsilon}} = [\boldsymbol{\varepsilon}_1, \boldsymbol{\varepsilon}_2, \ldots, \boldsymbol{\varepsilon}_{2^K}] \in \mathrm{Sym}_2(d)^{2^K}$. By introducing the symmetrized gradient operator[2] $\boldsymbol{D}_{\lambda_1\lambda_2} : (\mathrm{V}^d)^{2^K-1} \to \mathrm{Sym}_2(d)^{2^K}$, we express the phase strains

$$\vec{\boldsymbol{\varepsilon}} = \vec{\bar{\boldsymbol{\varepsilon}}} + \boldsymbol{D}_{\lambda_1\lambda_2}\vec{\boldsymbol{u}} \tag{5.26}$$

w.r.t. the macro strain increment $\bar{\boldsymbol{\varepsilon}} \in \mathrm{Sym}_2(d)$ and the unknown displacement jumps $\vec{\boldsymbol{u}}$. Here, the shorthand notation $\vec{\bar{\boldsymbol{\varepsilon}}} = [\bar{\boldsymbol{\varepsilon}}, \bar{\boldsymbol{\varepsilon}}, \ldots, \bar{\boldsymbol{\varepsilon}}] \in \mathrm{Sym}_2(d)^{2^K}$ is used. Indeed, for this chapter, the gradient operator, which encodes the DMN's topology and lamination directions, depends on the fiber orientation parameters λ_1 and λ_2. Since we defined the lamination directions $\boldsymbol{n}_k^i(\lambda_1, \lambda_2)$ to depend on the parameters λ_1 and λ_2 explicitly, the gradient operator depends on the fiber orientation, as well. We account for this situation in our notation by writing $\boldsymbol{D}_{\lambda_1\lambda_2}$. For the application at hand, i.e., integrating a DMN at every Gauss point during a two-scale simulation, the fiber orientation parameters λ_1 and λ_2 are held fixed. Indeed, we assume that the microstructure does not evolve under the applied load.

Let us define the vector of internal variables of the last converged time step $\vec{\boldsymbol{z}}^{\,n} = \left[\boldsymbol{z}_1^n, \boldsymbol{z}_2^n, \boldsymbol{z}_3^n, \ldots, \boldsymbol{z}_{2^K}^n\right] \in \bar{\mathcal{Z}} = (\mathcal{Z}_1 \oplus \mathcal{Z}_2)^{\oplus^{2^K-1}}$ and let $\bar{\Psi} : \mathrm{Sym}_2(d)^{2^K} \times \bar{\mathcal{Z}} \to \mathbb{R}$ be the averaged condensed free energy of the flattened laminate

$$\bar{\Psi}(\vec{\boldsymbol{\varepsilon}}, \vec{\boldsymbol{z}}^{\,n}) = \sum_{i=1}^{2^K} w_{K+1}^i \Psi_i(\boldsymbol{\varepsilon}_i, \boldsymbol{z}_i^n) \quad \text{where} \quad \Psi_i = \begin{cases} \Psi_1, & i \text{ odd}, \\ \Psi_2, & i \text{ even}, \end{cases} \tag{5.27}$$

[2] See Section 4.2.3 for a detailed derivation of the special structure of the symmetrized gradient operator $\boldsymbol{D}_{\lambda_1\lambda_2}$.

alternates between the two given condensed free energies Ψ_1 and Ψ_2. Then, we wish to solve the Euler-Lagrange equation of the DMN

$$\boldsymbol{D}_{\lambda_1\lambda_2}^{\mathsf{T}} \boldsymbol{W} \vec{\boldsymbol{\sigma}}(\vec{\bar{\boldsymbol{\varepsilon}}} + \boldsymbol{D}_{\lambda_1\lambda_2} \vec{\boldsymbol{u}}, \vec{\boldsymbol{z}}^{\,n}) = \boldsymbol{0} \tag{5.28}$$

for the unknown displacement jumps $\vec{\boldsymbol{u}}$, where

$$\vec{\boldsymbol{\sigma}} = [\boldsymbol{\sigma}_1, \ldots, \boldsymbol{\sigma}_{2^K}] \in \mathrm{Sym}_2(d)^{2^K} \quad \text{with} \quad \boldsymbol{\sigma}_i = \frac{\partial \Psi_i}{\partial \boldsymbol{\varepsilon}}(\boldsymbol{\varepsilon}_i, \boldsymbol{z}_i^n) \tag{5.29}$$

is the vector of phase stresses. The weight operator $\boldsymbol{W} : \mathrm{Sym}_2(d)^{2^K} \to \mathrm{Sym}_2(d)^{2^K}$ associates the weights $\vec{w}$ to the corresponding stresses $\vec{\boldsymbol{\sigma}}$. In matrix notation, $\boldsymbol{W}$ is given by a diagonal matrix with the weights w_{K+1}^i on the diagonal.

We solve the Euler-Lagrange equation (5.28) by Newton's method. For an initial guess $\vec{\boldsymbol{u}}_0 \in (\mathrm{V}^d)^{2^K-1}$, the displacement jump vector $\vec{\boldsymbol{u}}$ is iteratively updated $\vec{\boldsymbol{u}}_{j+1} = \vec{\boldsymbol{u}}_j + \beta_j \triangle \vec{\boldsymbol{u}}_j$, where the increment $\triangle \vec{\boldsymbol{u}}_j \in \left(\mathrm{V}^d\right)^{2^K-1}$ solves the linear system

$$\left[\boldsymbol{D}_{\lambda_1\lambda_2}^{\mathsf{T}} \boldsymbol{W} \frac{\partial \vec{\boldsymbol{\sigma}}}{\partial \vec{\bar{\boldsymbol{\varepsilon}}}}(\vec{\bar{\boldsymbol{\varepsilon}}} + \boldsymbol{D}_{\lambda_1\lambda_2} \vec{\boldsymbol{u}_j}, \vec{\boldsymbol{z}}^{\,n}) \boldsymbol{D}_{\lambda_1\lambda_2}\right] \triangle \vec{\boldsymbol{u}}_j = \\ - \boldsymbol{D}_{\lambda_1\lambda_2}^{\mathsf{T}} \boldsymbol{W} \vec{\boldsymbol{\sigma}}(\vec{\bar{\boldsymbol{\varepsilon}}} + \boldsymbol{D}_{\lambda_1\lambda_2} \vec{\boldsymbol{u}_j}, \vec{\boldsymbol{z}}^{\,n}). \tag{5.30}$$

A step size $\beta_j \in (0, 1]$ less than unity may arise by backtracking. The Jacobian $\partial \vec{\boldsymbol{\sigma}} / \partial \vec{\bar{\boldsymbol{\varepsilon}}}$ is a block-diagonal matrix containing the algorithmic tangents of the DMN's input materials, i.e.,

$$\frac{\partial \vec{\boldsymbol{\sigma}}}{\partial \vec{\bar{\boldsymbol{\varepsilon}}}}(\vec{\bar{\boldsymbol{\varepsilon}}}, \vec{\boldsymbol{z}}^{\,n}) = \text{block-diag} \left(\frac{\partial^2 \Psi_1}{\partial \boldsymbol{\varepsilon} \partial \boldsymbol{\varepsilon}}(\boldsymbol{\varepsilon}_1, \boldsymbol{z}_1^n), \ldots, \frac{\partial^2 \Psi_{2^K}}{\partial \boldsymbol{\varepsilon} \partial \boldsymbol{\varepsilon}}(\boldsymbol{\varepsilon}_{2^K}, \boldsymbol{z}_{2^K}^n) \right). \tag{5.31}$$

Upon convergence, the phase strains $\vec{\boldsymbol{\varepsilon}} = \bar{\vec{\boldsymbol{\varepsilon}}} + \boldsymbol{D}_{\lambda_1\lambda_2}\vec{\boldsymbol{u}}$ and, subsequently, the effective stress

$$\bar{\boldsymbol{\sigma}} = \sum_{i=1}^{2^K} w_{K+1}^i \boldsymbol{\sigma}_i(\boldsymbol{\varepsilon}_i, \boldsymbol{z}_i^n) \tag{5.32}$$

are computed by averaging. Alternatively, the expression

$$\bar{\boldsymbol{\sigma}} = [\mathbb{I}_\mathrm{s}, \ldots, \mathbb{I}_\mathrm{s}]^\mathsf{T} \boldsymbol{W} \vec{\boldsymbol{\sigma}}(\bar{\vec{\boldsymbol{\varepsilon}}} + \boldsymbol{D}_{\lambda_1\lambda_2}\vec{\boldsymbol{u}}, \vec{\boldsymbol{z}}^{\,n}) \tag{5.33}$$

may be used for computing the volume average of the phase stresses, where $\boldsymbol{W}$ denotes the weight operator and $[\mathbb{I}_\mathrm{s}, \ldots, \mathbb{I}_\mathrm{s}] \in \mathrm{Sym}_4(d)^{2^K}$, $\mathbb{I}_\mathrm{s} : \mathrm{Sym}_2(d) \to \mathrm{Sym}_2(d)$ stands for a vector of the identity operators on $\mathrm{Sym}_2(d)$.

The algorithmic tangent of the DMN admits the representation

$$\begin{aligned}\bar{\mathbb{C}}^{\text{algo}} = \frac{\partial \bar{\boldsymbol{\sigma}}}{\partial \bar{\boldsymbol{\varepsilon}}} = [\mathbb{I}_\mathrm{s}, \ldots, \mathbb{I}_\mathrm{s}]^\mathsf{T} \boldsymbol{W} \Bigg[&\frac{\partial \vec{\boldsymbol{\sigma}}}{\partial \bar{\vec{\boldsymbol{\varepsilon}}}}(\bar{\vec{\boldsymbol{\varepsilon}}} + \boldsymbol{D}_{\lambda_1\lambda_2}\vec{\boldsymbol{u}}, \vec{\boldsymbol{z}}^{\,n}) \\ &+ \frac{\partial \vec{\boldsymbol{\sigma}}}{\partial \vec{\boldsymbol{\varepsilon}}}(\bar{\vec{\boldsymbol{\varepsilon}}} + \boldsymbol{D}_{\lambda_1\lambda_2}\vec{\boldsymbol{u}}, \vec{\boldsymbol{z}}^{\,n}) \boldsymbol{D}_{\lambda_1\lambda_2} \frac{\partial \vec{\boldsymbol{u}}}{\partial \bar{\boldsymbol{\varepsilon}}} \Bigg]. \end{aligned} \tag{5.34}$$

The expression $\partial\vec{\boldsymbol{\sigma}}/\partial\bar{\boldsymbol{\varepsilon}}$ encodes the vector of algorithmic tangents of the phase materials

$$\frac{\partial \vec{\boldsymbol{\sigma}}}{\partial \vec{\boldsymbol{\varepsilon}}}(\vec{\boldsymbol{\varepsilon}}, \vec{\boldsymbol{z}}^{\,n}) = \left[\frac{\partial^2 \Psi_1}{\partial \boldsymbol{\varepsilon} \partial \boldsymbol{\varepsilon}}(\boldsymbol{\varepsilon}_1, \boldsymbol{z}_1^n), \ldots, \frac{\partial^2 \Psi_{2^K}}{\partial \boldsymbol{\varepsilon} \partial \boldsymbol{\varepsilon}}(\boldsymbol{\varepsilon}_{2^K}, \boldsymbol{z}_{2^K}^n) \right]. \tag{5.35}$$

To evaluate (5.34), the partial derivatives of the strain jumps with respect to the macrostrain $\partial\vec{\boldsymbol{u}}/\partial\bar{\boldsymbol{\varepsilon}}$ need to be determined first. To this end, differentiating the Euler-Lagrange equation (5.28) with respect to the

macrostrain $\bar{\varepsilon}$ yields the linear system

$$\left[\boldsymbol{D}_{\lambda_1\lambda_2}^{\mathsf{T}}\boldsymbol{W}\frac{\partial\vec{\boldsymbol{\sigma}}}{\partial\vec{\boldsymbol{\varepsilon}}}(\vec{\bar{\boldsymbol{\varepsilon}}}+\boldsymbol{D}_{\lambda_1\lambda_2}\vec{\boldsymbol{u}}_j,\vec{\boldsymbol{z}}^{\,n})\boldsymbol{D}_{\lambda_1\lambda_2}\right]\frac{\partial\vec{\boldsymbol{u}}}{\partial\bar{\boldsymbol{\varepsilon}}} = -\boldsymbol{D}_{\lambda_1\lambda_2}^{\mathsf{T}}\boldsymbol{W}\frac{\partial\vec{\boldsymbol{\sigma}}}{\partial\vec{\bar{\boldsymbol{\varepsilon}}}}(\vec{\bar{\boldsymbol{\varepsilon}}}+\boldsymbol{D}_{\lambda_1\lambda_2}\vec{\boldsymbol{u}},\vec{\boldsymbol{z}}^{\,n}), \quad (5.36)$$

which is solved for $\partial\vec{\boldsymbol{u}}/\partial\bar{\varepsilon}$. By comparing Equation (5.36) to Equation (5.30), we observe that both problems share the same linear operator, but with different right hand sides. When using a direct solver, e.g., a Cholesky decomposition, it is recommended to reuse the matrix decomposition for reasons of numerical efficiency.

To reduce the number of degrees of freedom and, thus, to speed up the solution process, we exploit that some weights become zero during training as explained in the previous section. We learned that in the offline training, we can dynamically build a binary tree with simplified topology but identical effective behavior. This is also true for the online evaluation of the DMN. The DMN's topology is encoded by the gradient operator $\boldsymbol{D}_{\lambda_1\lambda_2}$. Deleting laminate blocks from the binary tree is equivalent to deleting the associated rows and columns of $\boldsymbol{D}_{\lambda_1\lambda_2}$.

To illustrate this concept, consider the following example. For a two-phase DMN of depth three as depicted in Figure 5.5a, the symmetrized gradient operator $\boldsymbol{D}_{\lambda_1\lambda_2}$ takes the following (unreduced) form

$$\boldsymbol{D}_{\lambda_1\lambda_2} = \begin{bmatrix} -c_{3,2}^1\boldsymbol{N}_3^1 & \boldsymbol{0} & \boldsymbol{0} & \boldsymbol{0} & -c_{2,2}^1\boldsymbol{N}_2^1 & \boldsymbol{0} & -c_{1,2}^1\boldsymbol{N}_1^1 \\ c_{3,1}^1\boldsymbol{N}_3^1 & \boldsymbol{0} & \boldsymbol{0} & \boldsymbol{0} & -c_{2,2}^1\boldsymbol{N}_2^1 & \boldsymbol{0} & -c_{1,2}^1\boldsymbol{N}_1^1 \\ \boldsymbol{0} & -c_{3,2}^2\boldsymbol{N}_3^2 & \boldsymbol{0} & \boldsymbol{0} & c_{2,1}^1\boldsymbol{N}_2^1 & \boldsymbol{0} & -c_{1,2}^1\boldsymbol{N}_1^1 \\ \boldsymbol{0} & c_{3,1}^2\boldsymbol{N}_3^2 & \boldsymbol{0} & \boldsymbol{0} & c_{2,1}^1\boldsymbol{N}_2^1 & \boldsymbol{0} & -c_{1,2}^1\boldsymbol{N}_1^1 \\ \boldsymbol{0} & \boldsymbol{0} & -c_{3,2}^3\boldsymbol{N}_3^3 & \boldsymbol{0} & \boldsymbol{0} & -c_{2,2}^2\boldsymbol{N}_2^2 & c_{1,1}^1\boldsymbol{N}_1^1 \\ \boldsymbol{0} & \boldsymbol{0} & c_{3,1}^3\boldsymbol{N}_3^3 & \boldsymbol{0} & \boldsymbol{0} & -c_{2,2}^2\boldsymbol{N}_2^2 & c_{1,1}^1\boldsymbol{N}_1^1 \\ \boldsymbol{0} & \boldsymbol{0} & \boldsymbol{0} & -c_{3,2}^4\boldsymbol{N}_3^4 & \boldsymbol{0} & c_{2,1}^2\boldsymbol{N}_2^2 & c_{1,1}^1\boldsymbol{N}_1^1 \\ \boldsymbol{0} & \boldsymbol{0} & \boldsymbol{0} & c_{3,1}^4\boldsymbol{N}_3^4 & \boldsymbol{0} & c_{2,1}^2\boldsymbol{N}_2^2 & c_{1,1}^1\boldsymbol{N}_1^1 \end{bmatrix} \quad (5.37)$$

with the symmetrization operators w.r.t. the lamination direction

$$\boldsymbol{N}_k^i \boldsymbol{u} = \frac{1}{2} \left(\boldsymbol{u} \otimes \boldsymbol{n}_k^i(\lambda_1, \lambda_2) + \boldsymbol{n}_k^i(\lambda_1, \lambda_2) \otimes \boldsymbol{u} \right) \tag{5.38}$$

as building blocks[3]. In comparison, for the example shown in Figure 5.5b, we obtain the (reduced) gradient operator

$$\boldsymbol{D}_{\lambda_1 \lambda_2} = \begin{bmatrix} \mathbf{0} & \mathbf{0} & -c_{2,2}^1 \boldsymbol{N}_2^1 & -c_{1,2}^1 \boldsymbol{N}_1^1 \\ -c_{3,2}^2 \boldsymbol{N}_3^2 & \mathbf{0} & c_{2,1}^1 \boldsymbol{N}_2^1 & -c_{1,2}^1 \boldsymbol{N}_1^1 \\ c_{3,1}^2 \boldsymbol{N}_3^2 & \mathbf{0} & c_{2,1}^1 \boldsymbol{N}_2^1 & -c_{1,2}^1 \boldsymbol{N}_1^1 \\ \mathbf{0} & -c_{3,2}^3 \boldsymbol{N}_3^3 & \mathbf{0} & c_{1,1}^1 \boldsymbol{N}_1^1 \\ \mathbf{0} & c_{3,1}^3 \boldsymbol{N}_3^3 & \mathbf{0} & c_{1,1}^1 \boldsymbol{N}_1^1 \end{bmatrix} \tag{5.39}$$

by deleting the second, seventh and eight row and the first, fourth and sixth column. Indeed, the corresponding strains in $\vec{\boldsymbol{\varepsilon}}$, stresses in $\vec{\boldsymbol{\sigma}}$, weights in $\boldsymbol{W}$ and algorithmic tangents in $\partial \vec{\boldsymbol{\sigma}} / \partial \vec{\boldsymbol{\varepsilon}}$ and $\partial \vec{\boldsymbol{\sigma}} / \partial \bar{\boldsymbol{\varepsilon}}$ need to be removed as well.

5.4 Identifying the DMN surrogate model

5.4.1 Short glass fiber reinforced polyamide

We focus on a short glass fiber reinforced polyamide. We consider E-glass fibers with a length of $L_\mathrm{f} = 200\,\mu\mathrm{m}$ and a diameter of $D_\mathrm{f} = 10\,\mu\mathrm{m}$. The fiber volume fraction is set to $c_\mathrm{f} = 16\,\mathrm{vol}\%$ corresponding to a fiber mass fraction of approximately $30\,\mathrm{wt}\%$. As per Section 4.4.1, the E-glass fibers are isotropic, linear elastic and the matrix is assumed to be governed by J_2-elastoplasticity with an exponential-linear hardening

$$\sigma_\mathrm{Y} = \sigma_0 + k_\infty \varepsilon_\mathrm{p} + (\sigma_\infty - \sigma_0) \left(1 - \exp\left(-\frac{k_0 - k_\infty}{\sigma_\infty - \sigma_0} \varepsilon_\mathrm{p} \right) \right). \tag{5.40}$$

[3] Note that $\boldsymbol{N}_k^i$ depends on the fiber orientation parameters $(\lambda_1, \lambda_2) \in \Lambda$. However, for reasons of clarity, we refrain from writing $\boldsymbol{N}_k^i(\lambda_1, \lambda_2)$.

The mechanical properties used in the simulation are summarized in Table 4.1.

We rely upon the sequential addition and migration (SAM) method of Schneider (2017) for generating periodic volume elements with prescribed volume fraction and second-order fiber orientation tensor. The fiber length L_f, fiber diameter D_f, fiber volume fraction c_f and the axis aligned fiber orientation tensor $\boldsymbol{A}_2$, i.e., λ_1 and λ_2, serve as input parameters for the SAM method. Please note that we only consider fiber orientation states with $\lambda_3 \geq 0.01$, as purely planar fiber orientation states cannot be generated at high filler content essentially for geometric reasons, see Schneider (2017) for a discussion.

5.4.2 Necessary resolution and size of the RVE

For a start, we study the resolution necessary to obtain accurate effective properties in the purely elastic case, see also Gusev (1997); Kanit et al. (2003). For this purpose, we consider cubic microstructures with an edge length of $L = 384\,\mu\mathrm{m}$, i.e., roughly twice the fiber length of $L_\mathrm{f} = 200\,\mu\mathrm{m}$. We compute the effective stiffness with the help of an FFT-based computational micromechanics code (Moulinec and Suquet, 1994; 1998) as described in Schneider (2019a), using the staggered grid discretization (Schneider et al., 2016) and the conjugate gradient solver (Zeman et al., 2010; Brisard and Dormieux, 2010).

We consider the extreme orientations individually, i.e., unidirectional, isotropic and planar isotropic fiber orientation as shown in Figure 5.3, and vary the resolution from 1.7 to 13.3 voxels per fiber diameter in equidistant steps. This corresponds to volume element discretizations with 64^3 to 512^3 voxels. We measure the error relative to the effective stiffness $\bar{\mathbb{C}}$ and choose a resolution of 20 voxels per fiber diameter, i.e., a discretized by 768^3 voxels, as the reference. Figure 5.6a shows the relative error of the effective stiffness computed by the Frobenius norm of the corresponding Voigt matrices. For the crudest resolution, i.e.,

five voxels per fiber diameter, the relative error is well below $2\,\%$ for all three considered fiber orientations. Notice that the relative error for the volume elements with planar isotropic fiber orientation is consistently larger than the error for the unidirectional and isotropic orientations. As expected, the relative error decreases with increasing resolution. At a resolution of 6.7 voxels per fiber diameter, the relative errors of the unidirectional and isotropic fiber orientation fall below $1\,\%$. For 8.3 voxels per fiber diameter, the relative error of the planar isotropic fiber orientation is below $1\,\%$ as well. We consider a resolution of 6.7 voxels per fiber diameter as sufficient, i.e., relative errors below $1\,\%$ for isotropic and unidirectional fiber orientation and an error slightly above $1\,\%$ for the planar isotropic case. We fix this resolution and focus on finding the size of a representative volume element.

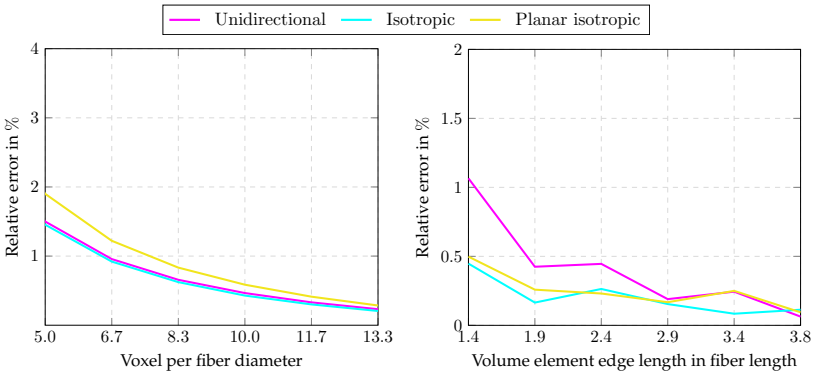

(a) Relative error vs. resolution

(b) Relative error vs. volume element size

Figure 5.6: Relative error of the effective stiffness $\bar{\mathbb{C}}$ for different resolutions (a) and different volume element sizes (b). We consider the three extreme cases of unidirectional, isotropic and planar isotropic fiber orientation. The reference stiffnesses are obtained for a resolution of 20 voxels per fiber diameter (a) and a volume element with edge length of 7.68 fiber lengths (b).

For a resolution of 6.7 voxels per fiber diameter, we investigate volume elements with edge lengths L ranging from 1.44 up to 3.84 fiber lengths corresponding to volume element discretizations with 192^3 up to 512^3 voxels. To obtain our reference, we generated a volume element with edge lengths of 7.68 fiber lengths discretized with 1024^3 voxels. As for studying the necessary resolution, we again consider the relative error in the effective stiffness as our error measure. From Figure 5.6b, we learn that for volume elements with edge lengths of 1.9 fiber length and above, the relative error is well below $0.5\,\%$ and does not further decrease significantly for increasing volume element size. For this reason, we consider volume elements with an edge length of $L = 384\,\mu\mathrm{m}$ as sufficient. To sum up, we finally choose a resolution of 6.7 voxel per fiber length, i.e., a voxel size of $1.5\,\mu\mathrm{m}$ and a discretization with 256^3 voxels, for this chapter.

5.4.3 Discretization of the fiber orientation triangle

To generate the linear elastic training data, we seek to sample from the space of input stiffnesses and fiber orientations uniformly. Apart from sampling input stiffnesses $(\mathbb{C}_1, \mathbb{C}_2) \in \mathrm{Sym}_4^+(d) \times \mathrm{Sym}_4^+(d)$, it is possible to sample the orientations $(\lambda_1, \lambda_2) \in \Lambda$ as well, e.g., via a low-discrepancy sequence such as the Sobol (1967) sequence or via Latin hypercube sampling (McKay et al., 1979). Due to the high dimension of the space $\mathrm{Sym}_4^+(d) \times \mathrm{Sym}_4^+(d)$, we follow the former approach for generating tuples of input stiffnesses. In contrast, the considered fiber orientations are parameterized by a two-dimensional space Λ. For its discretization, we follow geometric considerations.

We discretize the fiber orientation triangle Λ by partitioning it into four self-similar triangles, which may be subsequently partitioned, as well. We select the three points on the vertices of each triangle plus the centers of the triangles as sampling points $(\lambda_1^s, \lambda_2^s)$, where s denotes the sample index. We start with the full orientation triangle shown in Figure 5.7a.

The four sampling points, illustrated by four hollow circles, are located at the three corners and the center of the orientation triangle. After the first splitting, the orientation triangle comprises four triangles and ten points, see Figure 5.7b. After dividing the triangles one more time, we arrive at 31 sampling points. For each of these points in fiber orientation space, we generate a single volume element using the SAM method (Schneider, 2017) with edge lengths $L = 384\,\mu\mathrm{m}$ and a discretization with 256^3 voxels, see Section 5.4.2.

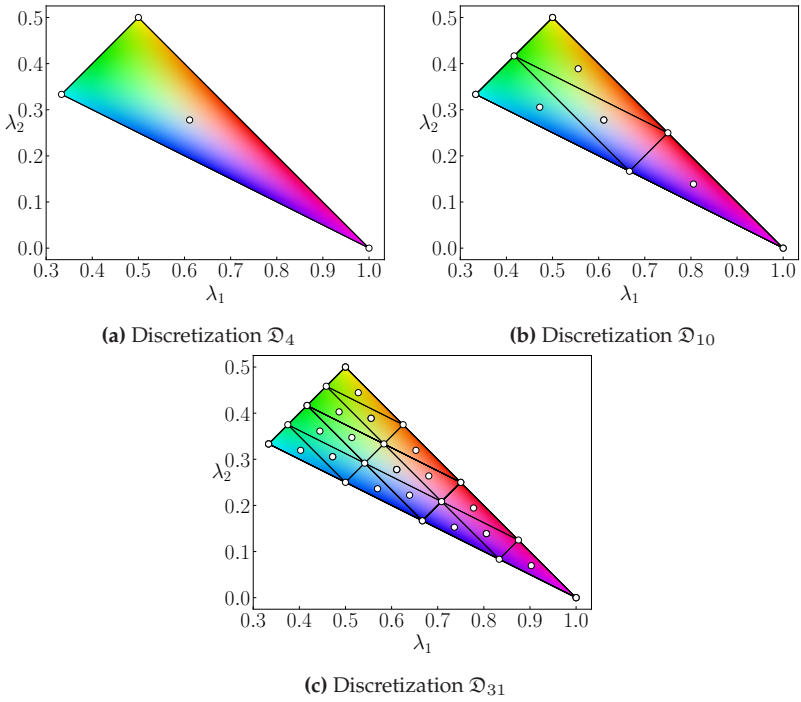

(a) Discretization $\mathfrak{D}_4$

(b) Discretization $\mathfrak{D}_{10}$

(c) Discretization $\mathfrak{D}_{31}$

Figure 5.7: The investigated fiber orientation discretizations: (a) four, (b) ten and (c) 31 sampling points

We consider the discretizations shown in Figure 5.7, i.e., we discretize the orientation triangle with four, ten and 31 sampling points, which we call $\mathfrak{D}_4$, $\mathfrak{D}_{10}$ and $\mathfrak{D}_{31}$, respectively. Choosing the sampling points in a hierarchical manner permits us to re-use already generated volume elements for the next finer discretization. For instance, going from $\mathfrak{D}_{10}$ to $\mathfrak{D}_{31}$ only requires generating 21 new volume elements. This restriction is not imposed by the SAM algorithm since generating volume elements with the given resolution and edge length is just a matter of milliseconds to seconds. In Section 5.4.6, we generate 78 additional volume elements to validate the DMN outside of its training regime and to check if the DMN generalizes sufficiently on the orientation triangle. To this end, we compare the DMNs predicted effective stress to the effective stress obtained by full-field simulations for twelve independent strain paths for every generated volume element and orientation state within the orientation discretization. Obtaining the full-field solutions is computationally expensive. Therefore, being able to reuse the full-field solutions from coarser discretizations for validating the finer discretizations comes in handy to keep the validation effort manageable.

5.4.4 Material sampling

There is some freedom in the selection of appropriate sampling strategies for the training data. For instance, Liu et al. (2019a), Liu and Wu (2019) and Gajek et al. (2020), sampled (axis aligned) orthotropic stiffnesses. We seek to decrease the number of degrees of freedom further, from 17 to 8, by taking into account that the glass fibers are linear elastic and the polyamide matrix is governed by J_2-elastoplasticity. For that reason, we assume that the samples $\mathbb{C}_1$, corresponding to the glass fibers, are isotropic, i.e., the equation

$$\mathbb{C}_1 = 3K_1\,\mathbb{P}_1 + 2G_1\,\mathbb{P}_2 \tag{5.41}$$

holds with the projection operators $\mathbb{P}_1 : \mathrm{Sym}_2(d) \to \mathrm{Sym}_2(d)$ and $\mathbb{P}_2 : \mathrm{Sym}_2(d) \to \mathrm{Sym}_2(d)$ on the spherical and deviatoric subspaces of $\mathrm{Sym}_2(d)$, which read

$$(\mathbb{P}_1)_{mnop} = \frac{1}{3}\delta_{mn}\delta_{op} \quad \text{and} \quad (\mathbb{P}_2)_{mnop} = \frac{1}{2}(\delta_{mo}\delta_{pn} + \delta_{mp}\delta_{on}) - \frac{1}{3}\delta_{mn}\delta_{op} \tag{5.42}$$

in Cartesian coordinates. Secondly, we assume that the samples corresponding to the polyamide matrix are isotropic minus a rank-one perturbation, i.e.,

$$\mathbb{C}_2 = 3K_2\,\mathbb{P}_1 + 2G_2\left(\mathbb{P}_2 - a\,\boldsymbol{N}' \otimes \boldsymbol{N}'\right). \tag{5.43}$$

Here, the tensor $\boldsymbol{N}' \in \mathcal{N}$ is normalized and deviatoric, i.e.,

$$\mathcal{N} = \{\boldsymbol{N} \in \mathrm{Sym}_2(d) \mid \mathrm{tr}\,(\boldsymbol{N}) = 0,\ \|\,\boldsymbol{N}\,\|_{\mathrm{F}} = 1\}. \tag{5.44}$$

The structure of the second stiffness $\mathbb{C}_2$ encompasses the possible algorithmic tangents of J_2-elastoplasticity, see Chapter 3 in Simo and Hughes (1998).

The set of all considered positive definite stiffness tuples $(\mathbb{C}_1, \mathbb{C}_2)$ may be parameterized via

$$\left(K_1, G_1, K_2, G_2, a, \boldsymbol{N}'\right) \in \mathbb{R}^4_{>0} \times [0, 1) \times \mathcal{N}, \tag{5.45}$$

where K_i and G_i have the dimensions of a Young's modulus and a and $\boldsymbol{N}'$ are dimensionless. Since the latter set is unbounded, we restrict to the subset of elements $\left(K_1, G_1, K_2, G_2, a, \boldsymbol{N}'\right)$ with

$$K_1 = 1\,\mathrm{GPa}, \quad G_1 = 10^{g_1}\,\mathrm{GPa}, \quad K_2 = 10^{k_2}\,\mathrm{GPa}, \quad G_2 = 10^{g_2}\,\mathrm{GPa} \tag{5.46}$$

and exponents $g_1, k_2, g_2 \in [-3, 3]$. By fixing the compression modulus K_1, we removed the redundancy due to homothetic rescaling via $(\mathbb{C}_1, \mathbb{C}_2) \mapsto (\lambda\mathbb{C}_1, \lambda\mathbb{C}_2)$ for $\lambda > 0$. For parameterizing $\boldsymbol{N}'$, we make

use of an eigenvalue decomposition $\boldsymbol{N}' = \boldsymbol{Q}\boldsymbol{N}\boldsymbol{Q}^{\mathrm{T}}$ with an orthogonal $\boldsymbol{Q} \in \mathrm{SO}(3)$ and a diagonal $\boldsymbol{N} \in \mathcal{N}$ matrix. We parameterize $\boldsymbol{N}$ by spherical coordinates

$$\boldsymbol{N} = \begin{bmatrix} \sin(\alpha)\cos(\beta) & 0 & 0 \\ 0 & \sin(\alpha)\sin(\beta) & 0 \\ 0 & 0 & \cos(\alpha) \end{bmatrix} \boldsymbol{e}_i \otimes \boldsymbol{e}_j \tag{5.47}$$

ensuring the condition $\| \boldsymbol{N} \|_{\mathrm{F}} = 1$ to hold. To account for the vanishing trace, $\mathrm{tr}(\boldsymbol{N}) = 0$, we eliminate the angle α in Equation (5.47) and arrive at the parameterization

$$\boldsymbol{N} = \frac{1}{\sqrt{\frac{\cos(\beta)\sin(\beta)+1}{2\cos(\beta)\sin(\beta)+1}}} \begin{bmatrix} -\frac{\sqrt{2}\cos(\beta)}{2\cos(\beta)+2\sin(\beta)} & 0 & 0 \\ 0 & -\frac{\sqrt{2}\sin(\beta)}{2\cos(\beta)+2\sin(\beta)} & 0 \\ 0 & 0 & \frac{1}{\sqrt{2}} \end{bmatrix} \boldsymbol{e}_i \otimes \boldsymbol{e}_j \tag{5.48}$$

in terms of a single remaining angle $\beta \in [0, 2\pi]$. As in Section 4.3.1, the special orthogonal group is parameterized via an axis-angle representation

$$\boldsymbol{Q} : \mathrm{V}^3 \to \mathrm{V}^3,\ \boldsymbol{x} \mapsto \cos(\theta)\,\boldsymbol{x} + \sin(\theta)\,\boldsymbol{v} \times \boldsymbol{x} + (1 - \cos(\theta))(\boldsymbol{v} \cdot \boldsymbol{x})\boldsymbol{v}, \tag{5.49}$$

for the axis $\boldsymbol{v} \mathrel{\hat{=}} [\sin(\psi)\cos(\varphi), \sin(\psi)\sin(\varphi), \cos(\psi)]$, and where the conditions $\theta - \sin(\theta) \in [0, \pi]$, $\cos(\psi) \in [-1, 1]$ and $\varphi \in [0, 2\pi]$ hold, see Miles (1965).

To sum up, we consider the following eight degrees of freedom

$$(a, g_1, k_2, g_2, \beta, \theta, \psi, \varphi) \tag{5.50}$$

with their respective domains specified above. To sample the input space evenly, we sample the parameters (5.50) by the Sobol (1967) sequence and subsequently construct the stiffness tensors $(\mathbb{C}_1, \mathbb{C}_2)$.

5.4.5 Offline training

For the offline training, we generate N_s pairs of stiffnesses $\{(\mathbb{C}_1^s, \mathbb{C}_2^s)\}_{s=1}^{N_\mathrm{s}}$ by the protocol described in Section 5.4.4. Then, for every sample s, we assign each stiffness tuple $(\mathbb{C}_1^s, \mathbb{C}_2^s)$ to one of the previously generated volume elements with orientation $(\lambda_1^s, \lambda_2^s)$ in a cyclic fashion, i.e., we set $(\lambda_1^s, \lambda_2^s) \mapsto (\lambda_1^{f(s)}, \lambda_2^{f(s)})$, where $f : \mathbb{N} \to \mathbb{N}$,

$$s \mapsto (s-1) \mod |\mathfrak{D}| + 1 \quad \text{with} \quad \mathfrak{D} \in \{\mathfrak{D}_4, \mathfrak{D}_{10}, \mathfrak{D}_{31}\} \tag{5.51}$$

cycles through the indices of the samples in $\mathfrak{D}_4$, $\mathfrak{D}_{10}$ and $\mathfrak{D}_{31}$, respectively. For instance, for the orientation discretization $\mathfrak{D}_4$, we assign $\left(\mathbb{C}_1^1, \mathbb{C}_2^1\right)$ to the volume element with fiber orientation $\left(\lambda_1^1, \lambda_2^1\right)$, $\left(\mathbb{C}_1^2, \mathbb{C}_2^2\right)$ to the volume element with $\left(\lambda_1^2, \lambda_2^2\right)$ and $\left(\mathbb{C}_1^5, \mathbb{C}_2^5\right)$ to the volume element with $\left(\lambda_1^1, \lambda_2^1\right)$ and so forth. For every quadruple $(\mathbb{C}_1^s, \mathbb{C}_2^s, \lambda_1^s, \lambda_2^s)$, we compute the associated effective stiffness $\bar{\mathbb{C}}^s$ with the help of an FFT-based computational micromechanics code (Moulinec and Suquet, 1994; 1998) as explained in Section 5.4.2.

The generated data $\left\{\left(\bar{\mathbb{C}}^s, \mathbb{C}_1^s, \mathbb{C}_2^s, \lambda_1^s, \lambda_2^s\right)\right\}_{i=1}^{N_\mathrm{s}}$ serves as training data for identifying the DMN. The number of samples depends on the discretization of the orientation triangle and is summarized in Table 5.2. For $\mathfrak{D}_4$, we generate 800 samples in total which corresponds to 200 samples per volume element. To keep the sampling and training effort manageable, we reduce the number of generated samples to 100 and 50 per microstructure when increasing the number of discrete orientations to ten and 31, respectively. For $\mathfrak{D}_4$, $\mathfrak{D}_{10}$ and $\mathfrak{D}_{31}$, we randomly split the pre-computed samples into a training and validation set, comprising $90\,\%$ and $10\,\%$ of the samples. We train the deep material network on mini-batches with a batch size of $N_b = 32$ samples. More precisely, we draw the batches randomly from the training set and drop the last batch, should the remaining batch size be smaller than 32.

	$\mathfrak{D}_4$	$\mathfrak{D}_{10}$	$\mathfrak{D}_{31}$
Total	800	1 000	1 550
Per microstructure	200	100	50
Training set	720	900	1 395
Validation set	80	100	155

Table 5.2: Number of generated samples and training and validation set sizes

We only consider direct DMNs with eight layers. In Chapter 4, we have seen that eight layers are necessary to achieve a sufficient approximation quality, in particular for inelastic computations. We train for $3\,000$ epochs and rely upon the AMSGrad method (Kingma and Ba, 2015; Reddi et al., 2018) combined with the warm restart technique suggested by Loshchilov and Hutter (2017), i.e., we make use of a modulation of the learning rate between a minimum learning rate β_{min} and a maximum learning rate β_{max},

$$\beta : \mathbb{N} \to \mathbb{R}_{\geq 0}, \quad m \mapsto \gamma^m \left(\beta_{\text{min}} + \frac{1}{2} \left(\beta_{\text{max}} - \beta_{\text{min}} \right) \left(1 + \cos\left(\pi \frac{m}{M} \right) \right) \right), \tag{5.52}$$

where $2M$ corresponds to the period and $M = 50$ is chosen. Additionally, we decay the learning rate at a geometric rate with $\gamma = 0.999$.

Since gradient descent is sensitive w.r.t. the proper choice of the step size, we determine the learning rates $\beta_{\vec{p}}$, $\beta_{\vec{q}}$ and $\beta_{\vec{v}}$ by a learning rate sweep as introduced by Smith and Topin (2018). The resulting learning rates are almost identical for all three parameter groups, and, therefore, we set $\beta_{\vec{p}} = \beta_{\vec{q}} = \beta_{\vec{v}} = \beta$ with a maximum learning rate of $\beta_{\text{max}} = 1.5 \cdot 10^{-2}$. The minimum learning rate is chosen to be an order of magnitude smaller than the maximum learning rate, i.e., $\beta_{\text{min}} = 1.5 \cdot 10^{-3}$. We sample the initial weights $\vec{v}_0$ from a uniform distribution on $[0, 1]$ and rescale the weights to sum to unity. The entries of the parameter vectors $\vec{p}_0$ and $\vec{q}_0$ are sampled from a uniform distribution on $[0, 2\pi]$. We set the penalty

parameter of the objective function (5.21) to $\lambda_\mathrm{p} = 10^3$ and choose the exponents to $p = 1$ and $q = 10$.

We assess the accuracy of the fit by the sample-wise error

$$\delta_s = \frac{\left\| \mathcal{DMN}_\Lambda^{\mathcal{L}} \left(\mathbb{C}_1^s, \mathbb{C}_2^s, \lambda_1^s, \lambda_2^s, \vec{p}, \vec{q}, \vec{w} \right) - \bar{\mathbb{C}}^s \right\|_1}{\left\| \bar{\mathbb{C}}^s \right\|_1}, \tag{5.53}$$

where $\| \cdot \|_1$ refers to the Frobenius-1 norm defined by the ℓ^1-norm of the stiffness components in Mandel's notation. Additionally, we use the maximum and mean errors of all samples

$$\delta_\mathrm{max} = \max_s \left(\delta_s \right) \quad \text{and} \quad \delta_\mathrm{mean} = \frac{1}{N_\mathrm{s}} \sum_{s=1}^{N_\mathrm{s}} \delta_s, \tag{5.54}$$

where N_s denotes the number of elements in the training or validation set, depending on the considered scenario.

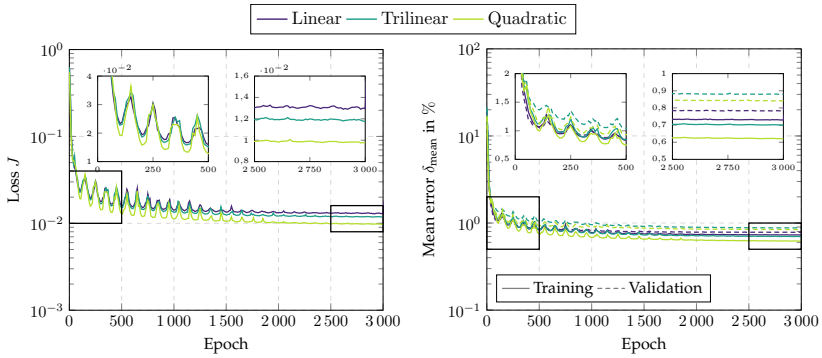

(a) Loss vs. training epoch

(b) Mean error vs. training epoch

Figure 5.8: Loss (a) and mean training and validation errors (b) during training for $\mathfrak{D}_{31}$

In Figure 5.8, the training progress for the $\mathfrak{D}_{31}$ orientation discretization and the investigated linear, trilinear and quadratic orientation inter-

polations is shown. In the first 500 epochs, the effect of the learning rate modulation becomes apparent. The loss and mean error fluctuate noticeably. In the last 500 epochs, the decay of the learning rate ensures convergence of the parameters. Conforming to intuition, increasing the degrees of freedom, i.e., choosing a trilinear or quadratic orientation interpolation over a linear orientation interpolation, decreases the loss at convergence. This trend carries over to the mean training errors as well. For the validation error, however, the linear orientation interpolation provides the best mean validation error. Such phenomena are not uncommon for training deep neural networks, where increasing the degrees of freedom not necessarily yields better generalization and validation results as we will see in Section 5.4.6. As training progresses, no increasing validation errors can be observed for the linear, trilinear and quadratic orientation interpolations. Thus, no significant model over-fitting w.r.t. the linear elastic training data is observed during training.

In Table 5.3, the training results for the investigated orientation discretizations and interpolations are summarized. Additionally, the number of non-zero weights w_{K+1}^i at the end of training are listed. In general, we observe the following trends: Mean and maximum training errors will decrease if a trilinear or quadratic orientation interpolation is chosen instead of a linear interpolation. The same observation holds for the mean validation error with the exception of $\mathfrak{D}_{31}$ and the linear orientation interpolation. The maximum validation error, on the other hand, does not necessarily decrease by introducing additional fitting parameters. Furthermore, the maximum validation error shows significant fluctuations. Indeed, for $\mathfrak{D}_4$ and the linear interpolation, it reaches almost $12\,\%$. Since the maximum validation error is dominated by a single sample, see Figure 4.8 or Figure 4.13 in Section 4.4, we consider the mean validation error to be a more appropriate indicator of the quality of the training results. If we go from $\mathfrak{D}_4$ to $\mathfrak{D}_{10}$ and $\mathfrak{D}_{31}$, the loss as well as

the training and validation errors will increase, in general. Indeed, the DMN has to predict the effective behavior of significantly more volume elements with different fiber orientations and this result does not come unexpected.

		J	$\delta^{\text{train}}_{\text{mean}}$	$\delta^{\text{train}}_{\text{max}}$	$\delta^{\text{valid}}_{\text{mean}}$	$\delta^{\text{valid}}_{\text{max}}$	active weights
$\mathfrak{D}_4$	Linear	$7.378 \cdot 10^{-3}$	0.462 %	1.236 %	0.669 %	7.088 %	71 %
	Trilinear	$6.456 \cdot 10^{-3}$	0.413 %	1.016 %	0.572 %	3.960 %	73 %
	Quadratic	$6.736 \cdot 10^{-3}$	0.431 %	1.054 %	0.563 %	2.948 %	71 %
$\mathfrak{D}_{10}$	Linear	$1.026 \cdot 10^{-2}$	0.638 %	1.610 %	0.982 %	11.982 %	70 %
	Trilinear	$9.109 \cdot 10^{-3}$	0.587 %	1.266 %	0.698 %	4.933 %	70 %
	Quadratic	$8.156 \cdot 10^{-3}$	0.541 %	1.127 %	0.665 %	2.969 %	68 %
$\mathfrak{D}_{31}$	Linear	$1.296 \cdot 10^{-2}$	0.730 %	2.173 %	0.783 %	3.935 %	67 %
	Trilinear	$1.175 \cdot 10^{-2}$	0.700 %	1.928 %	0.879 %	6.018 %	65 %
	Quadratic	$9.757 \cdot 10^{-3}$	0.620 %	1.361 %	0.841 %	7.051 %	68 %

Table 5.3: Training results of the interpolated direct DMNs for the investigated orientation interpolations and orientation discretizations

5.4.6 Online evaluation

We implement Newton's method, as described in Section 5.3.2, as a user-material subroutine in ABAQUS. In terms of implementation, the major difference compared to Chapter 4 is that, for this chapter, the gradient operator depends on the fiber orientation parameters λ_1 and λ_2, see Section 5.3.2. This does not infer any additional challenges, since the microstructure characteristics do not change during computation. Both parameters λ_1 and λ_2 are fixed during the online evaluation, and after assembling $\boldsymbol{D}_{\lambda_1\lambda_2}$, the effective stress $\bar{\boldsymbol{\sigma}}$ and algorithmic tangent $\bar{\mathbb{C}}^{\text{algo}}$ are computed by Newton's method in the proposed manner. For a summary of the main steps of the algorithm, i.e., computing phase strains and stresses, updating the displacement jumps, updating internal variables and computing the DMN's effective stress, we refer to Algorithm 1 in

Chapter 4 where the pseudo-code for the implementation of the online evaluation can be found.

Our goal in Section 5.5 is to employ deep material networks in a two-scale simulation using ABAQUS. For this purpose, we seek to speed up the inelastic computations as much as possible. As a first step, the elimination procedure described in Section 5.3 proves effective. The deleting is performed in an upstream pre-processing step after the offline training to avoid unnecessary computational overhead. Secondly, we exploit the sparsity pattern of all involved linear operators, i.e., the sparsity pattern of the gradient operator $\boldsymbol{D}_{\lambda_1\lambda_2}$ and the Jacobian $\partial\vec{\boldsymbol{\sigma}}/\partial\vec{\boldsymbol{\varepsilon}}$, containing the algorithmic tangents of the phases. To this end, we rely upon the Eigen3 library (Guennebaud et al., 2010) for all linear algebra operations and use sparse matrices whenever possible. For Newton's method, we use the following convergence criterion

$$\frac{\left\| \boldsymbol{D}_{\lambda_1\lambda_2}^{\mathsf{T}} \boldsymbol{W} \vec{\boldsymbol{\sigma}}(\vec{\bar{\boldsymbol{\varepsilon}}}^{\,n+1} + \boldsymbol{D}_{\lambda_1\lambda_2} \vec{\boldsymbol{u}}^{\,n+1}, \vec{\boldsymbol{z}}^{\,n}) \right\|_{\mathrm{F}}}{(2^K - 1) \left\| \bar{\boldsymbol{\sigma}}^{\,n+1} \right\|_{\mathrm{F}}} \leq \mathrm{tol}, \tag{5.55}$$

where we set the tolerance tol to 10^{-12} and $\|\cdot\|_{\mathrm{F}}$ refers to the Frobenius norm defined by the ℓ^2-norm of the involved matrices in Mandel's notation. We solve the linear system by means of a sparse Cholesky decomposition.

Before employing the DMN in a two-scale simulation, we turn our attention to validating the identified surrogate model. To investigate whether direct DMNs are capable of accurately predicting the effective stress outside of the training regime, additional orientations $(\lambda_1, \lambda_2) \in \Lambda$ are sampled and the respective volume elements are generated. We use $\mathfrak{D}_4$ as our point of departure and subdivide the orientation triangle three more times yielding 105 additional orientations (λ_1, λ_2). For $\mathfrak{D}_{10}$ and $\mathfrak{D}_{31}$, we subdivide the orientation triangle two and one more times, giving rise to 99 and 78 additional points (λ_1, λ_2), respectively.

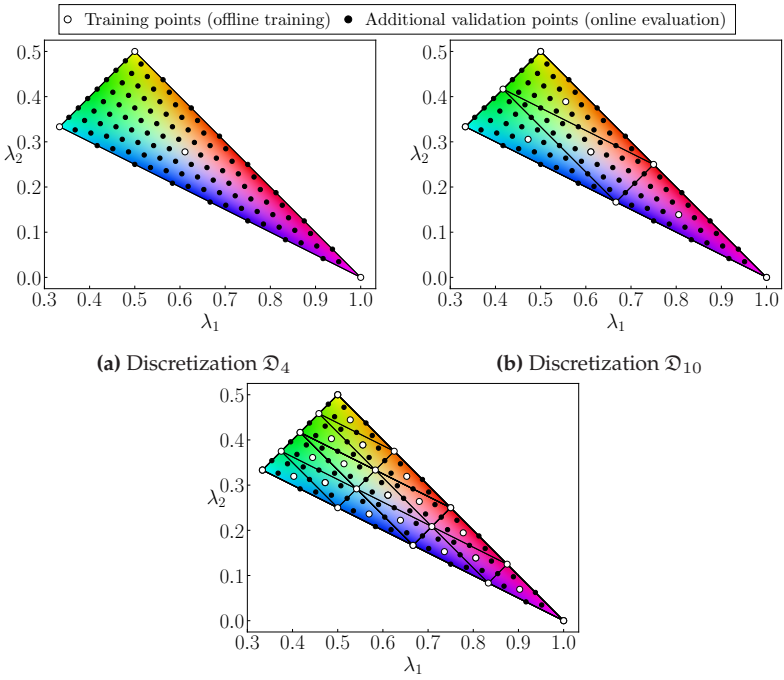

(a) Discretization $\mathfrak{D}_4$

(b) Discretization $\mathfrak{D}_{10}$

(c) Discretization $\mathfrak{D}_{31}$

Figure 5.9: Investigated fiber orientation discretizations comprising volume elements used in offline training and additionally generated volume elements for the online validation: (a) four training and 105 validation, (b) ten training and 99 validation and (c) 31 training and 78 validation points

In Figure 5.9, for all three discretizations, the sampled orientations (λ_1, λ_2) used for obtaining the training data (hollow circles) and exclusively used for the inelastic validations (black filled circles) are shown. For every additional point (λ_1, λ_2), we generated a volume element using the SAM method (Schneider, 2017). We keep using the volume elements already generated for offline training such that we have 109 generated volume elements in total for $\mathfrak{D}_4$, $\mathfrak{D}_{10}$ and $\mathfrak{D}_{31}$.

Using the material parameters of the short fiber reinforced polyamide given in Section 5.4.1, we investigate six independent uniaxial strain loadings

$$\begin{aligned} \bar{\boldsymbol{\varepsilon}} &= \frac{\bar{\varepsilon}}{2} \left(\boldsymbol{e}_i \otimes \boldsymbol{e}_j + \boldsymbol{e}_j \otimes \boldsymbol{e}_i \right), \\ (i,j) \in \mathcal{I}_1 &= \{(1,1),(2,2),(3,3),(2,3),(1,3),(1,2)\}. \end{aligned} \tag{5.56}$$

For every uniaxial strain loading direction in the index set $\mathcal{I}_1$, a full hysteresis with a strain amplitude of $\bar{\varepsilon} = 2.5\,\%$ over a time of $T = 4\,\mathrm{s}$ is computed in 80 equidistant load steps to account for load reversal. To consider more complex loading conditions, we investigate six independent biaxial strain loadings

$$\begin{aligned} \bar{\boldsymbol{\varepsilon}} &= \bar{\varepsilon}_1 \, \boldsymbol{e}_i \otimes \boldsymbol{e}_i + \bar{\varepsilon}_2 \, \boldsymbol{e}_j \otimes \boldsymbol{e}_j, \\ (i,j) \in \mathcal{I}_2 &= \{(1,2),(1,3),(2,1),(2,3),(3,1),(3,2)\} \end{aligned} \tag{5.57}$$

over a time of $T = 2\,\mathrm{s}$ and computed in 40 equidistant load steps. For every biaxial loading direction in the index set $\mathcal{I}_2$, a strain loading of $\bar{\varepsilon}_1 = 1.77\,\%$ is applied while the strain in the second direction is held constant $\bar{\varepsilon}_2 = 0\,\%$. After the load in the first direction is applied, a strain loading of $\bar{\varepsilon}_2 = 1.77\,\%$ is applied in the second direction as well. Both for the uniaxial and biaxial simulations, mixed boundary conditions (Kabel et al., 2016), i.e., stress free loading perpendicular to the loading direction, are used. As reference, we compute the volume elements' effective stress $\bar{\boldsymbol{\sigma}}^{\mathrm{FFT}}$ by means of an FFT-based computational micromechanics (Moulinec and Suquet, 1994; 1998) code and use an Eyre-Milton solver (Eyre and Milton, 1999; Schneider et al., 2019). To evaluate the approximation error in a quantitative way, we introduce the following error measures. For a fixed fiber orientation (λ_1, λ_2), we

define the relative error in the stress component (i, j) as

$$\eta_{ij,\lambda_1\lambda_2}(t) = \frac{\left|\bar{\sigma}^{\text{DMN}}_{ij,\lambda_1\lambda_2}(t) - \bar{\sigma}^{\text{FFT}}_{ij,\lambda_1\lambda_2}(t)\right|}{\max\limits_{\tau\in\mathcal{T}}\left|\bar{\sigma}^{\text{FFT}}_{ij,\lambda_1\lambda_2}(\tau)\right|}, \tag{5.58}$$

where $\mathcal{T} = [0, T]$ denotes the considered time interval. Furthermore, the mean and the maximum errors are defined by

$$\eta^{\text{mean}}_{\lambda_1\lambda_2} = \max_{i,j\in\{1,2,3\}} \frac{1}{T}\int_0^T \eta_{ij,\lambda_1\lambda_2}(t)\ \mathrm{d}t \tag{5.59}$$

and

$$\eta^{\text{max}}_{\lambda_1\lambda_2} = \max_{i,j\in\{1,2,3\}} \max_{t\in\mathcal{T}} \eta_{ij,\lambda_1\lambda_2}(t), \tag{5.60}$$

respectively.

For each of the sampled 109 fiber orientation states, we compute the previously mentioned twelve independent loading paths and evaluate these error measures. The resulting mean and maximum errors for all orientations are shown in Figure 5.10, for $\mathfrak{D}_{31}$ and the linear orientation interpolation. Comparing Figure 5.10a and 5.10b, we observe that the mean error fluctuates less on the orientation triangle than the maximum error, in particular in the vicinity of the isotropic fiber orientation state. The maximum relative error attains its maximum value of around $5.5\,\%$ for the unidirectional fiber orientation state. The mean error, on the other hand, fluctuates less and attains its maximum also for the unidirectional case. Still, with a maximum error of $5.5\,\%$, the DMN is capable of predicting the effective stress for all investigated 109 discrete fiber orientation states with sufficient accuracy.

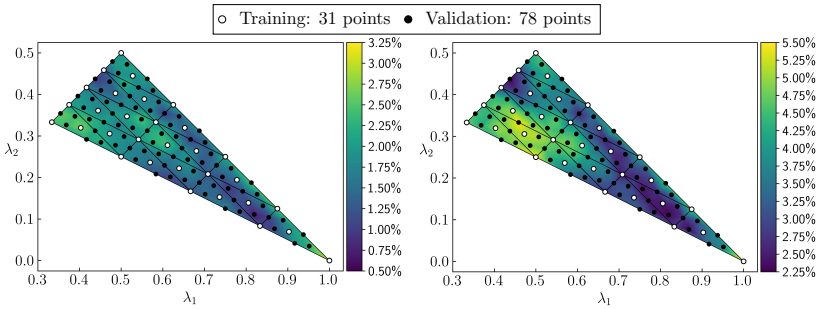

(a) Distribution of mean error $\eta^{\text{mean}}_{\lambda_1\lambda_2}$ **(b)** Distribution of maximum error $\eta^{\text{max}}_{\lambda_1\lambda_2}$

Figure 5.10: Distribution of mean (a) and maximum (b) error on the orientation triangle for $\mathfrak{D}_{31}$ and the linear orientation interpolation

Figure 5.11 gives an impression of how the mean and maximum errors shown in Figure 5.10 translate into actual stress-time curves. For the three extreme cases and a uniaxial extension in the e_1-direction, the 11-component of the effective stress predicted by the DMN and computed by an FFT-solver is shown in Figure 5.11a. For isotropic and planar isotropic fiber orientations, the DMN's effective stress $\bar{\sigma}^{\text{DMN}}_{11}$ and the full-field solution $\bar{\sigma}^{\text{FFT}}_{11}$ are almost indistinguishable. Even for the unidirectional fiber orientation, which exhibits the previously mentioned maximum error of $5.5\,\%$, $\bar{\sigma}^{\text{DMN}}_{11}$ and $\bar{\sigma}^{\text{FFT}}_{11}$ show a good agreement. In Figure 5.11b, the stress components for a biaxial extension in the e_1- and the e_2-direction are illustrated. As noted previously, we observe the largest relative error for the unidirectional fiber orientation, whereas the predictions of DMN and FFT for isotropic and planar isotropic fiber orientations are almost indistinguishable.

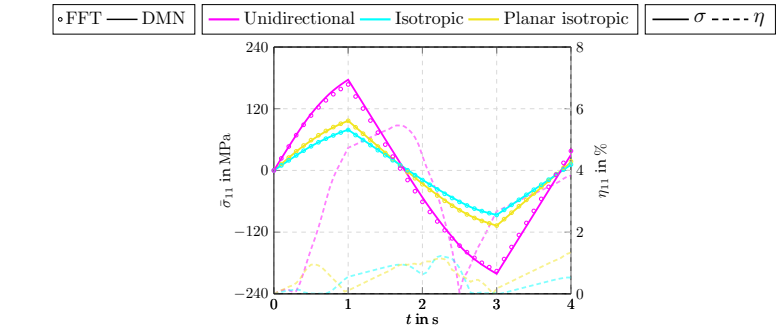

(a) Uniaxial extension in e_1-direction

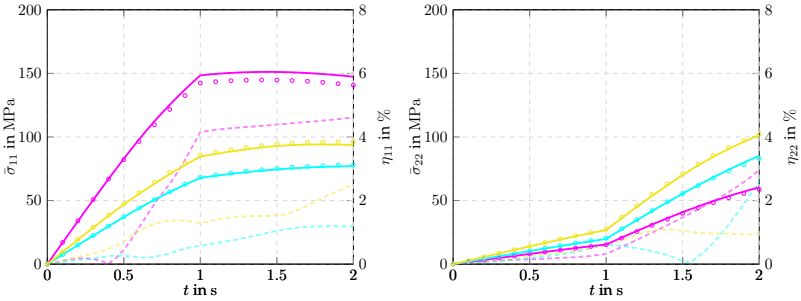

(b) Biaxial extension in e_1- and e_2-direction

Figure 5.11: Comparing the effective stresses predicted by the DMN and computed by an FFT-based micromechanics solver for a uniaxial (a) and a biaxial (b) extension for the three extreme fiber orientation states

Figure 5.12 summarizes the minimum, mean and maximum of the individual error measures w.r.t. the fiber orientation (λ_1, λ_2) for $\mathfrak{D}_4$, $\mathfrak{D}_{10}$, $\mathfrak{D}_{31}$ and linear, trilinear and quadratic orientation interpolations.

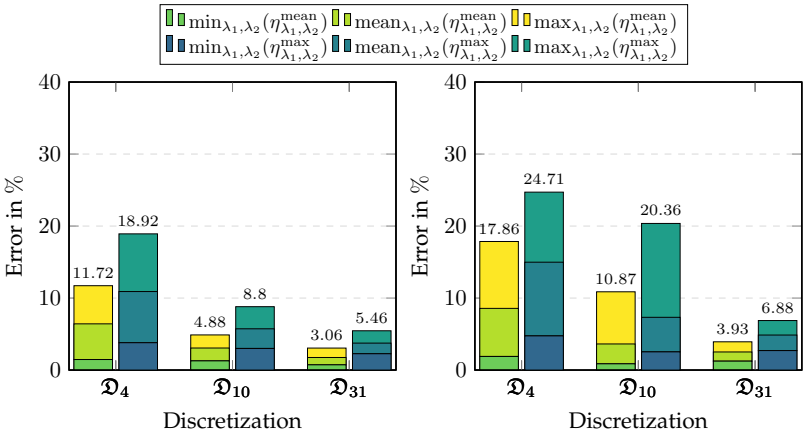

(a) Linear interpolation

(b) Trilinear interpolation

(c) Quadratic interpolation

Figure 5.12: Minimum, mean and maximum errors for the three considered orientation interpolations

Figure 5.12, which compares 11 772 computed DMN load paths with 1 308 full-field simulations, permits us to draw the following conclusions: For fixed type of orientation interpolation, a finer orientation discretization reduces the mean and maximum errors. The dependence of the mean and maximum error on the polynomial degree is more

complicated. Compared to the linear orientation interpolation, both the mean and the maximum error increase significantly for the trilinear and the quadratic interpolations. The former holds true for $\mathfrak{D}_4$, $\mathfrak{D}_{10}$ and $\mathfrak{D}_{31}$. Similar to the offline training, the loss and training errors decrease for higher order interpolations. Only the validation errors shows a slight increase. This suggests an overfitting with respect to the orientation interpolation, so that the linear approaches to the orientation interpolation is recommended, in the end.

5.5 A computational example

After validating that the DMN is able to provide sufficiently accurate results, we turn our attention to a component of industrial complexity. We choose a quadcopter frame, see Figure 5.1b, whose CAD geometry is publicly available (GrabCAD, 2022). We assume that the arms of the quadcopter are manufactured by injection molding. To obtain realistic fiber orientation data, we conducted a mold filling simulation for a single quadcopter arm and utilize the generated data for all four identical quadcopter arms. We use the publicly available software InjectionMoldingFoam (Ospald, 2014), which is based upon the two-phase, incompressible flow solver of OpenFOAM (Weller et al., 1998). We choose identical settings and material parameters as Köbler et al. (2018), i.e., we assume a homogeneous fiber volume fraction and select the following Carreau-WLF equation (Kennedy, 2013)

$$\mu(\theta, \dot{\gamma}) = \mu_0 \frac{e^{-A_2(\theta-\theta_{\text{ref}})}}{(1+(A_0\dot{\gamma})^2)^{\frac{1-A_1}{2}}}. \tag{5.61}$$

Here, θ denotes the absolute temperature and $\dot{\gamma}$ refers to the norm of the strain-rate tensor. The parameters for the injection molding simulation are summarized in Table 5.4 and originally stem from Bhat et al. (2014).

Mass density:	$1410\,\mathrm{kg/m^3}$
Injection temperature:	$548.15\,\mathrm{K}$
Mold temperature:	$313.15\,\mathrm{K}$
Heat capacity at constant pressure:	$2400\,\mathrm{J/(K\,kg)}$
Thermal conductivity:	$0.25\,\mathrm{W/(m\,K)}$
Initial fiber orientation distribution:	Isotropic
Fiber aspect ratio:	20
Folger-Tucker interaction coefficient:	0.01
Particle number:	0
Glass transition temperature θ_{ref}:	$503.15\,\mathrm{K}$
A_0:	$0.1\,\mathrm{s}$
A_1:	0.65
A_2:	$0.021\,1/\mathrm{K}$
Reference shear viscosity μ_0:	$100\,\mathrm{Pa\,s}$

Table 5.4: Parameters used for the injection molding simulation (Bhat et al., 2014)

The results of the injection molding simulation are shown in Figure 5.13, both for a top and a side view, and at three distinct instances of time, corresponding to a volume coverage of $50\,\%$, $75\,\%$ and $100\,\%$, respectively. The computed fiber orientations are represented by the color scale shown in Figure 5.3. We observe that, at the flow fronts, planar and isotropic fiber orientations dominate. For the rest of the drone arm, fiber orientations close to the unidirectional case are prevalent. Figure 5.13d illustrates the principal fiber orientations, i.e., the eigenvector corresponding to the largest eigenvalue of $\boldsymbol{A}_2$, after the mold is filled. As a result of the location of the injection points, pronounced weld lines formed on the left of the center of the drone arm, see Figure 5.13c.

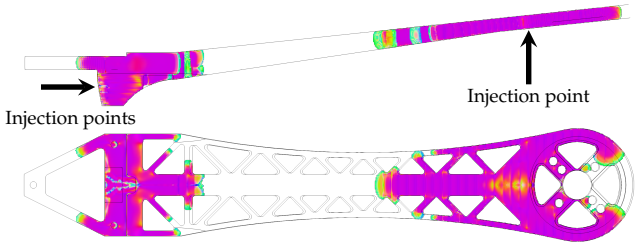

(a) Volume coverage of 50 %

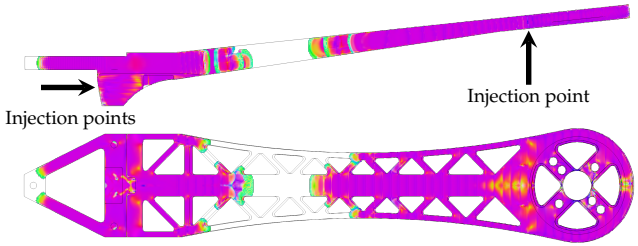

(b) Volume coverage of 75 %

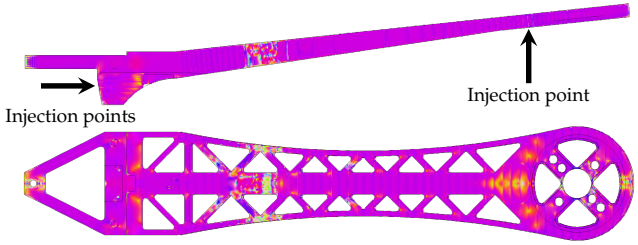

(c) Volume coverage of 100 %

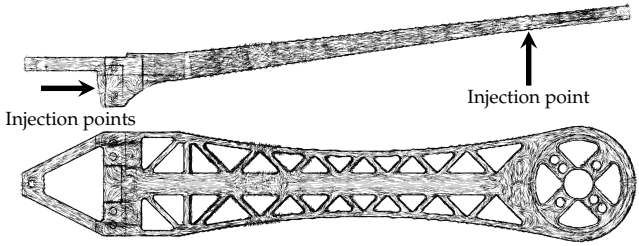

(d) Principal fiber orientation

Figure 5.13: Injection molding simulation results for 50 % (a), 75 % (b) and 100 % (c) volume coverage and principal fiber orientations (d) after filling

With the material behavior reported in Section 5.4.1, we perform a structural two-scale simulation on a single drone arm using ABAQUS. We mesh the drone arm by quadratic tetrahedron elements and investigate five different mesh densities ranging from 63 580 up to 1 005 862 elements in order to analyze convergence, wall-clock time and memory consumption, see Table 5.8. The computed fiber orientation tensors serve as the input for the simulation, i.e., the eigenvectors of $\boldsymbol{A}_2$ are mapped onto the ABAQUS mesh and determine the material orientation. The eigenvalues λ_1 and λ_2 are provided to the DMN subroutine via pre-defined fields. We apply a loading of $F = 80\,\mathrm{N}$ on the motor mount via a surface force and fix the left side of the drone arm, see Figure 5.14. The loading is applied in ten equidistantly spaced time increments.

Figure 5.14 shows the results for the finest discretization of about one million tetrahedron elements. In the top Figure 5.14a, the von Mises stress distribution for the last time increment and for an assumed homogeneous and isotropic fiber orientation $(\lambda_1, \lambda_2) \equiv (0.\overline{33}, 0.\overline{33})$ is shown. The bottom Figure 5.14b shows the computed stress for the mapped anisotropic, inhomogeneous fiber orientation. Running on two AMD EPYC 7642, both simulations took about $165\,\mathrm{min}$ to complete on 96 threads and required $133\,\mathrm{GB}$ of DRAM.

For the mapped anisotropic fiber orientation, stress fluctuations, especially in the vicinity of weld lines are clearly visible. In contrast, stress and strain concentrations at weld lines cannot be predicted for a homogeneous fiber orientation. Accounting for the entire process chain appears imperative in order to exploit the full lightweight potential of injection molded fiber reinforced components, as becomes evident when comparing the predicted total deflections. Indeed, for the assumed isotropic fiber orientation, the macro simulation predicts a deflection of $6.13\,\mathrm{mm}$. A deflection of $3.99\,\mathrm{mm}$ is predicted for the anisotropic fiber distribution. Thus, the isotropic variant underestimates the actual stiffness of the component by a factor of two.

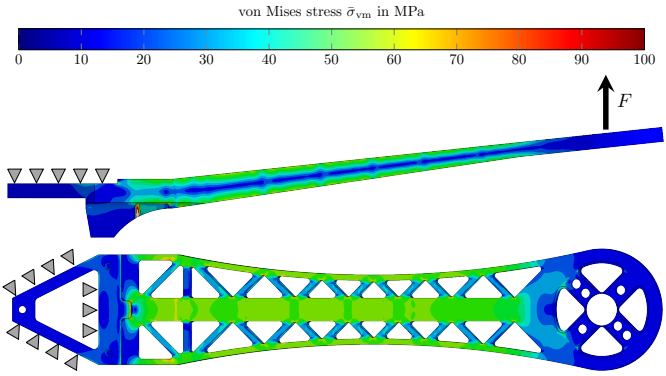

(a) Homogeneous isotropic fiber orientation

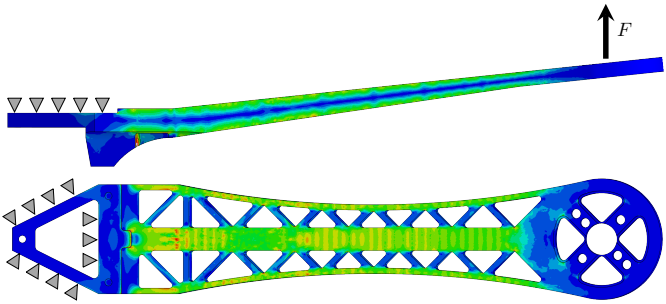

(b) Mapped anisotropic fiber orientation

Figure 5.14: Side and top view of the simulated drone arm for a homogeneous, isotropic fiber orientation (a) and the mapped anisotropic fiber orientation (b) from the injection molding simulation

To demonstrate the capabilities of the introduced multiscale method, we investigate the entire drone frame in a mechanical simulation, see Figure 5.15. The four drone arms are manufactured from injection molded, short fiber reinforced polyamide with mapped anisotropic fiber orientation. An interpolated direct DMN is integrated at every Gauss point. Both the upper and lower plates, which the drone arms are attached to, are made of aluminum. For this material, we use a

J_2-elastoplasticity model (Simo and Hughes, 1998) with power law hardening

$$\sigma_{\mathrm{Y}} = \sigma_0 + k\,\varepsilon_{\mathrm{p}}^{m}. \tag{5.62}$$

The material parameters, i.e., Young's modulus E, Poisson's ratio ν and hardening parameters σ_0, k and m are taken from Segurado et al. (2002) and summarized in Table 4.2.

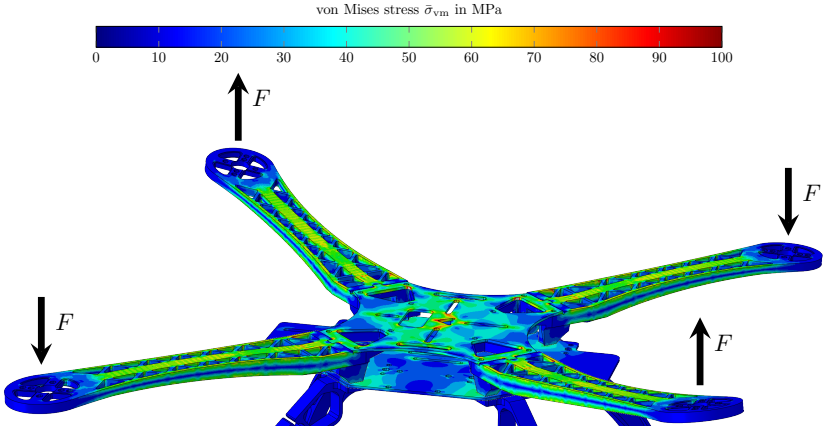

Figure 5.15: Simulated quadcopter drone frame

We assume the drone legs to be made of pure polyamide. For the latter, we assign a linear elastic material behavior, see Table 4.1. The simulation model consists of about two million elements with almost ten million degrees of freedom, see Table 5.9. The drone arms are loaded as shown in Figure 5.15 with a force of $F = 80\,\mathrm{N}$. The loading is applied in ten equidistantly spaced load steps. The simulation took about $4.5\,\mathrm{h}$ wall-clock time, running on 96 threads in parallel.

5.6 Computational cost

Last but not least, we discuss the computational cost of deep material networks accounting for the offline training and online evaluation separately. All computations were performed on a workstation equipped with two AMD EPYC 7642 with 48 physical cores each, enabled SMT and 1024 GB of DRAM.

The material sampling was performed in parallel, i.e., we computed six load steps in parallel using 16 threads for each individual simulation. All direct DMNs were trained in parallel on 4 threads each. The wall-clock times of the material sampling and the offline training are summarized in Table 5.5 and Table 5.6.

$\mathfrak{D}_4$	$\mathfrak{D}_{10}$	$\mathfrak{D}_{31}$
21.48 h	27.02 h	42.43 h
(800 samples)	(1 000 samples)	(1 550 samples)

Table 5.5: Wall-clock times for sampling the linear elastic training data

Apparently, the sampling and offline training effort increases linearly with the number of samples. Incidentally, the number of fitting parameters, which varies depending on the type of the orientation interpolation, has no significant influence on the runtime of the offline training.

Turning our attention to the online evaluation, we focus on the computational costs of the DMN evaluated at a single Gauss point. Integrating an interpolated direct DMN at a single Gauss point for a prescribed macro strain increment takes about 2 ms on a single thread, see Table 5.7. This is about 120 000 times faster than conducting a full-field simulation on a microstructure discretized by 256^3 voxels using an FFT-based computational micromechanics solver, also running on a single thread.

We exclusively considered DMNs with eight layers. For applications which permit using DMNs with a smaller number of layers, even higher speed-up factors may be reached.

	Wall-clock time			#FP
	$\mathfrak{D}_4$	$\mathfrak{D}_{10}$	$\mathfrak{D}_{31}$	
Linear	2.43 h	3.18 h	4.60 h	1 020
Trilinear	2.58 h	3.30 h	4.60 h	1 275
Quadratic	2.50 h	3.18 h	4.62 h	1 785

Table 5.6: Wall-clock times and number of fitting parameters (#FP) for training the interpolated direct DMNs

	FFT (1 thread)	DMN (1 thread)
Wall-clock time	242.69 s	2.03 ms
Speed-up	–	119 552
#DOF	6×256^3	513

Table 5.7: Wall-clock time, speed-up (compared to an FFT-base computational micromechanics solver) and degrees of freedom (#DOF) for a single time step of the inelastic micro simulation

Next, we focus on the component scale simulation of the quadcopter arm. The wall-clock times of all five examined discretizations ranging from 63 580 up to 1 005 862 quadratic tetrahedron elements and, computed on 96 threads, are summarized in Table 5.8. We observe that the DRAM footprint is roughly proportional to the number of elements. The wall-clock times, however, increase super-linearly. We attribute this effect to the complexity of the direct solver used by ABAQUS.

Apparently, the applicability of the method is more restricted by the memory requirements, and the computational effort plays a minor role. The required DRAM depends on the number of internal variables to be stored. For a DMN of eight layers, linear elastic fibers and an elastoplastic matrix, $128 \times (1 + 5) = 768$ floating-point numbers need to be stored for every Gauss point. To improve the convergence of Newton's method, the displacement jumps of the last converged time step are stored as well, i.e., $768 + 255 \times 3 = 1\,533$ scalars need to be kept in memory. Since we rely upon the thinned binary tree as introduced in Section 5.3.2, $1\,533$ serves as an upper bound. For the application at hand, the actual number of internal variables of the DMN surrogate model is $1\,297$. ABAQUS requires no more than two Newton iterations per load step, indicating a robust quadratic convergence independent of the mesh size. The slight increase from 1.8 to 2.0 Newton iterations per load step is minimal, and may be a result of the increased plastification of the material in the vicinity of finely resolved geometric features of the component.

	ABAQUS (96 threads)				
Elements	63 580	121 416	247 444	488 689	1 005 862
#DOF	308 987	572 688	1 134 597	2 194 091	4 418 695
Wall-clock time	9 min	15 min	32 min	63 min	165 min
Memory consumption	9 GB	15 GB	33 GB	62 GB	133 GB
Total Newton iterations	18	18	19	20	20

Table 5.8: Wall-clock time, memory consumption and total Newton iterations of the single drone arm for different mesh sizes

To analyze the drone arm, using less than one million elements for the discretization would be sufficient. Rather, by choosing such a fine discretization, we demonstrate that DMN-accelerated two-scale

simulations easily scale to components with high complexity. The hardware requirements implicated by Table 5.8 can be provided by any state-of-the-art workstation.

Computing all ten load steps on 96 threads for the entire quadcopter frame took 22 Newton iterations, 267 min and required 252 GB or DRAM, see Table 5.9. This corresponds to over two million elements and about ten million degrees of freedom.

Part	Materials	Discretization	
Arms	DMN	$4 \times 488\,689$	Quad. tetrahedron
Bottom plate	Aluminum	39 422	Quad. hexahedron
Top plate	Aluminum	19 028	Quad. hexahedron
Legs	Polyamide	$4 \times 20\,054$	Quad. tetrahedron
Total	-	2 093 422	-
#DOF			9 378 683
Wall-clock time			267 min
Memory consumption			252 GB
Total Newton iterations			22

Table 5.9: Wall-clock time, memory consumption and total Newton iterations for the simulation of the entire quadcopter frame

5.7 Conclusion

We investigated the capabilities of direct DMNs to provide a digital twin for short fiber reinforced plastic microstructures, which can be used in concurrent multiscale simulations. To realize the full lightweight potential of short fiber reinforced components, it is imperative to account for the locally varying fiber orientation in mechanical simulations on component scale.

Building upon the work of Köbler et al. (2018), we proposed a robust and computationally efficient approach to utilize direct DMNs for variable fiber orientations. Instead of identifying multiple deep material networks and interpolating the effective stress, we interpolated the DMN's microstructure characteristics on the fiber orientation triangle. Assuming that the local fiber volume fractions of the individual laminates in the hierarchy are independent of the local fiber orientation, it suffices to fix the fiber volume fraction and to interpolate the lamination directions only. This procedure gives rise to a single DMN surrogate model covering all fiber orientations. Presumably, the scheme easily extends to incorporating local variations in the fiber volume fraction by interpolating the DMN's volume fractions as well, see Chapter 6. By sampling the training data from up to 31 microstructure realizations with different fiber orientation, we fitted the DMN to multiple fiber orientations simultaneously. Subsequently, we showed that the DMN generalizes to the entire fiber orientation triangle with small error, also for the inelastic regime.

To evaluate the ensuing performance of our approach, we simulated the entire process chain of a quadcopter frame starting from an injection molding simulation. We mapped the computed fiber orientations upon a finite element mesh of the complete quadcopter frame and conducted a DMN-accelerated two-scale simulation of the full component. Our results indicate that direct DMNs enable two-scale simulations of structures with industrial complexity with moderate hardware requirements.

Chapter 6

Estimating process-induced uncertainties in sheet molding compound composites[1]

6.1 Introduction

Sheet molding compound (SMC) is a discontinuous fiber reinforced polymer material that is available in the form of sheets which are pre-impregnated with a thermoset resin. The manufacturing process leads to a random planar orientation distribution of bundled fibers in the prepreg sheets. These sheets are cut and stacked to form an initial charge that is subsequently molded to a part in a compression molding process. The resulting SMC parts have superior mechanical properties in comparison to injection molded parts due to their higher fiber length, while maintaining the ability to fill complex geometries. However, the manufacturing process leads to a spatially varying fiber volume fraction and a spatially varying and anisotropic fiber orientation, which

[1] This chapter is based on the publication "A probabilistic virtual process chain to quantify process-induced uncertainties in Sheet Molding Compounds" (Meyer et al., 2023). The focus is placed on the extension of the direct DMN framework to consider micro-oriented materials with spatially varying microstructure characteristics. For this purpose, only the relevant parts were taken from the aforementioned publication. For more detailed information on the process chain and the statistical evaluations, please refer to the original manuscript. The notation has been harmonized.

both strongly influence the mechanical performance of the resulting part (Schemmann et al., 2015; 2018). To fully exploit the lightweight-potential of such materials, it is imperative to capture both of these effects in a mechanical simulation of SMC components.

In this chapter, we use the framework of direct DMNs for accelerating two-scale simulations of SMC components. For this, we augment the framework by a fiber orientation and fiber volume fraction interpolation scheme. In contrast to Chapter 5, this approach allows for accurately resolving the spatially varying fiber volume fraction as well as the spatially varying fiber orientation in a component scale simulation. We focus on planar fiber orientation distributions, as the out-of-plane component in planar SMC components is typically rather small (Schöttl et al., 2021). This assumptions allows to parameterize the orientation state by a single variable. Thus, in combination with the fiber volume fraction, the surrogate model may be interpolated on a 2D continuum, which significantly simplifies the sampling, training and validation of the model.

To demonstrate the efficiency of our approach, we develop a virtual process chain in the spirit of Görthofer et al. (2019), acting as a digital twin for SMC specimens from compounding to mechanical testing in a testing rig. We vary the initial stack configuration in terms of the overall fiber volume fraction while keeping the overall fiber orientation, the material parameters and the boundary conditions constant. For each variation, we compute multiple realizations of SMC components and analyze these by means of DMN-accelerated two-scale simulations to capture process-induced uncertainties in the mechanical performance of the specimens.

6.2 Two-phase direct DMNs for a variable fiber volume fraction and fiber orientation

6.2.1 Two-phase micro-oriented direct DMNs

As introduced in Chapter 4, direct DMNs are restricted to microstructures without micro-oriented phases, i.e., considering anisotropic SMC bundles as second phase beside the isotropic unsaturated polyester polyurethane hybrid (UPPH) matrix, see Bücheler (2018) for information on the material system, is not possible. Thus, we augment the direct DMN framework with an additional rotation layer at the bottom of the binary tree, enabling the treatment of micro-oriented problems, see Figure 6.1 for an illustration and see also Comment 4 in Chapter 3 for an explanation.

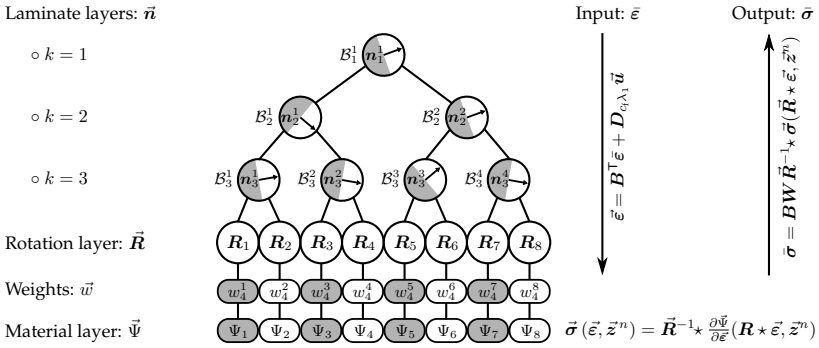

Figure 6.1: Schematic illustration of a micro-oriented direct DMN with two phases and a depth of three

We consider a micro-oriented direct DMN of two phases in three spatial dimensions and of depth K to consist of the following parts:

1. A vector $\vec{\boldsymbol{n}} = [\boldsymbol{n}_K^1, \boldsymbol{n}_K^2, \ldots, \boldsymbol{n}_1^2, \boldsymbol{n}_2^2, \boldsymbol{n}_1^1] \in (\mathrm{S}^{d-1})^{2^K-1}$, comprising the lamination directions of all laminate building blocks and inserted in a reversed breadth-first ordering.
2. A vector of non-negative weights $\vec{w} = [w_{K+1}^1, \ldots, w_{K+1}^{2^K}] \in \mathbb{R}_{\geq 0}^{2^K}$, summing to unity.
3. A vector of rotations $\vec{\boldsymbol{R}} = [\boldsymbol{R}_1, \ldots, \boldsymbol{R}_{2^K}] \in \mathrm{SO}(d)^{2^K}$, specifying the material orientation.

The vector of lamination directions $\vec{\boldsymbol{n}}$, the vector of weights $\vec{w}$ and the vector of rotation matrices $\vec{\boldsymbol{R}}$ uniquely determine the micro-oriented direct DMN and serve as the fitting parameters of the surrogate model.

6.2.2 Interpolating the fitting parameters

The parameters $\vec{\boldsymbol{p}} = [\vec{\boldsymbol{n}}, \vec{w}, \vec{\boldsymbol{R}}]$ only depend on the geometric composition of the underlying microstructure the model is fitted on and are independent of the constituents. However, for many material classes including SMC, the geometric composition of the microstructure fluctuates significantly on the macroscopic scale, an effect usually induced by the manufacturing process of the composite. As a consequence, a plethora of parameter vectors $\vec{\boldsymbol{p}}$, typically one for every Gauss point of the macroscopic simulation, needs to be identified in order to employ the DMN surrogate model in a two-scale simulation. As a remedy, the interpolation of the parameters $\vec{\boldsymbol{p}}$ has been proposed in Chapter 5. For interpolating the fitting parameters, we assume that $\vec{\boldsymbol{n}}$, $\vec{w}$ and $\vec{\boldsymbol{R}}$ depend continuously on the relevant microstructure characteristics such that only a single parameter identification process is necessary.

For SMC, the relevant microstructure characteristics are given by the fiber volume fraction and the second-order fiber orientation tensor. In principle, the fiber volume fraction $c_\mathrm{f} \in [0, 1]$ ranges between zero and one. Typically, the maximum fiber content is capped well below one,

mainly due to geometric reasons, e.g., the maximum packing density of cylinders acts as an upper bound.

By general covariance considerations, two fiber orientation states which differ only by an orthogonal transformation should give rise to effective material responses which differ only by this orthogonal transformation, see Section 5.2.2. Consequently, restricting to planar fiber orientation states, we may parameterize essentially different fiber orientation states by the following second-order fiber orientation tensor $\boldsymbol{A}_2 \in \mathrm{Sym}_2(3)$ (Advani and Tucker, 1987)

$$\boldsymbol{A}_2 = \begin{bmatrix} \lambda_1 & 0 & 0 \\ 0 & 1-\lambda_1 & 0 \\ 0 & 0 & 0 \end{bmatrix} \boldsymbol{e}_i \otimes \boldsymbol{e}_j, \tag{6.1}$$

which only depends on a single parameter $\lambda_1 \in [0.5, 1]$. For instance, for $\lambda_1 = 0.5$, we recover a planar orientation state, whereas for $\lambda_1 = 1$ a unidirectional state is observed.

To obtain a surrogate model admissible for any pair of fiber volume fraction and orientations $(c_\mathrm{f}, \lambda_1) \in \mathcal{C}\Lambda = [0,1] \times [0.5, 1]$, we define the interpolated parameter vector $\vec{\boldsymbol{p}}(c_\mathrm{f}, \lambda_1) = [\vec{\boldsymbol{n}}(\lambda_1), \vec{w}(c_\mathrm{f}), \vec{\boldsymbol{R}}(\lambda_1)]$. Here, we assume that the directions of lamination $\vec{\boldsymbol{n}}(\lambda_1)$ and the material orientation $\vec{\boldsymbol{R}}(\lambda_1)$ depend linearly on the fiber orientation parameter λ_1 and are independent of the fiber volume fraction c_f. We refer to Section 5.2.3 for a suitable parametrization. Furthermore, we assume that the weights $\vec{w}(c_\mathrm{f})$ are given by an (affine) linear function of the fiber volume fraction c_f and expressed in terms of the unconstrained weights $\vec{v} \in \mathbb{R}^{2^K}$ to ensure non-negativity, i.e.,

$$w_{K+1}^{2i}(c_\mathrm{f}) = c_\mathrm{f} \, \langle v_{2i} \rangle_+ \quad \text{and} \quad w_{K+1}^{2i-1}(c_\mathrm{f}) = (1 - c_\mathrm{f}) \, \langle v_{2i-1} \rangle_+ \tag{6.2}$$

hold, together with the consistency conditions

$$\sum_{i=1}^{2^{K-1}} \langle v_{2i} \rangle_+ = 1 \quad \text{and} \quad \sum_{i=1}^{2^{K-1}} \langle v_{2i-1} \rangle_+ = 1, \tag{6.3}$$

which ensure that

$$\sum_{i=1}^{2^{K-1}} w_{K+1}^i = 1 \tag{6.4}$$

holds for any fiber volume fraction c_f.

6.2.3 Efficient evaluation of the nonlinear homogenization function

For the efficient evaluation of the nonlinear homogenization function

$$\mathcal{DMN}_{\mathcal{CA}} : \mathcal{GSM} \times \mathcal{GSM} \to \mathcal{GSM}, \quad (\mathcal{G}_1, \mathcal{G}_2) \mapsto \bar{\mathcal{G}} \tag{6.5}$$

of a micro-oriented direct DMN of depth K, we assume that the parameter vector $\vec{\boldsymbol{p}}$ is given as the result of a suitable interpolation scheme $(c_\mathrm{f}, \lambda_1) \mapsto \vec{\boldsymbol{p}}(c_\mathrm{f}, \lambda_1) = [\vec{\boldsymbol{n}}(\lambda_1), \vec{w}(c_\mathrm{f}), \vec{\boldsymbol{R}}(\lambda_1)]$ and fixed.

First, we introduce the averaging operator $\boldsymbol{B} : \mathrm{Sym}_2(d)^{2^K} \to \mathrm{Sym}_2(d)$, a 2^K-fold copy of the identity on $\mathrm{Sym}_2(d)$ and the symmetrized gradient operator $\boldsymbol{D}_{c_\mathrm{f}\lambda_1} : (\mathrm{V}^d)^{2^K-1} \to \mathrm{Sym}_2(d)^{2^K}$, which depends on the fiber volume fraction c_f and the fiber orientation λ_1 and which encodes the DMN's topology into a single linear mapping, see Section 4.2.3. The vector of compatible strains $\vec{\boldsymbol{\varepsilon}} = [\boldsymbol{\varepsilon}_1, \ldots, \boldsymbol{\varepsilon}_{2^K}] \in \mathrm{Sym}_2(d)^{2^K}$ admits the representation

$$\vec{\boldsymbol{\varepsilon}} = \boldsymbol{B}^\mathsf{T} \bar{\boldsymbol{\varepsilon}} + \boldsymbol{D}_{c_\mathrm{f}\lambda_1} \vec{\boldsymbol{u}}, \tag{6.6}$$

where $\bar{\boldsymbol{\varepsilon}} \in \mathrm{Sym}_2(d)$ designates the macrostrain (increment) and $\vec{\boldsymbol{u}} \in (\mathrm{V}^d)^{2^K-1}$ stands for the vector of (unknown) displacement jumps.

We consider the two isothermal GSMs $\mathcal{G}_1$ and $\mathcal{G}_2$ as phases. We assign to each phase $i = 1, \dots, 2^K$ the isothermal GSM $\mathcal{G}_i$, which alternates between $\mathcal{G}_1$ and $\mathcal{G}_2$, i.e.,

$$\mathcal{G}_i = \begin{cases} \mathcal{G}_1 = (\mathcal{Z}_1, \psi_1, \phi_1, \boldsymbol{z}_{0,1}), & i \text{ odd}, \\ \mathcal{G}_2 = (\mathcal{Z}_2, \psi_2, \phi_2, \boldsymbol{z}_{0,2}), & i \text{ even}. \end{cases} \tag{6.7}$$

By a time discretization with the implicit Euler method and condensation of the internal variables, see Section 2.5, we obtain the vector of incremental algorithmic potentials $\vec{\Psi} = [\Psi_1, \dots, \Psi_{2^K}]$, alternating between the incremental potentials of both phases. After condensation, the microscopic vector of stresses is defined via

$$\vec{\boldsymbol{\sigma}}\,(\vec{\boldsymbol{\varepsilon}}, \vec{\boldsymbol{z}}^{\,n}) = \vec{\boldsymbol{R}}^{-1} \star \frac{\partial \vec{\Psi}}{\partial \vec{\boldsymbol{\varepsilon}}}(\boldsymbol{R} \star \vec{\boldsymbol{\varepsilon}}, \vec{\boldsymbol{z}}^{\,n}), \tag{6.8}$$

with

$$\frac{\partial \vec{\Psi}}{\partial \vec{\boldsymbol{\varepsilon}}}(\cdot, \vec{\boldsymbol{z}}^{\,n}) = \left[\frac{\partial \Psi_1}{\partial \vec{\boldsymbol{\varepsilon}}}\,(\cdot, \boldsymbol{z}_1^n), \dots, \frac{\partial \Psi_{2^K}}{\partial \vec{\boldsymbol{\varepsilon}}}\,(\cdot, \boldsymbol{z}_{2^K}^n) \right], \tag{6.9}$$

where $\vec{\boldsymbol{z}}^{\,n} = [\boldsymbol{z}_1, \dots, \boldsymbol{z}^{2^K}] \in \bar{\mathcal{Z}} = (\mathcal{Z}_1 \oplus \mathcal{Z}_2)^{\oplus^{2^K-1}}$ denotes the vector of internal variables of the last converged time step, the operator $\vec{\boldsymbol{R}} \star : \ \mathrm{Sym}_2(d)^{2^K} \to \mathrm{Sym}_2(d)^{2^K}$ encodes the forward rotation of the phase strains

$$\vec{\boldsymbol{\varepsilon}} \mapsto \vec{\boldsymbol{R}} \star \vec{\boldsymbol{\varepsilon}} = [\boldsymbol{R}_1^{\mathsf{T}} \boldsymbol{\varepsilon}_1 \boldsymbol{R}_1, \dots, \boldsymbol{R}_{2^K}^{\mathsf{T}} \boldsymbol{\varepsilon}_{2^K} \boldsymbol{R}_{2^K}] \tag{6.10}$$

and $\vec{\boldsymbol{R}}^{-1} \star : \ \mathrm{Sym}_2(d)^{2^K} \to \mathrm{Sym}_2(d)^{2^K}$ denotes the corresponding backward rotation of the phase stresses

$$\vec{\boldsymbol{\sigma}} \mapsto \vec{\boldsymbol{R}}^{-1} \star \vec{\boldsymbol{\sigma}} = [\boldsymbol{R}_1 \boldsymbol{\sigma}_1 \boldsymbol{R}_1^{\mathsf{T}}, \dots, \boldsymbol{R}_{2^K} \boldsymbol{\sigma}_{2^K} \boldsymbol{R}_{2^K}^{\mathsf{T}}], \tag{6.11}$$

both expressed in terms of the vector of rotations $\vec{\boldsymbol{R}}$.

For a prescribed macrostrain increment $\bar{\boldsymbol{\varepsilon}}$, we seek the vector of displacement jumps $\vec{\boldsymbol{u}}$, which solves the balance of linear momentum

$$\boldsymbol{D}_{c_\mathrm{f}\lambda_1}^{\mathsf{T}} \boldsymbol{W} \vec{\boldsymbol{R}}^{-1} \star \frac{\partial \vec{\Psi}}{\partial \vec{\boldsymbol{\varepsilon}}} (\vec{\boldsymbol{R}} \star (\boldsymbol{B}^{\mathsf{T}} \bar{\boldsymbol{\varepsilon}} + \boldsymbol{D}_{c_\mathrm{f}\lambda_1} \vec{\boldsymbol{u}}), \vec{\boldsymbol{z}}^{\,n}) = \boldsymbol{0}, \tag{6.12}$$

where $\boldsymbol{W} : \mathrm{Sym}_2(d)^{2^K} \rightarrow \mathrm{Sym}_2(d)^{2^K}$ designates the weight operator, which might be represented as a diagonal matrix comprising the weights $\vec{w}$ on the diagonal. In a subsequent step, the effective stress $\bar{\boldsymbol{\sigma}}$ is computed by averaging the phase stresses via

$$\bar{\boldsymbol{\sigma}} = \boldsymbol{B} \boldsymbol{W} \vec{\boldsymbol{R}}^{-1} \star \vec{\boldsymbol{\sigma}} (\vec{\boldsymbol{R}} \star (\boldsymbol{B}^{\mathsf{T}} \bar{\boldsymbol{\varepsilon}} + \boldsymbol{D}_{c_\mathrm{f}\lambda_1} \vec{\boldsymbol{u}}), \vec{\boldsymbol{z}}^{\,n}). \tag{6.13}$$

For a detailed summary of the implementation as a user-defined subroutine including the derivation of the algorithmic tangent, we refer to Chapter 5 for the purely mechanical and Chapter 7 for the thermomechanical case. Please note that the mere difference in implementation between this section and the aforementioned chapters is the additional rotation layer which rotates the computed stresses and strains (and algorithmic tangents) of the materials.

6.3 Identifying the DMN surrogate model

6.3.1 Modeling damage in sheet molding compound composites

A variety of experimental investigations (Meraghni et al., 1996; Ben Cheikh Larbi et al., 2006; Trauth et al., 2017; Schöttl et al., 2020) show that matrix and bundle damage are the dominant damage mechanisms in SMC composites. For modeling damage in the UPPH matrix and the fiber bundles, we rely upon the anisotropic and non-localizing damage model of Görthofer et al. (2022b). The model is formulated as

an isothermal GSM, see Section 2.5, comprising the free energy density $\psi : \mathrm{Sym}_2(d) \times \mathcal{Z} \to \mathbb{R}$,

$$\psi(\boldsymbol{\varepsilon}, \boldsymbol{z}) = \frac{1}{2}\boldsymbol{\varepsilon} \cdot \mathbb{S}^{-1}[\boldsymbol{\varepsilon}] + \sum_{i=1}^{M} \frac{H_i}{m_i + 1} q_i^{m_i+1}, \tag{6.14}$$

which consists of an elastic part and a part related to damage and where M denotes the number of different damage cases. The internal variables of the model are given by $\boldsymbol{z} = [\mathbb{S}, q_1, \ldots, q_M] \in \mathcal{Z} = \mathrm{Sym}_4^+(d) \oplus \mathbb{R}^M$, i.e., the model operates on the positive definite compliance tensors $\mathbb{S} \in \mathrm{Sym}_4^+(d)$ as the primary damage variable and a set of variables $q_i \in \mathbb{R}$, $i = 1, \ldots, M$, describing the shape and size of the damage surfaces. The hardening parameters $H_i \in \mathbb{R}_{>0}$ and exponents $m_i \in \mathbb{R}_{>0}$ control the growth of damage.

We introduce the force potential $\phi^* : \mathrm{Sym}_2(d) \times \mathbb{R}^M \to \mathbb{R} \cup \{+\infty\}$ in terms of M convex damage-activation functions

$$g_i(\boldsymbol{\sigma}, q_i) = \|\mathbb{B}_i[\boldsymbol{\sigma}]\|^2 - \sigma_{0,i}^2 - H_i^2 q_i^{m_i} \tag{6.15}$$

that bound the elastic regime in analogy to associated elasto-plastic models. We formulate the force potential ϕ^*, the continuous dual of the dissipation potential ϕ, in its simplified version

$$\phi^*(\boldsymbol{\sigma}, q_1, \ldots, , q_M) = \begin{cases} 0, & g_i(\boldsymbol{\sigma}, q_i) \leq 0, \quad \forall\, i = 1, \ldots, M, \\ +\infty, & \text{else.} \end{cases} \tag{6.16}$$

For damage to evolve, the stress state has to exceed a damage-activation threshold $\sigma_{0,i} \in \mathbb{R}_{>0}$ in combination with a part accounting for the onset of damage. Case-specific stresses are extracted via dedicated extraction tensors $\mathbb{B}_i$ that can be tailored to the application at hand. Using Biot's dual equation (Borwein and Lewis, 2006), we obtain the damaged stiffness $\mathbb{C}$ for any state of damage captured by the associated

damage variables

$$\mathbb{C} = \mathbb{S}^{-1} \quad \text{with} \quad \mathbb{S} = \mathbb{S}_0 + 2\sum_{i=1}^{M} \frac{q_i}{H_i}\mathbb{B}_i^2, \tag{6.17}$$

where $\mathbb{S}_0$ is the initial compliance. The model is thermodynamically consistent and satisfies Wulfinghoff's damage growth criterion (Wulfinghoff et al., 2017). Furthermore, it can be applied to any hardening-type damage material. An efficient predictor-corrector framework in analogy to problem settings in elasto-plasticity allows for an efficient computation. For a detailed overview on the model, the reader is referred to Görthofer et al. (2022b).

For the UPPH matrix, we restrict to an isotropic damage evolution as suggested by Görthofer et al. (2022a), i.e., we choose the corresponding extraction tensor as

$$\mathbb{B}_{\mathrm{M}} = \frac{1}{3}\boldsymbol{I} \otimes \boldsymbol{I}. \tag{6.18}$$

For the fiber bundles, we capture damage as a result of normal stresses perpendicular to the bundle direction and shear stresses in bundle direction (Görthofer et al., 2022b;a). We implement the associated extraction tensors as

$$\mathbb{B}_{\mathrm{B,N}} = \frac{\sqrt{2}}{2}(\boldsymbol{e}_2^{\otimes^2} + \boldsymbol{e}_3^{\otimes^2})^{\otimes^2} + \frac{\sqrt{2}}{4}(\boldsymbol{e}_2^{\otimes^2} - \boldsymbol{e}_3^{\otimes^2})^{\otimes^2} + \frac{1}{2}(\boldsymbol{e}_2 \otimes \boldsymbol{e}_3 + \boldsymbol{e}_3 \otimes \boldsymbol{e}_2)^{\otimes^2} \tag{6.19}$$

and

$$\mathbb{B}_{\mathrm{B,S}} = (\boldsymbol{e}_1 \otimes_{\mathrm{S}} \boldsymbol{e}_2)^{\otimes^2} + (\boldsymbol{e}_1 \otimes_{\mathrm{S}} \boldsymbol{e}_3)^{\otimes^2}. \tag{6.20}$$

The linear elastic material parameters of the UPPH matrix were characterized by Trauth (2020, Section 6.3.1). Relying on μCT scans (Schöttl et al., 2020; 2021), we assume the volume fraction of fibers within a bundle to be $70\,\%$ and obtain the bundle properties via homogenization. The linear elastic material properties of matrix and bundles both given in engineering notation are reported in Table 6.1.

Matrix	$E = 3.5\,\mathrm{GPa}$	$\nu = 0.385$	
Bundles	$E_\mathrm{L} = 51.5\,\mathrm{GPa}$	$\nu_\mathrm{TT} = 0.402$	$G_\mathrm{TT} = 6.6\,\mathrm{GPa}$
	$E_\mathrm{T} = 18.7\,\mathrm{GPa}$	$\nu_\mathrm{LT} = 0.260$	$G_\mathrm{LT} = 6.8\,\mathrm{GPa}$

Table 6.1: Elastic properties of matrix and bundles

Based on experimental data reported by Trauth (2020), the parameters describing the damage onset and evolution in matrix and bundles are identified using a Bayesian optimization approach using Gaussian regression as presented in Görthofer et al. (2022a). The results are listed in Table 6.2

Matrix	$\mathbb{B}_1 = \mathbb{B}_\mathrm{M}$	$\sigma_{0,1} = 36.9\,\mathrm{MPa}$	$H_1 = 213.9\,\mathrm{MPa}$	$m_1 = 1.0$
Bundles	$\mathbb{B}_2 = \mathbb{B}_\mathrm{B,N}$	$\sigma_{0,2} = 46.0\,\mathrm{MPa}$	$H_2 = 529.0\,\mathrm{MPa}$	$m_2 = 1.0$
	$\mathbb{B}_3 = \mathbb{B}_\mathrm{B,S}$	$\sigma_{0,3} = 44.1\,\mathrm{MPa}$	$H_3 = 283.9\,\mathrm{MPa}$	$m_3 = 1.0$

Table 6.2: Damage parameters of matrix and bundles

6.3.2 Offline training and model validation

The space of admissible fiber volume fractions and fiber orientations is given by the continuum $\mathcal{C}\Lambda$. Before sampling the training data, we seek a suitable discretization of $\mathcal{C}\Lambda$. For discretization, we choose for the fiber volume fraction $c_\mathrm{f} \in [0.15, 0.35]$ and for the fiber orientations $\lambda_1 \in [0.5, 0.8]$, see Meyer et al. (2023) for a discussion on how these bounds were obtained. The admissible space of fiber volume fractions and fiber orientations is discretized as shown in Figure 6.2.

The white dots in Figure 6.2 represent 41 tuples $\left\{\left(c_\mathrm{f}^s, \lambda_1^s\right)\right\}_{s=1}^{41}$ of the discretized space. We generate an artificial SMC microstructure for any of those tuples by the algorithm of Görthofer et al. (2020). In the next

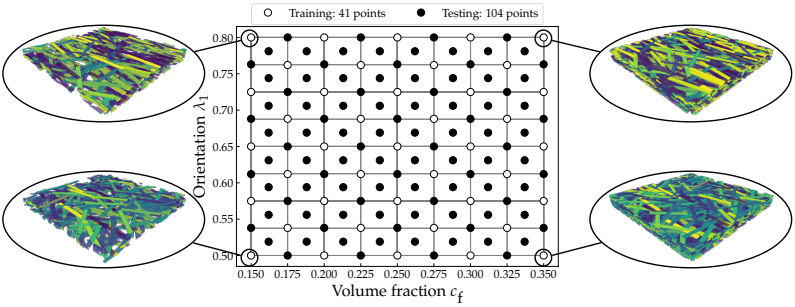

Figure 6.2: Discretization of the space of admissible fiber volume fractions and fiber orientations

step, we sample $N_s = 1\,230$ pairs of stiffnesses $(\mathbb{C}_1^s, \mathbb{C}_2^s)$, as explained in Section 4.3.1, assign each stiffness tuple to one of the generated SMC microstructures in a cyclic fashion

$$(c_f^s, \lambda_1^s) \mapsto (c_f^{(s-1) \mod 41+1}, \lambda_1^{(s-1) \mod 41+1}) \tag{6.21}$$

and compute the associated effective stiffness $\bar{\mathbb{C}}^s$ by means of an FFT-based computational micromechanics code, using the conjugate gradient solver (Zeman et al., 2010; Brisard and Dormieux, 2010) and the staggered grid discretization (Schneider et al., 2016).

We choose a DMN of $K = 8$ layers as such a depth is typically necessary to obtain accurate results, see Chapter 4 and 5. For parameter identification, we randomly split the pre-computed training data $\left\{(\mathbb{C}_1^s, \mathbb{C}_2^s, \bar{\mathbb{C}}^s, c_f^s, \lambda_1^s)\right\}_{s=1}^{N_s}$ into a training and validation set comprising 80% and 20% of the samples, respectively. The DMN is trained based on the loss function

$$J(\vec{\boldsymbol{p}}) = \sum_{s=1}^{N_s} J_s(\vec{\boldsymbol{p}}) + J_p(\vec{\boldsymbol{p}}) \to \min_{\vec{\boldsymbol{p}}}, \tag{6.22}$$

where the first part

$$J_s(\vec{\boldsymbol{p}}) = \frac{1}{N_\mathrm{s}} \frac{\|\mathcal{DMN}^{\mathcal{L}}_{\mathcal{CA}}(\mathbb{C}^s_1, \mathbb{C}^s_2, \vec{\boldsymbol{p}}(c^s_\mathrm{f}, \lambda^s_1)) - \bar{\mathbb{C}}^s\|_1}{\|\bar{\mathbb{C}}^s\|_1} \tag{6.23}$$

measures the proximity of the pre-computed effective stiffness $\bar{\mathbb{C}}^s$ to the DMN's effective stiffness $\bar{\mathbb{C}}^s_{\mathrm{DMN}} = \mathcal{DMN}^{\mathcal{L}}_{\mathcal{CA}}(\mathbb{C}^s_1, \mathbb{C}^s_2, \vec{\boldsymbol{p}}(c^s_\mathrm{f}, \lambda^s_1))$. The penalty term

$$J_\mathrm{p}(\vec{\boldsymbol{p}}) = \lambda_\mathrm{p} \left(\sum_{i=1}^{2^{K-1}} \langle v_{2i} \rangle_+ - 1 \right)^2 + \lambda_\mathrm{p} \left(\sum_{i=1}^{2^{K-1}} \langle v_{2i-1} \rangle_+ - 1 \right)^2 \tag{6.24}$$

with the penalty parameter $\lambda_\mathrm{p} = 1\,000$ serves as a regularizer and enforces that the weights sum to unity and the DMN is consistent w.r.t. the given volume fraction c_f, i.e., the equations

$$\sum_{i=1}^{2^K} w^i_{K+1} = 1, \quad \sum_{i=1}^{2^{K-1}} w^{2i}_{K+1} = c_\mathrm{f} \quad \text{and} \quad \sum_{i=1}^{2^{K-1}} w^{2i-1}_{K+1} = 1 - c_\mathrm{f} \tag{6.25}$$

hold.

To assess the accuracy of the fit, we define the sample-wise mean training $\delta^{\mathrm{train}}_{\mathrm{mean}}$ and validation $\delta^{\mathrm{valid}}_{\mathrm{mean}}$ errors via

$$\delta_{\mathrm{mean}} = \frac{1}{N_\mathrm{s}} \sum_{s=1}^{N_\mathrm{s}} \frac{\|\mathcal{DMN}^{\mathcal{L}}_{\mathcal{CA}}(\mathbb{C}^s_1, \mathbb{C}^s_2, \vec{\boldsymbol{p}}(c^s_\mathrm{f}, \lambda^s_1)) - \bar{\mathbb{C}}^s\|_1}{\|\bar{\mathbb{C}}^s\|_1}, \tag{6.26}$$

where N_s denotes the number of elements in the training and validation sets, respectively. To significantly reduce the number of training epochs and to improve the results in the nonlinear regime, we employ an early-stopping technique as proposed by Dey et al. (2022b). For this purpose, we use the identified material parameters of the UPPH matrix and the bundles summarized in Section 6.3.1 and simulate three unidirectional

strain loadings in direction $\boldsymbol{d} \in \mathrm{S}^d$,

$$\bar{\boldsymbol{\varepsilon}} = \bar{\varepsilon}\, \boldsymbol{d} \otimes \boldsymbol{d} \quad \text{for} \quad \boldsymbol{d} \mathrel{\hat{=}} [\cos(\alpha), \sin(\alpha), 0] \quad \text{and} \quad \alpha \in \{0°, 45°, 90°\}, \tag{6.27}$$

using mixed boundary conditions (Kabel et al., 2016) with a macrostrain amplitude of $\bar{\varepsilon} = 4\,\%$, applied in 40 equidistant load steps, for each of the 41 generated SMC microstructures. For obtaining the full-field reference solutions, we use an FFT-based computational micromechanics (Moulinec and Suquet, 1994; 1998) code and an inexact Newton-CG (Kabel et al., 2014) solver. We consider this generated nonlinear data as the basis for the employed early-stopping technique. To quantify the deviation, we compute the nonlinear mean and maximum validation errors via

$$\eta_{\text{mean}} = \max_{s \in \{1,\dots,N_\text{s}\}} \frac{1}{T} \int_0^T \eta_s(t)\, \mathrm{d}t \tag{6.28}$$

and

$$\eta_{\text{max}} = \max_{s \in \{1,\dots,N_\text{s}\}} \max_{t \in [0,T]} \eta_s(t) \quad \text{with} \quad \eta_s(t) = \frac{\|\bar{\boldsymbol{\sigma}}_s^{\text{DMN}}(t) - \bar{\boldsymbol{\sigma}}_s^{\text{FFT}}(t)\|_1}{\max\limits_{\tau \in [0,T]} \|\bar{\boldsymbol{\sigma}}_s^{\text{FFT}}(\tau)\|_1} \tag{6.29}$$

and track them every five epochs. In Figure 6.3 the training progress is shown.

The stepwise reduction of the loss observed in Figure 6.3a results from the used learning rate modulation which reduces the learning rate by a factor of two for every 100 epochs starting from an initial learning rate of $\beta_{\text{ini}} = 1.5 \cdot 10^{-2}$. A closer look at the elastic training $\delta_{\text{mean}}^{\text{train}}$ and validation $\delta_{\text{mean}}^{\text{valid}}$ errors in Figure 6.3b shows that there is no significant model overfitting w.r.t. the linear elastic training data. However, the maximum validation error $\eta_{\text{max}}^{\text{valid}}$ takes its minimum of $4.32\,\%$ at 190 epochs and increases thereafter. The early-stopping approach stops the training after another 300 epochs as the nonlinear errors have not

improved for the subsequent 60 steps. The best model (at 190 epochs) is then stored.

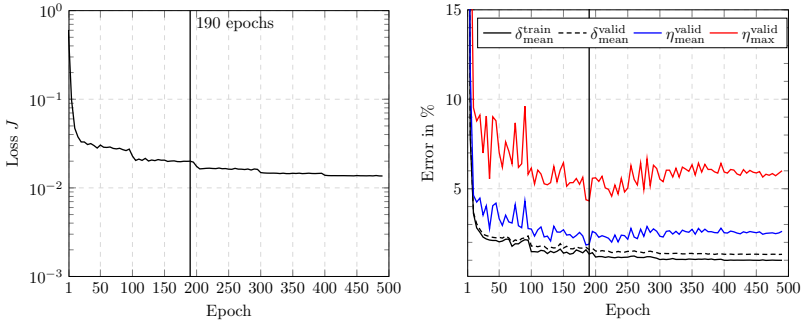

(a) Loss vs. training epoch

(b) Training and validation errors vs. training epoch

Figure 6.3: Loss (a) and model performance (b) during training

To ensure that the interpolated DMN generalizes well for all fiber volume fractions and fiber orientations $(c_\mathrm{f}, \lambda_1) \in [0.15, 0.35] \times [0.5, 0.8]$, we evaluate the DMN on an additional test set, i.e., microstructures the model has not seen before. To be more precise, for each black point in Figure 6.2, i.e., 104 microstructures in total, we generate an artificial SMC microstructure, perform three virtual uniaxial extension tests each (compare Equation (6.27)), and compute the corresponding nonlinear mean and maximum test errors (6.28). The results are summarized in Table 6.3. The nonlinear errors evaluated on the test set are only slightly increased compared to the training set. The maximum nonlinear test error as well as the nonlinear validation error are well below $5\,\%$, i.e., in the range of engineering requirements, for all considered fiber volume fractions and fiber orientations. Further information on the model validation can be found in Appendix C.

$\delta^{\text{train}}_{\text{mean}}$	$\delta^{\text{valid}}_{\text{mean}}$	$\eta^{\text{valid}}_{\text{mean}}$	$\eta^{\text{valid}}_{\text{max}}$	$\eta^{\text{test}}_{\text{mean}}$	$\eta^{\text{test}}_{\text{max}}$
$1.35\,\%$	$1.60\,\%$	$1.90\,\%$	$4.32\,\%$	$2.20\,\%$	$4.71\,\%$

Table 6.3: Model performance after training

6.4 A virtual process chain for sheet molding compound composites

After demonstrating that the interpolated DMN generalized well, we use the identified model to quantify uncertainties induced by the manufacturing process of sheet molding compound composites. For this, we simulate the process chain of several SMC specimen, starting from compression molding of plates up to mechanical simulations of specimen cut from those plates. For more details on the process chain, the assumptions made, technical details such as microstructure generation, finding necessary resolution and size of the RVEs, material parameters and mapping, we refer to Meyer et al. (2023).

For simplicity, we restrict to the sample geometry B2, see Figure 6.4 and Trauth (2020); Meyer et al. (2023), and simulate the compression molding of eight SMC plates using a direct bundle simulation approach as proposed by Meyer (2021). For four of these plates, we chose an overall fiber volume fraction of $22.5\,\%$ and the other four plates feature an overall fiber volume fraction of $26\,\%$. We chose this setup, because the overall fiber volume fraction in a SMC prepreg is typically not constant and varies spatially and temporally. These fluctuations often depend on external factors which cannot be easily controlled. For simplicity, the initial overall bundle orientation is chosen to be planar isotropic. After compression molding, the fiber volume fraction and the fiber orientation are computed via averaging and mapped onto 32 ABAQUS models

of the tensile test specimens, four for each plate. Figure 6.4 shows several realizations of sample geometry B2 generated in the described way. Indeed, the mold filling simulation predicts highly fluctuating fiber volume fractions and fiber orientations even for identical initial properties.

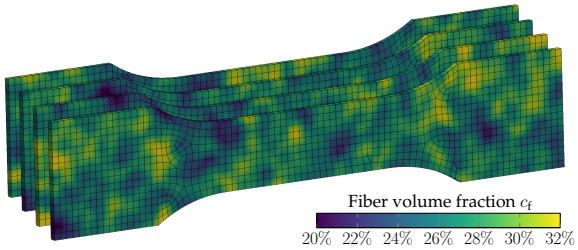

(a) Mapped fiber volume fraction

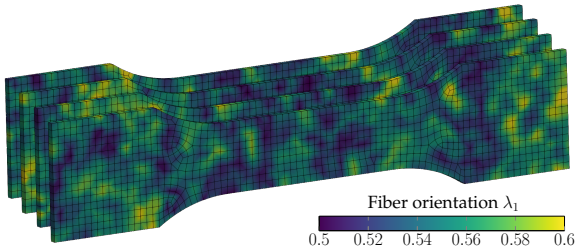

(b) Mapped fiber orientation

Figure 6.4: Fiber volume fraction (a) and fiber orientation (b) fields for different realizations obtained at identical specimen positions and with identical overall properties for the compression molding simulation

For the structural simulations, a unidirectional elongation of $3\,\mathrm{mm}$ is applied via the two reference points RP1 and RP2, which are coupled to the specimen arms, see Figure 6.5. In every Gauss point, a micro-oriented direct DMN is integrated implicitly to incorporate the fluctuating microstructure information into the simulation. For the strain measurement,

we follow the experimental setup as described in Trauth (2020) and record the strain via averaging over the shown gauge section with dimensions $70\,\mathrm{mm} \times 10\,\mathrm{mm}$. The stress is computed by tracking the reaction force at RP2 which is averaged over the cross section of the specimen.

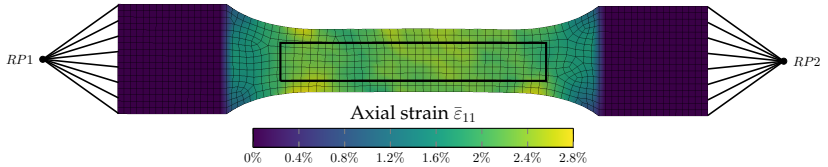

Figure 6.5: Distribution of the strain $\bar{\varepsilon}_{11}$ component as a result of the applied load in conjunction with the gauge used for averaging the strain

In Figure 6.6, we see the comparison of experimental data, as reported by Trauth (2020), with the simulation results. The experimental data was obtained from compression molded SMC specimens of identical geometry, extracted at identical positions and subjected to identical loadings. In Figure 6.6a, the stress-strain curves of 15 tensile tests, their mean and the $95\,\%$ confidence interval are illustrated. The stress-strain curves of the 32 simulated tensile tests, their mean and the $95\,\%$ confidence interval can be found in Figure 6.6b. In Figure 6.6c, the mean values and $95\,\%$ confidence intervals of experiments and simulations are shown. We observe that despite the simple test setup – only the initial overall volume fraction was varied in two steps and the initial overall bundle orientation was assumed to be isotropic – the simulations agree excellently with the experimental results. The former holds true both for the mean as well as the $95\,\%$ confidence interval.

To sum up, we have shown that by considering the compression molding process and thus capturing its influence on part performance, the experimentally observed scatter in mechanical properties can be captured

by simulative means. By accounting for the spatially varying fiber volume fraction and fiber orientation in a component scale simulation, the uncertainties in the mechanical behavior of SMC components can be accurately predicted. For a more detailed breakdown of different factors influencing uncertainty and a statistical evaluation, we refer to Meyer et al. (2023).

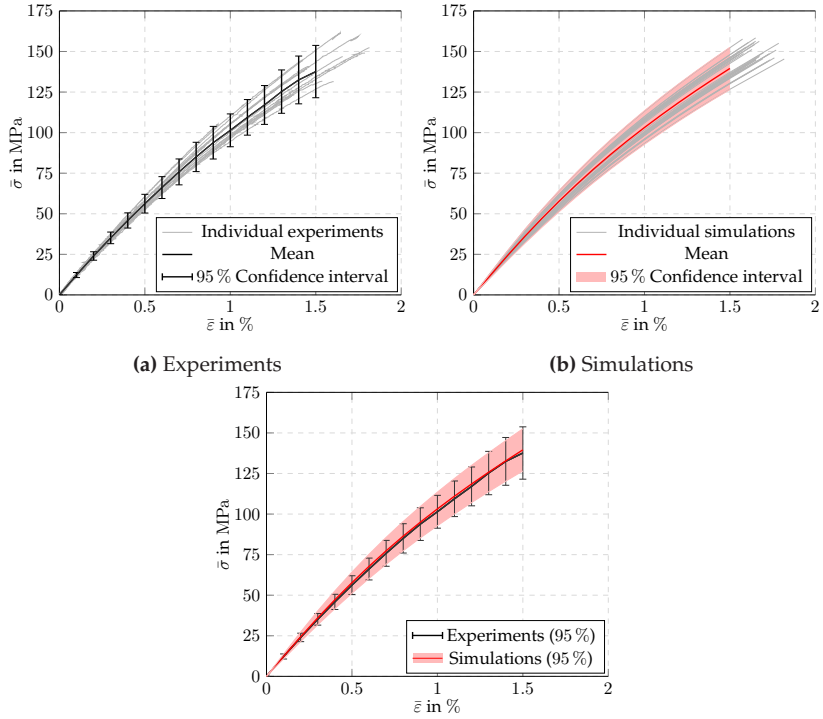

(a) Experiments

(b) Simulations

(c) Comparison of mean and confidence interval

Figure 6.6: Comparison of experimental results with simulations

6.5 Conclusion

In this chapter, we extended the direct DMN framework to problems with micro-oriented phases. Furthermore, we proposed an interpolation technique to account for a spatially varying fiber volume fraction and fiber orientation in mechanical simulations of SMC components.

Building upon the previous chapter, we extended the fiber orientation interpolation scheme by an additional fiber volume fraction interpolation. This procedure gives rise to a single surrogate model which allows for incorporating fluctuating microstructure characteristics into a components scale simulation. We sampled the training data from 41 SMC microstructure realizations. By generating 104 additional microstructures the model had not seen during training, we ensured that the interpolated micro-oriented direct DMN generalized well for all admissible fiber volume fractions and fiber orientations.

To demonstrate the efficiency of the proposed approach, we simulated the entire process chain of SMC specimens starting from multiple compression molding simulations up to mechanical testings in a virtual testing rig. The ensuing fiber volume fraction and fiber orientation fields were mapped onto ABAQUS meshes of SMC specimens which were subjected to a virtual tensile test. Comparing experimental data and simulation results, we showed that process-induced uncertainties in the mechanical properties of SMC components can be accurately predicted.

Chapter 7

Fully coupled two-scale simulations of thermomechanical composites[1]

7.1 Introduction

We extend the framework of direct DMNs, which were introduced in Chapter 4, to composites with full thermomechanical coupling, effectively enabling thermomechanical two-scale simulations of industrial problems. As point of departure, we recapitulate the results of Chatzigeorgiou et al. (2016) in Section 7.2, who introduced a framework for the first-order asymptotic homogenization of thermomechanical composites. Subsequently, we extend direct DMNs to thermomechanical composites in Section 7.3 by incorporating the coupling of microscopic mechanical deformation onto the macroscopic temperature and vice versa into our approach. For this purpose, we exploit the homogeneity of the absolute temperature on the microscopic scale to arrive at an efficient solution scheme for solving the balance of linear momentum of a direct DMN. To accelerate a component-scale simulation of industrial complexity, we

[1] This chapter is based on the publication "An FE-DMN method for the multiscale analysis of thermomechanical composites" (Gajek et al., 2022). The introduction has been shortened to avoid redundancy with Chapter 1. The notation has been harmonized.

discuss the efficient implementation of our approach as a user-material subroutine (UMAT) only relying on the provided interfaces.

To demonstrate the capabilities of the proposed approach, we consider a short fiber reinforced polyamide featuring a pronounced thermomechanical coupling. In Section 7.4, we elaborate on the material model and the training and validation of the DMN surrogate model. We show that the direct DMN is able to predict the effective stress, the effective dissipation as well as the deformation-induced temperature change of the composite with sufficient accuracy for all investigated loadings.

Later on in Section 7.5, we demonstrate the power of our approach by conducting a fully coupled thermomechanical two-scale simulation of an asymmetric notched specimen subjected to cyclic loading also considering heat conduction and convection on the macroscopic scale.

7.2 First-order asymptotic homogenization of thermomechanical composites

Chatzigeorgiou et al. (2016) introduced a framework for the (first-order) asymptotic homogenization of thermomechanical composites at small strains. More precisely, they considered quasi-static, non-isothermal generalized standard materials and derived governing equations for the microscopic and macroscopic scale.

In $d \in \{2, 3\}$ spatial dimensions, we consider a small-strain, quasi-static, non-isothermal GSM to be the quadruple $(\mathcal{Z}, \psi, \phi, \boldsymbol{z}_0) \in \mathcal{GSM}$, which consists of a Banach vector space $\mathcal{Z}$ of internal variables, a Helmholtz free energy density $\psi : \mathrm{Sym}_2(d) \times \mathbb{R}_{>0} \times \mathcal{Z} \to \mathbb{R}$, an extended-real-valued dissipation potential $\phi : \mathbb{R}_{>0} \times \mathcal{Z} \to \mathbb{R} \cup \{+\infty\}$ and an element $\boldsymbol{z}_0 \in \mathcal{Z}$ serving as initial condition for the dynamics. We refer to Section 2.5 for a more thorough introduction to the non-isothermal GSM framework.

We consider a macroscopic body $\Omega \subseteq \mathrm{V}^d$ with macroscopic point $\bar{\boldsymbol{x}} \in \Omega$. To every macroscopic point $\bar{\boldsymbol{x}}$, we associate a (rectangular) two-phase periodic microstructure $Y \subseteq \mathrm{V}^d$.

The microscopic cell problem

The periodic microstructure Y comprises as phases the two non-isothermal GSMs $(\mathcal{Z}_1, \psi_1, \phi_1, \boldsymbol{z}_{0,1})$ and $(\mathcal{Z}_2, \psi_2, \phi_2, \boldsymbol{z}_{0,2})$ with measurable characteristic functions $\chi_{1/2} : Y \to \{0, 1\}$ whose associated sets are mutually disjoint and cover all of Y, i.e., the conditions

$$\chi_1 \chi_2 = 0 \quad \text{and} \quad \chi_1 + \chi_2 = 1 \tag{7.1}$$

hold almost everywhere. Then, on the microscopic scale, the so-called thermomechanical cell problem of first-order homogenization, i.e., the (quasi-static) microscopic balance of linear momentum, reads

$$\mathrm{div}_{\boldsymbol{x}} \left[\sum_{i=1}^{2} \chi_i \frac{\partial \psi_i}{\partial \boldsymbol{\varepsilon}} (\bar{\boldsymbol{\varepsilon}} + \nabla^{\mathrm{s}}_{\boldsymbol{x}} \boldsymbol{u}, \bar{\theta}, \boldsymbol{z}_i) \right] = \boldsymbol{0}, \tag{7.2}$$

where $\mathrm{div}_{\boldsymbol{x}}$ and $\nabla^{\mathrm{s}}_{\boldsymbol{x}}$ refer to the divergence and the symmetrized gradient operator w.r.t. the microscopic point $\boldsymbol{x} \in Y$, respectively. Furthermore, $\bar{\boldsymbol{\varepsilon}} : \Omega \times [0, T] \to \mathrm{Sym}_2(d)$ denotes the macrostrain, $\boldsymbol{u} : \Omega \times Y \times [0, T] \to \mathrm{V}^d$ symbolizes the periodic displacement fluctuation with anti-periodic normal derivative and $\boldsymbol{z}_{1/2} : \Omega \times Y \times [0, T] \to \mathcal{Z}_{1/2}$ stands for the fields of internal variables.

In particular, provided the force term varies only slowly on the macroscopic scale, Chatzigeorgiou et al. (2016) deduced that the balance of linear momentum on the microscopic scale, the thermomechanical cell problem, only depends on the macroscopic temperature, i.e., temperature fluctuations on the microscopic scale constitute only a lower-order contribution to the effective stress. In other words, the absolute temperature is a macroscopic quantity and thus there is no

temperature fluctuation on the microscopic scale. Most importantly, there is no need to solve for the temperature on the microscopic scale. Thus, the macroscopic absolute temperature $\bar{\theta} : \Omega \times [0,T] \to \mathbb{R}_{>0}$ as well as the macrostrain $\bar{\boldsymbol{\varepsilon}}$ enter Equation (7.2) as inputs and constitute the one-way coupling between the macroscopic and the microscopic scale.

The macroscopic balance of linear momentum and the macroscopic heat equation

On the macroscopic scale, two governing equations emerge. First, the quasi-static balance of linear momentum, governing the evolution of the macrostrain $\bar{\boldsymbol{\varepsilon}}$, reads

$$\operatorname{div}_{\bar{\boldsymbol{x}}} \left\langle \sum_{i=1}^{2} \chi_i \frac{\partial \psi_i}{\partial \boldsymbol{\varepsilon}} (\bar{\boldsymbol{\varepsilon}} + \nabla^{\mathrm{s}}_{\boldsymbol{x}} \boldsymbol{u}, \bar{\theta}, \boldsymbol{z}_i) \right\rangle_Y + \boldsymbol{b} = \boldsymbol{0}, \tag{7.3}$$

where $\langle \square \rangle_Y$ denotes the volume average over Y

$$\langle \square \rangle_Y = \frac{1}{|Y|} \int_Y \square \, \mathrm{d}V. \tag{7.4}$$

Furthermore, $\boldsymbol{b} : \Omega \times [0,T] \to \mathrm{V}^d$ denotes the vector of volume forces and $\operatorname{div}_{\bar{\boldsymbol{x}}}$ designates the divergence operator w.r.t. the macroscopic point $\bar{\boldsymbol{x}} \in \Omega$. Secondly, the macroscopic heat equation reads

$$\bar{c}_\varepsilon \, \dot{\bar{\theta}} = \bar{h} - \operatorname{div}_{\bar{\boldsymbol{x}}}(\bar{\boldsymbol{q}}) + \bar{P}, \tag{7.5}$$

which governs the evolution of the macroscopic absolute temperature $\bar{\theta}$. Here, $\bar{h} : \Omega \times [0,T] \to \mathbb{R}$ denotes the macroscopic heat source and $\bar{\boldsymbol{q}} : \Omega \times [0,T] \to \mathrm{V}^d$ stands for the macroscopic heat flux[2]. The effective

[2] Strictly speaking, to compute the effective heat flux $\bar{\boldsymbol{q}}$ requires solving the cell problem of heat conduction. However, if we restrict to linear heat conduction and assume temperature-independent microscopic thermal conductivities, it suffices to work with the effective thermal conductivity instead, see Section 7.5.

heat capacity at constant strain $\bar{c}_\varepsilon$ is given explicitly by

$$\bar{c}_\varepsilon = -\bar{\theta} \left\langle \sum_{i=1}^{2} \chi_i \frac{\partial^2 \psi}{\partial \theta^2} (\bar{\boldsymbol{\varepsilon}} + \nabla_{\boldsymbol{x}}^{\mathrm{s}} \boldsymbol{u}, \bar{\theta}, \boldsymbol{z}_i) \right\rangle_Y . \tag{7.6}$$

To keep the notation reasonable, we introduced the thermomechanical coupling term

$$\begin{aligned} \bar{P} =& \bar{\theta} \left\langle \sum_{i=1}^{2} \chi_i \frac{\partial^2 \psi_i}{\partial \theta \partial \boldsymbol{\varepsilon}} (\bar{\boldsymbol{\varepsilon}} + \nabla_{\boldsymbol{x}}^{\mathrm{s}} \boldsymbol{u}, \bar{\theta}, \boldsymbol{z}_i) : (\dot{\bar{\boldsymbol{\varepsilon}}} + \nabla_{\boldsymbol{x}}^{\mathrm{s}} \dot{\boldsymbol{u}}) \right\rangle_Y \\ &+ \bar{\theta} \left\langle \sum_{i=1}^{2} \chi_i \frac{\partial^2 \psi_i}{\partial \theta \partial \boldsymbol{z}} (\bar{\boldsymbol{\varepsilon}} + \nabla_{\boldsymbol{x}}^{\mathrm{s}} \boldsymbol{u}, \bar{\theta}, \boldsymbol{z}_i) \cdot \dot{\boldsymbol{z}}_i \right\rangle_Y \\ &- \left\langle \sum_{i=1}^{2} \chi_i \frac{\partial \psi_i}{\partial \boldsymbol{z}} (\bar{\boldsymbol{\varepsilon}} + \nabla_{\boldsymbol{x}}^{\mathrm{s}} \boldsymbol{u}, \bar{\theta}, \boldsymbol{z}_i) \cdot \dot{\boldsymbol{z}}_i \right\rangle_Y \end{aligned} \tag{7.7}$$

as an additional source term of the macroscopic heat equation (7.5). The former constitutes the back-coupling between the microscopic scale and the evolution of the macroscopic temperature. Indeed, the coupling term $\bar{P}$ may be decomposed further. The first two terms are linked to changes in entropy, whereas the last summand is commonly referred to as the (mechanical) dissipation

$$\bar{\mathcal{D}} = - \left\langle \sum_{i=1}^{2} \chi_i \frac{\partial \psi_i}{\partial \boldsymbol{z}} (\bar{\boldsymbol{\varepsilon}} + \nabla_{\boldsymbol{x}}^{\mathrm{s}} \boldsymbol{u}, \bar{\theta}, \boldsymbol{z}_i) \cdot \dot{\boldsymbol{z}}_i \right\rangle_Y . \tag{7.8}$$

The dissipation measures the dissipated energy of the composite due to the evolution of the internal variables, e.g., the dissipated energy due to plastic flow, and is the primary cause for the self-heating of the material due to irreversible processes.

Typically, in a concurrent two-scale setting, the macroscopic balance of linear momentum (7.3) and the macroscopic heat equation (7.5) are solved on the macroscopic scale while, in every Gauss point of the

macroscopic model, the thermomechanical cell problem (7.2) is solved as well. Here, the above-mentioned two-way thermomechanical coupling prevails. On the one hand, the macrostrain $\bar{\varepsilon}$ and the macroscopic absolute temperature $\bar{\theta}$ influence the mechanical behavior on the microscopic scale. On the other hand, the evolution of the macroscopic absolute temperature is driven by the coupling term $\bar{P}$, which comprises deformation induced changes of entropy and dissipated energy on the microscopic scale.

In this chapter, we consider speeding up such a thermomechanical two-scale simulation by means of direct DMNs. In this context, a DMN might be regarded as a surrogate for the underlying microstructure for which the thermomechanical cell problem (7.2) can be solved efficiently. However, to use a DMN to speed up such a fully coupled thermomechanical two-scale simulation, the aforementioned two-way thermomechanical coupling needs to be taken into account.

7.3 Direct DMNs for thermomechanical composites

7.3.1 Two-phase direct DMNs

We consider two-phase direct DMNs as introduced in Section 4.2, i.e., we consider a perfect, ordered, rooted binary tree of depth K, where each node of the binary tree is given by a two-phase laminate $\mathcal{B}_k^i$ with unknown direction of lamination $\boldsymbol{n}_k^i$ and unknown volume fractions $c_{k,1}^i$ and $c_{k,2}^i$. We denote the depth of a node by the letter $k = 1, \ldots, K$ and consistently index the horizontal position by the letter $i = 1, \ldots, 2^{k-1}$.

The DMN's free parameters are given by the directions of lamination, which we collect in the form of a large vector

$$\vec{\boldsymbol{n}} = [\boldsymbol{n}_K^1, \dots, \boldsymbol{n}_K^{2^{K-1}}, \boldsymbol{n}_{K-1}^1, \dots, \boldsymbol{n}_{K-1}^{2^{K-2}}, \dots, \boldsymbol{n}_1^1] \in \left(\mathrm{S}^d\right)^{2^K-1}, \tag{7.9}$$

following a reversed breadth-first ordering, and the volume fractions of all laminates $c_{k,1}^i$ and $c_{k,2}^i$. For reasons of numerical stability, the volume fractions are expressed in terms of the (input) weights w_{K+1}^i, see Section 4.2 for an explanation. These weights are assigned to the laminates at the bottom layer and are required to be non-negative and sum to unity, i.e., the conditions

$$w_{K+1}^i \geq 0 \quad \text{and} \quad \sum_{i=1}^{2^K} w_{K+1}^i = 1 \tag{7.10}$$

hold. We collect the input weights w_{K+1}^i into the vector

$$\vec{w} = [w_{K+1}^1, \dots, w_{K+1}^{2^K}] \in \mathbb{R}_{\geq 0}^{2^K}. \tag{7.11}$$

The network topology of a two-phase direct DMN of depth K is uniquely determined by the vector $\vec{\boldsymbol{n}}$, containing $2^K - 1$ independent directions of lamination, and the vector $\vec{w}$ of weights comprising 2^K scalar parameters, for which $2^K - 1$ parameters are independent.

The process of identifying these free parameters is called the offline training. For isothermal problems DMNs are identified based on linear elastic data alone. However, we wish to predict the effective stress response of the composite for non-isothermal constituents. For this, we assume that the linear elastic training still suffices. Thus, Section 7.3.2 briefly recapitulates the basic idea of training direct DMNs.

After model identification, during the online evaluation, the free parameters $\vec{\boldsymbol{n}}$ and $\vec{w}$ are fixed. Then, the DMN acts as a high-fidelity surrogate model for inelastic computations on the microscopic scale involving

non-isothermal constituents. For this, we elaborate in Section 7.3.3 on how to incorporate the homogeneity of the absolute temperature into the framework and how to consider the back-coupling from the microscopic onto the macroscopic scale to treat multiscale problem with thermomechanical coupling.

7.3.2 Offline training

We represented the training data by a sequence of triples of stiffnesses $\left\{\left(\bar{\mathbb{C}}^s, \mathbb{C}_1^s, \mathbb{C}_2^s\right)\right\}_{s=1}^{N_\mathrm{s}}$ where s enumerates the sample index and N_s the number of samples. For now, we treat the training data as given and refer to Section 7.4.2 for more information on the sampling of the training data.

The direct DMN is trained by solving the regression problem

$$J(\vec{\boldsymbol{n}}, \langle \vec{v} \rangle_+) \longrightarrow \min_{\vec{\boldsymbol{n}}, \vec{v}}, \tag{7.12}$$

involving the loss function

$$J\left(\vec{\boldsymbol{n}}, \vec{w}\right) = \frac{1}{N_\mathrm{s}} \sqrt[q]{\sum_{s=1}^{N_\mathrm{s}} \left(\frac{\left\| \bar{\mathbb{C}}^s - \mathcal{DMN}_Y^{\mathcal{L}}\left(\mathbb{C}_1^s, \mathbb{C}_2^s, \vec{\boldsymbol{n}}, \vec{w}\right) \right\|_p}{\left\| \bar{\mathbb{C}}^s \right\|_p} \right)^q} + \lambda_\mathrm{p} \left(\sum_{i=1}^{2^K} w_{K+1}^i - 1 \right)^2 . \tag{7.13}$$

We solve the regression problem (7.12) by means of accelerated stochastic gradient descent using mini batches. More precisely, for every training epoch j, the loss function (7.13) is evaluated for all stiffness samples in a batch. Then, the gradients $\partial J / \partial \vec{\boldsymbol{n}}$, $\partial J / \partial \vec{v}$ are computed by means of automatic differentiation. Subsequently, the fitting parameters are

updated by

$$\vec{\boldsymbol{n}}_{j+1} = \vec{\boldsymbol{n}}_j - \beta_{\vec{\boldsymbol{n}}} \frac{\partial J}{\partial \vec{\boldsymbol{n}}} \left(\vec{\boldsymbol{n}}_j, \langle \vec{v}_j \rangle_+ \right), \quad \vec{v}_{j+1} = \vec{v}_j - \beta_{\vec{v}} \frac{\partial J}{\partial \vec{v}} \left(\vec{\boldsymbol{n}}_j, \langle \vec{v}_j \rangle_+ \right) \tag{7.14}$$

and

$$\vec{w}_{j+1} = \langle \vec{v}_{j+1} \rangle_+. \tag{7.15}$$

This procedure is repeated for all batches in the training set and for a pre-defined number of epochs. To speed up the training, we use the in Section 5.3.1 introduced procedure to compress the binary tree dynamically. Upon convergence of the algorithm, the unknown fitting parameters of the DMN, i.e., $\vec{\boldsymbol{n}}$ and $\vec{w}$, are given and fixed.

7.3.3 Online evaluation

For fixed fitting parameters $\vec{\boldsymbol{n}}$ and $\vec{w}$, the goal of the online evaluation is to efficiently integrate a direct DMN implicitly at a single Gauss point of a macroscopic FE simulation. Indeed, direct DMNs are defined as a hierarchy of nested laminates. For this reason, they inherit thermodynamic consistency and stress-strain monotonicity from their phases, see Section 4.2 for a discussion. Thus, extending direct DMNs to non-isothermal problems does not infer any challenges from the point of view of thermodynamics. The governing equation, i.e., the DMN's balance of linear momentum, emerges naturally by incorporating the homogeneity of the absolute temperature into the framework. Furthermore, considering the back-coupling from the microscopic onto the macroscopic scale is straightforward as well. Both will be explained in the following.

We consider a two-phase DMN of depth K comprising two non-isothermal GSMs $\mathcal{G}_1 = (\mathcal{Z}_1, \psi_1, \phi_1, \boldsymbol{z}_{0,1})$ and $\mathcal{G}_2 = (\mathcal{Z}_2, \psi_2, \phi_2, \boldsymbol{z}_{0,2})$ as phases. We consider the former as a single laminate with a complex kinematics, comprising 2^K independent phases in total, see Section 4.2.3

for a schematic. We index these phases by the letter $i = 1, \dots, 2^K$ and assign to each phase the non-isothermal GSM $\mathcal{G}_i$ which alternates between $\mathcal{G}_1$ and $\mathcal{G}_2$, i.e.,

$$\mathcal{G}_i = \begin{cases} \mathcal{G}_1 = (\mathcal{Z}_1, \psi_1, \phi_1, \boldsymbol{z}_{0,1}), & i \text{ odd}, \\ \mathcal{G}_2 = (\mathcal{Z}_2, \psi_2, \phi_2, \boldsymbol{z}_{0,2}), & i \text{ even}. \end{cases} \tag{7.16}$$

For each phase $i = 1, \dots, 2^K$, discretizing Biot's equation (2.44) in time with an implicit Euler method gives rise to the condensed free energy potential $\Psi_i : \mathrm{Sym}_2(d) \times \mathbb{R}_{>0} \times \mathcal{Z}_i \to \mathbb{R}$, see Equation (2.47) in Section 2.5, which only depends on the strain increment $\boldsymbol{\varepsilon}_i \in \mathrm{Sym}_2(d)$ and absolute temperature increment $\theta_i \in \mathbb{R}_{>0}$ and the internal variables $\boldsymbol{z}_i^n \in \mathcal{Z}_i$ of the last converged time step. After condensation and for a fixed temperature, the stress of phase i is given by the potential relation

$$\boldsymbol{\sigma}_i = \frac{\partial \Psi_i}{\partial \boldsymbol{\varepsilon}} \left(\boldsymbol{\varepsilon}_i, \theta_i, \boldsymbol{z}_i^n \right). \tag{7.17}$$

In Section 4.2.3, we have seen that the DMN's kinematics admits the representation

$$\vec{\boldsymbol{\varepsilon}} = \vec{\bar{\boldsymbol{\varepsilon}}} + \boldsymbol{D}\vec{\boldsymbol{u}}, \tag{7.18}$$

with the vector of macrostrains $\vec{\bar{\boldsymbol{\varepsilon}}} = [\bar{\boldsymbol{\varepsilon}}, \dots, \bar{\boldsymbol{\varepsilon}}] \in \mathrm{Sym}_2(d)^{2^K}$, the vector of strains $\vec{\boldsymbol{\varepsilon}} = [\boldsymbol{\varepsilon}_1, \dots, \boldsymbol{\varepsilon}_{2^K}] \in \mathrm{Sym}_2(d)^{2^K}$, the vector of displacement jumps $\vec{\boldsymbol{u}} \in (\mathrm{V}^d)^{2^K - 1}$ and the symmetrized gradient operator $\boldsymbol{D} : (\mathrm{V}^d)^{2^K-1} \to \mathrm{Sym}_2(d)^{2^K}$.

From Section 7.2 follows that the homogeneity of the absolute temperature on the microscopic scale implies that only the macroscopic absolute temperature $\bar{\theta}$ needs to be considered, i.e., $\theta_i \equiv \bar{\theta}$ holds for all phases $i = 1, \dots, 2^K$. Thus, the macroscopic absolute temperature $\bar{\theta}$ and the macrostrain $\bar{\boldsymbol{\varepsilon}}$ act as inputs to the DMN. Both are provided by the macroscopic finite element simulation for every Gauss point and for every increment of the global (Newton) solver. As outputs, the effective stress

$\bar{\boldsymbol{\sigma}}$, the thermomechanical coupling term $\bar{P}$ and algorithmic tangents, i.e., the partial derivatives of the effective stress and thermomechanical coupling term w.r.t. the effective strain and macroscopic temperature, need to be returned.

We start with deriving the governing equation of a thermomechanically coupled direct DMN. Let $\bar{\Psi} : \mathrm{Sym}_2(d)^{2^K} \times \bar{\mathcal{Z}} \to \mathbb{R}$ denote the averaged condensed free energy of the DMN

$$\bar{\Psi}(\vec{\boldsymbol{\varepsilon}}, \bar{\theta}, \vec{\boldsymbol{z}}^{\,n}) = \sum_{i=1}^{2^K} w_{K+1}^i \Psi_i(\boldsymbol{\varepsilon}_i, \bar{\theta}, \boldsymbol{z}_i^n) \tag{7.19}$$

where $\vec{\boldsymbol{z}}^{\,n} = \left[\boldsymbol{z}_1^n, \ldots, \boldsymbol{z}_{2^K}^n\right] \in \bar{\mathcal{Z}} = (\mathcal{Z}_1 \oplus \mathcal{Z}_2)^{\oplus^{2^K-1}}$ denotes the vector of internal variables of the last time step. Critical points of the optimization problem

$$\bar{\Psi}(\vec{\bar{\boldsymbol{\varepsilon}}} + \boldsymbol{D}\vec{\boldsymbol{u}}, \bar{\theta}, \vec{\boldsymbol{z}}^{\,n}) \longrightarrow \min_{\vec{\boldsymbol{u}}} \tag{7.20}$$

encode the DMN's (microscopic) balance of linear momentum

$$\boldsymbol{D}^{\mathsf{T}} \boldsymbol{W} \vec{\boldsymbol{\sigma}}(\vec{\bar{\boldsymbol{\varepsilon}}} + \boldsymbol{D}\vec{\boldsymbol{u}}, \bar{\theta}, \vec{\boldsymbol{z}}^{\,n}) = \boldsymbol{0}. \tag{7.21}$$

Here, $\vec{\boldsymbol{\sigma}} = [\boldsymbol{\sigma}_1, \ldots, \boldsymbol{\sigma}_{2^K}] \in \mathrm{Sym}_2(d)^{2^K}$ represents the vector of phase stresses for which Relation (7.17) holds. Furthermore, the weight operator $\boldsymbol{W} : \mathrm{Sym}_2(d)^{2^K} \to \mathrm{Sym}_2(d)^{2^K}$ associates the weights $\vec{w}$ to the corresponding phase stresses $\vec{\boldsymbol{\sigma}}$. The former might be represented as a diagonal matrix with the weights $\vec{w}$ on the diagonal. Indeed, $\boldsymbol{D}^{\mathsf{T}}\boldsymbol{W} : \mathrm{Sym}_2(d)^{2^K} \to (\mathrm{V}^d)^{2^K-1}$ may be regarded as a divergence-type operator, such that the similarity of Relation (7.21) to the thermomechanical cell problem in general form (7.2) is immediately revealed.

For solving the DMN's balance of linear momentum (7.21) for the unknown displacement jumps $\vec{\boldsymbol{u}}$, we rely upon Newton's method. Let j denote the j-th Newton increment. Then, for an initial guess $\vec{\boldsymbol{u}}_0 \in (\mathrm{V}^d)^{2^K-1}$, the unknown displacement jump vector is iteratively

updated,

$$\vec{\boldsymbol{u}}_{j+1} = \vec{\boldsymbol{u}}_j + \beta_j \triangle \vec{\boldsymbol{u}}_j, \tag{7.22}$$

for which the increment $\triangle \vec{\boldsymbol{u}}_j \in \left(\mathrm{V}^d\right)^{2^K-1}$ solves the linear system

$$\left[\boldsymbol{D}^{\mathsf{T}} \boldsymbol{W} \frac{\partial \vec{\boldsymbol{\sigma}}}{\partial \vec{\boldsymbol{\varepsilon}}}(\vec{\boldsymbol{\varepsilon}} + \boldsymbol{D}\vec{\boldsymbol{u}}_j, \bar{\theta}, \vec{\boldsymbol{z}}^{\,n}) \boldsymbol{D}\right] \triangle \vec{\boldsymbol{u}}_j = -\boldsymbol{D}^{\mathsf{T}} \boldsymbol{W} \vec{\boldsymbol{\sigma}}(\vec{\boldsymbol{\varepsilon}} + \boldsymbol{D}\vec{\boldsymbol{u}}_j, \bar{\theta}, \vec{\boldsymbol{z}}^{\,n}). \tag{7.23}$$

To ensure convergence, a step size $\beta_j \in (0, 1]$ less than unity may arise from backtracking with the backtracking factor $\gamma \in (0, 1]$. The Jacobian $\partial \vec{\boldsymbol{\sigma}} / \partial \vec{\boldsymbol{\varepsilon}}$ may be represented by a block-diagonal matrix comprising the (stress-strain related) algorithmic tangents of the phase materials $\partial \boldsymbol{\sigma}_i / \partial \boldsymbol{\varepsilon}$, i.e.,

$$\frac{\partial \vec{\boldsymbol{\sigma}}}{\partial \vec{\boldsymbol{\varepsilon}}}(\vec{\boldsymbol{\varepsilon}}, \bar{\theta}, \vec{\boldsymbol{z}}^{\,n}) = \text{block-diag}\left(\frac{\partial \boldsymbol{\sigma}_1}{\partial \boldsymbol{\varepsilon}}(\boldsymbol{\varepsilon}_1, \bar{\theta}, \boldsymbol{z}_1^n), \ldots, \frac{\partial \boldsymbol{\sigma}_{2^K}}{\partial \boldsymbol{\varepsilon}}(\boldsymbol{\varepsilon}_{2^K}, \bar{\theta}, \boldsymbol{z}_{2^K}^n)\right) \tag{7.24}$$

holds. Upon convergence, the DMN's effective stress $\bar{\boldsymbol{\sigma}}$ is computed via averaging the phase stresses

$$\bar{\boldsymbol{\sigma}} = [\mathbb{I}_{\mathrm{s}}, \ldots, \mathbb{I}_{\mathrm{s}}]^{\mathsf{T}} \boldsymbol{W} \vec{\boldsymbol{\sigma}}(\vec{\boldsymbol{\varepsilon}} + \boldsymbol{D}\vec{\boldsymbol{u}}, \bar{\theta}, \vec{\boldsymbol{z}}^{\,n}), \tag{7.25}$$

where $[\mathbb{I}_{\mathrm{s}}, \ldots, \mathbb{I}_{\mathrm{s}}] \in \mathrm{Sym}_4(d)^{2^K}$ stand for a vector of the identity operators on $\mathrm{Sym}_2(d)$.

In Section 7.2, we learned that the evolution of the macroscopic temperature $\bar{\theta}$ is coupled to the microscopic scale by the thermomechanical coupling term $\bar{P}$. For computing $\bar{P}$ efficiently, we introduce the phase-wise coupling term

$$\begin{aligned} P_i(\boldsymbol{\varepsilon}_i, \bar{\theta}, \boldsymbol{z}_i^n) = \bar{\theta} \frac{\partial^2 \Psi_i}{\partial \theta \partial \boldsymbol{\varepsilon}}(\boldsymbol{\varepsilon}_i, \bar{\theta}, \boldsymbol{z}_i^n) : \frac{\boldsymbol{\varepsilon}_i - \boldsymbol{\varepsilon}_i^n}{\triangle t} \\ + \left[\bar{\theta} \frac{\partial^2 \Psi_i}{\partial \theta \partial \boldsymbol{z}}(\boldsymbol{\varepsilon}_i, \bar{\theta}, \boldsymbol{z}_i^n) - \frac{\partial \Psi_i}{\partial \boldsymbol{z}}(\boldsymbol{\varepsilon}_i, \bar{\theta}, \boldsymbol{z}_i^n)\right] \cdot \frac{\boldsymbol{z}_i - \boldsymbol{z}_i^n}{\triangle t} \end{aligned} \tag{7.26}$$

for every phase $i = 1, \dots, 2^K$, individually. With the vector of coupling terms $\vec{P} = [P_1, \dots, P_{2^K}] \in \mathbb{R}^{2^K}$, the vector of ones $[1, \dots, 1] \in \mathbb{R}^{2^K}$ and the weight operator $\hat{\boldsymbol{W}} : \mathbb{R}^{2^K} \to \mathbb{R}^{2^K}$, which associates the weights $\vec{w}$ to the corresponding values in $\vec{P}$, we compute $\bar{P}$ by averaging, i.e.,

$$\bar{P} = [1, \dots, 1]^{\mathsf{T}} \hat{\boldsymbol{W}} \vec{P}(\vec{\bar{\varepsilon}} + \boldsymbol{D}\vec{\boldsymbol{u}}, \bar{\theta}, \vec{\boldsymbol{z}}^{\,n}) \tag{7.27}$$

holds.

To employ a direct DMN in a two-scale simulation, four algorithmic tangents need to be computed and provided to the macroscopic solver. We start with the algorithmic tangents related to the effective stress. Derivation of the effective stress $\bar{\boldsymbol{\sigma}}$ (7.25) w.r.t. the effective strain $\bar{\varepsilon}$ and the absolute temperature $\bar{\theta}$ gives rise to the DMN's (stress-related) algorithmic tangents

$$\bar{\mathbb{C}}^{\text{algo}}_{\bar{\varepsilon}} = \frac{\partial \bar{\boldsymbol{\sigma}}}{\partial \bar{\varepsilon}} = [\mathbb{I}_{\text{s}}, \dots, \mathbb{I}_{\text{s}}]^{\mathsf{T}} \boldsymbol{W} \left[\frac{\partial \vec{\boldsymbol{\sigma}}}{\partial \vec{\bar{\varepsilon}}}(\vec{\bar{\varepsilon}} + \boldsymbol{D}\vec{\boldsymbol{u}}, \bar{\theta}, \vec{\boldsymbol{z}}^{\,n}) + \frac{\partial \vec{\boldsymbol{\sigma}}}{\partial \vec{\bar{\varepsilon}}}(\vec{\bar{\varepsilon}} + \boldsymbol{D}\vec{\boldsymbol{u}}, \bar{\theta}, \vec{\boldsymbol{z}}^{\,n}) \boldsymbol{D} \frac{\partial \vec{\boldsymbol{u}}}{\partial \bar{\varepsilon}} \right] \tag{7.28}$$

and

$$\bar{\boldsymbol{C}}^{\text{algo}}_{\bar{\theta}} = \frac{\partial \bar{\boldsymbol{\sigma}}}{\partial \bar{\theta}} = [\mathbb{I}_{\text{s}}, \dots, \mathbb{I}_{\text{s}}]^{\mathsf{T}} \boldsymbol{W} \left[\frac{\partial \vec{\boldsymbol{\sigma}}}{\partial \bar{\theta}}(\vec{\bar{\varepsilon}} + \boldsymbol{D}\vec{\boldsymbol{u}}, \bar{\theta}, \vec{\boldsymbol{z}}^{\,n}) + \frac{\partial \vec{\boldsymbol{\sigma}}}{\partial \vec{\bar{\varepsilon}}}(\vec{\bar{\varepsilon}} + \boldsymbol{D}\vec{\boldsymbol{u}}, \bar{\theta}, \vec{\boldsymbol{z}}^{\,n}) \boldsymbol{D} \frac{\partial \vec{\boldsymbol{u}}}{\partial \bar{\theta}} \right]. \tag{7.29}$$

To get compact expressions, we introduced the vectors of algorithmic tangents

$$\frac{\partial \vec{\boldsymbol{\sigma}}}{\partial \vec{\bar{\varepsilon}}}(\vec{\varepsilon}, \bar{\theta}, \vec{\boldsymbol{z}}^{\,n}) = \left[\frac{\partial \boldsymbol{\sigma}_1}{\partial \boldsymbol{\varepsilon}}(\varepsilon_1, \bar{\theta}, \boldsymbol{z}_1^n), \dots, \frac{\partial \boldsymbol{\sigma}_{2^K}}{\partial \boldsymbol{\varepsilon}}(\varepsilon_{2^K}, \bar{\theta}, \boldsymbol{z}_{2^K}^n) \right] \tag{7.30}$$

and

$$\frac{\partial \vec{\boldsymbol{\sigma}}}{\partial \bar{\theta}}(\vec{\boldsymbol{\varepsilon}}, \bar{\theta}, \vec{\boldsymbol{z}}^{\,n}) = \left[\frac{\partial \boldsymbol{\sigma}_1}{\partial \theta}(\boldsymbol{\varepsilon}_1, \bar{\theta}, \boldsymbol{z}_1^n), \ldots, \frac{\partial \boldsymbol{\sigma}_{2^K}}{\partial \theta}(\boldsymbol{\varepsilon}_{2^K}, \bar{\theta}, \boldsymbol{z}_{2^K}^n) \right] \tag{7.31}$$

which arise by inserting $\partial \boldsymbol{\sigma}_i / \partial \boldsymbol{\varepsilon}$ and $\partial \boldsymbol{\sigma}_i / \partial \theta$ into column vectors. To evaluate Expressions (7.28) and (7.29), the partial derivatives of the displacement jump vector $\vec{\boldsymbol{u}}$ with respect to the macrostrain $\bar{\boldsymbol{\varepsilon}}$ and the absolute temperature $\bar{\theta}$ need to be computed first. To this end, differentiating the balance of linear momentum (7.21) with respect to the macrostrain $\bar{\boldsymbol{\varepsilon}}$ and the absolute temperature $\bar{\theta}$ yields the linear systems

$$\left[\boldsymbol{D}^{\mathsf{T}} \boldsymbol{W} \frac{\partial \vec{\boldsymbol{\sigma}}}{\partial \vec{\boldsymbol{\varepsilon}}}(\vec{\boldsymbol{\varepsilon}} + \boldsymbol{D}\vec{\boldsymbol{u}}, \bar{\theta}, \vec{\boldsymbol{z}}^{\,n}) \boldsymbol{D} \right] \frac{\partial \vec{\boldsymbol{u}}}{\partial \bar{\boldsymbol{\varepsilon}}} = -\boldsymbol{D}^{\mathsf{T}} \boldsymbol{W} \frac{\partial \vec{\boldsymbol{\sigma}}}{\partial \bar{\boldsymbol{\varepsilon}}}(\vec{\boldsymbol{\varepsilon}} + \boldsymbol{D}\vec{\boldsymbol{u}}, \bar{\theta}, \vec{\boldsymbol{z}}^{\,n}) \tag{7.32}$$

and

$$\left[\boldsymbol{D}^{\mathsf{T}} \boldsymbol{W} \frac{\partial \vec{\boldsymbol{\sigma}}}{\partial \vec{\boldsymbol{\varepsilon}}}(\vec{\boldsymbol{\varepsilon}} + \boldsymbol{D}\vec{\boldsymbol{u}}, \bar{\theta}, \vec{\boldsymbol{z}}^{\,n}) \boldsymbol{D} \right] \frac{\partial \vec{\boldsymbol{u}}}{\partial \bar{\theta}} = -\boldsymbol{D}^{\mathsf{T}} \boldsymbol{W} \frac{\partial \vec{\boldsymbol{\sigma}}}{\partial \bar{\theta}}(\vec{\boldsymbol{\varepsilon}} + \boldsymbol{D}\vec{\boldsymbol{u}}, \bar{\theta}, \vec{\boldsymbol{z}}^{\,n}) \tag{7.33}$$

which need to be solved for $\partial \vec{\boldsymbol{u}} / \partial \bar{\boldsymbol{\varepsilon}}$ and $\partial \vec{\boldsymbol{u}} / \partial \bar{\theta}$. By comparing Equations (7.32) and (7.33) to (7.23), we observe that all three problems share the same linear operator, i.e., only the right hand sides differ. Using a direct solver, e.g., a Cholesky decomposition, the matrix decomposition can be reused to minimize the computational overhead.

Derivation of the effective coupling term $\bar{P}$ (7.27) w.r.t. the macrostrain $\bar{\boldsymbol{\varepsilon}}$ and absolute temperature $\bar{\theta}$ gives rise to the DMN's (power-related) algorithmic tangents

$$\bar{\boldsymbol{K}}_{\bar{\varepsilon}}^{\text{algo}} = \frac{\partial \bar{P}}{\partial \bar{\boldsymbol{\varepsilon}}} = [1, \ldots, 1]^{\mathsf{T}} \hat{\boldsymbol{W}} \left[\frac{\partial \vec{P}}{\partial \vec{\boldsymbol{\varepsilon}}}(\vec{\boldsymbol{\varepsilon}} + \boldsymbol{D}\vec{\boldsymbol{u}}, \bar{\theta}, \vec{\boldsymbol{z}}^{\,n}) + \frac{\partial \vec{P}}{\partial \vec{\boldsymbol{\varepsilon}}}(\vec{\boldsymbol{\varepsilon}} + \boldsymbol{D}\vec{\boldsymbol{u}}, \bar{\theta}, \vec{\boldsymbol{z}}^{\,n}) \boldsymbol{D} \frac{\partial \vec{\boldsymbol{u}}}{\partial \bar{\boldsymbol{\varepsilon}}} \right] \tag{7.34}$$

and

$$\bar{K}_{\bar{\theta}}^{\text{algo}} = \frac{\partial \bar{P}}{\partial \bar{\theta}} = [1, \dots, 1]^{\mathsf{T}} \hat{\boldsymbol{W}} \left[\frac{\partial \vec{P}}{\partial \bar{\theta}} (\vec{\boldsymbol{\varepsilon}} + \boldsymbol{D}\vec{\boldsymbol{u}}, \bar{\theta}, \vec{\boldsymbol{z}}^{\,n}) + \frac{\partial \vec{P}}{\partial \vec{\boldsymbol{\varepsilon}}} (\vec{\boldsymbol{\varepsilon}} + \boldsymbol{D}\vec{\boldsymbol{u}}, \bar{\theta}, \vec{\boldsymbol{z}}^{\,n}) \boldsymbol{D} \frac{\partial \vec{\boldsymbol{u}}}{\partial \bar{\theta}} \right]. \quad (7.35)$$

As before, $\partial \vec{P} / \partial \vec{\boldsymbol{\varepsilon}}$ denotes the block-diagonal matrix of phase-wise algorithmic tangents

$$\frac{\partial \vec{P}}{\partial \vec{\boldsymbol{\varepsilon}}} (\vec{\boldsymbol{\varepsilon}}, \bar{\theta}, \vec{\boldsymbol{z}}^{\,n}) = \text{block-diag} \left(\frac{\partial P_1}{\partial \boldsymbol{\varepsilon}} (\boldsymbol{\varepsilon}_1, \bar{\theta}, \boldsymbol{z}_1^n), \dots, \frac{\partial P_{2^K}}{\partial \boldsymbol{\varepsilon}} (\boldsymbol{\varepsilon}_{2^K}, \bar{\theta}, \boldsymbol{z}_{2^K}^n) \right). \quad (7.36)$$

Furthermore, for brevity, the vectors of the (power-related) algorithmic tangents

$$\frac{\partial \vec{P}}{\partial \bar{\boldsymbol{\varepsilon}}} (\vec{\boldsymbol{\varepsilon}}, \bar{\theta}, \vec{\boldsymbol{z}}^{\,n}) = \left[\frac{\partial P_1}{\partial \boldsymbol{\varepsilon}} (\boldsymbol{\varepsilon}_1, \bar{\theta}, \boldsymbol{z}_1^n), \dots, \frac{\partial P_{2^K}}{\partial \boldsymbol{\varepsilon}} (\boldsymbol{\varepsilon}_{2^K}, \bar{\theta}, \boldsymbol{z}_{2^K}^n) \right] \quad (7.37)$$

and

$$\frac{\partial \vec{P}}{\partial \bar{\theta}} (\vec{\boldsymbol{\varepsilon}}, \bar{\theta}, \vec{\boldsymbol{z}}^{\,n}) = \left[\frac{\partial P_1}{\partial \theta} (\boldsymbol{\varepsilon}_1, \bar{\theta}, \boldsymbol{z}_1^n), \dots, \frac{\partial P_{2^K}}{\partial \theta} (\boldsymbol{\varepsilon}_{2^K}, \bar{\theta}, \boldsymbol{z}_{2^K}^n) \right] \quad (7.38)$$

were introduced. Indeed, to efficiently compute Relations (7.34) and (7.35), the already computed partial derivatives $\partial \vec{\boldsymbol{u}} / \partial \bar{\boldsymbol{\varepsilon}}$ and $\partial \vec{\boldsymbol{u}} / \partial \bar{\theta}$ are reused.

Later on in Section 7.4.5, we take a closer look at the effective dissipation $\bar{\mathcal{D}}$ to assess the self-heating of the DMN under cyclic and non-cyclic loading. For this reason, we compute the phase-wise dissipation by

$$\mathcal{D}_i(\boldsymbol{\varepsilon}_i, \bar{\theta}, \boldsymbol{z}_i^n) = -\frac{\partial \Psi_i}{\partial \boldsymbol{z}} (\boldsymbol{\varepsilon}_i, \bar{\theta}, \boldsymbol{z}_i^n) \cdot \frac{\boldsymbol{z}_i - \boldsymbol{z}_i^n}{\triangle t} \quad (7.39)$$

with

$$\vec{\mathcal{D}} = [\mathcal{D}_1, \ldots, \mathcal{D}_{2^K}] \in \mathbb{R}^{2^K}. \tag{7.40}$$

Then, the effective dissipation is computed by averaging

$$\bar{\mathcal{D}} = [1, \ldots, 1]^{\mathsf{T}} \hat{\boldsymbol{W}} \vec{\mathcal{D}}(\vec{\boldsymbol{\varepsilon}} + \boldsymbol{D}\vec{\boldsymbol{u}}, \bar{\theta}, \vec{\boldsymbol{z}}^{\,n}). \tag{7.41}$$

The pseudo-code summarizing the relevant steps of the algorithm can be found in Algorithm 2. Please note that the effective stress $\bar{\boldsymbol{\sigma}}$, the effective thermomechanical coupling term $\bar{P}$, the effective dissipation $\bar{\mathcal{D}}$ and the algorithmic tangents $\bar{\mathbb{C}}_{\bar{\varepsilon}}^{\text{algo}}$, $\bar{\boldsymbol{C}}_{\bar{\theta}}^{\text{algo}}$, $\bar{\boldsymbol{K}}_{\bar{\varepsilon}}^{\text{algo}}$ and $\bar{K}_{\bar{\theta}}^{\text{algo}}$ are computed after the convergence of Newton's method for reasons of numerical efficiency.

Algorithm 2 Pseudo-code for the online evaluation
Fixed parameters: tol, maxit, maxbacktrack, γ
Input: $\bar{\boldsymbol{\varepsilon}}^{n+1}$, $\bar{\theta}^{n+1}$, $\vec{\boldsymbol{z}}^{\,n}$, $\vec{\boldsymbol{u}}^{\,n}$
Output: $\bar{\boldsymbol{\sigma}}^{n+1}$, $\bar{P}^{n+1}$, $\bar{\mathbb{C}}^{\text{algo}}_{\bar{\varepsilon}}$, $\bar{\boldsymbol{C}}^{\text{algo}}_{\bar{\theta}}$, $\bar{\boldsymbol{K}}^{\text{algo}}_{\bar{\varepsilon}}$, $\bar{K}^{\text{algo}}_{\bar{\theta}}$, $\vec{\boldsymbol{z}}^{\,n+1}$, $\vec{\boldsymbol{u}}^{\,n+1}$

$\vec{\boldsymbol{u}}^{\,n+1} \leftarrow \vec{\boldsymbol{u}}^{\,n}$ ▷ Reuse old displacement jumps with $\vec{\boldsymbol{u}}^{\,0} \leftarrow \boldsymbol{0}$.
res $\leftarrow$ RESIDUAL$(\bar{\boldsymbol{\varepsilon}}^{n+1}, \bar{\theta}^{n+1}, \vec{\boldsymbol{u}}^{\,n+1}, \vec{\boldsymbol{z}}^{\,n})$ ▷ Compute residual
for $i = 1$ **to** maxit **do**
  $\left[\boldsymbol{D}^{\mathsf{T}}\boldsymbol{W}\frac{\partial \vec{\boldsymbol{\sigma}}}{\partial \vec{\boldsymbol{\varepsilon}}}\boldsymbol{D}\right] \triangle\vec{\boldsymbol{u}}^{\,n+1} = -\boldsymbol{D}^{\mathsf{T}}\boldsymbol{W}\vec{\boldsymbol{\sigma}}$ ▷ Solve linear system
  res $\leftarrow$ BACKTRACKING$(\bar{\boldsymbol{\varepsilon}}^{n+1}, \bar{\theta}^{n+1}, \vec{\boldsymbol{u}}^{\,n+1}, \triangle\vec{\boldsymbol{u}}^{\,n+1}, \vec{\boldsymbol{z}}^{\,n}, \text{res})$
  if res $<$ tol **then**
    break ▷ Break if residual is smaller than tolerance
  end if
end for
Update state variables $\vec{\boldsymbol{z}}^{\,n}$ to $\vec{\boldsymbol{z}}^{\,n+1}$ and compute $\bar{\boldsymbol{\sigma}}^{n+1}$, $\bar{P}^{n+1}$, $\bar{\mathcal{D}}^{n+1}$, $\bar{\mathbb{C}}^{\text{algo}}_{\bar{\varepsilon}}$, $\bar{\boldsymbol{C}}^{\text{algo}}_{\bar{\theta}}$, $\bar{\boldsymbol{K}}^{\text{algo}}_{\bar{\varepsilon}}$, $\bar{K}^{\text{algo}}_{\bar{\theta}}$

function RESIDUAL$(\bar{\boldsymbol{\varepsilon}}^{n+1}, \bar{\theta}^{n+1}, \vec{\boldsymbol{u}}^{\,n+1}, \vec{\boldsymbol{z}}^{\,n})$
  $\vec{\boldsymbol{\varepsilon}}^{\,n+1} \leftarrow \vec{\bar{\boldsymbol{\varepsilon}}}^{\,n+1} + \boldsymbol{D}\vec{\boldsymbol{u}}^{\,n+1}$ ▷ Compute phase strains
  for $i = 1$ **to** 2^K **do**
    $\boldsymbol{\sigma}_i^{n+1} \leftarrow \frac{\partial \Psi_i}{\partial \boldsymbol{\varepsilon}} \left(\boldsymbol{\varepsilon}_i^{n+1}, \bar{\theta}^{n+1}, \boldsymbol{z}_i^n\right)$ ▷ Evaluate material laws
  end for
  res $\leftarrow \frac{\| \boldsymbol{D}^{\mathsf{T}}\boldsymbol{W}\vec{\boldsymbol{\sigma}}^{n+1} \|_{\mathrm{F}}}{(2^K-1)\| \bar{\boldsymbol{\sigma}}^{\,n+1} \|_{\mathrm{F}}}$ with $\bar{\boldsymbol{\sigma}}^{n+1} \leftarrow \sum_{i=1}^{2^K} w_{K+1}^i \boldsymbol{\sigma}_i^{n+1}$
  return res
end function

function BACKTRACKING($\bar{\boldsymbol{\varepsilon}}^{n+1}$, $\bar{\theta}^{n+1}$, $\vec{\boldsymbol{u}}^{\,n+1}$, $\triangle\vec{\boldsymbol{u}}^{\,n+1}$, $\vec{\boldsymbol{z}}^{\,n}$, $\mathrm{res}_{\mathrm{old}}$)
  $\vec{\boldsymbol{u}}^{\,n+1} \leftarrow \vec{\boldsymbol{u}}^{\,n+1} + \triangle\vec{\boldsymbol{u}}^{\,n+1}$ ▷ Update displacement jumps
  res $\leftarrow$ RESIDUAL($\bar{\boldsymbol{\varepsilon}}^{n+1}, \bar{\theta}^{n+1}, \vec{\boldsymbol{u}}^{\,n+1}, \vec{\boldsymbol{z}}^{\,n}$) ▷ Update residual
  for $i \leftarrow 0$ **to** maxbacktrack $- 1$ **do**
    if res $<$ $\mathrm{res}_{\mathrm{old}}$ **then**
      break ▷ Break if residual decreases
    end if
    $\vec{\boldsymbol{u}}^{\,n+1} \leftarrow \vec{\boldsymbol{u}}^{\,n+1} - \gamma^i(1-\gamma)\triangle\vec{\boldsymbol{u}}^{\,n+1}$ ▷ Backtracking
    res $\leftarrow$ RESIDUAL($\bar{\boldsymbol{\varepsilon}}^{n+1}, \bar{\theta}^{n+1}, \vec{\boldsymbol{u}}^{\,n+1}, \vec{\boldsymbol{z}}^{\,n}$)
  end for
  return res
end function

7.4 Identifying the DMN surrogate model

7.4.1 Short fiber reinforced polyamide

In general, thermoplastic polymers feature a pronounced thermomechanical coupling. For this reason, we study a short fiber reinforced polyamide 6.6 (PA66) as our benchmark composite. As reinforcement, we consider E-glass fibers with a (uniform) fiber length of $L_{\mathrm{f}} = 200\,\mu\mathrm{m}$ and a fiber diameter of $D_{\mathrm{f}} = 10\,\mu\mathrm{m}$. We choose a fiber volume fraction of $c_{\mathrm{f}} = 16\,\mathrm{vol}\%$, which corresponds to a fiber mass fraction of approximately $30\,\mathrm{wt}\%$. The fiber orientation is described by a transversely isotropic fiber orientation tensor of second-order (Advani and Tucker, 1987) which reads

$$\boldsymbol{A}_2 = \begin{bmatrix} 0.8 & 0 & 0 \\ 0 & 0.1 & 0 \\ 0 & 0 & 0.1 \end{bmatrix} \boldsymbol{e}_i \otimes \boldsymbol{e}_j, \tag{7.42}$$

i.e., $80\,\%$ of the fibers point in the $\boldsymbol{e}_1$ direction, whereas $20\,\%$ of the fibers are uniformly distributed in the $\boldsymbol{e}_2$-$\boldsymbol{e}_3$ plane. Figure 7.1 illustrates an example of such a microstructure comprising 577 fibers.

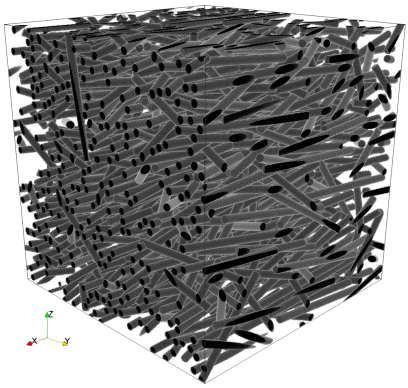

Figure 7.1: Artificial microstructure comprising 577 straight cylindrical fibers

E-glass fibers

We model the E-glass fibers as isotropic linear thermoelastic. We rely upon the commonly used additive splitting of the (volume-specific) Helmholtz free energy density

$$\psi(\boldsymbol{\varepsilon}, \theta) = \psi_{\text{mech}}(\boldsymbol{\varepsilon}, \theta) + \psi_{\text{heat}}(\theta) \tag{7.43}$$

into two parts. The first part $\psi_{\text{mech}}(\boldsymbol{\varepsilon}, \theta)$ represents the storage of mechanical energy whereas the second part $\psi_{\text{heat}}(\theta)$ represent the heat-storage alone. We assume the heat capacity at constant strain to be independent of the deformation $\boldsymbol{\varepsilon}$. Thus, the mechanical part of the Helmholtz free energy $\psi_{\text{mech}}(\boldsymbol{\varepsilon}, \theta)$ may at most be linear in the temperature and

$$c_{\varepsilon}(\theta) = -\theta \frac{\partial^2 \psi_{\text{heat}}}{\partial \theta^2}(\theta) \tag{7.44}$$

holds. For a constant heat capacity at constant strain $c_\varepsilon(\theta) = c_{\varepsilon,0}$, the heat storage part of the Helmholtz free energy reads

$$\psi_{\text{heat}}(\theta) = c_{\varepsilon,0}\left[(\theta - \theta_0) - \theta \ln\left(\frac{\theta}{\theta_0}\right)\right], \tag{7.45}$$

where θ_0 stands for the reference temperature. The mechanical part of the Helmholtz free energy is given by the following quadratic form

$$\psi_{\text{mech}}(\boldsymbol{\varepsilon}, \theta) = \frac{1}{2}\boldsymbol{\varepsilon} : \mathbb{C}\left[\boldsymbol{\varepsilon}\right] - \boldsymbol{\varepsilon} : \mathbb{C}[\boldsymbol{\alpha}(\theta - \theta_0)] \tag{7.46}$$

such that the stress response of the material computes to

$$\boldsymbol{\sigma} = \mathbb{C}\left[\boldsymbol{\varepsilon} - \boldsymbol{\alpha}(\theta - \theta_0)\right]. \tag{7.47}$$

Both the stiffness $\mathbb{C}$ and the coefficient of thermal expansion $\boldsymbol{\alpha}$ are assumed to be isotropic, i.e., the following relations

$$\mathbb{C} = 3K\mathbb{P}_1 + 2G\mathbb{P}_2 \quad \text{and} \quad \boldsymbol{\alpha} = \alpha_0 \boldsymbol{I} \tag{7.48}$$

hold with the projection operators $\mathbb{P}_1 : \mathrm{Sym}_2(d) \to \mathrm{Sym}_2(d)$ and $\mathbb{P}_2 : \mathrm{Sym}_2(d) \to \mathrm{Sym}_2(d)$ on the spherical and deviatoric subspaces of $\mathrm{Sym}_2(d)$, and $\boldsymbol{I} : \mathrm{V}^d \to \mathrm{V}^d$ denotes the identity on V^d. The bulk modulus $K \in \mathbb{R}_{>0}$ and the shear modulus $G \in \mathbb{R}_{>0}$ may be expressed in terms of the Young's modulus $E \in \mathbb{R}_{>0}$ and the Poisson's ratio $\nu \in (-1, 0.5)$, i.e.,

$$K = \frac{E}{3(1-2\nu)} \quad \text{and} \quad G = \frac{E}{2(1+\nu)}. \tag{7.49}$$

As the material is purely elastic, the dissipation potential vanishes identically $\phi(\theta) \equiv 0$ and $\mathcal{Z} = \{0\}$ holds. Thus, the thermomechanical

coupling term

$$\begin{aligned} P(\boldsymbol{\varepsilon}, \theta) &= \theta \frac{\partial^2 \psi}{\partial \theta \partial \boldsymbol{\varepsilon}}(\boldsymbol{\varepsilon}, \theta) : \dot{\boldsymbol{\varepsilon}} \\ &= -\theta\, \dot{\boldsymbol{\varepsilon}} : \mathbb{C}\,[\boldsymbol{\alpha}] \end{aligned} \tag{7.50}$$

is solely dependent on the strain rate $\dot{\boldsymbol{\varepsilon}}$ due to a vanishing dissipation, i.e., $\mathcal{D} \equiv 0$ holds. In fact, a non-vanishing strain rate causes self-cooling under hydrostatic extension and self-heating under hydrostatic compression. This effect is commonly referred to as Gough-Joule effect, see, e.g., Section 96 in Truesdell and Noll (2004). The material parameters for the E-glass fibers are taken from Tikarrouchine et al. (2019) and are summarized in Table 7.1.

Young's modulus	$E = 72.0\,\mathrm{GPa}$
Poisson's ratio	$\nu = 0.26$
Heat capacity	$c_{\varepsilon,0} = 2.1 \cdot 10^6\,\mathrm{J/(m^3K)}$
Thermal expansion	$\alpha_0 = 9 \cdot 10^{-6}\,1/\mathrm{K}$
Thermal conductivity	$\kappa_0 = 0.93\,\mathrm{W/(mK)}$

Table 7.1: Material parameters of the E-glass fibers (Tikarrouchine et al., 2019)

Polyamide 6.6 matrix

For modeling the material behavior of the PA66 matrix, we adapt the model proposed by Krairi et al. (2019), which was specifically derived for thermoplastic polymers under non-isothermal conditions. The model couples linear viscoelasticity, viscoplasticity and thermal effects such as thermal softening and dissipative self-heating. More precisely, the linear viscoelastic part of the model is given by a generalized Maxwell model comprising N_M Maxwell elements, and the viscoplastic part is governed by J_2-viscoplasticity. We refer to Krairi et al. (2019) for all underlying modeling assumptions and the experimental calibration of the model.

For the PA66 matrix, we prescribe the following heat-storage related free Helmholtz energy density

$$\psi_{\text{heat}}(\theta) = c_{\varepsilon,0}\left[(\theta-\theta_0) - \theta\ln\left(\frac{\theta}{\theta_0}\right)\right]. \tag{7.51}$$

Furthermore, the mechanical part of the Helmholtz free energy density reads

$$\begin{aligned}\psi_{\text{mech}}(\boldsymbol{\varepsilon},\theta,\boldsymbol{z}) = {}& \frac{1}{2}(\boldsymbol{\varepsilon}-\boldsymbol{\varepsilon}_{\text{vp}}) : \mathbb{C}_\infty[\boldsymbol{\varepsilon}-\boldsymbol{\varepsilon}_{\text{vp}}] - (\boldsymbol{\varepsilon}-\boldsymbol{\varepsilon}_{\text{vp}}) : \mathbb{C}_\infty[\boldsymbol{\alpha}(\theta-\theta_0)] \\ & + \frac{1}{2}\sum_{i=1}^{N_{\text{M}}}(\boldsymbol{\varepsilon}-\boldsymbol{\varepsilon}_{\text{vp}}-\boldsymbol{\varepsilon}_{\text{v},i}) : \mathbb{C}_i[\boldsymbol{\varepsilon}-\boldsymbol{\varepsilon}_{\text{vp}}-\boldsymbol{\varepsilon}_{\text{v},i}] \\ & - \sum_{i=1}^{N_{\text{M}}}(\boldsymbol{\varepsilon}-\boldsymbol{\varepsilon}_{\text{vp}}-\boldsymbol{\varepsilon}_{\text{v},i}) : \mathbb{C}_i[\boldsymbol{\alpha}(\theta-\theta_0)] \\ & + \int_0^{\varepsilon_{\text{vp}}} H(\theta,\hat{\varepsilon}_{\text{vp}})\ \mathrm{d}\hat{\varepsilon}_{\text{vp}}.\end{aligned} \tag{7.52}$$

For readability, we collected the state variables, i.e., the accumulated viscoplastic strain ε_{vp}, the viscoplastic strain $\boldsymbol{\varepsilon}_{\text{vp}}$ and the viscoelastic strains $\{\boldsymbol{\varepsilon}_{\text{v},i}\}_{i=1}^{N}$ into the state vector $\boldsymbol{z} = [\varepsilon_{\text{vp}}, \boldsymbol{\varepsilon}_{\text{vp}}, \boldsymbol{\varepsilon}_{\text{v},1}, \ldots, \boldsymbol{\varepsilon}_{\text{v},N}] \in \mathcal{Z} = \mathbb{R}_{\geq 0} \oplus \text{Dev}_2(d) \oplus \text{Sym}_2(d)^{N_{\text{M}}}$.

With the Helmholtz free energy density (7.52) at hand, the material's stress response computes to

$$\boldsymbol{\sigma} = \mathbb{C}_\infty[\boldsymbol{\varepsilon}-\boldsymbol{\varepsilon}_{\text{vp}}-\boldsymbol{\alpha}(\theta-\theta_0)] + \sum_{i=1}^{N_{\text{M}}}\mathbb{C}_i[\boldsymbol{\varepsilon}-\boldsymbol{\varepsilon}_{\text{vp}}-\boldsymbol{\varepsilon}_{\text{v},i}-\boldsymbol{\alpha}(\theta-\theta_0)]. \tag{7.53}$$

For a fixed viscoplastic strain $\boldsymbol{\varepsilon}_{\text{vp}}$, we assume the material to be linear and isotropic, both in its long-term elastic and its purely viscoelastic response and to feature an isotropic thermal expansion. More precisely, the stiffness governing infinitely slow processes $\mathbb{C}_\infty$, the stiffness $\mathbb{C}_i$

associated to the i-th dashpot and the coefficient of thermal expansion $\boldsymbol{\alpha}$ admit the representations

$$\mathbb{C}_\infty = 3K_\infty \mathbb{P}_1 + 2G_\infty \mathbb{P}_2, \quad \mathbb{C}_i = 3K_i \mathbb{P}_1 + 2G_i \mathbb{P}_2 \quad \text{and} \quad \boldsymbol{\alpha} = \alpha_0 \boldsymbol{I}. \tag{7.54}$$

The bulk $K_\infty,\ K_i \in \mathbb{R}_{>0}$ and shear moduli $G_\infty,\ G_i \in \mathbb{R}_{>0}$ are expressed in terms of the Young's moduli $E_\infty,\ E_i \in \mathbb{R}_{>0}$ and the Poisson's ratio $\nu \in (-1, 0.5)$, i.e., the following relations

$$\begin{aligned} K_\infty &= \frac{E_\infty}{3(1-2\nu)}, \quad K_i = \frac{E_i}{3(1-2\nu)}, \\ G_\infty &= \frac{E_\infty}{2(1+\nu)} \quad \text{and} \quad G_i = \frac{E_i}{2(1+\nu)} \end{aligned} \tag{7.55}$$

hold. Indeed, for the model at hand, the bulk and shear moduli K_i and G_i are coupled due to an assumed constant Poisson's ratio ν, see Krairi et al. (2019). Such an assumption is not unusual if only experimental data from uniaxial experiments are available.

Concerning the thermo-viscoelastic behavior, we assume the PA66 to be thermorheologically simple, i.e., the viscosity tensor $\mathbb{V}_i$ associated to the i-th dashpot of the generalized Maxwell model should have the form

$$\mathbb{V}_i = a_\theta(\theta) \left(3K_i \, \tau_{\mathrm{K},i} \, \mathbb{P}_1 + 2G_i \tau_{\mathrm{G},i} \, \mathbb{P}_2\right), \tag{7.56}$$

where $a_\theta : \mathbb{R}_{>0} \to \mathbb{R}_{>0}$ denotes a temperature-dependent shift function. For the i-th dashpot, the volumetric and deviatoric relaxation times

$$\tau_{\mathrm{K},i} = \frac{\tau_i E_i}{K_i} \quad \text{and} \quad \tau_{\mathrm{G},i} = \frac{\tau_i E_i}{G_i} \tag{7.57}$$

are expressed in terms of the Young's modulus E_i, the bulk and shear moduli K_i and G_i and the relaxation time τ_i. The fluidity tensor $\mathbb{F}_i$ is given by the pseudoinverse of the viscosity tensor $\mathbb{F}_i = \mathbb{V}_i^\dagger$, giving rise

to the evolution equation for the viscous strain

$$\dot{\boldsymbol{\varepsilon}}_{\mathrm{v},i} = \mathbb{F}_i \left[\boldsymbol{\sigma}_{\mathrm{v},i}\right], \tag{7.58}$$

where $\boldsymbol{\sigma}_{\mathrm{v},i}$ denotes the (viscous) partial stress

$$\boldsymbol{\sigma}_{\mathrm{v},i} = \mathbb{C}_i[\boldsymbol{\varepsilon} - \boldsymbol{\varepsilon}_{\mathrm{vp}} - \boldsymbol{\varepsilon}_{\mathrm{v},i} - \boldsymbol{\alpha}(\theta - \theta_0)] \tag{7.59}$$

of the i-th dashpot. As we consider temperatures above the glass transition, the temperature-dependent shift function is assumed to obey the Williams-Landel-Ferry (WLF) (Williams and Ferry, 1955) equation

$$\log_{10}(a_\theta(\theta)) = -\frac{C_1(\theta - \theta_{\mathrm{ref}})}{C_2 + (\theta - \theta_{\mathrm{ref}})}. \tag{7.60}$$

To capture thermal softening of the material, the yield stress

$$\sigma_{\mathrm{Y}} : \mathbb{R}_{>0} \to \mathbb{R}_{>0}, \quad \theta \mapsto \Gamma(\theta, \beta_1)\, \sigma_{\mathrm{Y},0}, \tag{7.61}$$

and the power-law hardening

$$H : \mathbb{R}_{>0} \times \mathbb{R}_{\geq 0} \to \mathbb{R}_{\geq 0}, \quad (\theta, \varepsilon_{\mathrm{vp}}) \mapsto \Gamma(\theta, \beta_1)\, k\, \varepsilon_{\mathrm{vp}}^n, \tag{7.62}$$

feature an explicit temperature-dependence. The temperature-degradation function

$$\Gamma : \mathbb{R}_{>0} \times \mathbb{R}_{\geq 0} \to \mathbb{R}_{>0}, \quad (\theta, \beta) \mapsto e^{-\beta(\theta - \theta_{\mathrm{ref}})}, \tag{7.63}$$

takes the temperature and the material parameter $\beta_1 \in \mathbb{R}_{\geq 0}$ as input and degrades both the yield stress and the isotropic hardening w.r.t. the temperature. As for classical J_2-viscoplasticity, the evolution of the plastic strain

$$\dot{\boldsymbol{\varepsilon}}_{\mathrm{vp}} = \sqrt{\frac{3}{2}}\dot{\varepsilon}_{\mathrm{vp}} \frac{\boldsymbol{\sigma}'}{\|\boldsymbol{\sigma}'\|} \tag{7.64}$$

is driven by the deviatoric part of the stress tensor $\boldsymbol{\sigma}'$. The accumulated viscoplastic strain rate $\dot{\varepsilon}_{\mathrm{vp}}$ is given by the following evolution equation

$$\dot{\varepsilon}_{\mathrm{vp}} = \frac{\sigma_{\mathrm{Y}}(\theta)}{\mu(\theta)} \left\langle \frac{\sqrt{\frac{3}{2}}\|\boldsymbol{\sigma}'\| - \sigma_{\mathrm{Y}}(\theta) - H(\theta, \varepsilon_{\mathrm{vp}})}{\sigma_{\mathrm{Y}}(\theta)} \right\rangle_{+}^{m}, \tag{7.65}$$

see Krairi et al. (2019), where the reference viscosity

$$\mu : \mathbb{R}_{>0} \to \mathbb{R}_{>0}, \quad \theta \mapsto \Gamma(\theta, \beta_2)\, \mu_0, \tag{7.66}$$

involves a temperature-dependence as well.

In addition to the Helmholtz free energy, the material's (extended-valued) dissipation potential takes the following form

$$\phi(\theta, \dot{\boldsymbol{z}}) = \begin{cases} \sigma_{\mathrm{Y}}(\theta)\, \dot{\varepsilon}_{\mathrm{vp}} + \sum_{i=1}^{N_{\mathrm{M}}} \boldsymbol{\sigma}_{\mathrm{v},i} : \dot{\boldsymbol{\varepsilon}}_{\mathrm{v},i}, & \dot{\varepsilon}_{\mathrm{vp}} = \sqrt{\frac{2}{3}}\|\dot{\boldsymbol{\varepsilon}}_{\mathrm{vp}}\|, \\ +\infty, & \text{otherwise.} \end{cases} \tag{7.67}$$

For the material at hand, the thermomechanical coupling term P computes to

$$\begin{aligned} P(\boldsymbol{\varepsilon}, \theta, \boldsymbol{z}) = {} & \theta \frac{\partial^2 \psi}{\partial \theta \partial \boldsymbol{\varepsilon}}(\boldsymbol{\varepsilon}, \theta, \boldsymbol{z}) : \dot{\boldsymbol{\varepsilon}} + \theta \frac{\partial^2 \psi}{\partial \theta \partial \boldsymbol{z}}(\boldsymbol{\varepsilon}, \theta, \boldsymbol{z}) \cdot \dot{\boldsymbol{z}} - \frac{\partial \psi}{\partial \boldsymbol{z}}(\boldsymbol{\varepsilon}, \theta, \boldsymbol{z}) \cdot \dot{\boldsymbol{z}} \\ = {} & -\theta\, (\dot{\boldsymbol{\varepsilon}} - \dot{\boldsymbol{\varepsilon}}_{\mathrm{vp}}) : \mathbb{C}_{\infty}\, [\boldsymbol{\alpha}] - \theta \sum_{i=1}^{N_{\mathrm{M}}} (\dot{\boldsymbol{\varepsilon}} - \dot{\boldsymbol{\varepsilon}}_{\mathrm{vp}} - \dot{\boldsymbol{\varepsilon}}_{\mathrm{v},i}) : \mathbb{C}_i\, [\boldsymbol{\alpha}] \\ & + \theta \frac{\partial H}{\partial \theta}(\theta, \varepsilon_{\mathrm{vp}})\, \dot{\varepsilon}_{\mathrm{vp}} + \sigma_{\mathrm{Y}}(\theta)\, \dot{\varepsilon}_{\mathrm{vp}} + \sum_{i=1}^{N_{\mathrm{M}}} \boldsymbol{\sigma}_{\mathrm{v},i} : \dot{\boldsymbol{\varepsilon}}_{\mathrm{v},i}, \end{aligned} \tag{7.68}$$

which is composed of three independent parts. The first two terms are responsible for the Joule-Gough effect. The third term is related to

thermal softening and the last two terms, i.e., the dissipation

$$\mathcal{D}(\boldsymbol{\varepsilon}, \theta, \boldsymbol{z}) = \sigma_{\mathrm{Y}}(\theta)\, \dot{\varepsilon}_{\mathrm{vp}} + \sum_{i=1}^{N_{\mathrm{M}}} \boldsymbol{\sigma}_{\mathrm{v},i} : \dot{\boldsymbol{\varepsilon}}_{\mathrm{v},i}, \tag{7.69}$$

comprises the dissipated energy due to viscoplastic and viscoelastic flow. The latter is responsible for self-heating of the material due to viscoelastic or viscoplastic deformations. The full set of material parameters for the PA66, involving $N_{\mathrm{M}} = 12$ Maxwell elements, are summarized in Table 7.2.

Young's modulus	$E_\infty = 1.5\,\mathrm{GPa}$	
Poisson's ratio	$\nu = 0.42$	
Viscoelastic parameters	$E_1 = 265\,\mathrm{MPa}$	$\log_{10}(\tau_1/\mathrm{s}) = -4.22$
	$E_2 = 262\,\mathrm{MPa}$	$\log_{10}(\tau_2/\mathrm{s}) = -3.42$
	$E_3 = 248\,\mathrm{MPa}$	$\log_{10}(\tau_3/\mathrm{s}) = -2.63$
	$E_4 = 231\,\mathrm{MPa}$	$\log_{10}(\tau_4/\mathrm{s}) = -1.84$
	$E_5 = 211\,\mathrm{MPa}$	$\log_{10}(\tau_5/\mathrm{s}) = -1.05$
	$E_6 = 190\,\mathrm{MPa}$	$\log_{10}(\tau_6/\mathrm{s}) = -0.26$
	$E_7 = 170\,\mathrm{MPa}$	$\log_{10}(\tau_7/\mathrm{s}) = 0.53$
	$E_8 = 92\,\mathrm{MPa}$	$\log_{10}(\tau_8/\mathrm{s}) = 1.32$
	$E_9 = 78\,\mathrm{MPa}$	$\log_{10}(\tau_9/\mathrm{s}) = 2.12$
	$E_{10} = 65\,\mathrm{MPa}$	$\log_{10}(\tau_{10}/\mathrm{s}) = 2.91$
	$E_{11} = 54\,\mathrm{MPa}$	$\log_{10}(\tau_{11}/\mathrm{s}) = 3.70$
	$E_{12} = 48\,\mathrm{MPa}$	$\log_{10}(\tau_{12}/\mathrm{s}) = 4.49$
WLF parameters	$C_1 = 26.21$	
	$C_2 = 446.31\,\mathrm{K}$	
Isotropic hardening	$\sigma_{\mathrm{Y},0} = 15.5\,\mathrm{MPa}$	
	$k = 103\,\mathrm{MPa}$	
	$n = 0.32$	
Viscoplastic parameters	$\mu_0 = 74\,\mathrm{MPa\,s}$	
	$m = 2$	
Thermal softening	$\beta_1 = 0.011\,1/\mathrm{K}$	
	$\beta_2 = 0.07\,1/\mathrm{K}$	
	$\theta_{\mathrm{ref}} = 298.15\,\mathrm{K}$	
Heat capacity	$c_{\varepsilon,0} = 1.9 \cdot 10^6\,\mathrm{J/(m^3K)}$	
Thermal expansion	$\alpha_0 = 70 \cdot 10^{-6}\,1/\mathrm{K}$	
Thermal conductivity	$\kappa_0 = 0.27\,\mathrm{W/(mK)}$	

Table 7.2: Material parameters of the PA66 (Krairi et al., 2019)

7.4.2 Material sampling

We start with the sampling of $N_\mathrm{s} = 1\,000$ tuples of input stiffnesses $\{(\mathbb{C}_1^s, \mathbb{C}_2^s)\}_{s=1}^{N_\mathrm{s}}$ in the way as proposed in Section 5.4.4. We turn our attention to the computation of the associated effective stiffnesses. For this purpose, a representative volume element (RVE) with a suitable resolution and size needs to be generated first. To this end, we take a closer look at the sampled input stiffnesses. More precisely, we consider the distribution of the material contrast ζ which is defined, for the sample s, as

$$\zeta^s = \max\left(\frac{C_{1,+}^s}{C_{2,-}^s}, \frac{C_{2,+}^s}{C_{1,-}^s}\right). \tag{7.70}$$

Here, $C_{1/2,+}^s$ and $C_{1/2,-}^s$ denote the largest and smallest eigenvalues of stiffnesses $\mathbb{C}_1^s$ and $\mathbb{C}_2^s$, respectively. Figure 7.2a illustrates the sorted material contrast vs. the $1\,000$ samples.

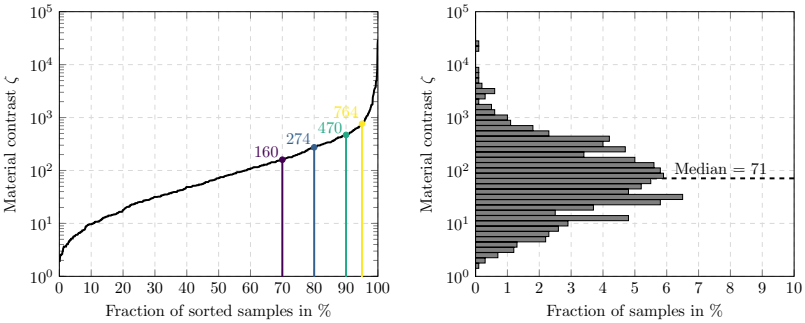

(a) Sorted material contrast vs. samples

(b) Distribution of material contrast

Figure 7.2: Distribution of the material contrast in the sample set

We observe that the material contrast starts at around two and goes up to around $23\,000$. To get a better understanding of how the material

contrast is distributed on the sample set, Figure 7.2b shows the respective histogram with 50 evenly log-spaced bins. We observe that the median of the distribution is well below a material contrast of 100 and that only $3\,\%$ of the samples exceed a material contrast of $1\,000$. With these findings at hand, we consider finding a suitable resolution and size of the volume element.

7.4.3 Necessary resolution and size of the RVE

Finding a suitable resolution and RVE size is necessary to obtain accurate effective properties. However, performing a resolution and RVE size study for any tuple of input stiffnesses $(\mathbb{C}_1^s, \mathbb{C}_2^s)$ is computationally expensive. The former is especially relevant for samples with a high material contrast, i.e., greater than $1\,000$, which only occur with a small frequency in the sample set. For this reason, we conduct a resolution and RVE size study for selected samples alone. To be more precise, we choose samples from the sampling set $\{(\mathbb{C}_1^s, \mathbb{C}_2^s)\}_{s=1}^{N_\mathrm{s}}$ corresponding to the 70th, 80th, 90th and 95th percentile i.e., samples with a material contrast of $\zeta = 160$, $\zeta = 274$, $\zeta = 470$ and $\zeta = 764$, respectively, see Figure 7.2a for an illustration and color coding.

For a start, we consider generated cubic microstructures with a variable resolution and with a fixed edge length of $L = 384\,\mu\mathrm{m}$, i.e., roughly twice the fiber length of $L_\mathrm{f} = 200\,\mu\mathrm{m}$. We vary the resolution from 3.3 to 13.3 voxels per fiber diameter in equidistant steps. The former corresponds to volume element discretizations with 128^3 to 512^3 voxels. We choose a resolution of 20 voxels per fiber diameter, i.e., discretized by 768^3 voxels, as reference. For generating the volume elements, we rely upon the sequential addition and migration (SAM) (Schneider, 2017) method, using the exact closure approximation (Montgomery-Smith et al., 2011). The effective stiffnesses are computed with the help of an FFT-based computational micromechanics code (Moulinec and Suquet, 1994; 1998) using the conjugate gradient solver (Zeman et al., 2010; Brisard and

Dormieux, 2010) and the staggered grid discretization (Schneider et al., 2016).

Figure 7.3a shows the relative error of the effective stiffness computed by the Frobenius norm of the corresponding Voigt matrices. For the crudest resolution of 3.33 voxels per fiber diameter, the relative error exceeds 10 %. Increasing the resolution decreases the relative error for the four considered material contrasts. At a resolution of ten voxels per fiber diameter, the relative error of the sample corresponding to the 95th percentile falls below 3 %. For the samples corresponding to the 90th, 80th/70th percentile, the relative error is below 2 % and 1 %, respectively. As material contrasts of $\zeta = 764$ and above only occur with frequency of less than 5 %, we consider the resolution of 10 voxels per fiber diameter as sufficient. We fix this resolution and focus on finding a suitable size of the RVE.

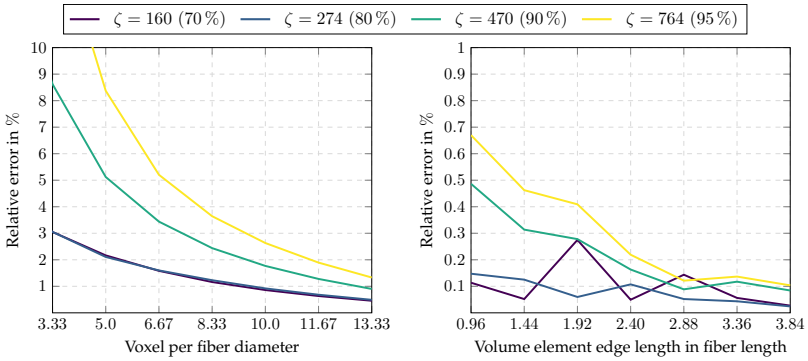

(a) Relative error vs. resolution **(b)** Relative error vs. volume element size

Figure 7.3: Study to determine necessary resolution and size of the RVE. Shown is the relative error of the computed effective stiffness vs. the resolution and volume element size.

We investigate volume elements with edge length L ranging from 0.96 up to 3.84 fiber lengths. The former corresponds to volume element discretizations with 192^3 up to 768^3 voxels. To obtain the reference, we generate a volume element with edge length of 5.76 fiber lengths and discretized by $1\,152^3$ voxels. As before, we consider the relative error in the effective stiffness as error measure. For all considered edge lengths, the relative error is well below $1\,\%$, see Figure 7.3b. Indeed, even the smallest volume element, i.e., an edge length smaller than the fiber length, the relative error is below $0.5\,\%$. Increasing the volume element edge length from 0.96 to 3.84 further decreased the error.

We consider a volume element length of 1.92 fiber lengths, i.e., a edge lengths of $L = 384\,\mu\mathrm{m}$, as sufficient to keep the computational costs for the sampling of the training data reasonable. With the optimal resolution and RVE size at hand, i.e., a resolution of 10 voxels per fiber diameter and a volume element discretization with 384^3 voxels, we compute the effective stiffnesses of all generated $N_\mathrm{s} = 1\,000$ stiffness samples and turn our attention to the training of the DMN.

7.4.4 Offline training

The offline training is implemented in PyTorch (Paszke et al., 2017), see Chapter 4 for more details. From Chapter 4 and 5, we know that at least eight layers are necessary to achieve a sufficient approximation quality for inelastic computations. For this reason, we restrict to a two-phase DMN with $K = 8$ layers. We randomly split the training data $\left\{\left(\bar{\mathbb{C}}^s, \mathbb{C}_1^s, \mathbb{C}_2^s\right)\right\}_{s=1}^{N_\mathrm{s}}$ into a training and a validation set, comprising $90\,\%$ and $10\,\%$ samples, respectively. The DMN is trained with mini batches with a batch size of $N_\mathrm{b} = 32$ samples, which are drawn randomly from the training set. Batches with less than 32 samples are discarded. Prior to the offline training, we sample the initial directions of lamination $\vec{\boldsymbol{n}}_0$ from a uniform distribution on the unit sphere and the initial weights

$\vec{v}_0$ are sampled from a uniform distribution on $[0, 1]$ and subsequently rescaled to sum to unity.

As per Chapter 5, we rely on the AMSGrad method (Kingma and Ba, 2015; Reddi et al., 2018). To aid finding a suitable minimizer for J (7.13), we employ the warm restart technique as suggested by Loshchilov and Hutter (2017). The warm restarts are realized by a harmonic learning rate modulation (5.52) of the learning rates $\beta_{\vec{n}}$ and $\beta_{\vec{v}}$ in combination with a geometric decay to enforce convergence. We determine appropriate learning rates $\beta_{\vec{n}}$ and $\beta_{\vec{v}}$ by a learning rate sweep as proposed by Smith and Topin (2018). The former yields almost identical maximum learning rates, i.e., $\beta_{\vec{n},\max} = \beta_{\vec{v},\max} = 1.5 \cdot 10^{-2}$. The minimum learning rates are set to $\beta_{\vec{n},\min} = \beta_{\vec{v},\min} = 1.5 \cdot 10^{-3}$. We choose $M = 50$ as well as $\gamma = 0.999$ for the learning rate modulation (5.52) and set $p = 1$, $q = 10$ and $\lambda_\mathrm{p} = 10^3$ for the loss function (7.13). We measure the accuracy of the fit by the mean error δ_mean and the maximum error δ_max as defined in Equations (4.68).

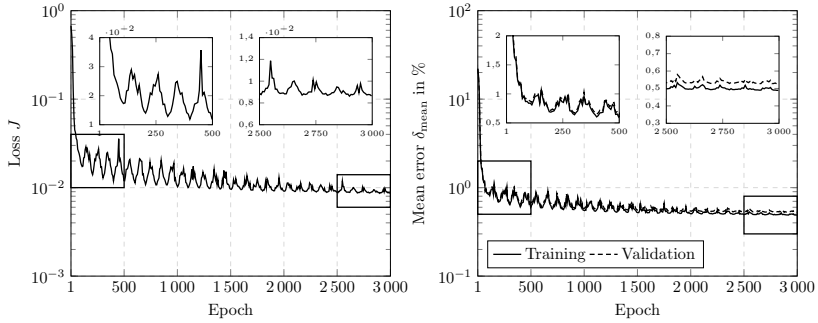

(a) Loss vs. training epoch

(b) Mean error vs. training epoch

Figure 7.4: Loss (a) and mean training and validation errors (b) for the 3000 training epochs

In Figure 7.4, the training progress in terms of the loss J and the mean error δ_{mean} is illustrated. Overall, the effect of the learning rate modulation becomes apparent. The loss as well as the mean training and validation errors fluctuate heavily, especially for the first 500 epochs. The fluctuation decreases due to the learning rate decay such that in the last 500 epochs, convergence is ensured. During the training, no significant model over-fitting can be observed as the validation error does not increase noticeably during training.

7.4.5 Online validation

We start with validating the identified DMN surrogate model for the inelastic regime. To this end, we compare the DMN's predicted effective stress $\bar{\boldsymbol{\sigma}}$, the associated effective dissipation $\bar{\mathcal{D}}$ as well as the change of the absolute temperature $\triangle\bar{\theta} = \bar{\theta} - \bar{\theta}_0$ to a high-fidelity full-field solution on the microscopic scale. To compute the reference solution, we use the implicit staggered solution scheme of Wicht et al. (2020b), an inexact Newton-CG (Kabel et al., 2014) solver and the discretization by trigonometric polynomials as introduced by Moulinec and Suquet (1994; 1998).

First, to obtain accurate inelastic results, a suitable resolution and size of the RVE needs to be determined first. In Section 7.4.3, we learned that the RVE size has a minor influence on the effective elastic response of the composite. For this reason, we fix the volume element's edge length of $L = 384\,\mu\text{m}$ and only vary the RVE's resolutions from 5 to 10 voxels per fiber diameter in equidistant steps. The former corresponds to volume element discretizations with 192^3 to 384^3 voxels, respectively. As loading, we consider a uniaxial extension in the principal fiber direction

$$\bar{\boldsymbol{\varepsilon}} = \bar{\varepsilon}\, \boldsymbol{e}_1 \otimes \boldsymbol{e}_1 \tag{7.71}$$

and use mixed boundary conditions (Kabel et al., 2016), i.e., stress free loading perpendicular to the loading direction. The strain loading is applied in 40 equidistant load steps with a strain rate of $\dot{\bar{\varepsilon}} = 5 \cdot 10^{-4}\,1/\mathrm{s}$. The reference temperature is set to $\bar{\theta}_0 = 293.15\,\mathrm{K}$. For simplicity, we assume adiabatic conditions as we consider a single macroscopic point without any additional macroscopic heat sources.

In Figure 7.5, the computed effective stress $\bar{\boldsymbol{\sigma}}$, the change of the absolute temperature $\triangle\bar{\theta}$ and the effective dissipation $\bar{\mathcal{D}}$ are shown for all four considered resolutions. For a macrostrain of $\bar{\varepsilon} = 1.0\,\%$ and below, the Joule-Gough effect, i.e., an almost linear temperature decrease due to hydrostatic extension, becomes apparent. This regime is captured well, even for the coarsest resolution. At around $\bar{\varepsilon} = 1.0\,\%$ macrostrain, the matrix starts to deform plastically. Due to an increasing dissipation, self-heating of the composite occurs and the four solutions start to deviate noticeably. Thus, to accurately capture self-heating effects, a resolution of at least 8.33 fibers per fiber diameter is necessary. Such a resolution suffices to accurately compute the effective stress and the effective dissipation as well. For this reason, we consider a resolution of 8.33 voxels per fiber diameter, i.e., a volume element discretization with 320^3 voxels, as sufficient for the inelastic computations.

With the identified resolution at hand, we turn back to the validation of the DMN surrogate model. For this purpose, we implemented the procedure introduced in Section 7.3.3 as an implicit user-material subroutine. A computationally efficient implementation of the UMAT is critical. For this reason, we use the binary tree compression as introduced in Section 5.3.2 and exploit the sparsity pattern of the gradient operator $\boldsymbol{D}$ and the Jacobians $\partial\vec{\boldsymbol{\sigma}}/\partial\vec{\boldsymbol{\varepsilon}}$ and $\partial\vec{P}/\partial\vec{\boldsymbol{\varepsilon}}$. For this reason, we rely upon the Eigen3 library (Guennebaud et al., 2010) for all linear algebra operations. We set the tolerance for the convergence criterion (5.55) to $\mathrm{tol} = 10^{-12}$ and solve the linear system with the help of a sparse Cholesky decomposition. The former allows for reusing the decomposition for computing

the algorithmic tangents $\bar{\mathbb{C}}_{\bar{\varepsilon}}^{\text{algo}}$, $\bar{\boldsymbol{C}}_{\bar{\theta}}^{\text{algo}}$, $\bar{\boldsymbol{K}}_{\bar{\varepsilon}}^{\text{algo}}$ and $\bar{K}_{\bar{\theta}}^{\text{algo}}$ with minimal computational overhead.

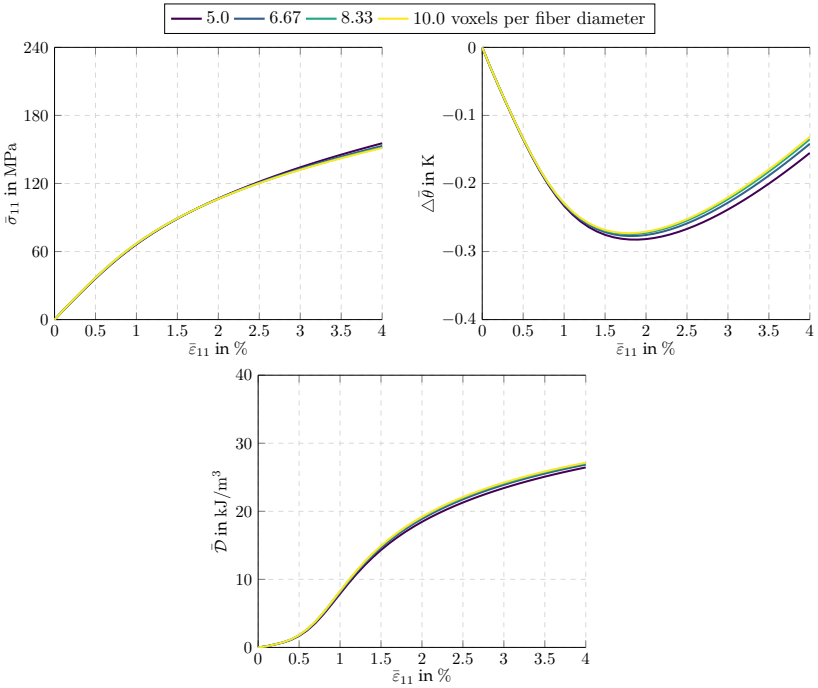

Figure 7.5: Effective stress, temperature change and effective dissipation for the four considered resolutions and a uniaxial extension in the e_1-direction with a strain rate of $\dot{\bar{\varepsilon}} = 5 \cdot 10^{-4}\,1/\text{s}$

Strain-controlled monotonic and non-monotonic virtual experiments

We first consider strain-controlled virtual experiments. Using the material parameters summarized in Section 7.4.1, we investigate six mono-

tonic uniaxial strain loadings

$$\bar{\boldsymbol{\varepsilon}} = \frac{\bar{\varepsilon}}{2} \left(\boldsymbol{e}_i \otimes \boldsymbol{e}_j + \boldsymbol{e}_j \otimes \boldsymbol{e}_i \right) \tag{7.72}$$

with

$$(i,j) \in \mathcal{I}_1 = \{(1,1),(2,2),(3,3),(1,2),(1,3),(2,3)\}\,. \tag{7.73}$$

For every uniaxial strain loading direction in the index set $\mathcal{I}_1$, a monotonic strain loading amplitude of $\bar{\varepsilon} = 4.0\,\%$ is applied in 40 equidistant load steps. To capture the rate dependence of the polyamide matrix, we investigate four individual strain rates which are logarithmically spaced from $\dot{\bar{\varepsilon}} = 5 \cdot 10^{-4}\,1/\mathrm{s}$ to $\dot{\bar{\varepsilon}} = 5 \cdot 10^{-1}\,1/\mathrm{s}$.

To evaluate the approximation errors of the direct DMN in a quantitative way, we introduce the following error measures. For a load in direction (i,j), we define the relative error in the effective stress component $\bar{\sigma}_{ij}$, the change in absolute temperature $\triangle\bar{\theta}$ and the effective dissipation $\bar{\mathcal{D}}$ as

$$\eta_{ij}^{\bar{\sigma}}(t) = \frac{\left|\bar{\sigma}_{ij}^{\mathrm{DMN}}(t) - \bar{\sigma}_{ij}^{\mathrm{FFT}}(t)\right|}{\max\limits_{\tau\in\mathcal{T}} \left|\bar{\sigma}_{ij}^{\mathrm{FFT}}(\tau)\right|}, \quad \eta_{ij}^{\triangle\bar{\theta}}(t) = \frac{\left|\triangle\bar{\theta}^{\,\mathrm{DMN}}(t) - \triangle\bar{\theta}^{\,\mathrm{FFT}}(t)\right|}{\max\limits_{\tau\in\mathcal{T}} \left|\triangle\bar{\theta}^{\,\mathrm{FFT}}(\tau)\right|},$$
$$\eta_{ij}^{\bar{\mathcal{D}}}(t) = \frac{\left|\bar{\mathcal{D}}^{\,\mathrm{DMN}}(t) - \bar{\mathcal{D}}^{\,\mathrm{FFT}}(t)\right|}{\max\limits_{\tau\in\mathcal{T}} \left|\bar{\mathcal{D}}^{\,\mathrm{FFT}}(\tau)\right|}, \tag{7.74}$$

where $\mathcal{T} = [0,T]$ denotes the considered time interval of the simulation. Furthermore, the mean and the maximum errors are defined by

$$\eta_{\mathrm{mean}} = \max_{i,j\in\{1,2,3\}} \frac{1}{T} \int_0^T \eta_{ij}\,(t)\,\mathrm{d}t \quad \text{and} \quad \eta_{\mathrm{max}} = \max_{i,j\in\{1,2,3\}} \max_{t\in\mathcal{T}} \eta_{ij}\,(t). \tag{7.75}$$

In Figure 7.6, the results for the monotonic loading in the principal fiber direction, i.e., $(i,j) \equiv (1,1)$, are shown. We observe that, up to the

maximum load of $\bar{\varepsilon} = 4.0\,\%$, the effective stress predicted by the DMN and the full-field solution are almost indistinguishable. The relative stress error for all four considered strain rates is well below $2.0\,\%$. The same holds for the temperature change $\triangle\bar{\theta}$ and the effective dissipation $\bar{\mathcal{D}}$ for a strain loadings of up to $2.0\,\%$.

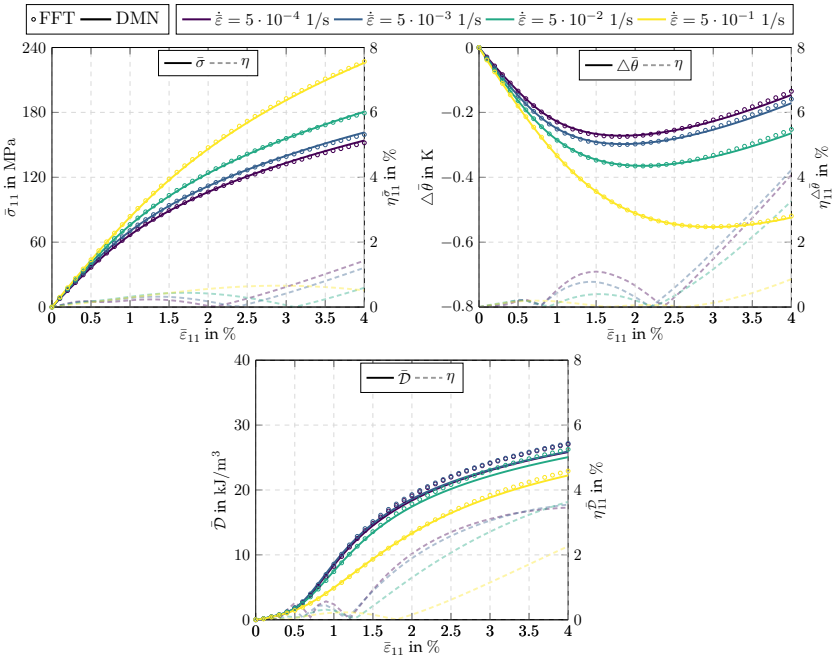

Figure 7.6: Strain-controlled monotonic loading: Uniaxial extension in principal fiber direction

Only from $2.0\,\%$ macroscopic strain and above, deviations in the effective dissipation, and, thus, also the temperature change, become noticeable. The former is a result of the power-law hardening of the polyamide

matrix. Indeed, due to the power-law hardening, local clusters of significant plastic deformation form in the microstructure.

Figure 7.7 visualizes this effect by showing the evolution of the accumulated viscoplastic strain $\varepsilon_{\mathrm{vp}}$, for the strain rate $\dot{\bar{\varepsilon}} = 5 \cdot 10^{-4}\,1/\mathrm{s}$, on a slice in the $\boldsymbol{e}_1$-$\boldsymbol{e}_2$-plane of the 3D microstructure.

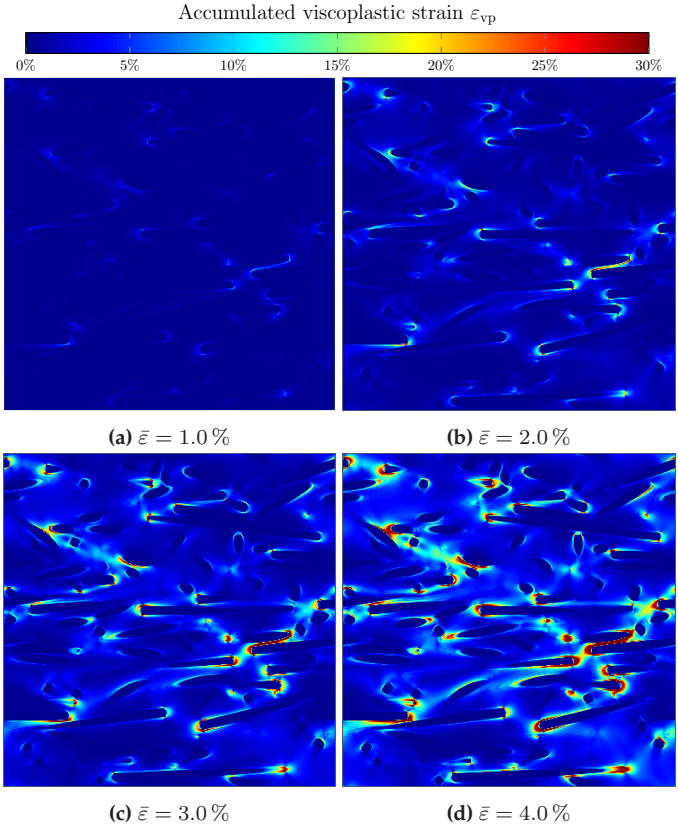

Figure 7.7: Accumulated viscoplastic strain $\varepsilon_{\mathrm{vp}}$ for a $4.0\,\%$ uniaxial extension in principal fiber direction with a strain rate of $\dot{\bar{\varepsilon}} = 5 \cdot 10^{-4}\,1/\mathrm{s}$

Figure 7.7 illustrates that for the chosen loading, clusters with more than $30\,\%$ accumulated viscoplastic strain form in the vicinity of fiber ends. This strong plastification leads to a pronounced energy dissipation, which is slightly underestimated by the DMN, see Figure 7.6. For this reason, the DMN underestimates the self-heating of the composite as it does not fully capture such localization phenomena.

To account for more complex loading conditions, i.e., load reversal or biaxial loadings, we investigate six independent non-monotonic loadings and six independent biaxial loadings in Appendix D.1 and D.2. The relative errors in the effective stress, the temperature change and the effective dissipation for all four considered strain rates and all considered load cases are summarized in Table 7.3.

	$\eta^{\bar{\sigma}}_{\text{mean}}$ / $\eta^{\bar{\sigma}}_{\text{max}}$	$\eta^{\triangle\bar{\theta}}_{\text{mean}}$ / $\eta^{\triangle\bar{\theta}}_{\text{max}}$	$\eta^{\bar{\mathcal{D}}}_{\text{mean}}$ / $\eta^{\bar{\mathcal{D}}}_{\text{max}}$
6 monotonic loadings	$1.35\,\%$ / $3.17\,\%$	$1.11\,\%$ / $4.23\,\%$	$2.33\,\%$ / $4.57\,\%$
6 non-monotonic loadings	$0.77\,\%$ / $1.42\,\%$	$0.56\,\%$ / $1.23\,\%$	$0.98\,\%$ / $4.68\,\%$
6 biaxial loadings	$1.00\,\%$ / $2.02\,\%$	$1.10\,\%$ / $1.82\,\%$	$1.24\,\%$ / $3.63\,\%$

Table 7.3: Mean and maximum relative errors for the investigated strain-controlled uniaxial and biaxial virtual experiments

Stress-controlled cyclic loading

In the previous section, we investigated the identified DMN surrogate model for monotonic and non-monotonic, uniaxial and biaxial loadings. Indeed, for such loadings, self-heating effects played a minor role. However, polymers, in general, show a significant self-heating under cyclic loading, see, e.g., Benaarbia et al. (2015). For this reason, we conclude this section with the validation of the DMN surrogate model for cyclic loading and conduct stress-controlled virtual experiments

$$\bar{\boldsymbol{\sigma}}(t) = \frac{\bar{\sigma}(t)}{2}\,(\boldsymbol{e}_i \otimes \boldsymbol{e}_j + \boldsymbol{e}_j \otimes \boldsymbol{e}_i) \tag{7.76}$$

with

$$\bar{\sigma}(t) = \bar{\sigma}^{\,\mathrm{ampl}} \sin\left(2\pi \frac{t}{T_\mathrm{c}}\right) \quad \text{and} \quad (i,j) \in \mathcal{I}_4 = \{(1,1),(2,2)\}\,. \tag{7.77}$$

More precisely, for both loading directions in the index set $\mathcal{I}_4$, we apply a uniaxial, sinusoidal stress load. Here, $\bar{\sigma}^{\,\mathrm{ampl}}$ denotes the stress amplitude and T_c represent the period of the harmonic loading. As self-heating effects depend on the loading amplitude, we consider four linearly spaced stress amplitudes, ranging from $\bar{\sigma}^{\,\mathrm{ampl}} = 20\,\mathrm{MPa}$ to $\bar{\sigma}^{\,\mathrm{ampl}} = 80\,\mathrm{MPa}$. We simulate 100 cycles, where every cycle is discretized with 20 equidistant load steps, i.e., $2\,000$ load steps in total. The stress load is applied with a frequency of $f = 10\,\mathrm{Hz}$, i.e., the period is $T_\mathrm{c} = 0.1\,\mathrm{s}$, and adiabatic conditions are assumed due to the short simulation time of $10\,\mathrm{s}$. Please note that we consider small stress amplitudes up to $\bar{\sigma}^{\,\mathrm{ampl}} = 80\,\mathrm{MPa}$ resulting in strain amplitudes well below $2.5\,\%$. For this load, resolutions of the volume element smaller than 8.33 voxels per fiber diameter are admissible, see Figure 7.5. For this purpose, we use a volume element resolved with 256^3 voxels, corresponding to 6.67 voxels per diameter, to keep computational costs reasonable.

In Figure 7.8, the results for the cyclic loading perpendicular to the principal fiber direction, i.e., $(i,j) \equiv (2,2)$, are shown. The strain amplitude $\bar{\varepsilon}_{22}^{\mathrm{ampl}}$, which is computed by

$$\bar{\varepsilon}_{22}^{\mathrm{ampl}}(n) = \frac{1}{2}\left(\max_{t\in\mathcal{T}_\mathrm{c}(n)} (\bar{\boldsymbol{\varepsilon}}(t)\cdot \boldsymbol{e}_2\otimes\boldsymbol{e}_2) - \min_{t\in\mathcal{T}_\mathrm{c}(n)} (\bar{\boldsymbol{\varepsilon}}(t)\cdot \boldsymbol{e}_2\otimes\boldsymbol{e}_2)\right) \tag{7.78}$$

with

$$\mathcal{T}_\mathrm{c}(n) = [(n-1)T_\mathrm{c}, nT_\mathrm{c}] \tag{7.79}$$

for a cycle n, is shown vs. the cycles for all four considered amplitudes. We observe that for stress amplitudes of $\bar{\sigma}^{\,\mathrm{ampl}} = 60\,\mathrm{MPa}$ and above, the composite exhibits viscoplastic flow, resulting in a decrease of the strain amplitude in the first few cycles due to hardening. Subsequently, for

the two largest amplitudes, the strain amplitude increases again due to self-heating induced thermal softening of the composite. Beside the strain amplitude, the temperature change and the dissipated energy are illustrated as well in Figure 7.8. Here, for cycle n, $\triangle\bar{\theta}^{\,\mathrm{cycle}}$ denotes the mean temperature change and $\bar{\mathcal{D}}^{\,\mathrm{cycle}}$ expresses the total dissipated energy, i.e.,

$$\triangle\bar{\theta}^{\,\mathrm{cycle}}(n) = \frac{1}{T_\mathrm{c}} \int_{\mathcal{T}_\mathrm{c}(n)} \triangle\bar{\theta}(t)\,\mathrm{d}t \quad \text{and} \quad \bar{\mathcal{D}}^{\,\mathrm{cycle}}(n) = \int_{\mathcal{T}_\mathrm{c}(n)} \bar{\mathcal{D}}(t)\,\mathrm{d}t \tag{7.80}$$

hold.

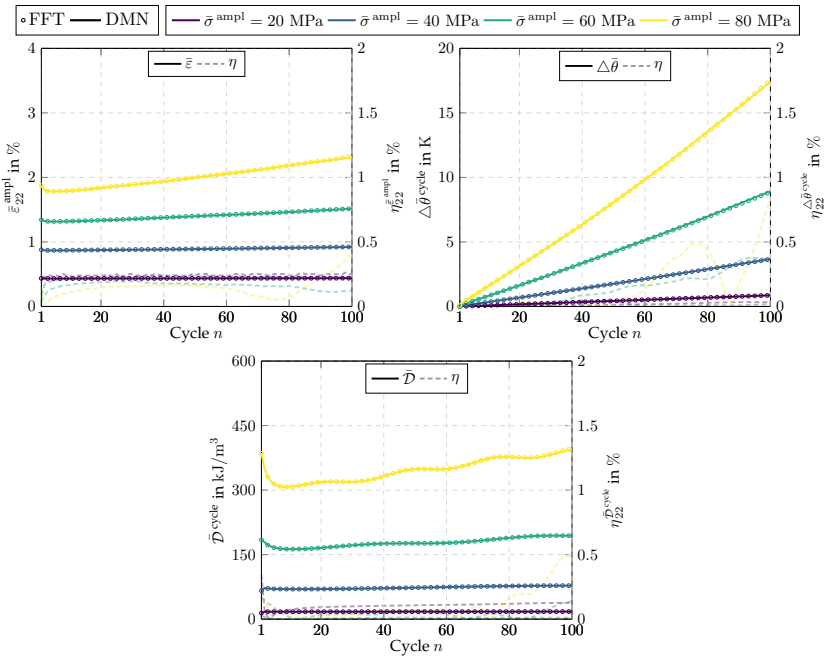

Figure 7.8: Stress-controlled cyclic loading: Uniaxial extension perpendicular to the principal fiber direction

We observe an almost linear self-heating of the composite for all considered amplitudes. In the first few cycles, the total dissipated energy is dominated by viscoplastic flow which decreases for an increasing number of cycles due to hardening. Furthermore, we observe a noticeable temperature-dependence of the dissipated energy, i.e., a noticeable oscillation of the dissipation starting at around 10 cycles. Both effects are particularly visible for the two highest amplitudes. The former can be attributed to the Maxwell elements which are, due to the employed WLF shift function, activated and deactivated depending on the temperature. With an increasing number of cycles, the dissipated energy increases again as the material starts to soften resulting in higher strain amplitudes and thus a higher dissipation.

Comparing the DMN and the full-field solution, we observe an excellent agreement. The strain amplitude, temperature change and dissipated energy of the DMN compared to the full-field solution are almost indistinguishable. To quantify the approximation errors, we evaluate the mean η_{mean} and maximum η_{max} error (7.75), for the strain amplitude $\bar{\varepsilon}^{\text{ampl}}$, the mean temperature change $\triangle\bar{\theta}^{\text{cycle}}$ and the total dissipation $\bar{\mathcal{D}}^{\text{cycle}}$, respectively. These results are summarized in Table 7.4 for the cyclic loading parallel and perpendicular to the principal fiber direction.

$\eta^{\bar{\varepsilon}^{\text{ampl}}}_{\text{mean}}$ / $\eta^{\bar{\varepsilon}^{\text{ampl}}}_{\text{max}}$	$\eta^{\triangle\bar{\theta}^{\text{cycle}}}_{\text{mean}}$ / $\eta^{\triangle\bar{\theta}^{\text{cycle}}}_{\text{max}}$	$\eta^{\bar{\mathcal{D}}^{\text{cycle}}}_{\text{mean}}$ / $\eta^{\bar{\mathcal{D}}^{\text{cycle}}}_{\text{max}}$
0.37 % / 0.43 %	1.11 % / 2.32 %	2.17 % / 2.41 %

Table 7.4: Mean and maximum relative errors for the investigated cyclic uniaxial stress-controlled virtual experiments

Summing up, we investigated monotonic, non-monotonic uniaxial, biaxial and cyclic loading scenarios to validate the identified DMN surrogate model for thermomechanically coupled simulations on the microscopic

scale. Indeed, the direct DMN is able to provide a digital twin for the investigated short fiber reinforced plastic microstructure of thermo-mechanically coupled constituents. The approximation errors for the effective stress in the inelastic setting were well below $3.5\,\%$ for every investigated loading condition. Even the effective dissipation and the predicted temperature change only range up to $5\,\%$, depending on the considered scenario.

7.5 A computational example

With the identified DMN at hand, we turn our attention to conducting a DMN-accelerated concurrent two-scale thermomechanical simulation. More precisely, we study the macroscopic response of a non-symmetric notched plate subjected to cyclic loading using the FE software ABAQUS. The effective material response of the short fiber reinforced polyamide is provided by the identified DMN surrogate model. The local orientation of the material, i.e., the principal fiber direction, aligns with the loading direction. The geometry of the structure is similar to Tikarrouchine et al. (2019) and is illustrated in Figure 7.9.

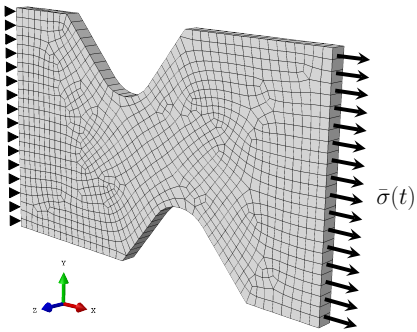

Figure 7.9: Non-symmetric notched plate subjected to a cyclic loading (Tikarrouchine et al., 2019)

The structure is clamped on the left hand side and is subjected to a cyclic stress load

$$\bar{\sigma}(t) = \bar{\sigma}^{\,\mathrm{ampl}} \sin\left(2\pi \frac{t}{T_\mathrm{c}}\right) \tag{7.81}$$

with $\bar{\sigma}^{\,\mathrm{ampl}} = 50\,\mathrm{MPa}$ on the right hand side of the plate. We simulate $3\,000$ cycles, and every cycle is discretized by 20 equidistant load steps, i.e., $60\,000$ load steps in total. The stress load is applied with a frequency of $f = 10\,\mathrm{Hz}$, i.e., the period is $T_\mathrm{c} = 0.1\,\mathrm{s}$. Due to the long simulation time of $200\,\mathrm{s}$, the assumption of adiabatic conditions is not appropriate. For this reason, we prescribe a convective boundary condition on the free surfaces of the plate, i.e., the heat flux across the surface of the plate

$$\bar{q}_\mathrm{s} = -h_\mathrm{t}(\bar{\theta}_\mathrm{s} - \bar{\theta}_0) \tag{7.82}$$

is a function of the heat transfer coefficient h_t and the difference of the surface temperature $\bar{\theta}_\mathrm{s}$ and the ambient temperature $\bar{\theta}_0 = 293.15\,\mathrm{MPa}$. We assume a free convection. Thus, the heat transfer coefficient for air is set to

$$h_\mathrm{t} = 10 \frac{\mathrm{W}}{\mathrm{m^2 K}}, \tag{7.83}$$

see Kosky et al. (2013). To account for heat conduction on the macroscopic scale, we assume Fourier's law

$$\bar{\boldsymbol{q}} = -\bar{\boldsymbol{\kappa}} \, \nabla_{\bar{\boldsymbol{x}}} \, \bar{\theta} \tag{7.84}$$

to hold, where $\nabla_{\bar{\boldsymbol{x}}}$ denotes the gradient operator w.r.t. the macroscopic point $\bar{\boldsymbol{x}} \in \Omega$. We use the temperature-independent thermal conductivities of the glass fibers and the polyamide matrix from Table 7.1 and 7.2 and compute the effective thermal conductivity tensor $\bar{\boldsymbol{\kappa}}$ by means of an FFT-based computational homogenization code (Moulinec and Suquet, 1994; 1998; Dorn and Schneider, 2019). Indeed, the effective thermal

conductivity is almost isotropic and reads

$$\bar{\boldsymbol{\kappa}} = \begin{bmatrix} 0.361 & 0 & 0 \\ 0 & 0.33 & 0 \\ 0 & 0 & 0.33 \end{bmatrix} \frac{\mathrm{W}}{\mathrm{m\,K}} \, \boldsymbol{e}_i \otimes \boldsymbol{e}_j. \tag{7.85}$$

We neglect any additional macroscopic heat sources $\bar{h} \equiv 0$.

The notched plate is discretized by $1\,099$ thermally coupled quadratic hexahedron elements. In every Gauss point, a direct DMN is integrated implicitly. For solving the global system, we rely on the direct Newton solver in ABAQUS, which solves for the displacements and absolute temperature simultaneously.

In Figure 7.10, the evolution of the mean temperature change $\triangle\bar{\theta}^{\,\mathrm{cycle}}$ is shown. For the first 250 cycles, a slight self-heating of the plate is observed in the vicinity of the two notches where the viscoelastic and viscoplastic deformation localizes. For an increasing number of cycles, the inner part of the plate starts to heat up as well both due to energy dissipation as well as heat conduction.

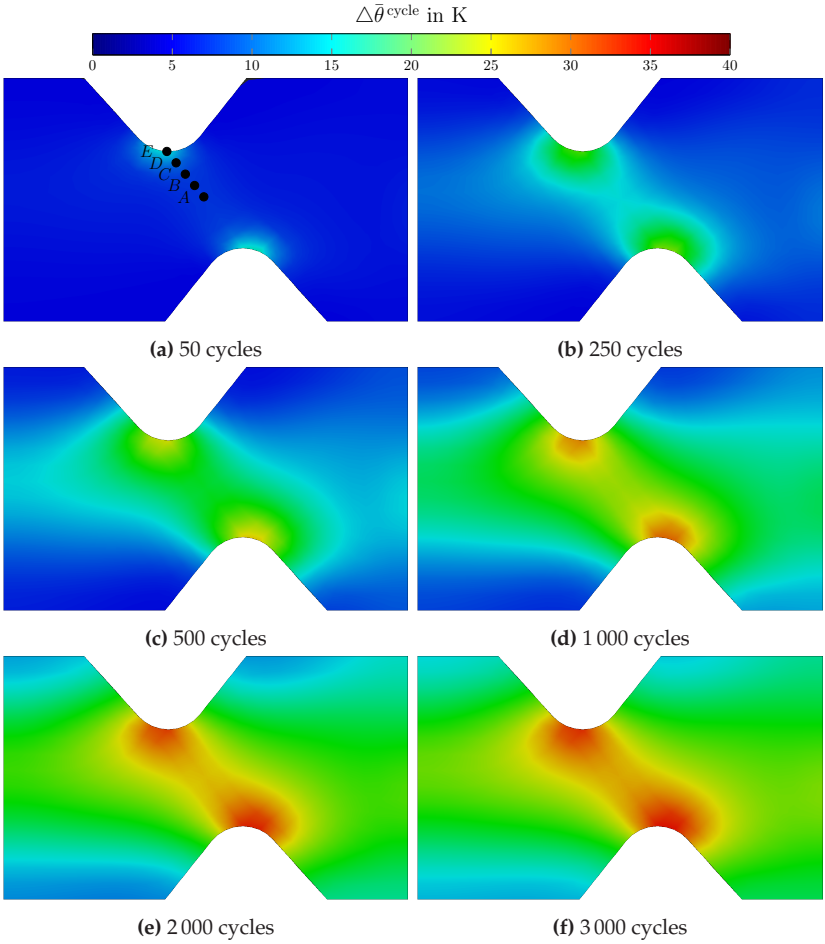

(a) 50 cycles **(b)** 250 cycles

(c) 500 cycles **(d)** 1 000 cycles

(e) 2 000 cycles **(f)** 3 000 cycles

Figure 7.10: Evolution of the absolute temperature on the surface of the notched plate subjected to a cyclic loading

In addition to the contour plots, Figure 7.11 shows the temporal evolution of the strain amplitude $\bar{\varepsilon}^{\,\mathrm{ampl}}$, mean temperature change $\triangle\bar{\theta}^{\,\mathrm{cycle}}$ and the dissipated energy $\bar{\mathcal{D}}^{\,\mathrm{cycle}}$ for five distinct points A to E, see

Figure 7.10a. Here, in the macroscopic setting, we compute the strain amplitude $\bar{\varepsilon}^{\text{ampl}}$ of cycle n by

$$\bar{\varepsilon}^{\text{ampl}}(n) = \frac{1}{2}\left(\max_{t\in\mathcal{T}_c(n)}(\lambda_{\bar{\varepsilon}}^{\max}(t)) - \min_{t\in\mathcal{T}_c(n)}(\lambda_{\bar{\varepsilon}}^{\min}(t))\right), \tag{7.86}$$

where $\lambda_{\bar{\varepsilon}}^{\min}$ and $\lambda_{\bar{\varepsilon}}^{\max}$ denote the smallest and the largest eigenvalue of the macroscopic strain tensor $\bar{\varepsilon}$.

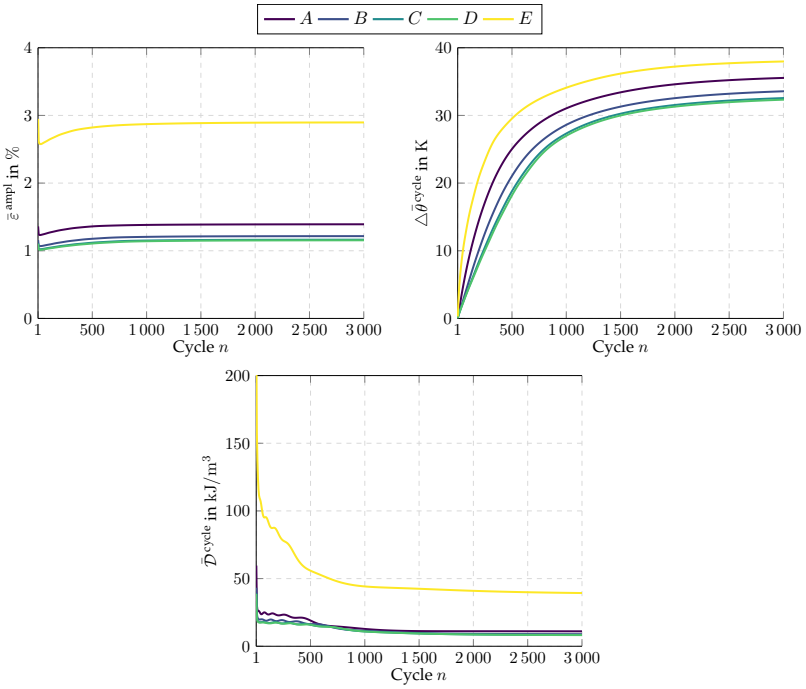

Figure 7.11: Evolution of the strain amplitude, the absolute temperature and the dissipated energy vs. the number of cycles for the five locations shown in Figure 7.10a

A closer look at the evolution of the strain amplitude shows that, as in the microscopic setting, the hardening of the viscoplastic matrix results in a decrease of the strain amplitude in the first few cycles for all five investigated points. Afterwards, the strain amplitude increases again until a steady-state is reached. The reason for the renewed increase of the strain amplitude and subsequent saturation becomes clear by inspecting the evolution of the absolute temperature. In the first few cycles, the temperature increases rapidly in all considered points as a result of the dissipated energy due to the viscoelastic and viscoplastic flow. This increase is more pronounced in the vicinity of the two notches and decreases towards the inner part of the plate. The temperature increase results in the thermal softening of the material, and, in turn, the strain amplitude increases. After about $1\,000$ cycles, the temperature increase saturates and a steady-state is reached. This steady-state is the result of two effects. One one hand, the dissipated energy in a cycle decreases with increasing temperature due to thermal softening. On the other hand, the heat conduction due to the free convection increases with an increasing surface temperature.

7.6 Computational cost

For all numerical computations, we used a workstation equipped with two AMD EPYC 7642 with 48 physical cores each and 1024 GB of DRAM. The material sampling was performed in parallel, i.e., six independent load steps for computing the effective stiffnesses using 16 threads each. The training of the direct DMN was carried out on four threads. The wall-clock times of the sampling and the offline training are summarized in Table 7.5. Indeed, sampling of the training data took $74\,\mathrm{h}$ whereas the training finished in under $2\,\mathrm{h}$. As we only considered direct DMNs with a depth of $K = 8$, 765 independent fitting parameters were determined during the offline training.

	Wall-clock time	#Fitting parameters
Sampling	$74\,\mathrm{h}$	–
Training	$1.5\,\mathrm{h}$	765

Table 7.5: Wall-clock times for sampling, training and number of fitting parameters

Turning our attention to the online evaluation, we focus on the computational costs of the direct DMN evaluated at a single Gauss point. Solving the thermomechanical cell problem for a microstructure discretized by 320^3 voxels for prescribed macrostrain and absolute temperature takes about $2\,737\mathrm{s}$ on average on a single thread. In contrast, integrating a direct DMN at a single Gauss point takes less than $6\,\mathrm{ms}$. Thus, we achieve a speed-up of about half a million times compared to solving the cell problem by means of an FFT-based micromechanics solver. For applications which admit using direct DMNs with less than eight layers, speed-ups in the range of several millions may be possible.

	FFT (1 thread)	DMN (1 thread)
Wall-clock time	45.62 min	5.64 ms
Speed-up	–	485 284

Table 7.6: Wall-clock times and speed-up (compared to an FFT-base computational micromechanics solver) for a single time step of the inelastic micro simulation

Wall-clock time and memory consumption for the component-scale simulation are reported in Table 7.7. Indeed, the macroscopic FE model was discretized by 1 099 elements resulting in 9 706 degrees of freedom. Computing all 60 000 time steps involved 161 240 total Newton iterations, took about 117 h on 96 threads and required about 2 GB of DRAM. Indeed, ABAQUS only required about 2.7 Newton iterations (on average) per load increment, indicating a robust quadratic convergence.

	ABAQUS (96 threads)
Elements	1 099
#DOF	9 706
Increments	60 000
Wall-clock time	117 h
Memory consumption	1.8 GB
Total Newton iterations	161 240

Table 7.7: Wall-clock time, memory consumption and total Newton iterations of the concurrent two-scale simulation

7.7 Conclusion

In this chapter, we extended the framework of direct DMNs to fully coupled thermomechanical two-scale simulations. More precisely, we

incorporated the intrinsic two-way thermomechanical coupling between the microscopic and macroscopic scale into the framework. Considering the former is essential to accurately capture the mechanical response of common engineering materials, e.g., short fiber reinforced thermoplastics, in structural simulations.

For this purpose, we built upon the first-order homogenization framework of thermomechanical composites established by Chatzigeorgiou et al. (2016), who showed that there is no fluctuation of the absolute temperature on the microscopic scale. For this reason, both the absolute temperature and the macrostrain are regarded as inputs to the DMN's (microscopic) balance of linear momentum. This way, the one-way thermomechanical coupling from the macroscopic onto the microscopic scale is accounted for. Furthermore, we incorporated the back-coupling from the microscopic scale onto the evolution of the macroscopic temperature into the framework. To this end, changes of entropy and dissipated energy are computed and propagated to the macroscopic scale where both combined, act as an additional source term to the macroscopic heat equation. This way, the two-way thermomechanical coupling was incorporated into the framework of direct DMNs. To accelerate a thermomechanically coupled two-scale simulation, we explained how our approach was implemented as an implicit user-material subroutine.

Choosing a short fiber reinforced polyamide 6.6 with industrial aspect ratio and filler fraction, we demonstrated that the trained direct DMN was able to predict, for a macroscopic point, the effective stress, the effective dissipation and the ensuing temperature change of the composite with high accuracy for a set of different strain rates and loading conditions. Indeed, DMNs are trained on linear elastic data alone. Predicting the dissipated energy at a macroscopic point, which in turn is intrinsically associated to nonlinear effects on the underlying microstructure, e.g., plasticity, is a remarkable result.

To evaluate the performance of our approach in a concurrent two-scale setting, we conducted a thermomechanically coupled simulation of an asymmetric notched plate. The notched plate was subjected to a cyclic stress load also considering heat conduction and convection. The observed mechanical behavior of the notched plate, i.e., the saturating temperature increase and the temperature-dependent mechanical behavior, could only be reproduced in a macroscopic setting, since heat conduction and convection had to be considered. This shows that only relying on microscopic simulations for characterizing thermomechanically coupled composites by simulative means does not suffice.

Chapter 8

Summary and conclusion

Deep material networks, introduced by Liu et al. (2019a) and Liu and Wu (2019), are a data-driven homogenization technique based on an explicit microstructure model, i.e., hierarchical laminates. They serve as high-fidelity surrogates for full-field simulations on microstructures with inelastic constituents and thus can be used to accelerate concurrent two-scale simulations, offering speed-ups of several orders of magnitude compared to more conventional, full-field solution techniques.

In contrast to other machine learning approaches, which seek to approximate the effective properties of a microstructure and constituents, DMNs may be thought of as a drop-in replacement for microstructures alone. More precisely, DMNs seek to approximate the homogenization function of a fixed microstructure. They are exclusively fitted on linear elastic data by considering the effective stiffness of a microstructure as a function of the input stiffness tensors of the constituents. For the parameter identification, classical machine learning techniques are used, i.e., automatic differentiation and stochastic gradient descent.

After the parameter identification, the fitting parameters of the DMN are fixed and the surrogate model can be evaluated for an arbitrarily nonlinear material behavior of the constituents, even at finite strains, with impressive accuracy. The former contrasts with more classical approaches, for which the model identification and evaluation are interdependent.

In this thesis, we investigated the framework of deep material networks from the viewpoint of classical small-strain micromechanics. In the following, an individual summary of each chapter is given:

In **Chapter 3**, we were interested in the basic concepts and micromechanical principles of deep material networks. For this, we introduced the notion of homogenization functions. We argued that the effective inelastic behavior of a microstructure with small-strain generalized standard material constituents is determined, to first order in the strain rate, by the homogenization of linear elasticity with eigenstrains. The key tool to our analysis was a multiple-input-multiple-output (MIMO) dynamical system associated to a small-strain generalized standard material. Indeed, the former result is not restricted to deep material networks and holds true for any N-phase microstructure. Furthermore, we showed that for the special case of two phases, it is not necessary to track the (phase-wise average) strain localization tensors – which are required to homogenize elasticity with eigenstrains. In particular, for a two-phase microstructure, we showed that it suffices to track the effective stiffness alone. With these results, we provided the mathematical underpinnings of the approach of Liu et al. (2019a) and Liu and Wu (2019). Furthermore, we showed that for materials with more than two phases, linear elastic localization needs to be learned instead of linear elastic homogenization, i.e., eigenstrains need to be considered as well.

In **Chapter 4**, we introduced direct deep material networks, a novel formulation which omits intermittent rotations and utilizes laminate building blocks with variable directions of lamination. Following this approach came with a reduced number of free parameters to be identified. By flattening the tree of laminates, we proposed a versatile and robust solution strategy for nonlinear direct DMNs, which is general enough to encompass arbitrary trees of laminates. Furthermore, we showed that (direct) DMNs inherit thermodynamic consistency and stress-strain monotonicity from their phases. The former constitutes a

key feature both in terms of physics and numerical implementation, and represents an additional reason for DMNs' extraordinary approximation capabilities.

We proposed a novel DMN-accelerated two-scale strategy for the analysis of short fiber reinforced composites in **Chapter 5**. To account for a spatially varying fiber orientation, we interpolated the fitting parameters of the direct DMN on the fiber orientation triangle. With this, we fitted a single DMN on the elastic response of up to 31 microstructure realizations. We showed that the identified surrogate model generalizes well for inelastic problems on the entire fiber orientation triangle. We proved the efficiency of our approach by capturing the complete process chain of an injection molded quadcopter frame and showed that the approach allows for the multiscale analysis of industrial-scale problems comprising millions of elements on commodity hardware alone.

In **Chapter 6**, we introduced micro-oriented direct DMNs to account for microstructures with micro-oriented phases. In addition, we extended the proposed interpolation technique by a volume fraction interpolation to treat sheet molding compound composites. We used the identified surrogate model to investigate process-induced fluctuations of the mechanical performance of SMC components within a virtual process chain. We demonstrated that our approach is capable of quantifying uncertainties in the macroscopic mechanical response of SMC components with great accuracy.

In **Chapter 7**, we extended direct DMNs to accelerate multiscale simulations of thermomechanical composites by incorporating the intrinsic two-way thermomechanical coupling between the microscopic and macroscopic scale into the framework. We showed that the identified DMN is able to predict the effective stress, the effective dissipation and the ensuing temperature change of the composite with high accuracy for a set of different loading directions and strain rates. Indeed, predicting the dissipated energy at a macroscopic point, which in turn is intrinsi-

cally associated to nonlinear effects on the underlying microstructure, is a remarkable result which can be attributed to the DMNs internal structure. We demonstrated the performance of the approach by conducting a two-scale simulation of a short fiber reinforced polyamide component to assess self-heating effects under cyclic loading.

Summing up, we contributed to the framework of deep material networks by shedding further light on their micromechanical principles. We analyzed the linear training and the extrapolation to nonlinear phase materials. We proposed a novel formulation which is characterized by a reduced number of degrees of freedom compared to the original formulation, and which is applicable to microstructures with and without micro-oriented phases. We presented a general, efficient and robust solution technique that is general enough to encompass arbitrary trees of N-phase laminates. By interpolating the free parameters of direct DMNs, we were able to treat composites for which the microstructure characteristics fluctuate on the component scale. Manufacturing process-induced fluctuating microstructure characteristics often constitute weak spots in the structure and even might contribute to preliminary failure. Thus, it is crucial to account for such effects in two-scale simulations to reduce safety factors and to fully exploit the lightweight potential of composite materials. We showed that interpolated direct DMNs are a powerful piece of technology for accelerating concurrent two-scale simulations, which allow for resolving such fluctuating microstructure characteristics on the macroscopic scale with minimal computational effort. Furthermore, accounting for thermodynamic coupling in such two-scale simulations permits effects such as self-heating or thermal softening to be considered with great accuracy. For instance, accounting for thermal softening in the analysis of polymer-based composites such as short-fiber reinforced thermoplastics is of utmost importance, since the mechanical behavior of the thermoplastic matrix may change drastically even for minor temperature changes. Especially in weak spots

such as weld lines, a localizing deformation and deformation-induced self-heating and thermal softening may lead to preliminary failure of the overall component and must therefore be capture by simulative means.

Due to their extraordinary accuracy and the possibility of providing speed-ups of five to six orders of magnitude, the FE-DMN method enables large-scale concurrent two-scale simulations comprising millions of elements. In this way, the FE-DMN method finally realizes the promise of fully coupled two-scale simulations of large-scale industrial problems, and promises to become a standard tool for engineering applications.

Despite the apparent success in practice and preliminary results discussed in Chapter 3, there is still a need for theoretical results which shed light on the approximation capabilities and the limitations of DMNs, possibly drawing from corresponding results for neural networks, see Cybenko (1989) and Hornik (1991). Indeed, whether every fixed two-phase microstructure and variable constituents has a microstructure twin of a hierarchical laminate with identical effective properties, appears to be unresolved, see Problem 4 in Milton (2020). Interestingly, there exist counter examples for five-phase composites where the former is false, see Milton (1986).

Appendix A

Appendix to Chapter 3

A.1 Homogenization of linear viscoelasticity (without transforms)

An isothermal GSM $(\mathcal{Z}, \psi, \phi, \boldsymbol{z}_0) \in \mathcal{GSM}$ is called linear viscoelastic if W is a Hilbert space and

$$\psi(\boldsymbol{\varepsilon}, \boldsymbol{z}) = \frac{1}{2}(\boldsymbol{\varepsilon} - \boldsymbol{P}\boldsymbol{z}) : \mathbb{C}[\boldsymbol{\varepsilon} - \boldsymbol{P}\boldsymbol{z}] \quad \text{and} \quad \phi(\dot{\boldsymbol{z}}) = \frac{1}{2}\boldsymbol{Q}(\dot{\boldsymbol{z}})[\dot{\boldsymbol{z}}] \tag{A.1}$$

hold, where $\mathbb{C} \in \mathrm{Sym}_4^+(d)$ is a stiffness tensor, $\boldsymbol{P} : W \to \mathrm{Sym}_2(d)$ is a (surjective) bounded linear operator and $\boldsymbol{Q} : W \to W'$ represents a coercive, symmetric bilinear form. This formulation incorporates, for instance, Maxwell models with an arbitrary (even infinite) number of Maxwell elements. Also, homogenized viscoelastic models are covered. We denote the set of all linear viscoelastic GSMs by $\mathcal{LV} \subset \mathcal{GSM}$.

Before continuing, we derive an equivalent representation of the stress function $\boldsymbol{\sigma} : [0, T] \to \mathrm{Sym}_2(d)$ associated to a linear viscoelastic material $(\mathcal{Z}, \psi, \phi, \boldsymbol{z}_0) \in \mathcal{LV}$ and an arbitrary strain path $\boldsymbol{\varepsilon} : [0, T] \to \mathrm{Sym}_2(d)$. The stress, see Equation (3.1), is computed from Hooke's law

$$\boldsymbol{\sigma} = \mathbb{C}[\boldsymbol{\varepsilon} - \boldsymbol{P}\boldsymbol{z}], \tag{A.2}$$

whereas Biot's equation (3.2) becomes

$$-\boldsymbol{P}^* : \boldsymbol{\sigma} + \boldsymbol{Q}\dot{\boldsymbol{z}} = \boldsymbol{0}, \quad \text{i.e.,} \quad \dot{\boldsymbol{z}} = \boldsymbol{Q}^{-1}\boldsymbol{P}^* : \boldsymbol{\sigma} \tag{A.3}$$

in terms of the adjoint $\boldsymbol{P}^* : \mathrm{Sym}_2(d) \to W'$ of $\boldsymbol{P}$. Inserting the latter into Hooke's law (A.2), differentiated in time, leads to the ODE

$$\dot{\boldsymbol{\sigma}} = \mathbb{C}[\dot{\boldsymbol{\varepsilon}}] - \mathbb{C} : \boldsymbol{P}\boldsymbol{Q}^{-1}\boldsymbol{P}^* : \boldsymbol{\sigma}, \quad \boldsymbol{\sigma}(0) = -\mathbb{C} : \boldsymbol{P}\boldsymbol{z}_0, \tag{A.4}$$

which no longer contains the internal variables $\boldsymbol{z} : [0,T] \to \mathcal{Z}$. Integrating the linear ODE (A.4) yields the explicit form

$$\boldsymbol{\sigma}(t) = e^{-\mathbb{C}:\boldsymbol{P}\boldsymbol{Q}^{-1}\boldsymbol{P}^* t} : \mathbb{C} : \boldsymbol{P}\boldsymbol{z}_0 + \int_0^t e^{-\mathbb{C}:\boldsymbol{P}\boldsymbol{Q}^{-1}\boldsymbol{P}^*(t-\tau)} : \mathbb{C}[\dot{\boldsymbol{\varepsilon}}(\tau)] \, \mathrm{d}\tau, \tag{A.5}$$

which we write, for brevity, in the form

$$\boldsymbol{\sigma}(t) = \int_0^t \mathbb{G}(t-\tau)[\dot{\boldsymbol{\varepsilon}}(\tau) - \boldsymbol{\varepsilon}_{\mathrm{in}}(\tau)] \, \mathrm{d}\tau \tag{A.6}$$

with residual strain

$$\boldsymbol{\varepsilon}_{\mathrm{in}}(\tau) = -\frac{1}{t}\mathbb{G}^{-1}(t-\tau) : e^{-\mathbb{C}:\boldsymbol{P}\boldsymbol{Q}^{-1}\boldsymbol{P}^* t} : \mathbb{C} : \boldsymbol{P}\boldsymbol{z}_0 \tag{A.7}$$

and relaxation function

$$\mathbb{G}(t-\tau) = e^{-\mathbb{C}:\boldsymbol{P}\boldsymbol{Q}^{-1}\boldsymbol{P}^*(t-\tau)} : \mathbb{C}. \tag{A.8}$$

With this result in hand, it is not difficult to see that, for two N-phase microstructures Y_1 and Y_2 the equivalence of affine-linear elastic homogenization, $\mathcal{M}^{\mathcal{AL}}_{Y_1} = \mathcal{M}^{\mathcal{AL}}_{Y_2}$, implies the equivalence of linear viscoelastic homogenization, i.e., the equivalence of $\mathcal{M}^{\mathcal{LV}}_{Y_1}$ and $\mathcal{M}^{\mathcal{LV}}_{Y_2}$. For that purpose, fix a strain path $\boldsymbol{\varepsilon} : [0,T] \to \mathrm{Sym}_2(d)$ as well as N linear viscoelastic materials and represent them in hereditary integral form (A.6) with

relaxation functions $\mathbb{G}_i$ and residual strains $\boldsymbol{\varepsilon}_{\text{in},i}$. We seek a solution $\boldsymbol{u} : Y \times [0,T] \to \mathrm{V}^d$ to the balance of linear momentum

$$\operatorname{div}\left[\int_0^t \sum_{i=1}^N \chi_i \mathbb{G}_i(t-\tau)[\dot{\boldsymbol{\varepsilon}}(\tau) + \nabla^{\mathrm{s}}\dot{\boldsymbol{u}}(\cdot,\tau) - \boldsymbol{\varepsilon}_{\text{in},i}(\tau)]\ \mathrm{d}\tau\right] = \boldsymbol{0}, \quad \text{(A.9)}$$

s.t. the effective stress which is computed as

$$\bar{\boldsymbol{\sigma}}(t) = \left\langle \int_0^t \sum_{i=1}^N \chi_i \mathbb{G}_i(t-\tau)[\dot{\boldsymbol{\varepsilon}}(\tau) + \nabla^{\mathrm{s}}\dot{\boldsymbol{u}}(\cdot,\tau) - \boldsymbol{\varepsilon}_{\text{in},i}(\tau)]\ \mathrm{d}\tau \right\rangle_Y . \quad \text{(A.10)}$$

Let, for fixed $\tau \in [0,\ t]$, $\boldsymbol{u}_\tau \in H^1_{\#}(Y;\mathrm{V}^d)$ denote the (periodic) solution of the affine-linear elastic problem

$$\operatorname{div}\left[\sum_{i=1}^N \chi_i \mathbb{G}_i(t-\tau)[\dot{\boldsymbol{\varepsilon}}(\tau) + \nabla^{\mathrm{s}}\boldsymbol{u}_\tau - \boldsymbol{\varepsilon}_{\text{in},i}(\tau)]\right] = \boldsymbol{0}. \quad \text{(A.11)}$$

Then, the solution of Equation (A.9) is given as

$$\boldsymbol{u}(y,t) = \int_0^t \boldsymbol{u}_\tau(y)\ \mathrm{d}\tau. \quad \text{(A.12)}$$

Thus, if we denote the N viscoelastic materials as $\mathcal{G}_1, \dots \mathcal{G}_N$ and, for fixed $\tau \in [0,t]$, the N affine-linear elastic materials entering Equation (A.11) by $\mathfrak{g}_1^\tau, \dots \mathfrak{g}_N^\tau$, we get

$$\bar{\boldsymbol{\sigma}}(t) = \int_0^t \mathcal{M}_Y^{\mathcal{AC}}(\mathfrak{g}_1^\tau, \dots \mathfrak{g}_N^\tau)[\dot{\boldsymbol{\varepsilon}}(\tau)]\ \mathrm{d}\tau, \quad \text{(A.13)}$$

where we write $[\cdot]$-brackets for the stress evaluation of a affine-linear elastic medium. Thus, the viscoelastic stress response is completely determined by the affine-linear elastic homogenization function. As this holds for all input viscoelastic materials $\mathcal{G}_i \in \mathcal{LV}$ and all strain paths $\boldsymbol{\varepsilon} : [0,T] \to \mathrm{Sym}_2(d)$, we see that, up to equivalence of GSMs, the linear

viscoelastic homogenization function $\mathcal{M}_Y^{\mathcal{LV}}$ is completely determined by the affine-linear elastic homogenization function $\mathcal{M}_Y^{\mathcal{AL}}$.

A.2 Carleman bilinearization and Volterra series expansion for MIMO systems

In this section, we discuss a formal Volterra series expansion for nonlinear dynamical systems of the form (3.22)

$$\begin{aligned} \dot{\boldsymbol{\xi}} &= \boldsymbol{f}(\boldsymbol{\xi}) + \boldsymbol{g}(\boldsymbol{\xi}) : \dot{\varepsilon} \\ \boldsymbol{\sigma} &= \boldsymbol{P}\boldsymbol{\xi} \end{aligned} \tag{A.14}$$

for analytic functions $\boldsymbol{f}$ and $\boldsymbol{g}$ and with initial condition $\boldsymbol{\xi}(0) = \boldsymbol{\xi}_0$ and $\varepsilon(t) = \mathbf{0}$ $(t \leq 0)$. This result is standard in the appropriate literature, e.g., see Rugh (1981), in the context of single-input-single-output (SISO) systems. However, in our context, we need both vector input and vector output, referred to as a multiple-input-multiple-output (MIMO) system. Our derivation based on Carleman bilinearization (1932) is standard and does not add anything innovative. However, as the specific form of the Volterra series expansion we need is not easily found in the literature, e.g., Rugh (1981), we provide a streamlined presentation.
Before continuing, notice that we may alternatively consider systems

$$\begin{aligned} \dot{\boldsymbol{\xi}} &= \boldsymbol{f}(\boldsymbol{\xi}) + \boldsymbol{g}(\boldsymbol{\xi}) : \dot{\varepsilon} \\ \boldsymbol{\sigma} &= \boldsymbol{P}\boldsymbol{\xi} - \boldsymbol{\sigma}_0 \end{aligned} \tag{A.15}$$

with zero initial condition, but affine-linear output by transforming $\boldsymbol{\xi} \mapsto \boldsymbol{\xi} - \boldsymbol{\xi}_0$. Here, $\boldsymbol{\sigma}_0$ is constant in time. As a first step, we apply Carleman bilinearization to System (A.15), which states that, for analytic $\boldsymbol{f}$ and $\boldsymbol{g}$, System (A.15) is formally equivalent to the bilinear system

$$\begin{aligned} \dot{\boldsymbol{s}} &= \boldsymbol{A}\boldsymbol{s} + \boldsymbol{D}[\boldsymbol{s}, \dot{\varepsilon}] + \boldsymbol{B} : \dot{\varepsilon} \\ \boldsymbol{\sigma} &= \boldsymbol{C}\boldsymbol{s} - \boldsymbol{\sigma}_0 \end{aligned} \tag{A.16}$$

with initial condition $\boldsymbol{s}(0) = \mathbf{0}$ for some vector-valued signal $\boldsymbol{s}$ and linear mappings $\boldsymbol{A}$ and $\boldsymbol{C}$ as well as a bilinear mapping $\boldsymbol{D}$. Deriving this result is straightforward by defining $\boldsymbol{s}$ to collect all multivariate monomials in $\boldsymbol{\xi}$ and writing down the bilinear ODEs in an inductive way, see Section 3.3 in Rugh (1981). As in Rugh (1981), we restrict to an algebraic treatment, assuming formal power series. In practice, similar conclusions can be drawn for merely continuous $\boldsymbol{f}$ and $\boldsymbol{g}$ by approximating $\boldsymbol{f}$ and $\boldsymbol{g}$ by polynomials (following the Stone-Weierstrass theorem (Stone, 1948)). In particular, the Carleman system (A.16) can be realized as a finite-dimensional system. However, the latter approach necessitates quantitative estimates which we believe may obfuscate the main arguments. Thus, we work with formal power series, instead.

To derive the Volterra expansion of the solution $\boldsymbol{s}$ of System (A.16), we first note that the (formal) solution of System (A.16) for $\dot{\boldsymbol{\varepsilon}} \equiv \mathbf{0}$ and initial condition $\boldsymbol{s}(0) = \boldsymbol{z}$ is given by $\boldsymbol{s} = e^{\boldsymbol{A}t}\boldsymbol{z}$. Variation of constants, i.e., the ansatz $\boldsymbol{s}(t) = e^{\boldsymbol{A}t}\boldsymbol{z}(t)$, leads to the system

$$\dot{\boldsymbol{z}} = \widetilde{\boldsymbol{D}}[\boldsymbol{z}, \dot{\boldsymbol{\varepsilon}}] + \widetilde{\boldsymbol{B}} : \dot{\boldsymbol{\varepsilon}} \tag{A.17}$$

with initial condition $\boldsymbol{z}(0) = \mathbf{0}$ and

$$\widetilde{\boldsymbol{D}}[\boldsymbol{z}, \dot{\boldsymbol{\varepsilon}}] = e^{-\boldsymbol{A}t}\boldsymbol{D}[e^{\boldsymbol{A}t}\boldsymbol{z}, \dot{\boldsymbol{\varepsilon}}] \quad \text{and} \quad \widetilde{\boldsymbol{B}} : \dot{\boldsymbol{\varepsilon}} = e^{-\boldsymbol{A}t}\boldsymbol{B} : \dot{\boldsymbol{\varepsilon}}. \tag{A.18}$$

Integrating Relation (A.17) and taking into account the initial condition $\boldsymbol{z}(0) = \mathbf{0}$ yields the equivalent integral formulation

$$\boldsymbol{z}(t) = \int_0^t \widetilde{\boldsymbol{D}}(\tau)[\boldsymbol{z}(\tau), \dot{\boldsymbol{\varepsilon}}(\tau)] + \widetilde{\boldsymbol{B}}(\tau) : \dot{\boldsymbol{\varepsilon}}(\tau)\, \mathrm{d}\tau, \tag{A.19}$$

which we rewrite, for notational brevity, in operator form

$$\boldsymbol{z} = \boldsymbol{K}_{\dot{\varepsilon}}\boldsymbol{z} + \boldsymbol{L}\dot{\boldsymbol{\varepsilon}} \tag{A.20}$$

with

$$(\boldsymbol{K}_{\dot{\varepsilon}}\boldsymbol{z})(t) = \int_0^t \widetilde{\boldsymbol{D}}(\tau)[\boldsymbol{z}(\tau), \dot{\boldsymbol{\varepsilon}}(\tau)]\ \mathrm{d}\tau \tag{A.21}$$

and

$$(\boldsymbol{L}\dot{\boldsymbol{\varepsilon}})(t) = \int_0^t \widetilde{\boldsymbol{B}}(\tau) : \dot{\boldsymbol{\varepsilon}}(\tau)\ \mathrm{d}\tau. \tag{A.22}$$

The Neumann series associated to Relation (A.20) reads

$$\boldsymbol{z} = \sum_{k=0}^{\infty} \boldsymbol{K}_{\dot{\varepsilon}}^k \boldsymbol{L}\dot{\boldsymbol{\varepsilon}}, \tag{A.23}$$

which takes the form

$$\boldsymbol{s} = \sum_{k=0}^{\infty} e^{\boldsymbol{A}t} \boldsymbol{K}_{\dot{\varepsilon}}^k \boldsymbol{L}\dot{\boldsymbol{\varepsilon}} \tag{A.24}$$

for the original variable $\boldsymbol{s}$ and the form

$$\boldsymbol{\sigma} = \sum_{k=0}^{\infty} \boldsymbol{C}e^{\boldsymbol{A}t} \boldsymbol{K}_{\dot{\varepsilon}}^k \boldsymbol{L}\dot{\boldsymbol{\varepsilon}} - \boldsymbol{\sigma}_0 \tag{A.25}$$

for the stress. Thus, with Relation (A.25), we have obtained an abstract version of the Volterra series associated to an analytic GSM. Notice that the k-th summand on the right hand side of Relation (A.25) is $(k+1)$-homogeneous in $\dot{\boldsymbol{\varepsilon}}$. Furthermore, both the control variable $\dot{\boldsymbol{\varepsilon}}$ and the output $\boldsymbol{\sigma}$ are finite-dimensional, although the intermediate operations involve operators on infinite-dimensional spaces. The abstract Representation (A.25) is convenient for derivation, but offers little insight into the type of hereditary integrals involved. To gain further insight, we write out the first three summands of Relation (A.25) explicitly

$$\left(\boldsymbol{C}e^{\boldsymbol{A}t}\boldsymbol{L}\dot{\boldsymbol{\varepsilon}}\right)(t) = \int_0^t \boldsymbol{C}e^{\boldsymbol{A}(t-\tau)}\boldsymbol{B} : \dot{\boldsymbol{\varepsilon}}(\tau)\ \mathrm{d}\tau, \tag{A.26}$$

$$\left(\boldsymbol{C}e^{\boldsymbol{A}t}\boldsymbol{K}_{\dot{\varepsilon}}\boldsymbol{L}\dot{\boldsymbol{\varepsilon}}\right)(t) = \int_0^t \int_0^{\tau_1} \boldsymbol{C}e^{\boldsymbol{A}(t-\tau_1)}\boldsymbol{D} \left[e^{\boldsymbol{A}(\tau_1-\tau_2)}\boldsymbol{B} : \dot{\boldsymbol{\varepsilon}}(\tau_2), \dot{\boldsymbol{\varepsilon}}(\tau_1)\right] \mathrm{d}\tau_2 \, \mathrm{d}\tau_1 \quad \text{(A.27)}$$

and

$$\left(\boldsymbol{C}e^{\boldsymbol{A}t}\boldsymbol{K}_{\dot{\varepsilon}}^2\boldsymbol{L}\dot{\boldsymbol{\varepsilon}}\right)(t) = \int_0^t \int_0^{\tau_1} \int_0^{\tau_2} \boldsymbol{C}e^{\boldsymbol{A}(t-\tau_1)}\boldsymbol{D} \left[e^{\boldsymbol{A}(\tau_1-\tau_2)}\boldsymbol{D}\left[e^{\boldsymbol{A}(\tau_2-\tau_3)}\boldsymbol{B} : \dot{\boldsymbol{\varepsilon}}(\tau_3), \dot{\boldsymbol{\varepsilon}}(\tau_2)\right], \dot{\boldsymbol{\varepsilon}}(\tau_1)\right] \mathrm{d}\tau_3 \, \mathrm{d}\tau_2 \, \mathrm{d}\tau_1. \quad \text{(A.28)}$$

Hence, we see that the abstract Volterra series (A.25) can also be explicitly written in the form

$$\boldsymbol{\sigma}(t) + \boldsymbol{\sigma}_0 = \sum_{k=1}^{\infty} \int_0^t \int_0^{\tau_1} \cdots \int_0^{\tau_{k-1}} \mathbb{G}_k(t-\tau_1, \tau_1-\tau_2, \ldots, \tau_{k-1}-\tau_k) [\dot{\boldsymbol{\varepsilon}}(\tau_k), \dot{\boldsymbol{\varepsilon}}(\tau_{k-1}), \ldots, \dot{\boldsymbol{\varepsilon}}(\tau_1)] \mathrm{d}\tau_k \, \mathrm{d}\tau_{k-1} \cdots \mathrm{d}\tau_1 \quad \text{(A.29)}$$

in terms of kernel functions of relaxation type

$$\mathbb{G}_k : \mathbb{R}^k \times \mathrm{Sym}_2(d)^k \to \mathrm{Sym}_2(d), \quad \text{(A.30)}$$

which are multilinear in the k strain rate inputs, i.e., we could also interpret $\mathbb{G}_k : \mathbb{R}^k \times \mathrm{Sym}_2(d)^{\otimes^k} \to \mathrm{Sym}_2(d)$.

We have arrived at our desired Volterra series expansion (A.29) of our initial dynamical system (A.15). Although our derivation was formal, we briefly discuss the convergence of the Volterra expansion, which is nothing but the Neumann series associated to Relation (A.20). Thus, if we work in a Banach space setting, a sufficient condition for the convergence of the expansion is that the operator norm of $\boldsymbol{K}_{\dot{\varepsilon}}$ needs to be smaller than unity. This holds provided $\tilde{\boldsymbol{D}}$ remains bounded (in

operator norm) on bounded sets and the quantity

$$\int_0^t \|\dot{\boldsymbol{\varepsilon}}(\tau)\| \, \mathrm{d}\tau \tag{A.31}$$

is sufficiently small. We can achieve this either by prescribing $\dot{\boldsymbol{\varepsilon}}$ and restricting to a possibly small time interval, or by fixing the final time and assuming smallness in strain rate. Notice the inequality

$$\|\boldsymbol{\varepsilon}(t)\| \leq \int_0^t \|\dot{\boldsymbol{\varepsilon}}(\tau)\| \, \mathrm{d}\tau, \tag{A.32}$$

which is consequence of the triangle inequality for integrals. Thus, smallness of the integrated strain rate norm is stronger than a mere small strain assumption as it, for instance, accounts for load reversal.

Appendix B

Appendix to Chapter 4

Periodic homogenization preserves monotonicity and Lipschitz continuity of the algorithmic stress function. A precise statement of this fact and a stream-lined derivation are collected in this section.

Let Y be a unit cell in V^d, and suppose that a locally integrable stress function

$$\boldsymbol{\sigma} : \mathrm{Sym}_2(d) \times Y \to \mathrm{Sym}_2(d), \quad (\boldsymbol{\varepsilon}, \boldsymbol{x}) \mapsto \boldsymbol{\sigma}(\boldsymbol{\varepsilon}, \boldsymbol{x}) \tag{B.1}$$

is given, which may also correspond to the "algorithmic" stress of a time-discretized GSM for frozen internal variables. We assume that there are positive constants C_- and C_+, s.t. $\boldsymbol{\sigma}$ is C_--strongly monotonic

$$\begin{gathered}(\boldsymbol{\sigma}(\boldsymbol{\varepsilon}_1, \boldsymbol{x}) - \boldsymbol{\sigma}(\boldsymbol{\varepsilon}_2, \boldsymbol{x})) : (\boldsymbol{\varepsilon}_1 - \boldsymbol{\varepsilon}_2) \geq C_- \|\boldsymbol{\varepsilon}_1 - \boldsymbol{\varepsilon}_2\|^2, \\ \boldsymbol{x} \in Y, \quad \boldsymbol{\varepsilon}_1, \boldsymbol{\varepsilon}_2 \in \mathrm{Sym}_2(d),\end{gathered} \tag{B.2}$$

and C_+-Lipschitz continuous

$$\|\boldsymbol{\sigma}(\boldsymbol{\varepsilon}_1, \boldsymbol{x}) - \boldsymbol{\sigma}(\boldsymbol{\varepsilon}_2, \boldsymbol{x}))\| \leq C_+ \|\boldsymbol{\varepsilon}_1 - \boldsymbol{\varepsilon}_2\|, \quad \boldsymbol{x} \in Y, \quad \boldsymbol{\varepsilon}_1, \boldsymbol{\varepsilon}_2 \in \mathrm{Sym}_2(d), \tag{B.3}$$

where $\|\boldsymbol{A}\|^2 = \mathrm{tr}\left(\boldsymbol{A}^2\right)$ denotes the Frobenius norm on $\mathrm{Sym}_2(d)$. Formula (B.2) quantifies how fast the stress grows with increased stress difference. Formula (B.3) translates that the increase in stress grows at most linearly. For small strain materials, this is typical – softening or

hardening typically does not increase the stiffness, i.e., the initial linear elastic behavior serves as an upper bound.

The effective stress, associated to the given stress function (B.1), is the function

$$\bar{\boldsymbol{\sigma}} : \mathrm{Sym}_2(d) \to \mathrm{Sym}_2(d), \quad \text{defined via} \quad \bar{\boldsymbol{\sigma}}(\bar{\varepsilon}) = \langle \boldsymbol{\sigma}(\bar{\varepsilon} + \nabla^{\mathrm{s}} \boldsymbol{u}, \cdot) \rangle_Y \,, \tag{B.4}$$

where $\boldsymbol{u} : Y \to \mathrm{V}^d$ is the displacement fluctuation satisfying the static balance of linear momentum on the microscopic scale

$$\mathrm{div}(\boldsymbol{\sigma}(\bar{\varepsilon} + \nabla^{\mathrm{s}} \boldsymbol{u}, \cdot)) = \mathbf{0} \tag{B.5}$$

in the sense of distributions. Showing existence and uniqueness of $\boldsymbol{u}$, up to the addition of a constant, is a direct consequence of the Browder-Minty theorem, see Theorem 10.49 in Renardy and Rogers (2004), provided Formulae (B.2) and (B.3) hold. We wish to show that these two properties are inherited by the effective stress function (B.4).

Let us consider strong monotonicity (B.2) first. Fix $\bar{\varepsilon}_1, \bar{\varepsilon}_2 \in \mathrm{Sym}_2(d)$ and denote by $\boldsymbol{u}_i$, the displacement fluctuation solving Formula (B.5) for $\bar{\varepsilon} = \bar{\varepsilon}_i$, $i = 1, 2$. Setting $\boldsymbol{\varepsilon}_i = \bar{\varepsilon}_i + \nabla^{\mathrm{s}} \boldsymbol{u}_i$ in Formula (B.2) and taking the volume average yields

$$\langle (\boldsymbol{\sigma}(\boldsymbol{\varepsilon}_1, \cdot) - \boldsymbol{\sigma}(\boldsymbol{\varepsilon}_2, \cdot)) : (\boldsymbol{\varepsilon}_1 - \boldsymbol{\varepsilon}_2) \rangle_Y \geq C_- \left\langle \|\boldsymbol{\varepsilon}_1 - \boldsymbol{\varepsilon}_2\|^2 \right\rangle_Y . \tag{B.6}$$

We manipulate the left hand side,

$$\begin{aligned}\langle(\boldsymbol{\sigma}(\boldsymbol{\varepsilon}_1,\cdot)-\boldsymbol{\sigma}(\boldsymbol{\varepsilon}_2,\cdot)):(\boldsymbol{\varepsilon}_1-\boldsymbol{\varepsilon}_2)\rangle_Y&\\ &=\langle(\boldsymbol{\sigma}(\boldsymbol{\varepsilon}_1,\cdot)-\boldsymbol{\sigma}(\boldsymbol{\varepsilon}_2,\cdot)):(\bar{\boldsymbol{\varepsilon}}_1-\bar{\boldsymbol{\varepsilon}}_2)\rangle_Y\\ &+\langle(\boldsymbol{\sigma}(\boldsymbol{\varepsilon}_1,\cdot)-\boldsymbol{\sigma}(\boldsymbol{\varepsilon}_2,\cdot)):\nabla^{\mathrm{s}}(\boldsymbol{u}_1-\boldsymbol{u}_2)\rangle_Y\\ &=\langle(\boldsymbol{\sigma}(\boldsymbol{\varepsilon}_1,\cdot)-\boldsymbol{\sigma}(\boldsymbol{\varepsilon}_2,\cdot)):(\bar{\boldsymbol{\varepsilon}}_1-\bar{\boldsymbol{\varepsilon}}_2)\rangle_Y\\ &=(\langle\boldsymbol{\sigma}(\boldsymbol{\varepsilon}_1,\cdot)\rangle_Y-\langle\boldsymbol{\sigma}(\boldsymbol{\varepsilon}_2,\cdot)\rangle_Y):(\bar{\boldsymbol{\varepsilon}}_1-\bar{\boldsymbol{\varepsilon}}_2)\\ &=(\bar{\boldsymbol{\sigma}}(\bar{\boldsymbol{\varepsilon}}_1)-\bar{\boldsymbol{\sigma}}(\bar{\boldsymbol{\varepsilon}}_2)):(\bar{\boldsymbol{\varepsilon}}_1-\bar{\boldsymbol{\varepsilon}}_2),\end{aligned}\tag{B.7}$$

where we have used the balance of linear momentum (B.5) in the first line. For the right hand side of Formula (B.6),

$$\left\langle\|\boldsymbol{\varepsilon}_1-\boldsymbol{\varepsilon}_2\|^2\right\rangle_Y=\left\langle\|\bar{\boldsymbol{\varepsilon}}_1-\bar{\boldsymbol{\varepsilon}}_2\|^2\right\rangle_Y+\left\langle\|\nabla^{\mathrm{s}}(\boldsymbol{u}_1-\boldsymbol{u}_2)\|^2\right\rangle_Y\geq\|\bar{\boldsymbol{\varepsilon}}_1-\bar{\boldsymbol{\varepsilon}}_2\|^2\tag{B.8}$$

holds by the Helmholtz decomposition of elasticity, see Chapter 12 in Milton (2002). Combining these two observations yields

$$(\bar{\boldsymbol{\sigma}}(\bar{\boldsymbol{\varepsilon}}_1)-\bar{\boldsymbol{\sigma}}(\bar{\boldsymbol{\varepsilon}}_2)):(\bar{\boldsymbol{\varepsilon}}_1-\bar{\boldsymbol{\varepsilon}}_2)\geq C_-\|\bar{\boldsymbol{\varepsilon}}_1-\bar{\boldsymbol{\varepsilon}}_2\|^2,\tag{B.9}$$

as claimed. The upper bound

$$\|\bar{\boldsymbol{\sigma}}(\bar{\boldsymbol{\varepsilon}}_1)-\bar{\boldsymbol{\sigma}}(\bar{\boldsymbol{\varepsilon}}_2)\|\ \leq\ C_+\|\bar{\boldsymbol{\varepsilon}}_1-\bar{\boldsymbol{\varepsilon}}_2\|\tag{B.10}$$

is proved by duality arguments. Indeed, the inverse of a C_+-Lipschitz continuous monotone operator is $\frac{1}{C_+}$-strongly monotonic. Thus, operating in the dual framework (Wicht et al., 2020a) and mirroring the arguments yields the claim.

Appendix C

Appendix to Chapter 6

Figure C.1a and C.1b summarize the nonlinear mean and maximum errors on the space of admissible fiber volume fractions and fiber orientations. Both errors are strongly correlated, i.e., large nonlinear mean errors imply large nonlinear maximum errors and vice versa. Furthermore, both errors fluctuate noticeably without indicating any distinguished dependence on certain fiber volume fractions or fiber orientations. For all considered microstructure realizations, even the ones the DMN was not trained but only interpolated on, the DMN gives nonlinear maximum errors well below $5\,\%$.

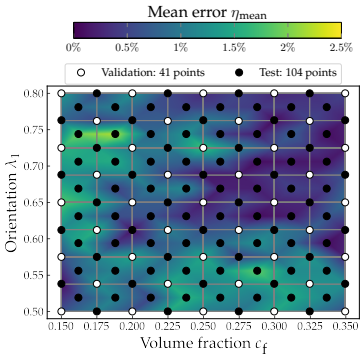

(a) Mean nonlinear validation and test errors

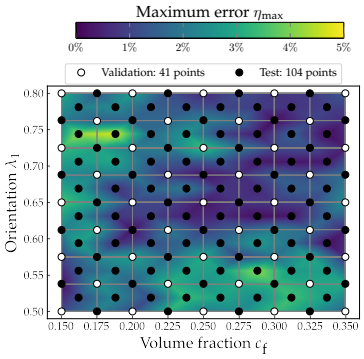

(b) Maximum nonlinear validation and test errors

Figure C.1: Distribution of mean and maximum nonlinear validation and test errors on the space of admissible fiber volume fractions and fiber orientations

Figure C.2 gives an impression on how the computed nonlinear errors listed in Table 6.3 translate into actual stress-strain curves. Illustrated are the effective stress $\bar{\sigma}_{11}$ as well as the nonlinear error η for a uniaxial extension in the $\boldsymbol{e}_1$-direction computed in 40 equidistant time steps and a macroscopic strain of $\bar{\varepsilon} = 4\,\%$. The results for the planar fiber orientation $\lambda_1 = 0.5$ as well as for the more aligned cases of $\lambda_1 = 0.65$ and $\lambda_1 = 0.80$ are reported in Figure C.2. Furthermore, the fiber volume fractions are varied from $c_\mathrm{f} = 0.15$ to $c_\mathrm{f} = 0.35$ in five equidistant steps.

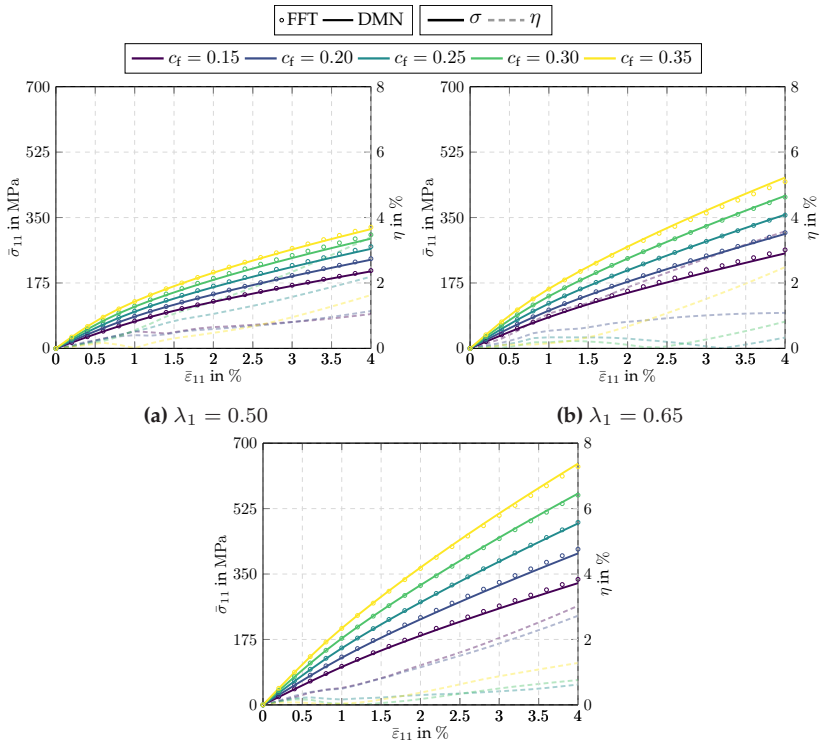

(a) $\lambda_1 = 0.50$

(b) $\lambda_1 = 0.65$

(c) $\lambda_1 = 0.80$

Figure C.2: Comparison of full-field solution and meta model for a variety of fiber orientations and fiber volume fractions

We observe that the effective stresses depend significantly on the fiber volume fraction as well as the fiber orientation. For all considered cases, the DMN gives an excellent prediction with nonlinear errors well below $4\,\%$.

Appendix D

Appendix to Chapter 7

D.1 Strain-controlled non-monotonic loading

To account for load reversal, we investigate six non-monotonic loadings

$$\bar{\boldsymbol{\varepsilon}} = \frac{\bar{\varepsilon}}{2} \left(\boldsymbol{e}_i \otimes \boldsymbol{e}_j + \boldsymbol{e}_j \otimes \boldsymbol{e}_i \right) \tag{D.1}$$

with

$$(i,j) \in \mathcal{I}_2 = \{(1,1),(2,2),(3,3),(1,2),(1,3),(2,3)\} \,. \tag{D.2}$$

For every direction in the index set $\mathcal{I}_2$, a full hysteresis with a strain amplitude of $\bar{\varepsilon} = 2.0\,\%$ in 80 equidistant load steps is computed. Additionally, we use mixed boundary conditions (Kabel et al., 2016) to ensure a stress-free loading perpendicular to the loading direction. As in Section 7.4.5, we investigate four individual strain rates to capture the rate dependence of the composite. In Figure D.1.1, the results for the non-monotonic loading in the principal fiber direction, i.e., $(i,j) \equiv (1,1)$, are shown for all four considered strain rates. We observe that for the full hysteresis, the DMN and the full-field solution are almost indistinguishable in terms of the effective stress and temperature change. The corresponding relative errors are around $1\,\%$ for all considered strain rates. Only for the effective dissipation, we observe slight disagreements between the DMN predictions and the full-field results. Still, these

deviations are around $4\,\%$, i.e., in the range of engineering requirements. The relative errors w.r.t. to the effective stress, temperature change and effective dissipation are summarized in Table 7.3 for all six considered loading directions.

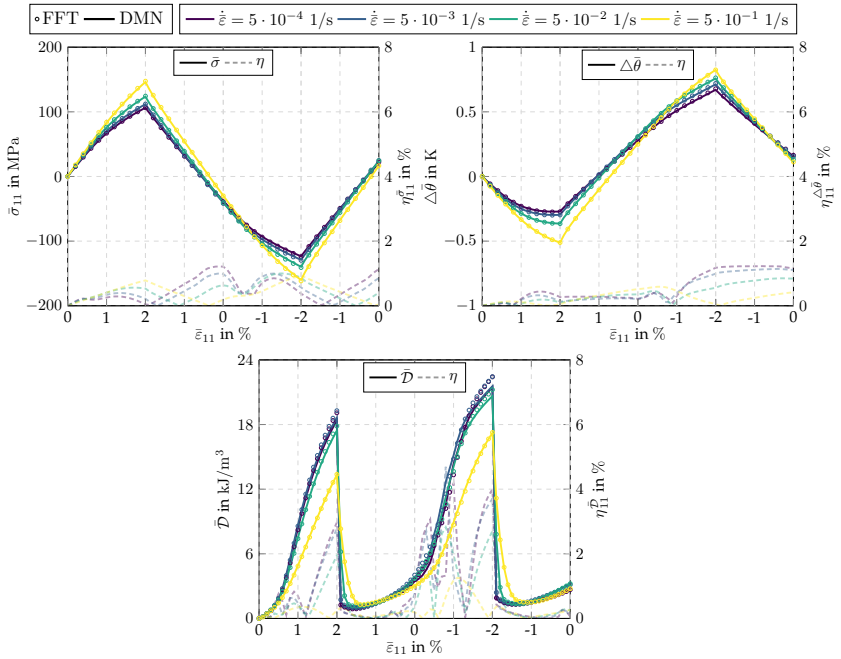

Figure D.1.1: Strain-controlled non-monotonic loading: Uniaxial extension in principal fiber direction

D.2 Strain-controlled biaxial loading

In addition to the monotonic and non-monotonic loadings, we investigate six independent biaxial strain loadings

$$\bar{\boldsymbol{\varepsilon}} = \bar{\varepsilon}_1 \, \boldsymbol{e}_i \otimes \boldsymbol{e}_i + \bar{\varepsilon}_2 \, \boldsymbol{e}_j \otimes \boldsymbol{e}_j \tag{D.3}$$

with

$$(i, j) \in \mathcal{I}_3 = \{(1,2), (1,3), (2,1), (2,3), (3,1), (3,2)\} \, . \tag{D.4}$$

For every loading direction in the index set $\mathcal{I}_3$, a strain loading of $\bar{\varepsilon}_1 = 2.0\,\%$ is applied while the strain in the second direction is held constant $\bar{\varepsilon}_2 = 0\,\%$. Afterwards, a strain load of $\bar{\varepsilon}_2 = 2.0\,\%$ is applied in the second direction, as well. Meanwhile, the strain in the first direction is held constant $\bar{\varepsilon}_1 = 2.0\,\%$. The biaxial loadings are computed in 40 equidistant load steps, and mixed boundary conditions (Kabel et al., 2016) are applied.

In Figure D.2.1, the results for the biaxial loading in the $\boldsymbol{e}_1$- and $\boldsymbol{e}_2$-direction, i.e., $(i, j) \equiv (1, 2)$, are illustrated. As we consider a biaxial loading, the effective stress components in both directions are shown in addition to the temperature change and the effective dissipation. Please note that the error measure $\eta_{ij}^{\sigma_{mn}}$ denotes the relative error of the (m, n) stress component for a load in the (i, j) direction. As before, the DMN matches the full-field solutions remarkably well. Relative errors lie below $2\,\%$ for the effective stress and temperature change and do not exceed $3.5\,\%$ for the effective dissipation. The relative errors for all considered load cases are summarized in Table 7.3.

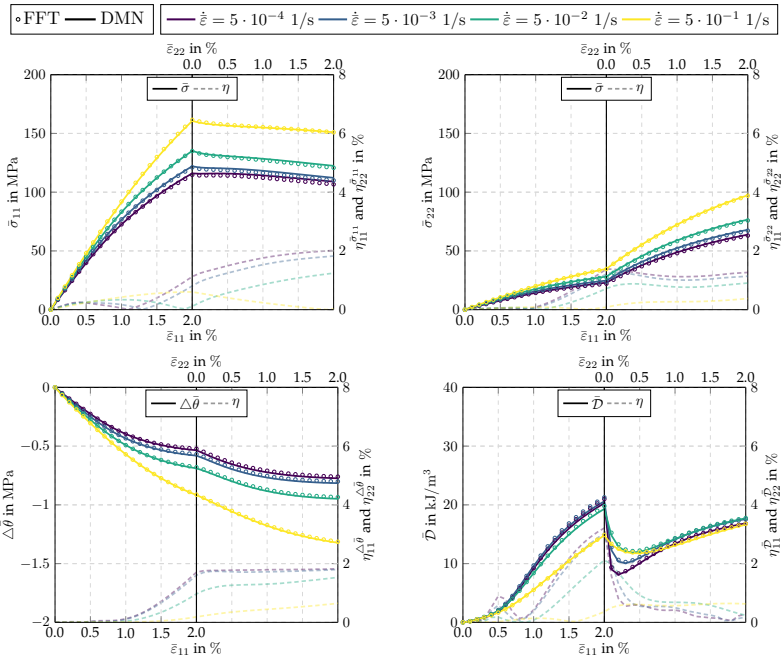

Figure D.2.1: Strain-controlled biaxial loading: Extension in principal fiber direction followed by an extension perpendicular to the principal fiber direction

Bibliography

Acuna, J., Afanasenko, V., Rupp, T., Sonner, M., Klingler, M., Kallfass, I., 2020. Application of Neural Networks to Accelerate Thermomechanical Simulations of Power Modules for Lifetime Prediction. In: CIPS 2020; 11th International Conference on Integrated Power Electronics Systems. Berlin.

Advani, S. G., Tucker, C. L., 1987. The Use of Tensors to Describe and Predict Fiber Orientation in Short Fiber Composites. Journal of Rheology 31 (8), 751–784.

Aizenberg, I., Aizenberg, N. N., Vandewalle, J. P. L., 2013. Multi-Valued and Universal Binary Neurons: Theory, Learning and Applications. Springer, New York.

Bakhvalov, N., Panasenko, G., 1989. Homogenization: Averaging Processes in Periodic Media. Springer, Dordrecht.

Balzani, D., Brands, D., Schröder, J., 2014. Plasticity and Beyond: Microstructures, Crystal-Plasticity and Phase Transitions. Springer, Vienna, Ch. Construction of Statistically Similar Representative Volume Elements, pp. 355–412.

Bargmann, S., Klusemann, B., Markmann, J., Schnabel, J. E., Schneider, K., Soyarslan, C., Wilmers, J., 2018. Generation of 3D representative volume elements for heterogeneous materials: A review. Progress in Materials Science 96, 322–384.

Behnel, S., Bradshaw, R., Citro, C., Dalcin, L., Seljebotn, D. S., Smith, K., 2011. Cython: The Best of Both Worlds. Computing in Science Engineering 13 (2), 31–39.

Ben Cheikh Larbi, A., Sai, K., Sidhom, H., Baptiste, D., 2006. Constitutive Model of Micromechanical Damage to Predict Reduction in Stiffness of a Fatigued SMC Composite. Journal of Materials Engineering and Performance 15 (5), 575–580.

Benaarbia, A., Chrysochoos, A., Robert, G., 2015. Thermomechanical behavior of PA6.6 composites subjected to low cycle fatigue. Composites Part B: Engineering 76, 52–64.

Bensoussan, A., Lions, J.-L., Papanicolaou, G., 1978. Asymptotic Analysis for Periodic Structures. Studies in Mathematics and its Applications. American Mathematical Society, Providence.

Bere, P., Berce, P., Nemes, O., 2012. Phenomenological fracture model for biaxial fibre reinforced composites. Composites Part B: Engineering 43 (5), 2237–2243.

Bertram, A., 2005. Elasticity and Plasticity of Large Deformations. Springer, Heidelberg.

Bhat, H. A., Subramaniam, S., Pillai, A., Krishnan, L. E., Elangovan, M. A., 2014. Analysis and design of mold for plastic side release buckle using moldflow software. International Journal of Research in Engineering and Technology 03, 366–372.

Biot, M. A., 1954. Theory of Stress-Strain Relations in Anisotropic Viscoelasticity and Relaxation Phenomena. Journal of Applied Physics 25 (11), 1385–1391.

Borwein, J., Lewis, A., 2006. Convex Analysis and Nonlinear Optimization: Theory and Examples. Springer, New York.

Boyd, S., Chua, L., 1985. Fading memory and the problem of approximating nonlinear operators with Volterra series. IEEE Transactions on Circuits and Systems 32 (11), 1150–1161.

Brisard, S., Dormieux, L., 2010. FFT-based methods for the mechanics of composites: A general variational framework. Computational Materials Science 49 (3), 663–671.

Bücheler, D., 2018. Locally continuous-fiber reinforced sheet molding compound. Doctoral thesis, Wissenschaftliche Schriftenreihe des Fraunhofer ICT Nr. 79, Karlsruhe Institute of Technology (KIT), Fraunhofer Verlag, Stuttgart.

Camanho, P., Bessa, M., Catalanotti, G., Vogler, M., Rolfes, R., 2013. Modeling the inelastic deformation and fracture of polymer composites – Part II: Smeared crack model. Mechanics of Materials 59, 36–49.

Carleman, T., 1932. Application de la théorie des équations intégrales linéaires aux systèmes d'équations différentielles non linéaires. Acta Mathematica 59, 63–87.

Carrere, N., Maire, J.-F., Kruch, S., Chaboche, J.-L., 2004. Multiscale analysis of SiC/Ti composites. Materials Science and Engineering: A 365 (1), 275–281.

Chaboche, J.-L., Kanouté, P., Roos, A., 2005. On the capabilities of mean-field approaches for the description of plasticity in metal matrix composites. International Journal of Plasticity 21, 1409–1434.

Chaboche, J.-L., Kruch, S., Maire, J. F., Pottier, T., 2001. Towards a micromechanics based inelastic and damage modeling of composites. International Journal of Plasticity 17 (4), 411–439.

Chatzigeorgiou, G., Charalambakis, N., Chemisky, Y., Meraghni, F., 2016. Periodic homogenization for fully coupled thermomechanical modeling of dissipative generalized standard materials. International Journal of Plasticity 81, 18–39.

Cimmelli, V. A., Jou, D., Ruggeri, T., Ván, P., 2014. Entropy Principle and Recent Results in Non-Equilibrium Theories. Entropy 16 (3), 1756–1807.

Coleman, B. D., Noll, W., 1963. The thermodynamics of elastic materials with heat conduction and viscosity. Archive for Rational Mechanics and Analysis 13 (1), 167–178.

Cybenko, C., 1989. Approximation by superpositions of a sigmoidal function. Mathematics of Control, Signals and Systems 2 (4), 303–314.

de Paiva, R. F., Bisiaux, M., Lynch, J., Rosenberg, E., 1996. High resolution x-ray tomography in an electron microprobe. Review of Scientific Instruments 67 (6), 2251–2256.

de Souza Neto, E. A., Peri, D., Owen, D. R. J., 2008. Computational Methods for Plasticity. John Wiley & Sons, Ltd, Chichester.

Dey, A. P., Welschinger, F., Schneider, M., Gajek, S., Böhlke, T., 2022a. Rapid inverse calibration of a multiscale model for the viscoplastic and creep behavior of short fiber-reinforced thermoplastics based on Deep Material Networks. (Submitted to International Journal of Plasticity) .

Dey, A. P., Welschinger, F., Schneider, M., Gajek, S., Böhlke, T., 2022b. Training deep material networks to reproduce creep loading of short fiber-reinforced thermoplastics with an inelastically-informed strategy. Archive of Applied Mechanics 92, 2733–2755.

Doghri, I., Brassart, L., Adam, L., Gérard, J.-S., 2011. A second-moment incremental formulation for the mean-field homogenization of elasto-plastic composites. International Journal of Plasticity 27, 352–371.

Dorn, C., Schneider, M., 2019. Lippmann-Schwinger solvers for the explicit jump discretization for thermal computational homogenization problems. International Journal for Numerical Methods in Engineering 118 (11), 631–653.

Doškář, M., Novák, J., Zeman, J., 2014. Aperiodic compression and reconstruction of real-world material systems based on Wang tiles. Physical Review E 90, 062118.

Doškář, M., Zeman, J., Daniel, R., Novák, J., 2020. Level-set Based Design of Wang Tiles for Modelling Complex Microstructures. Computer-Aided Design 123, 102827.

Dvorak, G., Bahei-El-Din, Y., Wafa, A., 1994a. Implementation of the transformation field analysis. Computational Mechanics 14 (14), 201–228.

Dvorak, G., Bahei-El-Din, Y., Wafa, A., 1994b. The modeling of inelastic composite materials with the transformation field analysis. Modelling and Simulation in Material Science and Engineering 2 (2), 571–586.

Dvorak, G., Benveniste, Y., 1992. On transformation strains and uniform fields in multiphase elastic media. Proceedings of the Royal Society A 437, 291–310.

Dyck, A., Böhlke, T., 2020. A micro-mechanically motivated phenomenological yield function for cubic crystal aggregates. ZAMM-Journal of Applied Mathematics and Mechanics 100 (4), e202000061.

Eshelby, J. D., 1957. The determination of the elastic field of an ellipsoidal inclusion, and related problems. Proceedings of the Royal Society of London. Series A. Mathematical and Physical Sciences 241 (1226), 376–396.

Eshelby, J. D., 1959. The elastic field outside an ellipsoidal inclusion. Proceedings of the Royal Society of London. Series A. Mathematical and Physical Sciences 252 (1271), 561–569.

Ettemeyer, F., Lechner, P., Hofmann, T., Andrä, H., Schneider, M., Grund, D., Volk, W., Günther, D., 2020. Digital Sand Core Physics: Predicting physical properties of sand cores by simulations on digital microstructures. International Journal of Solids and Structures 188-189, 155–168.

Eyre, D. J., Milton, G. W., 1999. A fast numerical scheme for computing the response of composites using grid refinement. The European Physical Journal - Applied Physics 6 (1), 41–47.

Fernández, M., Fritzen, F., Weeger, O., 2022. Material modeling for parametric, anisotropic finite strain hyperelasticity based on machine learning with application in optimization of metamaterials. International Journal for Numerical Methods in Engineering 123 (2), 577–609.

Fernández, M., Jamshidian, M., Böhlke, T., Kersting, K., Weeger, O., 2021. Anisotropic hyperelastic constitutive models for finite deformations combining material theory and data-driven approaches with application to cubic lattice metamaterials. Computational Mechanics 67 (2), 653–677.

Feyel, F., 1999. Multiscale FE2 elastoviscoplastic analysis of composite structures. Computational Materials Science 16 (1), 344–354.

Feyel, F., 2003. A multilevel finite element method FE2 to describe the response of highly non-linear structures using generalized continua. Computer Methods in Applied Mechanics and Engineering 192 (28-30), 3233–3244.

Feyel, F., Chaboche, J.-L., 2000. FE2 multiscale approach for modelling the elastoviscoplastic behaviour of long fibre SiC/Ti composite materials. Computer Methods in Applied Mechanics and Engineering 183 (3-4), 309–330.

Fish, J., Belytschko, T., 2008. A First Course in Finite Elements. John Wiley & Sons, Ltd, Chichester.

Frigo, M., Johnson, S. G., 2005. The Design and Implementation of FFTW3. In: Proceedings of the IEEE. Vol. 93. New York.

Fritzen, F., Böhlke, T., 2011. Nonlinear homogenization using the nonuniform transformation field analysis. PAMM 11 (1), 519–522.

Fritzen, F., Böhlke, T., 2013. Reduced basis homogenization of viscoelastic composites. Composites Science and Technology 76, 84–91.

Fritzen, F., Fernández, M., Larsson, F., 2019. On-the-Fly Adaptivity for Nonlinear Twoscale Simulations Using Artificial Neural Networks and Reduced Order Modeling. Frontiers in Materials 6, 75.

Fritzen, F., Hodapp, M., 2016. The finite element square reduced (FE2R) method with GPU acceleration: towards three-dimensional two-scale simulations. International Journal for Numerical Methods in Engineering 107 (10), 853–881.

Fritzen, F., Hodapp, M., Leuschner, M., 2014. GPU accelerated computational homogenization based on a variational approach in a reduced basis framework. Computer Methods in Applied Mechanics and Engineering 278, 186–217.

Fritzen, F., Leuschner, M., 2013. Reduced basis hybrid computational homogenization based on a mixed incremental formulation. Computer Methods in Applied Mechanics and Engineering 260, 143–154.

Gajek, S., Schneider, M., Böhlke, T., 2020. On the micromechanics of deep material networks. Journal of the Mechanics and Physics of Solids 142, 103984.

Gajek, S., Schneider, M., Böhlke, T., 2021a. An FE-DMN method for the multiscale analysis of short fiber reinforced plastic components. Computer Methods in Applied Mechanics and Engineering 384, 113952.

Gajek, S., Schneider, M., Böhlke, T., 2021b. Efficient two-scale simulations of microstructured materials using deep material networks. PAMM 21 (1), e202100069.

Gajek, S., Schneider, M., Böhlke, T., 2022. An FE-DMN method for the multiscale analysis of thermomechanical composites. Computational Mechanics 69 (5), 1087–1113.

Gärtner, T., Fernández, M., Weeger, O., 2021. Nonlinear multiscale simulation of elastic beam lattices with anisotropic homogenized constitutive models based on artificial neural networks. Computational Mechanics 68 (5), 1111–1130.

Geers, M. G. D., Kouznetsova, V. G., Brekelmans, W. A. M., 2010. Multi-scale computational homogenization: Trends and challenges. Journal of Computational and Applied Mathematics 234 (7), 2175–2182.

Germain, P., Nguyen, Q., Suquet, P., 1983. Continuum Thermodynamics. Journal of Applied Mechanics 50, 1010–1020.

Ghavamian, F., Simone, A., 2019. Accelerating multiscale finite element simulations of history-dependent materials using a recurrent neural network. Computer Methods in Applied Mechanics and Engineering 357, 112594.

Glüge, R., Kalisch, J., 2014. The effective stiffness and stress concentrations of a multi-layer laminate. Composite Structures 111, 580–586.

Gorji, M. B., Mozaffar, M., Heidenreich, J. N., Cao, J., Mohr, D., 2020. On the potential of recurrent neural networks for modeling path dependent plasticity. Journal of the Mechanics and Physics of Solids 143, 103972.

Görthofer, J., Meyer, N., Pallicity, T. D., Schöttl, L., Trauth, A., Schemmann, M., Hohberg, M., Pinter, P., Elsner, P., Henning, F., Hrymak, A., Seelig, T., Weidenmann, K., Kärger, L., Böhlke, T., 2019. Virtual process chain of sheet molding compound: Development, validation and perspectives. Composites Part B: Engineering 169, 133–147.

Görthofer, J., Schneider, M., Hrymak, A., Böhlke, T., 2022a. A computational multiscale model for anisotropic failure of sheet molding compound composites. Composite Structures 288, 115322.

Görthofer, J., Schneider, M., Hrymak, A., Böhlke, T., 2022b. A convex anisotropic damage model based on the compliance tensor. International Journal of Damage Mechanics 31 (1), 43–86.

Görthofer, J., Schneider, M., Ospald, F., Hrymak, A., Böhlke, T., 2020. Computational homogenization of sheet molding compound composites based on high fidelity representative volume elements. Computational Materials Science 174, 109456.

GrabCAD, 2022. S500 Frame. (visited on August 21, 2022).
URL `https://grabcad.com/library/s500-frame-1`

Guennebaud, G., Jacob, B., et al., 2010. Eigen v3. (visited on August 21, 2022).
URL `http://eigen.tuxfamily.org`

Guo, Y., Wu, X., 1999. A phenomenological model for predicting crack growth in fiber-reinforced metal laminates under constant-amplitude loading. Composites Science and Technology 59 (12), 1825–1831.

Gurson, A. L., 1977. Continuum theory of ductile rupture by void nucleation and growth: Part i—yield criteria and flow rules for porous ductile media. Journal of Engineering Materials and Technology 99 (1), 2–15.

Gusev, A. A., 1997. Representative volume element size for elastic composites: A numerical study. Journal of the Mechanics and Physics of Solids 45 (9), 1449–1459.

Halphen, N., Nguyen, Q., 1975. Sur les matériaux standards generalisés. Journal de Mécanique 14, 508–520.

Hashin, Z., 1970. Complex moduli of viscoelastic composites—I. General theory and application to particulate composites. International Journal of Solids and Structures 6 (5), 539–552.

Hashin, Z., Shtrikman, S., 1961. Note on a variational approach to the theory of composite elastic materials. Journal of the Franklin Institute 271 (4), 336–341.

Hashin, Z., Shtrikman, S., 1962. A variational approach to the theory of the elastic behaviour of polycrystals. Journal of the Mechanics and Physics of Solids 10 (4), 343–352.

Haupt, P., 2002. Continuum Mechanics and Theory of Materials. Springer, Berlin.

Henkes, A., Wessels, H., Mahnken, R., 2022. Physics informed neural networks for continuum micromechanics. Computer Methods in Applied Mechanics and Engineering 393, 114790.

Hill, R., 1948. A theory of the yielding and plastic flow of anisotropic metals. Proceedings of the Royal Society of London. Series A. Mathematical and Physical Sciences 193 (1033), 281–297.

Hill, R., 1963. Elastic properties of reinforced solids: Some theoretical principles. Journal of the Mechanics and Physics of Solids 11 (5), 357–372.

Hill, R., 1965. A self-consistent mechanics of composite materials. Journal of the Mechanics and Physics of Solids 13 (4), 213–222.

Hornik, K., 1991. Approximation capabilities of multilayer feedforward networks. Neural Networks 4 (2), 251–257.

Huang, T., Liu, Z., Wu, C. T., Chen, W., 2022. Microstructure-guided deep material network for rapid nonlinear material modeling and uncertainty quantification. Computer Methods in Applied Mechanics and Engineering 398, 115197.

Hutchinson, J. W., 1976. Bounds and Self-Consistent Estimates for Creep of Polycrystalline Materials. Proceedings of the Royal Society A: Mathematical, Physical and Engineering Sciences 348 (1652), 101–127.

Isidori, A., 1995. Nonlinear Control Systems. Springer, London.

Jadid, M. N., 1997. Prediction of Stress-strain Relationships for Reinforced Concrete Sections by Implementing Neural Network Techniques. Journal of King Saud University - Engineering Sciences 9 (2), 169–188.

Ji, G., Li, F., Li, Q., Li, H., Li, Z., 2011. A comparative study on Arrhenius-type constitutive model and artificial neural network model to predict high-temperature deformation behaviour in Aermet100 steel. Materials Science and Engineering: A 528 (13), 4774–4782.

Kabel, M., Böhlke, T., Schneider, M., 2014. Efficient fixed point and Newton-Krylov solvers for FFT-based homogenization of elasticity at large deformations. Computational Mechanics 54 (6), 1497–1514.

Kabel, M., Fink, A., Schneider, M., 2017. The composite voxel technique for inelastic problems. Computer Methods in Applied Mechanics and Engineering 322, 396–418.

Kabel, M., Fliegener, S., Schneider, M., 2016. Mixed boundary conditions for FFT-based homogenization at finite strains. Computational Mechanics 57 (2), 193–210.

Kabel, M., Merkert, D., Schneider, M., 2015. Use of composite voxels in FFT-based homogenization. Computer Methods in Applied Mechanics and Engineering 294, 168–188.

Kalina, K. A., Linden, L., Brummund, J., Kästner, M., 2022. FE^{ANN} - An efficient data-driven multiscale approach based on physics-constrained neural networks and automated data mining. arXiv:2207.01045 .

Kanit, T., Forest, S., Galliet, I., Mounoury, V., Jeulin, D., 2003. Determination of the size of the representative volume element for random composites: statistical and numerical approach. International Journal of Solids and Structures 40 (13-14), 3647–3679.

Katunin, A., 2019. Criticality of the Self-Heating Effect in Polymers and Polymer Matrix Composites during Fatigue, and Their Application in Non-Destructive Testing. Polymers 11 (1), 1–29.

Kehrer, L., Wood, J. T., Böhlke, T., 2020. Mean-field homogenization of thermoelastic material properties of a long fiber-reinforced thermoset and experimental investigation. Journal of Composite Materials 54 (25), 3777–3799.

Kennedy, P. K., 2013. Flow analysis of injection molds, 2nd Edition. Hanser, Munich.

Kingma, D. P., Ba, J., 2015. Adam: A Method for Stochastic Optimization. In: 3rd International Conference on Learning Representations (ICLR). San Diego.

Klein, D. K., Fernández, M., Martin, R. J., Neff, P., Weeger, O., 2022. Polyconvex anisotropic hyperelasticity with neural networks. Journal of the Mechanics and Physics of Solids 159, 104703.

Köbler, J., Magino, N., Andrä, H., Welschinger, F., Müller, R., Schneider, M., 2021. A computational multi-scale model for the stiffness degradation of short-fiber reinforced plastics subjected to fatigue loading. Computer Methods in Applied Mechanics and Engineering 373, 113522.

Köbler, J., Schneider, M., Ospald, F., Andrä, H., Müller, R., 2018. Fiber orientation interpolation for the multiscale analysis of short fiber reinforced composite parts. Computational Mechanics 61 (6), 729–750.

Kochmann, J., Ehle, L., Wulfinghoff, S., Mayer, J., Svendsen, B., Reese, S., 2018. Multiscale Modeling of Heterogeneous Structures. Springer, Cham, Ch. Efficient Multiscale FE-FFT-Based Modeling and Simulation of Macroscopic Deformation Processes with Non-linear Heterogeneous Microstructures, pp. 129–146.

Kochmann, J., Wulfinghoff, S., Reese, S., Mianroodi, J. R., Svendsen, B., 2016. Two-scale FE–FFT- and phase-field-based computational modeling of bulk microstructural evolution and macroscopic material behavior. Computer Methods in Applied Mechanics and Engineering 305, 89–110.

Koeppe, A., Bamer, F., Markert, B., 2019. An efficient Monte Carlo strategy for elasto-plastic structures based on recurrent neural networks. Acta Mechanica 230, 3279–3293.

Kosky, P., Balmer, R., Keat, W., Wise, G., 2013. Exploring Engineering. Academic Press, Boston.

Krairi, A., Doghri, I., Schalnat, J., Robert, G., Van Paepegem, W., 2019. Thermo-mechanical coupling of a viscoelastic-viscoplastic model for thermoplastic polymers: Thermodynamical derivation and experimental assessment. International Journal of Plasticity 115, 154–177.

Kuhn, J., Schneider, M., Sonnweber-Ribic, P., Böhlke, T., 2020. Fast methods for computing centroidal Laguerre tessellations for prescribed volume fractions with applications to microstructure generation of polycrystalline materials. Computer Methods in Applied Mechanics and Engineering 369, 113175.

Kuhn, J., Schneider, M., Sonnweber-Ribic, P., Böhlke, T., 2022. Generating polycrystalline microstructures with prescribed texture coefficients. Computational Mechanics accepted, 1–27.

Ladecký, M., Leute, R. J., Falsafi, A., Pultarová, I., Pastewka, L., Junge, T., Zeman, J., 2022. Optimal FFT-accelerated Finite Element Solver for Homogenization. arXiv:2203.02962 .

Lahellec, N., Suquet, P., 2007a. Effective behavior of linear viscoelastic composites: A time-integration approach. International Journal of Solids and Structures 44 (2), 507–529.

Lahellec, N., Suquet, P., 2007b. On the effective behavior of nonlinear inelastic composites: I. Incremental variatonal principles. Journal of the Mechanics and Physics of Solids 55, 1932–1963.

Largenton, R., Michel, J.-C., Suquet, P., 2014. Extension of the nonuniform transformation field analysis to linear viscoelastic composites in the presence of aging and swelling. Mechanics of Materials 73, 76–100.

Le, B. A., Yvonnet, J., He, Q.-C., 2015. Computational homogenization of nonlinear elastic materials using neural networks. International Journal for Numerical Methods in Engineering 104 (12), 1061–1084.

Levin, V. M., 1967. On the coefficients of thermal expansion of heterogeneous materials. Mechanics of Solids 2, 58–61.

Li, H.-Y., Wei, D.-D., Li, Y.-H., Wang, X.-F., 2012. Application of artificial neural network and constitutive equations to describe the hot compressive behavior of 28CrMnMoV steel. Materials & Design 35, 557–562.

Li, J., Romero, I., Segurado, J., 2019. Development of a thermo-mechanically coupled crystal plasticity modeling framework: Application to polycrystalline homogenization. International Journal of Plasticity 119, 313–330.

Liu, I., 2002. Continuum mechanics. Springer, Berlin.

Liu, Z., 2020. Deep material network with cohesive layers: Multi-stage training and interfacial failure analysis. Computer Methods in Applied Mechanics and Engineering 363, 112913.

Liu, Z., 2021. Cell division in deep material networks applied to multiscale strain localization modeling. Computer Methods in Applied Mechanics and Engineering 384, 113914.

Liu, Z., Bessa, M. A., Liu, W. K., 2016. Self-consistent clustering analysis: An efficient multi-scale scheme for inelastic heterogeneous materials. Computer Methods in Applied Mechanics and Engineering 306, 319–341.

Liu, Z., Fleming, M., Liu, W. K., 2018a. Microstructural material database for self-consistent clustering analysis of elastoplastic strain softening materials. Computer Methods in Applied Mechanics and Engineering 330, 547–577.

Liu, Z., Kafka, O. L., Yu, C., Liu, W. K., 2018b. Data-driven self-consistent clustering analysis of heterogeneous materials with crystal plasticity. In: Advances in Computational Plasticity. Cham.

Liu, Z., Wei, H., Huang, T., Wu, C. T., 2020. Intelligent multiscale simulation based on process-guided composite database. In: 16th International LS-DYNA Users Conference. Detroit.

Liu, Z., Wu, C. T., 2019. Exploring the 3D architectures of deep material network in data-driven multiscale mechanics. Journal of the Mechanics and Physics of Solids 127, 20–46.

Liu, Z., Wu, C. T., Koishi, M., 2019a. A deep material network for multiscale topology learning and accelerated nonlinear modeling of heterogeneous materials. Computer Methods in Applied Mechanics and Engineering 345, 1138–1168.

Liu, Z., Wu, C. T., Koishi, M., 2019b. Transfer learning of deep material network for seamless structure–property predictions. Computational Mechanics 64 (2), 451–465.

Loshchilov, I., Hutter, F., 2017. SGDR: Stochastic Gradient Descent with Warm Restarts. In: 5th International Conference on Learning Representations (ICLR). Toulon.

Magino, N., Köbler, J., Andrä, H., Welschinger, F., Müller, R., Schneider, M., 2022a. A multiscale high-cycle fatigue-damage model for the stiffness degradation of fiber-reinforced materials based on a mixed variational framework. Computer Methods in Applied Mechanics and Engineering 388, 114198.

Magino, N., Köbler, J., Andrä, H., Welschinger, F., Müller, R., Schneider, M., 2022b. A space-time upscaling technique for modeling high-cycle fatigue-damage of short-fiber reinforced composites. Composites Science and Technology 233, 109340.

Mandel, J., 1965. Generalisation de la theorie de plasticite de W. T. Koiter. International Journal of Solids and Structures 1 (3), 273–295.

Marfia, S., 2005. Micro–macro analysis of shape memory alloy composites. International Journal of Solids and Structures 42 (13), 3677–3699.

Marfia, S., Sacco, E., 03 2005. Micromechanics and Homogenization of SMA-Wire-Reinforced Materials. Journal of Applied Mechanics 72 (2), 259–268.

Marfia, S., Sacco, E., 2007. Analysis of SMA composite laminates using a multiscale modelling technique. International Journal for Numerical Methods in Engineering 70 (10), 1182–1208.

Masi, F., Stefanou, I., 2022. Multiscale modeling of inelastic materials with Thermodynamics-based Artificial Neural Networks (TANN). Computer Methods in Applied Mechanics and Engineering 398, 115190.

Masi, F., Stefanou, I., Vannucci, P., Maffi-Berthier, V., 2021a. Material modeling via Thermodynamics-based Artificial Neural Networks. In: Workshop on Joint Structures and Common Foundations of Statistical Physics, Information Geometry and Inference for Learning. Vol. 361. Cham.

Masi, F., Stefanou, I., Vannucci, P., Maffi-Berthier, V., 2021b. Thermodynamics-based Artificial Neural Networks for constitutive modeling. Journal of the Mechanics and Physics of Solids 147, 104277.

Matouš, K., Geers, M. G. D., Kouznetsova, V. G., Gillman, A., 2017. A review of predictive nonlinear theories for multiscale modeling of heterogeneous materials. Journal of Computational Physics 330, 192–220.

McKay, M. D., Beckman, R. J., Conover, W. J., 1979. A Comparison of Three Methods for Selecting Values of Input Variables in the Analysis of Output from a Computer Code. Technometrics 21 (2), 239–245.

Mehta, A., Schneider, M., 2022. A sequential addition and migration method for generating microstructures of short fibers with prescribed length distribution. Computational Mechanics , 1–23.

Meraghni, F., Blakeman, C. J., Benzeggagh, M. L., 1996. Effect of interfacial decohesion on stiffness reduction in a random discontinuous-fibre composite containing matrix microcracks. Composites Science and Technology 56 (5), 541–555.

Meyer, N., 2021. Mesoscale simulation of the mold filling process of Sheet Molding Compound. Doctoral thesis, Karlsruher Institut für Technologie (KIT), Karlsruhe.

Meyer, N., Gajek, S., Görthofer, J., Hrymak, A., Kärger, L., Henning, F., Schneider, M., Böhlke, T., 2023. A probabilistic virtual process chain to quantify process-induced uncertainties in Sheet Molding Compounds. Composites Part B: Engineering 249, 110380.

Michel, J. C., Suquet, P., 2003. Nonuniform transformation field analysis. International Journal of Solids and Structures 40, 6937–6955.

Michel, J.-C., Suquet, P., 2004. Computational analysis of nonlinear composite structures using the nonuniform transformation field analysis. Computer Methods in Applied Mechanics and Engineering 193 (48), 5477–5502.

Michel, J.-C., Suquet, P., 2016a. A model-reduction approach in micromechanics of materials preserving the variational structure of constitutive relations. Journal of the Mechanics and Physics of Solids 90, 254–285.

Michel, J.-C., Suquet, P., 2016b. A model-reduction approach to the micromechanical analysis of polycristalline materials. Computational Mechanics 57 (3), 483–508.

Michel, J.-C., Suquet, P., 2017. Effective potentials in nonlinear polycrystals and quadrature formulae. Proceedings of the Royal Society A 473, 20170213.

Mielke, A., 2006. Multifield Problems in Solid and Fluid Mechanics. Springer, Berlin, Ch. A Mathematical Framework for Generalized Standard Materials in the Rate-Independent Case, pp. 399–428.

Miles, R. E., 1965. On Random Rotations in $\mathbb{R}^3$. Biometrika 52 (3/4), 636–639.

Milton, G. W., 1986. Modelling the Properties of Composites by Laminates. In: Homogenization and Effective Moduli of Materials and Media. The IMA Volumes in Mathematics and its Applications. New York.

Milton, G. W., 2002. The Theory of Composites. Cambridge University Press, Cambridge.

Milton, G. W., 2020. Some open problems in the theory of composites. arXiv:2008.03394 .

Mojumder, S., Gao, J., Liu, W. K., 2021. Self-consistent clustering analysis for modeling of theromelastic heterogeneous materials. AIP Conference Proceedings 2324 (1), 030029.

Montgomery-Smith, S., He, W., Jack, D. A., Smith, D. E., 2011. Exact tensor closures for the three-dimensional Jeffery's equation. Journal of Fluid Mechanics 680, 321–335.

Mori, T., Tanaka, K., 1973. Average stress in matrix and average elastic energy of materials with misfitting inclusions. Acta Metallurgica 21 (5), 571–574.

Moulinec, H., Suquet, P., 1994. A fast numerical method for computing the linear and nonlinear mechanical properties of composites. Comptes Rendus de l'Académie des Sciences. Série II 318 (11), 1417–1423.

Moulinec, H., Suquet, P., 1998. A numerical method for computing the overall response of nonlinear composites with complex microstructure. Computer Methods in Applied Mechanics and Engineering 157, 69–94.

Mozaffar, M., Bostanabad, R., Chen, W., Ehmann, K., Cao, J., Bessa, M. A., 2019. Deep learning predicts path-dependent plasticity. Proceedings of the National Academy of Sciences 116 (52), 26414–26420.

Müller, I., 1985. Thermodynamics. Interaction of Mechanics and Mathematics Series. Pitman, Boston.

Nebozhyn, M. V., Gilormini, P., Ponte Castañeda, P., 2001. Variational self-consistent estimates for cubic viscoplastic polycrystals: The effects of grain anisotropy and shape. Journal of the Mechanics and Physics of Solids 49, 313–340.

Neumann, R., Böhlke, T., 02 2016. Hashin-Shtrikman type mean field model for the two-scale simulation of the thermomechanical processing of steel. International Journal of Plasticity 77, 1–29.

Nguyen, V. D., Noels, L., 2022. Interaction-based material network: A general framework for (porous) microstructured materials. Computer Methods in Applied Mechanics and Engineering 389, 114300.

Nguyen-Thanh, V. M., Nguyen, L. T. K., Rabczuk, T., Zhuang, X., 2019. A surrogate model for computational homogenization of elastostatics at finite strain using the HDMR-based neural network approximator. arXiv:1906.02005 .

Norris, A. N., 1985. A differential scheme for the effective moduli of composites. Mechanics of Materials 4 (1), 1–16.

Novák, J., Kučerová, A., Zeman, J., 2012. Compressing random microstructures via stochastic Wang tilings. Physical Review E 86, 040104.

Novák, J., Kučerová, A., Zeman, J., 2013. Microstructural enrichment functions based on stochastic Wang tilings. Modelling and Simulation in Materials Science and Engineering 21 (2), 025014.

Ospald, F., 2014. Numerical simulation of injection molding using openfoam. PAMM 14 (1), 673–674.

Özdemir, I., Brekelmans, W. A. M., Geers, M. G. D., 2008a. Computational homogenization for heat conduction in heterogeneous solids. International Journal for Numerical Methods in Engineering 73 (2), 185–204.

Özdemir, I., Brekelmans, W. A. M., Geers, M. G. D., 2008b. FE^2 computational homogenization for the thermo-mechanical analysis of heterogeneous solids. Computer Methods in Applied Mechanics and Engineering 198 (3), 602–613.

Paszke, A., Gross, S., Chintala, S., Chanan, G., Yang, E., DeVito, Z., Lin, Z., Desmaison, A., Antiga, L., Lerer, A., 2017. Automatic Differentiation in PyTorch. In: NIPS 2017 Workshop on Autodiff. Long Beach.

Penumadu, D., Zhao, R., 1999. Triaxial compression behavior of sand and gravel using artificial neural networks (ANN). Computers and Geotechnics 24 (3), 207–230.

Ponte Castañeda, P., Suquet, P., 1997. Nonlinear Composites. In: Advances in Applied Mechanics. Vol. 34 of Advances in Applied Mechanics. Elsevier, Amsterdam, pp. 171–302.

Raissi, M., Perdikaris, P., Karniadakis, G. E., 2019. Physics-informed neural networks: A deep learning framework for solving forward and inverse problems involving nonlinear partial differential equations. Journal of Computational Physics 378, 686–707.

Rall, L. B., 1981. Automatic Differentiation: Techniques and Applications. Springer, Berlin.

Reddi, S. J., Kale, S., Kumar, S., 2018. On the Convergence of Adam and Beyond. In: 6th International Conference on Learning Representations (ICLR). Vancouver.

Renard, J., Marmonier, M. F., 1987. Etude de l'initiation de l'endommagement dans la matrice d'un materiau composite par une methode d'homogenisation. Aerospace Science and Technology 9, 37–51.

Renardy, M., Rogers, R. C., 2004. An introduction to partial differential equations. Springer, New York.

Rix, J., Haas, S., Teixeira, J., 1995. Virtual prototyping: Virtual environments and the product design process. Springer, New York.

Rockafellar, R. T., 1970. Convex Analysis. Princeton University Press, Princeton.

Ruder, S., 2016. An overview of gradient descent optimization algorithms. arXiv:1609.04747 .

Rugh, W. J., 1981. Nonlinear System Theory: The Volterra/Wiener Approach. The Johns Hopkins University Press, Baltimore.

Rumelhart, D. E., Hinton, G. E., Williams, R. J., 1986a. Learning representations by back-propagating errors. Nature 323 (6088), 533–536.

Rumelhart, D. E., McClelland, J. L., Group, P. R., 1986b. Parallel Distributed Processing: Explorations in the Microstructure of Cognition, Vol. 1: Foundations. MIT Press, Cambridge.

Sanchez-Palencia, E., 1980. Non-homogeneous media and vibration theory. No. 127 in Lecture Notes in Physics. Springer, New York.

Sandberg, I. W., 1982a. Expansions for nonlinear systems. The Bell System Technical Journal 61 (2), 159–199.

Sandberg, I. W., 1982b. Volterra Expansions for Time-Varying Nonlinear Systems. Bell System Technical Journal 61 (2), 201–225.

Sandberg, I. W., 1983. Series expansions for nonlinear systems. Circuits, Systems and Signal Processing 2 (1), 77–87.

Schemmann, M., Brylka, B., Gajek, S., Böhlke, T., 2015. Parameter Identification by Inverse Modelling of Biaxial Tensile Tests for Discontinous Fiber Reinforced Polymers. PAMM 15 (1), 355–356.

Schemmann, M., Gajek, S., Böhlke, T., 2018. Biaxial Tensile Tests and Microstructure-Based Inverse Parameter Identification of Inhomogeneous SMC Composites. In: Advances in Mechanics of Materials and Structural Analysis: In Honor of Reinhold Kienzler. Vol. 80. Springer, Berlin, pp. 329–342.

Scheunemann, L., Balzani, D., Brands, D., Schröder, J., 2015. Analysis and Computation of Microstructure in Finite Plasticity. Springer, New York, Ch. Construction of Statistically Similar RVEs, pp. 219–256.

Schneider, M., 2017. The Sequential Addition and Migration method to generate representative volume elements for the homogenization of short fiber reinforced plastics. Computational Mechanics 59, 247–263.

Schneider, M., 2019a. On the Barzilai-Borwein basic scheme in FFT-based computational homogenization. International Journal for Numerical Methods in Engineering 118 (8), 482–494.

Schneider, M., 2019b. On the mathematical foundations of the self-consistent clustering analysis for non-linear materials at small strains. Computer Methods in Applied Mechanics and Engineering 354, 783–801.

Schneider, M., 2021. A review of nonlinear FFT-based computational homogenization methods. Acta Mechanica 232 (6), 2051–2100.

Schneider, M., Hofmann, T., Andrä, H., Lechner, P., Ettemeyer, F., Volk, W., Steeb, H., 2018. Modelling the microstructure and computing effective elastic properties of sand core materials. International Journal of Solids and Structures 143, 1–17.

Schneider, M., Ospald, F., Kabel, M., 2016. Computational homogenization of elasticity on a staggered grid. International Journal for Numerical Methods in Engineering 105 (9), 693–720.

Schneider, M., Wicht, D., Böhlke, T., 2019. On polarization-based schemes for the FFT-based computational homogenization of inelastic materials. Computational Mechanics 64 (4), 1073–1095.

Schöttl, L., Dörr, D., Pinter, P., Weidenmann, K. A., Elsner, P., Kärger, L., 2020. A novel approach for segmenting and mapping of local fiber orientation of continuous fiber-reinforced composite laminates based on volumetric images. NDT & E International 110, 102194.

Schöttl, L., Kolb, P., Liebig, W. V., Weidenmann, K. A., Inal, K., Elsner, P., 2020. Crack characterization of discontinuous fiber-reinforced composites by using micro-computed tomography: Cyclic in-situ testing, crack segmentation and crack volume fraction. Composites Communications 21, 100384.

Schöttl, L., Weidenmann, K. A., Sabiston, T., Inal, K., Elsner, P., 2021. Fiber bundle tracking method to analyze sheet molding compound microstructure based on computed tomography images. NDT & E International 117, 102370.

Segurado, J., Llorca, J., González, C., 2002. On the accuracy of mean-field approaches to simulate the plastic deformation of composites. Scripta Materialia 46 (7), 525–529.

Sengupta, A., Papadopoulos, P., Taylor, R. L., 2012. A multiscale finite element method for modeling fully coupled thermomechanical problems in solids. International Journal for Numerical Methods in Engineering 91 (13), 1386–1405.

Shen, H., Nutt, S., Hull, D., 2004a. Direct observation and measurement of fiber architecture in short fiber-polymer composite foam through micro-CT imaging. Composites Science and Technology 64 (13), 2113–2120.

Shen, Y., Chandrashekhara, K., Breig, W. F., Oliver, L. R., 2004b. Neural Network Based Constitutive Model for Rubber Material. Rubber Chemistry and Technology 77 (2), 257–277.

Simo, J. C., Hughes, T. J. R., 1998. Computational Inelasticity. Springer, New York.

Smit, R. J. M., Brekelmans, W. A. M., Meijer, H. E. H., 1998. Prediction of the mechanical behavior of nonlinear heterogeneous systems by multi-level finite element modeling. Computer Methods in Applied Mechanics and Engineering 155 (1), 181–192.

Smith, L. N., Topin, N., 2018. Super-convergence: very fast training of neural networks using large learning rates. In: 6th International Conference on Learning Representations (ICLR). Vancouver.

Sobol, I. M., 1967. Distribution of points in a cube and approximate evaluation of integrals. USSR Computational Mathematics and Mathematical Physics 7, 86–112.

Spahn, J., Andrä, H., Kabel, M., Müller, R., 2014. A multiscale approach for modeling progressive damage of composite materials using fast Fourier transforms. Computer Methods in Applied Mechanics and Engineering 268, 871–883.

Srinivasu, G., Rao, R. N., Nandy, T. K., Bhattacharjee, A., 2012. Artificial neural network approach for prediction of titanium alloy stress-strain curve. Procedia Engineering 38, 3709–3714.

Stone, M. H., 1948. The Generalized Weierstrass Approximation Theorem. Mathematics Magazine 21 (4), 167–184.

Stránský, J., Vorel, J., Zeman, J., Šejnoha, M., 2011. Mori-Tanaka Based Estimates of Effective Thermal Conductivity of Various Engineering Materials. Micromachines 2 (2), 129–149.

Suquet, P., 1985. Elements of Homogenization for Inelastic Solid Mechanics. In: Homogenization Techniques for Composite Media. Springer, New York, Ch. 4, pp. 193–278.

Suquet, P. (Ed.), 1997. Continuum Micromechanics. Springer, Berlin.

Tikarrouchine, E., Chatzigeorgiou, G., Chemisky, Y., Meraghni, F., 2019. Fully coupled thermo-viscoplastic analysis of composite structures by means of multi-scale three-dimensional finite element computations. International Journal of Solids and Structures 164, 120–140.

Torquato, S., 2005. Random Heterogeneous Materials: Microstructure and Macroscopic Properties. Interdisciplinary Applied Mathematics. Springer, New York.

Trauth, A., 2020. Characterisation and Modelling of Continuous-Discontinuous Sheet Moulding Compound Composites for Structural Applications. Doctoral thesis, Karlsruhe Institute of Technology (KIT), Karlsruhe.

Trauth, A., Pinter, P., Weidenmann, K. A., 2017. Investigation of Quasi-Static and Dynamic Material Properties of a Structural Sheet Molding Compound Combined with Acoustic Emission Damage Analysis. Journal of Composites Science 1 (2), 1–18.

Truesdell, C., 1984. Rational Thermodynamics. Springer, New York.

Truesdell, C., Noll, W., 2004. The Non-Linear Field Theories of Mechanics. Springer, Berlin.

Truesdell, C., Toupin, R. A., 1960. Encyclopedia of Physics: Principles ofThermodynamics and Statics. Springer, Berlin.

v. Mises, R., 1913. Mechanik der festen Körper im plastisch-deformablen Zustand. Nachrichten von der Gesellschaft der Wissenschaften zu Göttingen, Mathematisch-Physikalische Klasse 1913, 582–592.

Vince, J., 2017. Mathematics for Computer Graphics. Undergraduate Topics in Computer Science. Springer, London.

Volterra, V., 1887. Sopra le funzioni che dipendono da altre funzioni. Tipografia della R. Accademia dei Lincei, Rome.

Šilhavý, M., 1997. The Mechanics and Thermodynamics of Continuous Media. Texts and Monographs in Physics. Springer, Berlin.

Weller, H. G., Tabor, G., Jasak, H., Fureby, C., 1998. A tensorial approach to computational continuum mechanics using object-oriented techniques. Computers in Physics 12 (6), 620–631.

Wessels, H., Weißenfels, C., Wriggers, P., 2020. The neural particle method – An updated Lagrangian physics informed neural network for computational fluid dynamics. Computer Methods in Applied Mechanics and Engineering 368, 113127.

Wicht, D., Schneider, M., Böhlke, T., 2020a. An efficient solution scheme for small-strain crystal-elasto-viscoplasticity in a dual framework. Computer Methods in Applied Mechanics and Engineering 358, 112611.

Wicht, D., Schneider, M., Böhlke, T., 2020b. Computing the effective response of heterogeneous materials with thermomechanically coupled constituents by an implicit FFT-based approach. International Journal for Numerical Methods in Engineering 122 (5), 1307–1332.

Wicht, D., Schneider, M., Böhlke, T., 2020c. On Quasi-Newton methods in FFT-based micromechanics. International Journal for Numerical Methods in Engineering online, 1–34.

Williams, M. L., Ferry, R. F. L. J. D., 1955. The Temperature Dependence of Relaxation Mechanisms in Amorphous Polymers and Other Glass-forming Liquids. Journal of the American Chemical Society 77 (14), 3701–3707.

Williams, S., Philipse, A., 2003. Random packings of spheres and spherocylinders simulated by mechanical contraction. Physical Review E 67, 1–9.

Wu, L., Nguyen, V. D., Kilingar, N. G., Noels, L., 2020. A recurrent neural network-accelerated multi-scale model for elasto-plastic heterogeneous materials subjected to random cyclic and non-proportional loading paths. Computer Methods in Applied Mechanics and Engineering 369, 113234.

Wulfinghoff, S., Cavaliere, F., Reese, S., 2018. Model order reduction of nonlinear homogenization problems using a Hashin-Shtrikman type finite element method. Computer Methods in Applied Mechanics and Engineering 330, 149–179.

Wulfinghoff, S., Fassin, M., Reese, S., 2017. A damage growth criterion for anisotropic damage models motivated from micromechanics. International Journal of Solids and Structures 121, 21–32.

Xu, K., Huang, D. Z., Darve, E., 2021. Learning constitutive relations using symmetric positive definite neural networks. Journal of Computational Physics 428, 110072.

Yu, C., Kafka, O. L., Liu, W. K., 2018. Self-consistent clustering analysis for multiscale modeling at finite strains. Computer Methods in Applied Mechanics and Engineering in press, 1–34.

Yvonnet, J., Gonzalez, D., He, Q.-C., 07 2009. Numerically explicit potentials for the homogenization of nonlinear elastic heterogeneous materials. Computer Methods in Applied Mechanics and Engineering 198, 2723–2737.

Yvonnet, J., Monteiro, E., He, Q.-C., 2013. Computational homogenization method and reduced database model for hyperelastic heterogeneous structures. International Journal for Multiscale Computational Engineering 11 (3), 201–225.

Zeman, J., de Geus, T. W. J., Vondřejc, J., Peerlings, R. H. J., Geers, M. G. D., 2017. A finite element perspective on nonlinear FFT-based micromechanical simulations. International Journal for Numerical Methods in Engineering 111 (10), 903–926.

Zeman, J., Vondřejc, J., Novak, J., Marek, I., 2010. Accelerating a FFT-based solver for numerical homogenization of periodic media by conjugate gradients. Journal of Computational Physics 229 (21), 8065–8071.

Zhao, H., Huang, Z., Zou, Z., 2014. Simulating the Stress-Strain Relationship of Geomaterials by Support Vector Machine. Mathematical Problems in Engineering 2014, 1–7.

Zhou, X., Shen, J., 2015. Least Squares Support Vector Machine for Constitutive Modeling of Clay. International Journal of Engineering 28 (11), 1571–1578.

Zhu, Q., Liu, Z., Yan, J., 2021. Machine Learning for Metal Additive Manufacturing: Predicting Temperature and Melt Pool Fluid Dynamics Using Physics-Informed Neural Networks. Computational Mechanics 67 (2), 619–635.

Schriftenreihe Kontinuumsmechanik im Maschinenbau
Karlsruher Institut für Technologie (KIT)
(ISSN 2192-693X)

Band 1 Felix Fritzen
Microstructural modeling and computational homogenization of the physically linear and nonlinear constitutive behavior of micro-heterogeneous materials.
ISBN 978-3-86644-699-1

Band 2 Rumena Tsotsova
Texturbasierte Modellierung anisotroper Fließpotentiale.
ISBN 978-3-86644-764-6

Band 3 Johannes Wippler
Micromechanical finite element simulations of crack propagation in silicon nitride.
ISBN 978-3-86644-818-6

Band 4 Katja Jöchen
Homogenization of the linear and non-linear mechanical behavior of polycrystals.
ISBN 978-3-86644-971-8

Band 5 Stephan Wulfinghoff
Numerically Efficient Gradient Crystal Plasticity with a Grain Boundary Yield Criterion and Dislocation-based Work-Hardening.
ISBN 978-3-7315-0245-6

Band 6 Viktor Müller
Micromechanical modeling of short-fiber reinforced composites.
ISBN 978-3-7315-0454-2

Die Bände sind unter www.ksp.kit.edu als PDF frei verfügbar oder als Druckausgabe bestellbar.

Band 7 Florian Rieger
Work-hardening of dual-phase steel.
ISBN 978-3-7315-0513-6

Band 8 Vedran Glavas
Micromechanical Modeling and Simulation of Forming Processes.
ISBN 978-3-7315-0602-7

Band 9 Eric Bayerschen
Single-crystal gradient plasticity with an accumulated plastic slip: Theory and applications.
ISBN 978-3-7315-0606-5

Band 10 Bartholomäus Brylka
Charakterisierung und Modellierung der Steifigkeit von langfaserverstärktem Polypropylen.
ISBN 978-3-7315-0680-5

Band 11 Rudolf Neumann
Two-Scale Thermomechanical Simulation of Hot Stamping.
ISBN 978-3-7315-0714-7

Band 12 Mauricio Lobos Fernández
Homogenization and materials design of mechanical properties of textured materials based on zeroth-, first- and second-order bounds of linear behavior.
ISBN 978-3-7315-0770-3

Band 13 Malte Schemmann
Biaxial Characterization and Mean-field Based Damage Modeling of Sheet Molding Compound Composites.
ISBN 978-3-7315-0818-2

Band 14 Jürgen Albiez
Finite element simulation of dislocation based plasticity and diffusion in multiphase materials at high temperature.
ISBN 978-3-7315-0918-9

Die Bände sind unter www.ksp.kit.edu als PDF frei verfügbar oder als Druckausgabe bestellbar.

Band 15 Maria Loredana Kehrer
Thermomechanical Mean-Field Modeling and Experimental Characterization of Long Fiber-Reinforced Sheet Molding Compound Composites.
ISBN 978-3-7315-0924-0

Band 16 Peter Hölz
A dynamic and statistical analysis of the temperature- and fatigue behavior of a race power unit – The effect of different thermodynamic states.
ISBN 978-3-7315-0988-2

Band 17 Andreas Prahs
A Gradient Crystal Plasticity Theory Based on an Extended Energy Balance.
ISBN 978-3-7315-1025-3

Band 18 Johannes Ruck
Modeling martensitic phase transformation in dual phase steels based on a sharp interface theory.
ISBN 978-3-7315-1072-7

Band 19 Hannes Erdle
Modeling of Dislocation - Grain Boundary Interactions in Gradient Crystal Plasticity Theories.
ISBN 978-3-7315-1196-0

Band 20 Johannes Görthofer
Microstructure generation and micromechanical modeling of sheet molding compound composites.
ISBN 978-3-7315-1205-9

Band 21 Daniel Wicht
Efficient fast Fourier transform-based solvers for computing the thermomechanical behavior of applied materials.
ISBN 978-3-7315-1220-2

Band 22 Juliane Lang
Thermomechanical Modeling and Experimental Characterization of Sheet Molding Compound Composites.
ISBN 978-3-7315-1232-5

Die Bände sind unter www.ksp.kit.edu als PDF frei verfügbar oder als Druckausgabe bestellbar.

Band 23 Julian Karl Bauer
Fiber Orientation Tensors and Mean Field Homogenization: Application to Sheet Molding Compound.
ISBN 978-3-7315-1262-2

Band 24 Sebastian Gajek
Deep material networks for efficient scale-bridging in thermomechanical simulations of solids.
ISBN 978-3-7315-1278-3

We investigate the data-driven and micromechanics-inspired homogenization approach called deep material networks (DMN), which act as surrogate models for the microscopic problem in two-scale simulations. We lay the mathematical foundation of DMNs by showing that the effective inelastic material behavior of a composite is determined by linear elastic localization to first order in the strain rate. Furthermore, we present a new DMN formulation, which is characterized by a reduced number of degrees of freedom. We present a robust and efficient solution technique for nonlinear DMNs allowing for accelerating complex macroscopic two-scale simulations with minimal computational effort.

A new interpolation technique is presented to account for fluctuating microstructure characteristics in macroscopic simulations. We demonstrate the efficiency of the approach by considering a complete process chain of a component made of a short fiber reinforced polyamide. Furthermore, the approach is used to determine process-induced uncertainties in sheet molding compound components.

We extend the DMN framework to treat thermomechanically coupled multiscale problems. We show that our approach predicts self-heating effects in short fiber reinforced polymers with high accuracy and demonstrate that considering such effects is essential for the multiscale analysis of polymer-based composite materials.

ISSN 2192-693X
ISBN 978-3-7315-1278-3

Gedruckt auf FSC-zertifiziertem Papier